On the Spin-Dynamics of the Quasi-One-Dimensional, Frustrated Quantum Magnet Li_2CuO_2

Studies by means of Inelastic Neutron Scattering and Thermodynamic Methods

Dissertation

zur Erlangung des akademischen Grades
Doctor rerum naturalium
(Dr. rer. nat.)

vorgelegt

der Fakultät Mathematik und Naturwissenschaften
der Technical University Dresden

von

Dipl. Phys. Wolfram E. A. Lorenz
geboren am 23. April 1978 in Dresden

Eingereicht am 15. April 2011

Die Dissertation wurde in der Zeit von Apr. 2007
bis Apr. 2011 am IFW Dresden angefertigt.

TECHNISCHE
UNIVERSITÄT
DRESDEN

Leibniz Institute
for Solid State and
Materials Research
Dresden

"throwing fire at the sun" [1]

1. Gutachter: Prof. Dr. rer. nat. habil. Bernd Büchner
2. Gutachter: Prof. Dr. rer. nat. Rüdiger Klingeler

Verteidigt am 27. Juni 2011

Kurzfassung

Die magnetischen Eigenschaften von Li_2CuO_2 sind seit mehr als zwei Jahrzehnten Gegenstand theoretischen und experimentellen Interesses. Über die genaue Natur der magnetischen Wechselwirkungen in diesem Isolator konnte jedoch keine Einigkeit erzielt werden. Während das Material von Seiten theoretischer Untersuchungen als quasi-eindimensionaler Magnet mit starken ferromagnetischen Kopplungen entlang der Kette verstanden wurde, legten experimentelle Studien dominierende dreidimensionale Zwischenkettenkopplungen nahe.

Im Rahmen dieser Dissertation werden auf der Grundlage von Untersuchungen des magnetischen Anregungsspektrums mittels inelastischer Neutronenstreuung und dessen Analyse innerhalb eines Spinwellenmodels die führenden magnetischen Wechselwirkungen in Li_2CuO_2 bestimmt. Es wird zweifelsfrei nachgewiesen, dass das Material eine quasi-eindimensionale Spinkettenverbindung darstellt. Insbesondere kann die Konkurrenz von ferro- und antiferromagnetischen Wechselwirkungen entlang der Ketten nachgewiesen werden. Die Anwendbarkeit einer Spinwellenanalyse dieses niedrigdimensionalen Spin-1/2 Systems wird gezeigt. Das magnetische Phasendiagramm wird mittels Messungen von spezifischer Wärme, thermischer Ausdehnung und Magnetostriktion sowie der Magnetisierung in statischen und gepulsten Magnetfeldern untersucht und im Bezug auf die Austauschwechselwirkungen diskutiert. Aufgrund seiner einfachen kristallographischen und magnetischen Struktur stellt Li_2CuO_2 ein potentiell wertvolles Modellsystem in der Klasse der Spinkettenverbindungen mit konkurrierenden ferro- und antiferromagnetischen Wechselwirkungen dar.

Abstract

The magnetic properties of Li_2CuO_2 have attracted interest since more than two decades, both in theory and experiment. Despite these efforts, the precise nature of the magnetic interactions in this insulator remained an issue of controversial debate. From theoretical studies, the compound was understood as a quasi-one-dimensional magnet with strong ferromagnetic interactions along the chain, while in contrast, experimentally studies suggested dominant three-dimensional inter-chain interactions.

In this thesis, the leading magnetic exchange interactions of Li_2CuO_2 are determined on the basis of a detailed inelastic neutron scattering study of the magnetic excitation spectrum, analyzed within spin-wave theory. It is unequivocally shown, that the material represents a quasi-one-dimensional spin-chain compound. In particular, the competition of ferro- and antiferromagnetic interactions in the chain has been evidenced. The applicability of a spin-wave model for analysis of this low-dimensional spin-1/2 system is shown. The magnetic phase diagram of Li_2CuO_2 is studied by specific heat, thermal expansion and magnetostriction measurements as well as magnetization measurements in both static and pulsed magnetic fields. The phase diagram is discussed with respect to the exchange interactions. With its simple crystallographic and magnetic structure, Li_2CuO_2 may serve as a worthwhile model system in the class of spin-chain compounds with competing ferromagnetic and antiferromagnetic interactions.

Contents

1. Motivation

The notion of the existence of a single objective world beyond mere subjective perception is a commonly accepted concept. It may serve to describe a principle of science, characterizing it as a form of communication intended to achieve agreement on descriptions of perceptions in a society formed by individuals. Modern natural science limits its activity to the processing of generalizing descriptions that can be verified empirically. The fundamental demand on its proposed descriptions of some system is reproducibility. This severe limitation has proven useful, as in particular engineering can draw profit from it. Another aspect of the descriptions developed in natural science is that in narrow contexts they are found related to another in a hierarchical or causal manner. Narrow means, that on the extreme end the construction of the universe from sub-atomic particles is presumably the best example of the chicken or egg problem, but also the fact that any potential description of a piece of metal by a 10^{23} particle wave function is not a meaningful description thereof [2]. Relations of such descriptions give rise to the discovery of laws applying to systems composed of comparable constituents or possessing related symmetries or topologies. The apparent existence of such laws not only guaranties, that the description of a piece of iron achieved today is of good use for the description of equally manufactured pieces of iron of not too different shape and size tomorrow, it furthermore ensures that this description is helpful to understand the properties of a newly developed iron-based alloy, a piece of copper or melting water ice.

This thesis is dedicated to experimental studies of the low temperature magnetic properties of the crystalline material Li_2CuO_2. The scientific interest in the properties of this material, which are studied already since 1970 [3] is not much motivated by promising technical applications. In fact, possible utilization of the material as an additive in Lithium-ion batteries (e.g. [4–6]) has been studied, as well as its potential for chemisorption of CO_2 at high temperatures [7]. At the same time, any application of its room temperature magnetic properties, of which detailed understanding has been achieved only recently [8, 9], appears far from tangible. The primary motivation to investigate this material originates from its simplicity.

Having a simple system at hand, it is tempting to address the challenge of finding a set of descriptions that capture its fundamental properties. Such attempt is even more appealing if it reaches out beyond the sake of itself, i.e. promises insight into a broad range of interesting, akin, but more complex systems. Continued systematic research on strongly correlated materials has proven a great potential to disclose unanticipated prospects to utilize non-trivial new mechanisms and emerging properties (see e.g. [10]). These materials are however often complex and in order to understand their physics, the comparison with model compounds is an often crucial approach.

It is in this sense that Li_2CuO_2 may be appreciated as an indeed simple system of which to gain deep and extensive understanding is potentially promising. This thesis strives to represent a valiant step into this direction.

The compound is of interest in a variety of fields of condensed matter physics. First of all, it is a structurally simple cuprate with well localized magnetic moments on all sites, no structural transitions and rather weak magnetic interactions. Its edge-sharing CuO_4-plaquettes make it an interesting system to study the general electronic properties of cuprates. Secondly, it is a prototypical representative of ferromagnetic-antiferromagnetically frustrated spin-chain compounds which only recently have attracted a lot of attention as they exhibit unconventional excitations, ground states and respective quantum phase transitions. Being well investigated and easily accessible to both experimental and theoretical studies, Li_2CuO_2 may serve as a reference compound towards the understanding of the more complex members of this class of spin-chain systems. Eventually, Li_2CuO_2 also exhibits notable inter-chain couplings which compete with another. Due to the simplicity of its low temperature magnetic structure, the compound is excellently qualified to gain insight into the influence of inter-chain interactions onto the behavior of the spin-chains. The materials closely related to Li_2CuO_2 all possess non-negligible inter-chain couplings. It is therefor of interest to study the stability of the properties of the isolated chains under the presence of inter-chain interactions.

The results of this work are captured in this document. Its general layout is as follows:

- In Part I, the material Li_2CuO_2 is introduced on the basis of a review of earlier investigations. It is shown that the study of the material can be helpful to tackle unsettled questions on familiar correlated systems. The selected choice of experimentally studied properties is discussed and the experimental methods and the measured sample are introduced.
- Part II is dedicated to inelastic neutron scattering studies of the low temperature magnetic excitation spectrum. The relevant magnetic exchange interactions are derived thereof and their interplay is discussed.
- The studied thermodynamic properties of the compound are explicated in Part III. These studies allude to the response of Li_2CuO_2 to externally applied temperature, pressure and magnetic field.
- A conclusion to this thesis is presented in Part IV as a set of substantial achieved results and prospects reaching further.

Part I.

Introduction

It is true that numerous instances
are not always necessary to establish
a law, provided the essential and
relevant circumstances can easily
be disentangled.

Bertrand Russell

2. Li_2CuO_2

2.1. ... as a cuprate

The compound studied in this thesis is one out of the enormously manifold class of magnetic transition metal compounds. These materials have proven a rich variety of fascinating properties, including as diverse effects as giant magneto-resistance, high temperature superconductivity or multiferroicity. This variety is understood to originate from largely complex interaction patterns between somewhat localized magnetic moments, which are moreover strongly coupled to potential charge, orbital and lattice degrees of freedom. If such interactions are weak, as in paramagnetic salts or can be captured as a mean-field, like in simple metals, magnetic transition metal compounds can also exhibit comparably trivial behavior. One origin of non-trivial properties is the interaction of localized magnetic moments. These moments may be orbital moments (f-orbitals, Gd^{3+} in particular) or unpaired electron spins with weak orbital contribution (d-orbitals). While, a number of correlated $4d$-compounds (e.g. Ca_2RuO_4 [11], $Sr_3Ru_2O_7$ [12], $Tl_2Ru_2O_7$ [13]) and a few $5d$-compounds (e.g. Sr_2IrO_4 [14]) have attracted considerable interest, research focusses on $3d$- and $4f$-compounds. In the latter, the respective orbitals are indeed well localized, but not necessarily in the case of $3d$-orbitals. In compounds, where the transition metal is coordinated by atoms with high electron affinity as oxygen or fluorine, the bond is often largely ionic. For increasingly important covalency of the bond, more metallic behavior can be expected [15, 16]. Iron pnictides provide an example of $3d$-systems, whose metallic behavior is far from ordinary.

Amongst the magnetic $3d$-compounds, cuprates represent an outstanding case. The tremendous efforts which have been undertaken in order to grasp the nature of high-temperature superconductors (HTSCs) have generated new experimental and theoretical methods which are fundamental for today's condensed matter physics and material science. In a pragmatic sense, it is a lucky fact that room temperature superconductors have not been discovered already in the early 1990's, motivating that transition metal compounds have gained the deserved attention.

With only one hole in the $3d$-shell of Cu^{2+} cuprates are somewhat simple transition metal compounds. The Cu^{2+}-ion is always associated with a spin $S = 1/2$, whatever the exact coordination of the ion. However, cuprates are therefor subject to strong quantum fluctuations. In the HTSCs and related compounds these fluctuations are particularly pronounced, due to strong antiferromagnetic interactions between the spins and their reduced dimensionality. These fluctuations are considered to play a decisive role in the stabilization of Cooper-pairs against thermal fluctuations and such as to be important for the observed high superconducting temperatures.

In order to understand the behavior of strongly correlated materials, studies of their local properties are mandatory. A crucial ingredient to theoretical studies, e.g. within the Hubbard-model, is the knowledge of the precise nature of the electronic structure. A very typical coordination of the Cu^{+2}-ions in cuprates, is the rather planar CuO_4-plaquette. This building block is found in all the cuprate-HTSCs, but also in Li_2CuO_2. The topology of the respective CuO_2-lattices is however largely different. It is therefore of interest to investigate and understand differences and similarities between the two.

Due to the correlated nature of cuprates, any theoretical modeling demands potentially too crude approximation and needs verification. Detailed experimental studies are thus of crucial importance as a starting point and decisive reference. Measurements of the electronic excitations provide deep insight into the electronic structure. The electronic structure of Li_2CuO_2 has attracted a lot of interest both in experiment and theory. Experimental studies on this subject include X-ray absorption spectroscopy [17–19], optical conductivity [20], electron energy loss spectroscopy [21, 22], X-ray emission spectroscopy [23] and (resonant) inelastic X-ray scattering [24–27]. Modeling the electronic structure and the observed excitations has provided deepened understanding of Li_2CuO_2 and related compounds [20, 28–38]. In the spectra, charge transfer excitations, $d-d$ and most prominently Zhang-Rice singlet and triplet excitations have been identified.

In corner-sharing cuprates, as the HTSCs parent compounds or chain compounds like Sr_2CuO_3, all magnetic interactions are completely dominated by the antiferromagnetic super-exchange and correlations form accordingly. The exchange interactions in edge-sharing cuprates however are weaker and can even be ferromagnetic. Zhang-Rice excitations have thus turned out to be a sensitive probe for ferro- and antiferromagnetic spin-spin correlations in Li_2CuO_2 and other edge-sharing cuprates [8, 9, 38].

From theoretical models, the strength of the magnetic exchange interactions can be calculated, provided the proper choice of relevant parameters and their value. These can be determined from electronic structure calculations and from the analysis of spectroscopic data. For Li_2CuO_2, various conflicting sets of exchange parameters have been proposed in the literature. The contribution of this thesis to the understanding of the electronic structure of cuprates is to have determined the exchange interactions in an independent and very reliable approach (cf. Chapter 5) and hence to have provided a way to justify or refine microscopic parameters as used in the respective theoretical models. Due to the weakness of the nearest neighbor antiferromagnetic exchange, Li_2CuO_2 and related compounds are particularly effective to investigate the strength of the direct Cu-O exchange [39–41].

2.2. ... as a quasi-one dimensional magnet

The presence of quasi-one-dimensional Cu^{2+}-$S = 1/2$-chains along the b-axis in $\mathrm{Li_2CuO_2}$ can be deduced effectively from the crystallographic structure of the compound and its low electric conductivity alone (cf. Section 2.3.1, Fig. 2.2). $S = 1/2$-chain systems are investigated continuously since the the early days of quantum mechanics. These systems are interesting for theoretical studies due to their reduced complexity. In 1931 Bethe has provided an exact solution for the one-dimensional $S = 1/2$ Heisenberg spin-Hamiltonian

$$\mathcal{H} = -J \sum_{n=1}^{N} \mathcal{S}_n \mathcal{S}_{n+1}. \tag{2.1}$$

The Bethe-ansatz has been extended and employed in the study of various more general spin Hamiltonians (see e.g. [42]). These studies have shown that one-dimensional magnets exhibit a broad variety of physical properties that differ much from the behavior of "ordinary" three-dimensional systems. The origin thereof are enhanced fluctuations. As shown in the Mermin-Wagner-Hohenberg-theorem [43, 44] and later by Coleman [45], in systems with a dimension $d \leq 2$ continuous symmetries cannot be broken spontaneously, for any temperature $T > 0$. Accordingly, in pure isotropic one- or two-dimensional systems, there will be no long range order of magnetic moments. True one dimensional systems have no realization in the three-dimensional world, however by now a large number of quasi-one-dimensional materials are known. In such systems, the interactions between magnetic sites are pronounced along one spacial direction, but weak perpendicular to it. In these materials the moments typically interact via an antiferromagnetic super-exchange-path. Research has focussed on systems with spin $S = 1/2$ and $S = 1$, exhibiting peculiar quantum ground states and excitations, while $S \geq 3/2$ systems behave already more like classical $S \to \infty$ systems [46].

A broad set of physical phenomena have been observed experimentally which are well explained in one-dimensional theoretical models. To list a few: for integer S spin-chains the ground state has been proposed to be gapped by F. D. M. Haldane [47] which has been verified for various nickelates ($S = 1$), e.g. for $\mathrm{Y_2BaNiO_5}$ [48]. Excitation gaps are also found in $S = 1/2$ spin-chains, if coupled to another antiferromagnetically (for an even number of chains) [49] or strongly ferromagnetically (pseudo $S = 1$) [50]. Single $S = 1/2$ chains are gapless, with elementary fermionic excitations (spinons) giving rise to a continuum of excitations [51, 52]. Solitons and breathers as predicted in sine-Gordon-models have been observed as bound spinon states in the alternating chain compound $\mathrm{(CuCl)_2 \cdot 2((CH_3)_2SO)}$ [53]. Further reports describe the separation of spin and charge in $\mathrm{SrCuO_2}$ [54], the possible observation of a spin-liquid with chiral ordering [55] and spin-Peierls transitions in e.g. $\mathrm{TTFCuS_4C_4(CF_3)_4}$ [56] and $\mathrm{CuGeO_3}$ [57]. In $\mathrm{CuGeO_3}$ the competition between nearest and next-nearest neighbor antiferromagnetic interactions has been demonstrated [58]. For the weakly coupled spin-chains in $KCuF_3$, the evolution of longitudinal fluctuations is found to signal an instability of the spinon excitations. The evolution of magnon excitations from the spinon continuum has been studied in $BaCu_2Si_2O_7$ [59].

In all the above examples, the leading interaction is an antiferromagnetic coupling between neighboring spins in the chain[1]. Spin-chain materials with nearest-neighbor ferromagnetic interactions are however scarce. According to the KANAMORI-GOODENOUGH-ANDERSON-rules [61–63], the coupling along the Cu-O-Cu super-exchange path can be ferromagnetic if the bond angle is close to 90°. Mizuno *et al.* [20] explain the phenomenon as follows: In this configuration the strong antiferromagnetic super-exchange via a single Op-orbital ceases and the Cu moments couple to orthogonal Op-orbitals. Both Op-orbitals are coupled strongly ferromagnetically via HUND's rule coupling K_p. The sign and strength of the interaction between neighboring Cu-moments depends on the direct Cu-O exchange coupling K_{pd}, which is ferromagnetic but rather weak for Cu-O. If the Cu-O-Cu binding angle deviates by more than a few degrees from 90°, the usual antiferromagnetic exchange wins (e.g. $CuGeO_3$). Between Cu-sites, typically two O-sites are located. Direct hopping between these sites gives rise to an antiferromagnetic contribution to the Cu-Cu interaction. The strength of the ferromagnetic Cu-Cu coupling is therefore maximized for a Cu-O-Cu binding angle slightly smaller than 90°. The strength of the Cu-O-Cu exchange coupling has been shown to also depend sensitively on the ligands of the chain [64]. Materials with such $\approx 90°$ Cu-O-Cu exchange path are interesting not only by providing a ferromagnetic coupling between the magnetic moments, but also because they are intrinsically frustrated. Hopping between neighboring Op-orbitals along the chain gives rise to an antiferromagnetic coupling between next-nearest neighbor Cu-sites which is of the same order of magnitude as the nearest neighbor coupling.

Li_2CuO_2, with a Cu-O-Cu bond angle of $\approx 94°$ [3] is the first material recognized as promising candidate for a strongly ferromagnetically coupled spin-chain compound in 1988 [65]. Since than, the number of known inorganic compounds with $\approx 90°$ Cu-O-Cu bonds increases steadily. The already mentioned $CuGeO_3$ has a similar chain, with however a bond angle $\approx 99°$ [20] and antiferromagnetic nearest neighbor coupling. The chains in $(La,Sr,Ca)_{14}Cu_{24}O_{41}$ are understood to show ferromagnetic nearest neighbor coupling [66]. This system has attracted much attention, as with the Ca content the doping of the chains can be controlled. The same applies to $Ca_{2+x}Y_{2-x}Cu_5O_{10}$ where half-filling is given for $x = 0$ [67]. Further materials with nearest neighbor ferromagnetic exchange include ACu_2O_2 (A = Li, Na) [68, 69], $A_2Cu_2Mo_3O_{12}$ (A = Rb, Cs) [70], $LiVCuO_4$ [71], Li_2ZrCuO_4 [72] and the recently much noticed $PbCu(SO_4)(OH)_2$ [73]. Anhydrous $CuCl_2$ has been shown to be a closely related spin-chain compound [74]. Other inorganic materials exhibiting

---

[1] In $SrCuO_2$ the nearest neighbor coupling is actually ferromagnetic, but its dominant exchange interaction is the antiferromagnetic next-nearest neighbor coupling [60].

corresponding Cu^{2+} chains are known, with their magnetic properties barely studied, amongst them $Cu(OH)_2$ [75]. Clearly, chains of ferromagnetically-antiferromagnetically frustrated moments cannot be expected in Cu^{2+} compounds only. With α-$TeVO_4$ an $S = 1/2$ vanadate has been suggested to exhibit comparable chains [76]. Various (metallo-)organic chain compounds with ferromagnetic nearest neighbor interaction have been reported, including TMCuC [77], $(C_6H_{11}NH_3)CuBr_3$ [78, 79] as well as p-NPNN [80, 81] and $C_{10}H_{10}N_4SCl$ [82]. (Metallo-)organic compounds with non-negligible next-nearest neighbor coupling can be expected to exist. As a consequence, the experimental survey of spin-chain materials with ferromagnetic in-chain interactions has only just started and much more is to be expected in the future.

Such survey is promising indeed. Theoretical investigation on chains with ferromagnetic exchange J_{NN} frustrated by an antiferromagnetic nearest neighbor coupling J_{NNN} have unraveled complex phase diagrams with extraordinary magnetic phases. The HAMILTONian studied can be written as

$$\begin{aligned} \mathcal{H} &= - \sum_{n=1}^{N} \left(\vec{S}_n \vec{S}_{n+1} + \delta_1 S_n^z S_{n+1}^z \right) \\ & \quad + \alpha \sum_{n=1}^{N} \left(\vec{S}_n \vec{S}_{n+2} + \delta_2 S_n^z S_{n+2}^z \right) - h \sum_{n=1}^{N} S_n^z, \end{aligned} \tag{2.2}$$

$$\text{with} \qquad \alpha = J_{\mathrm{NNN}}/|J_{\mathrm{NN}}|, \tag{2.3}$$

exchange anisotropies δ_1 and δ_2 and an external magnetic field h in units of J_{NN}. This HAMILTONian has been subject of much recent interest and only a few results will be presented here. Various regions of the magnetic phase diagram have been studied at $T = 0$. The most well known quantum critical point is given by the second order transition at $\alpha_c = 1/4$ in the isotropic, zero field case. For $\alpha < \alpha_c$ the ground state is degenerate and a gapped ferromagnet for any symmetry breaking field h or anisotropy $\delta_1 > 0$. For $\alpha > \alpha_c$ one has an incommensurate singlet ground state. Using the density matrix renormalization group (DMRG) method the dimerization of next-nearest neighbors in the chain has been shown numerically [83]. The existence of a tiny dimerization gap is still under debate [84, 85].

For $\alpha < \alpha_c$, the anisotropy δ_1 (with $\delta_2 = 0$ or $\delta_2 = \delta_1$) causes a first order spin flop transition between the ferromagnetic phase ($\delta_1 > 0$) and a spin liquid phase ($\delta < 0$) [89]. The general phase diagram of Eqn. 2.2 has been studied for $h = 0$ in different numerical methods (cf. Fig. 2.1) [86, 87]. For $\alpha > \alpha_c(\delta)$ with $\delta_1 = \delta_2 = \delta > 0$ and $h = 0$, Harada *et al.* showed that bound states of magnons can give rise to magnetized states [90]. Chubukov pointed out, that both easy axis anisotropies as well as external magnetic fields stabilize corresponding octupolar and quadrupolar nematic phases [91]. Theoretical studies of the properties of Eqn. 2.2 with finite h have been strongly motivated by the observation of magnetization anomalies in high field studies of $Rb_2Cu_2Mo_3O_{12}$ [92]

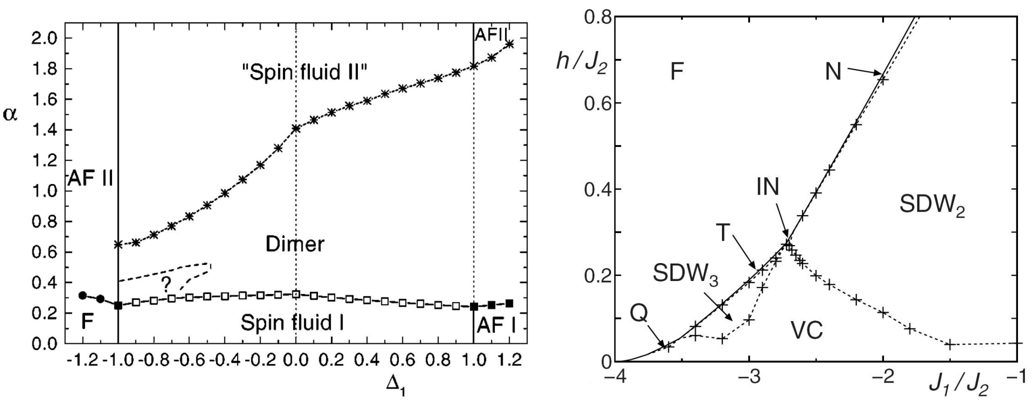

Figure 2.1.: left: Magnetic phase diagram of Eqn. 2.2 as obtained by Somma and Aligia [86]. Here $\Delta_1 + 1 = \delta_1 = \delta_2$. Shown are ferromagnetic (F), antiferromagnetic (AF), spin liquid and dimer phases. Note that other phase diagrams have been suggested. Jafari and Langari [87] show, that the dimer phase is only observed for $\Delta_1 \gtrsim -0.5$ and the spin fluid phases have a common phase boundary near $\alpha \approx 1/6$.
right: Magnetic phase diagram for the isotropic chain as obtained by Hikihara *et al.* [88]. The axes labels J_1/J_2 and h/J_2 correspond to $-1/\alpha$ and h/α in Eqn. 2.2, respectively. In magnetic field vector chiral (VC), nematic/quadrupolar (N), an incommensurate nematic (IN), triatic/octupolar (T), quartic/hexadecupolar (Q), ferromagnetic (F) and two different spin density wave (SDW) phases are predicted.

and recently $LiVCuO_4$ [37, 93]. The magnetic phase diagram for the frustrated chain in magnetic field has been elaborated by Hikihara *et al.* [88] (cf. Fig. 2.1) and Sudan *et al.* [94] including detailed calculations of spin, chiral and multipolar correlation functions as well as the zero field pitch angle. DMRG studies including anisotropies as well as magnetic field by Heidrich-Meisner *et al.* [95] show that easy axis anisotropies stabilize bound-magnon/multipolar states, while easy plane anisotropies stabilize chiral ground states. The finite temperature thermodynamic properties have been studied for yet a few of these phases [96–98], including the temperature dependence of the pitch angle [99].

All the above applies to mere one-dimensional systems. However, interesting physics can also be expected to be induced by the chains in the three-dimensionally ordered state. When inter-chain couplings are present, the material will undergo magnetic long range, typically antiferromagnetic order at low temperature. If the compound assumes a state with incommensurate in-chain order ($\alpha_c^{3D} > \alpha_c^{1D}$ for antiferromagnetic inter-chain interactions [35])[2] at T_{N} both time and spacial symmetries are simultaneously broken, which can give rise to multiferroicity [101]. Indeed, for the helically ordering compounds $LiCu_2O_2$ [102], $LiVCuO_4$ [103], $CuCl_2$ [104] and $PbCu(SO_4)(OH)_2$ [105] mul-

---

[2] The influence of inter-chain coupling onto the pitch angle has been studied in detail by Zinke *et al.* [100].

tiferroicity has been reported. It should be noted, that for $LiCu_2O_2$ impurity effects are suggested to be important for the observed multiferroic behavior [106].

All the interesting physics in ferromagnetic-antiferromagnetic frustrated spin-chain systems depends strongly on the ratio of the intra-chain couplings α and the strength of the inter-chain couplings. To determine the value of these interactions for some compound is however non-trivial, in particular if the ground state is subject to strong quantum fluctuations (see e.g. [107]). In Li_2CuO_2 however, quantum fluctuations are likely weak. While in this compound, where inter-chain couplings are not weak and helical order is absent, the influence of all the above, fascinating physical phenomena must be expected to be weak, the compound is excellently qualified to study the strength of the exchange interactions. Also, the influence of inter-chain couplings onto a largely one-dimensional system can be investigated. Both these aspects are of relevance for the understanding of the related, but more complex compounds and are experimentally investigated in this thesis.

2.3. Literature review on magnetic properties

2.3.1. Crystallographic structure

The crystallographic structure of Li_2CuO_2 has first been reported in 1962 (see [3] and references therein). The material is found to crystallize in an orthorhombic structure with space group $Immm$ and one formula unit per basis of the lattice. It contains CuO_4-plaquettes which share edges and form chains along the b-axis (cf. Fig. 2.2). The chain as well as the accompanying Li-ions are found exactly constraint to the (b, c)-plane. The lattice and structural parameters have been refined from powder and single crystal X-ray diffraction data [3, 108, 109] as well as neutron diffraction data [110–112]. Measurements taken at room temperature and $T = 1.5\,\mathrm{K}$ do not indicate any structural transitions. At low temperature, the lattice parameters (a, b, c) determined by Sapiña *et al.* read $(3.6545, 2.8602, 9.377)\,\text{Å}$, with Cu-O distances in the chain of $1.956\,\text{Å}$ (Cu-O-Cu bond angle 94.0°).

2.3.2. Magnetic structure and magnetic properties

In 1989 Hoffmann *et al.* [110] observed the onset of long range antiferromagnetic order in Li_2CuO_2 below $10\,\mathrm{K}$ and investigated its ordered magnetic structure by $^7Li_2CuO_2$ neutron powder diffraction. They have been able to deduce a magnetic structure model, with however some uncertainty due to restricted experimental resolution. The proposed structure was corrected by Sapiña *et al.* a year later [111]. The observed antiferromagnetic structure breaks the inversion symmetry of the the crystallographic structure and magnetic reflexes at positions $h+k+l \neq 2n$ $(n \in \mathbb{Z})$ become observable. The magnetic structure

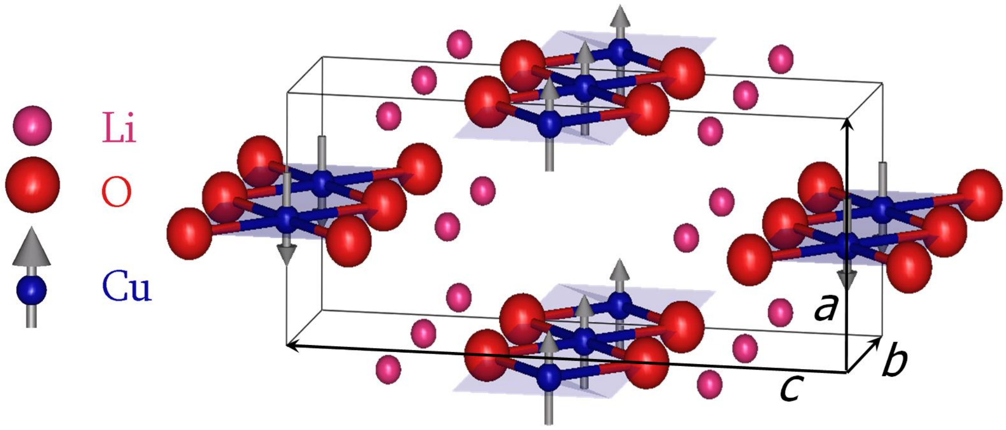

Figure 2.2.: Crystallographic and magnetic structure of Li_2CuO_2. Note the planar chains composed of CuO_2-units running along the b-axis. The magnetic structure is composed of ferromagnetic chains with the a-axis being the magnetic easy axis.

hence has a propagation vector $\tau = (0, 0, 1)$ (or equivalently $\tau = (1, 0, 0)$). The structure can be described by ferromagnetic chains along the b-axis forming ferromagnetic sheets in the (a, b)-plane which are coupled antiferromagnetically along the c-axis. The magnetic moments have been suggested to be aligned along the a-axis (cf. Fig. 2.2). An almost uniaxial anisotropy along the a-axis has been verified in electron spin resonance (ESR) measurements by Ohta *et al.* [113]. While the magnetic easy a-axis could meanwhile be explained theoretically to originate from the nearest neighbor intra-chain coupling, its calculated magnitude overestimates the experimental value by more than a factor of 4 [36, 114]. Understanding of the exchange anisotropy gap is thus yet missing. Interestingly, Ohta *et al.* [113] also note that the line-shape displayed of the paramagnetic resonance (EPR) is GAUSSian, in contrast to an expected LORENTZian shape expected for three-dimensional systems. From single crystal ESR measurements at room temperature, Kawamata *et al.* deduced g-factors $g_a = 2.264$, $g_a = 2.047$ and $g_c = 2.033$ at room temperature [115]. The observed line-width is found temperature dependent down to lowest measured temperatures, indicating short range correlations over the whole temperature range including room temperature.

The origin of the ferromagnetic moment alignment along the chain remained an open question. Magnetization measurements have indicated a CURIE-WEISS-like behavior of $M(T)$. A large associated CURIE-WEISS-temperature $\theta_{\mathrm{CW}} \approx -42\,\mathrm{K}$, as repeatedly presented in literature was interpreted as to originate from a dominant antiferromagnetic inter-chain interaction [65, 110, 111, 116, 117]. The large negative θ_{CW} was moreover understood as to indicate rather weak ferromagnetic couplings between nearest neighbors along the chain. From analysis of specific heat data a first proposal $J = -(15 - 30)\,\mathrm{K}$ for the intra-chain coupling was presented [116]. The correspondingly largely three-dimensional nature of the compound was further supported by the large ordered moment $0.96(4)\,\mu_{\mathrm{B}}/\mathrm{f.u.}$ as observed in neutron diffraction experiments [110, 111].

An interesting result from L(S)DA is the prediction of a large magnetic moment residing at the O-ions [28, 33, 36]. An oxygen moment formation is experimentally supported by muon spin rotation (μSR) measurements [118], which suggest a significantly different temperature dependence of the ordered Cu and O moments below T_{N}. Data from low temperature neutron diffraction are refined with magnetic moments $\mu(\mathrm{Cu}) = 0.96\,\mu_{\mathrm{B}}$ and $\mu(\mathrm{O}) = 0.10\,\mu_{\mathrm{B}}$ by Chung *et al.* [112][3]. ^{7}Li-NMR measurements show, that the magnetic field at the Li-sites is small and can be explained already from dipolar field induced by Cu moments [119].

In 1998 Boehm *et al.* have studied the magnetic excitation spectrum of single crystalline $\mathrm{Li_2CuO_2}$ at low temperatures by means of inelastic neutron scattering experiments [117, 120]. A well defined mode of collective excitations was observed for momentum transfer perpendicular to the chain, however for momentum transfer along the chain, strongly broadened excitations with a weak dispersion have been reported. An anisotropy gap of 1.4(1) meV has been reported, confirming the ESR-studies by Ohta *et al.* . Boehm *et al.* note, that this large anisotropy may play in important role for the low reduction of the ordered moment in the compound. The dispersion of the excitations was analyzed within a spin-wave theory model. The derived exchange integrals include a dominant antiferromagnetic inter-chain coupling along the body diagonal. Further, weaker antiferromagnetic inter-chain interactions are found along the a-axis and the (a, b)-diagonal. For the intra-chain interactions an antiferromagnetic nearest neighbor coupling and a ferromagnetic next-nearest neighbor coupling have been obtained. Both these interactions are unexpectedly weak (5.6 K and −3.7 K) and moreover of opposite sign as compared to predictions of the KANAMORI-GOODENOUGH-ANDERSON-rules. Just before publication of this neutron scattering study, Mizuno *et al.* proposed couplings of −100 K and 62 K instead, from the analysis of optical conductivity and magnetic susceptibility data applying the exact diagonalization method of a single chain cluster [20]. Motivated by the largely different results from neutron scattering Mizuno *et al.* implemented inter-chain couplings to their model and obtained a significantly smaller next-nearest neighbor coupling of 40 K [32], still in stark contrast to the inelastic neutron scattering data. This discrepancy rose the question if some fundamental properties of the chains in $\mathrm{Li_2CuO_2}$ have not yet been understood. The sign and size of the nearest neighbor coupling are indeed very sensitive to the Cu-O-Cu bond angle and the coordination of the chain, such that a disagreement between the theoretical results and experimental observation is not too severe. However, a ferromagnetic super-exchange between next-nearest neighbors is generally not to be expected [28]. Nevertheless, Yushankhai *et al.* [121] could show, that ferromagnetic next-nearest neighbor

---

[3] Refined moments in fits with canted moment orientation are slightly different.

coupling could be induced by a ring-exchange mechanism. Further theoretical studies within quantum chemistry calculations [34], L(S)DA+U [36], GGA+U [122] and exact diagonalization of a 5-band HUBBARD-model [37] however supported the exchange parameters proposed by Mizuno *et al.* No agreement was however achieved on magnitude of the obtained exchange integrals and their ratio in particular. These parameters are of essential importance. If modeling them satisfactorily for the structurally simple compound Li_2CuO_2 fails, calculations on its more complex relatives cannot be much reliable. A major goal of this thesis was therefore the reinvestigation of the magnetic spectrum by inelastic neutron scattering and to establish a reliable set of exchange parameters. To start with, it remained to be shown if Li_2CuO_2 is actually a quasi-one-dimensional magnet, as theoretically predicted, or if its magnetic properties are dominated by inter-chain couplings.

The thermodynamic studies performed on the compound did yield a number of interesting details. For the observed antiferromagnetic ordering temperatures T_N, various values are reported in literature, ranging from 8.3 K [111] to 9.3 K [116, 123]. Ebisu *et al.* could show in a doping experiment, replacing Cu by Ni (which is found in a low spin $S = 0$ configuration) that non-magnetic impurities can strongly suppress T_N [123]. They further analyze deviations of $M(T)$ from the CURIE-WEISS-law and short range order effects in c_p above T_N. Attempts to describe these within an isotropic exchange model (one dominant J) have however not been successful. At low temperature $T_2 \approx 2.6\,\mathrm{K}$ Ortega *et al.* [124] observed a weak ferromagnetic component in magnetization data. This observation was shown to be an intrinsic property of the compound by μSR measurements [118]. Below $T \approx 2.8\,\mathrm{K}$, splitting of muon frequency lines was observed. The lines were interpreted to represent muons susceptible to the magnetization at the O-sites and the splitting due to a weak canting of moments by 0.7°. The above mentioned single crystal diffraction data by Chung *et al.* where interpreted to picture a moment canting of up to 14° at the Cu-site and even larger at the O-sites [112]. In a detailed magnetization study by Klingeler the easy axis magnetic phase diagram was derived [125]. The meta-magnetic transition was found to be shifted strongly to higher values with increasing temperature. At low temperature 2.5 K, the meta-magnetic transition was observed at $\approx 10\,\mathrm{T}$. From the magnetization data obtained between 10 T and 16 T it was shown that the meta-magnetic transition does not correspond to a spin-flop transition. Further anisotropies beyond a uniaxial exchange anisotropy have been suggested.

The low temperature thermodynamic properties of the compound are largely determined by the interaction of magnetic moments. In order to gain more detailed insight into the interplay of the exchange interactions, this thesis has a strong focus on the evolution of the thermodynamic properties of the compound if exposed to changes of external magnetic field, pressure and temperature.

3. Employed experimental techniques

Li_2CuO_2 is one of the most well studied compounds in the class of ferromagnetic-antiferromagnetic frustrated spin chain compounds, both theoretically as well as experimentally. However, many basic properties have not yet been investigated. This thesis focusses on two subjects, an extensive inspection of the low temperature thermodynamic properties and the detailed investigation of the magnetic excitation spectrum. These two subjects are closely related and complement another. On one hand, the thermodynamic studies show, that the low temperature properties of the system must be understood as dominated by magnetic degrees of freedom. The study of thermodynamic properties therefor is the starting point to a identify the prominent phenomena of the compound. On the other hand, the investigation of the magnetic excitation spectrum promises insight into the relevant magnetic interactions, which provide a basis for the understanding the thermodynamic properties from a microscopic point of view.

3.1. Thermodynamic studies

We have examined the properties of Li_2CuO_2 under standard low temperature physics conditions, i.e. the sample was typically well coupled to a thermal bath[1] and a constant external magnetic field and pressure have been applied. Under these conditions, thermodynamic systems assume a minimum of the Gibbs free energy G. Equivalently, the Gibbs free energy is a complete description of a system under these equilibrium conditions. The change of the Gibbs free energy of a system can be investigated experimentally. It is given as

$$\mathrm{d}G = -S\mathrm{d}T + V\mathrm{d}p - \mu_0 m\mathrm{d}H - PV\mathrm{d}E \tag{3.1}$$

where S denotes the entropy, T system temperature, V the volume, p the applied pressure, m the magnetic moment[2], H the externally applied magnetic field, P the (assumed to be constant) polarization density and E the applied electric field. Below, the extensive functions G, S, V and m are used as

---

[1] In pulsed magnetic field experiments, the coupling to the bath may be too weak and the thermodynamic potential is then not an isothermal one but quasi-adiabatic.

[2] $m = MV$, with the magnetization M.

normalized to 1 mol of formula units (f.u.). Moreover, the influence of electric fields will be disregarded in the below discussions[3].

In the following, the experimental techniques for the study of the Gibbs free energy are related to the properties of Eqn. 3.1. Basic knowledge on the experiential methods themselves is assumed and the discussion is restricted to the presentation of the notation used. The chapters of this thesis concerned with the respective measurements are specified. The change of the Gibbs free energy under applied magnetic field and pressure can be studied directly. The respective derivatives of G and experimental methods are given:

$$\frac{1}{\mu_0}\left(\frac{\partial G}{\partial H}\right)_{T,p} = m_{T,p}(H) \qquad \text{magnetization} \tag{3.2}$$

$$\left(\frac{\partial G}{\partial p}\right)_{T,H} = V_{T,H}(p) \qquad \text{diffraction} \tag{3.3}$$

$$\left(\frac{\partial G}{\partial T}\right)_{p,H} = S_{p,H}(T) \qquad \varnothing \tag{3.4}$$

In this thesis, measurements of the magnetic moment $m(H)_{T,p\to 0}$ are presented (cf. Section 8.2). X-ray diffraction studies under applied pressure up to 32.5 GPa, from which $V(p)_{T\approx 300\,\mathrm{K},H\to 0}$ is obtained have been presented by You *et al.* [126]. The entropy $S = (\partial G/\partial T)_{p,H}$ itself cannot be measured directly, however specific heat measurements allow to detect its temperature dependence:

$$\left(\frac{\partial S}{\partial T}\right)_{p,H} = \frac{c_{p,H}(T)}{T} \qquad \text{specific heat} \tag{3.5}$$

Data and analysis of the specific heat $c_{p\to 0,0\leq\mu_0 H\leq 13.9\,\mathrm{T}}(T)$ are presented in Chapter 9. The interrelation of the state variables S, V and m can be studied making use of the Maxwell-relations for the Gibbs Free Energy. For each, the right side of the equations has been probed experimentally.

$$\left(\frac{\partial S}{\partial H}\right)_{T,p} = \left(\frac{\partial m}{\partial T}\right)_{p,H} \qquad \text{magnetization} \tag{3.6}$$

$$-\left(\frac{\partial S}{\partial p}\right)_{T,H} = \left(\frac{\partial V}{\partial T}\right)_{p,H} \qquad \text{thermalexpansion} \tag{3.7}$$

$$-\left(\frac{\partial m}{\partial p}\right)_{T,H} = \left(\frac{\partial V}{\partial H}\right)_{T,p} \qquad \text{magnetostriction.} \tag{3.8}$$

In the course of this thesis, $(\partial m/\partial T)_{p,H}$ was obtained from measurements of the magnetic moment $m_{p\leq 0.65\ \mathrm{GPa},0\leq\mu_0 H\leq 7\,\mathrm{T}}(T)$. Data at pressure $p \to 0$ are

---

[3] The AC-conductivity of the compound has been probed at a frequency of 1 kHz between $T = 2\,\mathrm{K}$ and 300 K and magnetic fields up to 16 T applied along the easy axis. Within the limited experimental precision, the relative dielectric permittivity ϵ_r was found $\leq$ 4 throughout the magnetic phase diagram. Changes of the detected signal at phase transitions have been observed, but could not be attributed to ϵ_r, but appear explainable by lattice expansion effects.

presented in Section 8.1 and measurements under constant applied pressure in Section 10.2. Making use of the respective MAXWELL-relation, the magnetic field dependence of the entropy $(\partial S/\partial H)_{T,p\to 0}$ is discussed in Section 9.3. While changes of the volume V with temperature or applied magnetic field are in principle also accessible to diffraction studies but are restricted in resolution, here thermal expansion and magnetostriction studies are performed by capacitive dilatometry. The main disadvantage of the method in this context and compared to diffraction is that data can be obtained only at low pressure (here $p \to 0$). This technique measures the relative length change

$$\Delta l_{i,j}/l_{i,T_{\mathrm{ref}}}^{H_{\mathrm{ref}}} \tag{3.9}$$

of a solid sample along some direction i with magnetic field applied along some direction j. The term $l_{i,T_{\mathrm{ref}}}^{H_{\mathrm{ref}}}$ denotes the length of the sample as obtained at some reference point $(H_{\mathrm{ref}}, T_{\mathrm{ref}})$ in the phase diagram, typically room temperature and ambient magnetic field and pressure. Thermal expansion measurements refer to measurements of the relative length change with temperature $\Delta l_i(T)/l_i$, while magnetostriction measures the magnetic field dependence $\Delta l_i(H)/l_i$, respectively. From the length changes along the crystallographic axes $i = (a, b, c)$, the volume change of an orthorhombic crystal is obtained as

$$\frac{\mathrm{d}V}{V} = \sum_i \frac{\Delta l_i}{l_i}. \tag{3.10}$$

Here, it is assumed that with the typical $\Delta l_i \ll l_i$ quadratic terms $\propto \Delta l_i \Delta l_j$ can be neglected. Throughout this thesis, the derivatives of the relative length change are discussed. These are denoted as

$$\alpha_{i,H\|j}(T) = \left.\frac{\partial(\Delta l_i/l_i)}{\partial T}\right|_{H\|j=const.} \tag{3.11}$$

as obtained from thermal expansion measurements. The function $\alpha(T)$ is referred to as thermal expansion coefficient. The corresponding magnetostriction coefficient $\beta(H)$ is derived as[4]

$$\beta_{i,H\|j,T}(H) = \left.\frac{1}{\mu_0}\frac{\partial(\Delta l_i/l_i)}{\partial H}\right|_{T=const.}. \tag{3.12}$$

For further details on thermal expansion and magnetostriction see e.g. [127, 128]. The thermal expansion and magnetostriction data obtained on $\mathrm{Li_2CuO_2}$ are discussed in Chapter 10.

The data obtained from the different thermodynamic studies have been used to determine the magnetic phase diagram of $\mathrm{Li_2CuO_2}$, which is described in

---

[4] Note, that in literature the magnetostriction coefficient is often written as λ, while β denotes the thermal volume expansion coefficient.

Chapter 7. Their interrelation is discussed in the respective chapters. Moreover, approaches to correlate the observed thermodynamic behavior to microscopic properties are discussed, in particular of the low temperature specific heat (cf. Section 9.4) and the anisotropic thermal expansion and magnetostriction (cf. Section 10.3.3).

3.2. Inelastic magnetic neutron scattering

Next to the above mentioned thermodynamic studies, the other main part of this thesis is concerned with the magnetic excitation spectrum of Li_2CuO_2. For such purpose, inelastic neutron scattering is the ideal choice of method. In general, neutrons are an extraordinarily versatile probe for the study of condensed matter. The main issue about the utilization of neutrons is the low brilliance of the beam produced by even the most powerful modern neutron sources. Compared to the today's most intense X-ray sources (XFEL type), neutron scattering techniques life on a lot less that ten orders of magnitude lower intensity. Nevertheless, neutrons combine a number of valuable properties that make them unchallenged for the study of a number of interesting material properties. First of all, neutrons are unchanged particles, such that they interact weakly with matter and can be used to study bulk properties[5]. Neutrons, being baryons interact with nuclei and carrying spin $S = 1/2$ they interact with unpaired electrons. The first property is seemingly unpleasant, as isotope disorder and nuclear spin disorder give rise to incoherent elastic scattering[6]. However, as the nuclear scattering length depends on the isotope and not on the charge of the nucleus, neutrons are able to detect hydrogen in compounds with heavy elements as well as to distinguish between neighbors in the periodic system as like nickel and iron. The strength of the interaction with magnetic moments is typically weaker than with the nuclei, but nevertheless strong, which makes neutrons a valuable probe for the study of magnetic materials. The last property to mention for our purposes is the large mass of neutrons. As a consequence thereof, neutrons at wavelength in the Å-regime carry energies of meV only ($E \approx 82\,\mathrm{meV}\,\text{Å}^2/\lambda^2$). Therefore, inelastic neutron scattering is a highly sensitive method to study excitations in the meV energy range (from 0.3 μeV in backscattering (e.g. IN10/ILL), even neV in spin echo spectroscopy (e.g. J-NSE/FRMII) up to few eV (e.g. MAPS/ISIS)). Inelastic neutron scattering is an elaborate experimental technique and described in various extensive publications. In the following, the basic theoretical concepts are discussed as presented in [129–131].

In magnetic neutron scattering experiments, the double differential cross section $\mathrm{d}^2\sigma/\mathrm{d}\Omega \mathrm{d}E_f$ is probed, where Ω denotes the solid scattering angle and E_f the energy of the scattered neutron. The double differential scattering cross

---

[5] Using neutron reflectometry, thin film and interface properties are studied.

[6] The incoherent scattering from different isotopes (^{1}H, ^{2}D) can be utilized in contrast variation experiments.

section is given by the so-called master equation of neutron scattering

$$\frac{\mathrm{d}^2\sigma}{\mathrm{d}\Omega\mathrm{d}E_f} = \left(\frac{m_\mathrm{n}}{2\pi\hbar}\right)^2 \frac{k_f}{k_i} \sum_{\sigma_i\sigma_f} p_{\sigma_i} \sum_{\lambda_i} p_{\lambda_i} \sum_{\lambda_f} \left|\left\langle k_f\sigma_f\lambda_f|\hat{V}|k_i\sigma_i\lambda_i\right\rangle\right|^2 \cdot \\ \cdot \ \delta(E_{\lambda_i} - E_{\lambda_f} + E_i - E_f) \quad (3.13)$$

where i and f denote the initial and final state of the sample λ and the neutron, described by the momentum k, the spin σ and the energy E. The KRONECKER-δ function describes energy conservation of the scattering process, $\hat{V}$ the interaction potential between the neutron and the sample and p_{λ_i} denotes the probability of scattering at an initial state λ_i of the sample. The mass of the neutron enters as m_n and the probability for an initial neutron spin σ_i is given by p_{σ_i}. The interaction potential for neutron scattering at a magnetic site is given as

$$\hat{V} = -\gamma\mu_\mathrm{n}^2\,\mu_\mathrm{B}\hat{\sigma}\left[\nabla \times \left(\frac{\hat{s}\times\hat{R}}{R^2}\right) + \frac{1}{\hbar}\frac{\hat{p}\times\hat{R}}{R^2}\right] \quad (3.14)$$

where γ is the neutron gyromagnetic ratio, μ_n the proton magnetic moment and $\hat{\sigma}$ the neutron spin. In brackets, the interaction between the neutron with the unpaired electron spin $\hat{s}$ and its orbital momentum is distinguished. Evaluating Eqn. 3.13 with Eqn. 3.14, one finds that neutron scattering measures the FOURIER transform of the magnetization density perpendicular to the momentum transfer of both spin and orbital momenta.

On a magnetic BRAVAIS-lattice the unpolarized neutron scattering double differential cross section can be written as

$$\frac{\mathrm{d}^2\sigma}{\mathrm{d}\Omega\mathrm{d}E_f} = \frac{(\gamma r_0)^2}{2\pi\hbar} \sum_{\alpha\beta} (\delta_{\alpha\beta} - \hat{q}_\alpha\hat{q}_\beta) \sum_{mn} f_m^*(\vec{q}) f_n(\vec{q}) \cdot \\ \cdot \int \mathrm{d}t e^{-iEt/\hbar} [J_{mn}^{\alpha\beta}(\infty) + J_{mn}^{\prime\alpha\beta}(t)][I_{mn}^{\alpha\beta}(\vec{q},\infty) + I_{mn}^{\prime\alpha\beta}(\vec{q},t)]. \quad (3.15)$$

Here, r_0 is the classical electron radius, α and β represent the x, y and z components, m and n sum up over lattice sites. The term $(\delta_{\alpha\beta} - \hat{q}_\alpha\hat{q}_\beta)$ selects the projection of the integral perpendicular to the momentum transfer. The so-called magnetic form factor $f_n(\vec{q})$ is the FOURIER transform of the spin density of the nth site. In the dipole approximation $f(\vec{q})$ is given as

$$f(q) = \langle j_0(q)\rangle + (1 - 2/g)\langle j_2(q)\rangle \quad (3.16)$$

with $\langle j_n(q)\rangle = \int \mathrm{d}r j_n(qr)|\Psi(r)|^2$, where j_n are the spherical BESSEL functions and Ψ is the electronic wave function. Series expansions of $\langle j_n(q)\rangle$ are tabulated [132, 133]. In Fig. 3.1, the magnetic form factor of Cu^{2+} is presented and compared to the low q magnetic reflex positions in Li_2CuO_2. Due the the spatially spread out spin density, magnetic diffraction experiments are done typically at the lowest accessible q.

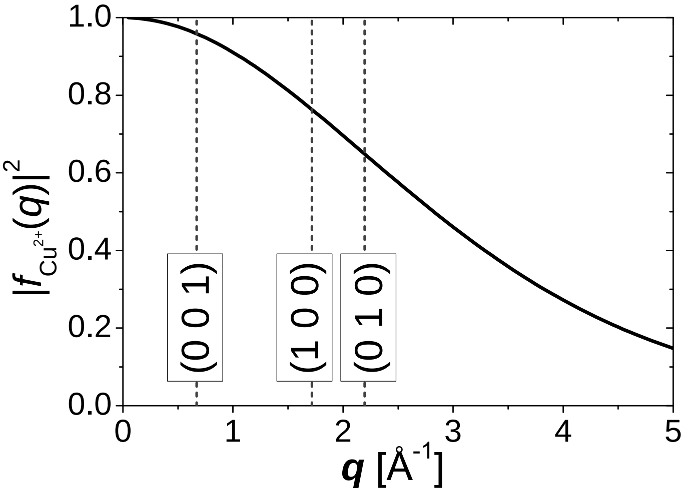

Figure 3.1: The magnetic form factor of a Cu^{2+} ion. The **q**-positions of the first magnetic superstructure reflexes in Li_2CuO_2 are indicated.

The matrices I and J in Eqn. 3.15 are introduced in order to separate the time independent (i.e. static) and time dependent part of the lattice (I) and magnetic (J) contributions as

$$I^{\alpha\beta}_{mn}(\vec{q},\infty) + I'^{\alpha\beta}_{mn}(\vec{q},t) = \langle \exp\left(-i\vec{q}\vec{r}_n(0)\right) \exp\left(-i\vec{q}\vec{r}_m(t)\right)\rangle \qquad (3.17)$$

$$J^{\alpha\beta}_{mn}(\infty) + J'^{\alpha\beta}_{mn}(t) = \langle \mu_{m\alpha}(0)\mu_{n\beta}(t)\rangle \,. \qquad (3.18)$$

Here, $\vec{\mu}$ denotes the local magnetic moment. In this notation, one term of Eqn. 3.15 contains the time-independent product $I^{\alpha\beta}_{mn}(\vec{q},\infty)\cdot J^{\alpha\beta}_{mn}(\infty)$. For diffraction the differential cross section can be written as

$$\left(\frac{\mathrm{d}\sigma}{\mathrm{d}\Omega}\right)_{\mathrm{elastic}} = \frac{2\pi^3}{V^*}\sum_{\vec{\tau}_{\mathrm{M}}} \delta(\vec{q}-\vec{\tau}_{\mathrm{M}})\,|\vec{q}\times F_{\mathrm{M}}(\vec{\tau}_{\mathrm{M}})\times\vec{q}|^2 \qquad (3.19)$$

with

$$F_{\mathrm{M}}(\vec{q}) = \gamma r_0 \sum_m f_m(\vec{q})\langle\mu_m\rangle \exp\left(i\vec{q}\vec{r}_m\right)\exp\left(-W_m(\vec{q})\right). \qquad (3.20)$$

Here, V^* denotes the reciprocal unit cell volume, τ_{M} the reciprocal lattice vector in the magnetic unit cell and $W(\vec{q})$ the Debye-Waller factor. From Eqn. 3.19, one can see, that the scattered intensity in diffraction is proportional to $|\langle\mu\rangle|^2$. It is moreover immediately clear, that no scattering is observable if the magnetic moments are aligned parallel to the scattering vector $\vec{q}$. For Li_2CuO_2, where moments are aligned parallel to the a-axis, magnetic Bragg reflexes at $\vec{q}$ positions $(n,0,0)$, $n\in\mathbb{Z}$ in reciprocal lattice units can thus not be observed. This property is used in Section 7.4 in order to investigate a proposed canting of moments at low temperature.

Returning to Eqn. 3.15, the second term of interest is the product of the time-independent lattice contributions and the time-dependent magnetic contribution $I^{\alpha\beta}_{mn}(\vec{q},\infty)\cdot J'^{\alpha\beta}_{mn}(t)$, which describes magnetic excitations. The respective double differential cross section can be written as

$$\left(\frac{\mathrm{d}^2\sigma}{\mathrm{d}\Omega\mathrm{d}E_f}\right)_{excit.} = N_\mathrm{m}\frac{(\gamma r_0)^2}{2\pi\hbar}\left|\frac{g}{2}f(\vec{q})\right|^2\frac{k_f}{k_i}\exp\left(-2W(\vec{q})\right)\sum_{\alpha\beta}(\delta_{\alpha\beta}-\hat{q}_\alpha\hat{q}_\beta)\cdot$$
$$\cdot\sum_l\exp\left(i\vec{q}\vec{r}_l\right)\int\mathrm{d}te^{-iEt/\hbar}\left\langle S_{0\alpha}(0)S_{l\beta}(t)\right\rangle. \qquad (3.21)$$

The spin-spin correlation function $\langle S_{0\alpha}(0)S_{l\beta}(t)\rangle$ of classical spin systems can be evaluated within spin-wave theory and written in terms of magnon creation and annihilation operators. For a simple HEISENBERG ferromagnet with only nearest neighbor interaction and moments aligned along the z-axis, the double differential cross section reads

$$\left(\frac{\mathrm{d}^2\sigma}{\mathrm{d}\Omega\mathrm{d}E_f}\right)_{excit.} = (\gamma r_0)^2\frac{(2\pi)^3}{2V^*}\frac{S}{2}(1+q_z^2)\left|\frac{g}{2}f(\vec{q})\right|^2\exp\left(-2W(\vec{q})\right)\cdot$$
$$\cdot\Big[\sum_{\vec{Q},\vec{\tau}}\left\langle n_{\vec{Q}}+1\right\rangle\delta(\vec{q}-\vec{Q}-\vec{\tau})\delta(E-\hbar\omega(\vec{q}))$$
$$\sum_{\vec{Q},\vec{\tau}}\left\langle n_{\vec{Q}}\right\rangle\delta(\vec{q}+\vec{Q}-\vec{\tau})\delta(E+\hbar\omega(\vec{q}))\Big] \qquad (3.22)$$

where the magnon dispersion is denoted as $\omega(\vec{q})$ and $\left\langle n_{\vec{Q}}\right\rangle$ is the thermal population factor of $\omega(\vec{q})$. Here, and throughout this thesis $\vec{q}$ refers to the total momentum transfer, while $\vec{Q}$ denotes the momentum transfer within a BRILLOUIN zone. Note, that in contrast to elastic scattering, the inelastic signal depends linearly on the spin. Also, the polarization term $(1+q_z^2)$ acts differently, being maximized for momentum transfer parallel to the spin orientation and minimized for perpendicular momentum transfer. For simple antiferromagnets, the spin and polarization dependence are alike. For $\mathrm{Li_2CuO_2}$, a dedicated calculation of the scattering cross section has however not been done within this thesis.

Experimental neutron scattering studies on $\mathrm{Li_2CuO_2}$ have been performed employing three-axis spectrometers at the *Institut Laue-Langevin* and the *Laboratoire Léon Brillouin*. The obtained data and analysis are described in Chapter 5 and Chapter 6. In the presentation of the data the measured intensity is given as counts in the detector normalized by counts in the secondary monitor and abbreviated as cts/mon.. Momentum transfers are mainly given as (H, K, L) in reciprocal lattice units (r.l.u.) or in absolute units $\mathrm{\AA}^{-1}$.

4. Sample properties and characterization

4.1. A sample for INS

For successful inelastic neutron scattering experiments it is a critical issue to attain sufficiently strong signals to be detected. If obtainable, an explicitly well scattering sample should be provided. A mere increase of the sample mass is however restricted by two factors.

- Firstly, multiple scattering events are commonly undesirable. Multiple scattering can occur, where strong reflexes act as a primary beam to further reflexes. This so-called RENNINGER-effect is to be taken care for especially in very high quality single crystals. Sequent inelastic scattering can be expected negligible, but elastic and subsequent inelastic scattering (and vice versa) can yield spurious inelastic intensity.
- Secondly, neutron absorption by the sample is to be considered. For samples containing strongly absorbing isotopes, the optimal sample thickness is restricted by the sample's absorption cross-section. If available, substitution of isotopes with less absorbing ones is to be preconceived. Common substitutions are ${}^{6}_{3}\mathrm{Li} \rightarrow {}^{7}_{3}\mathrm{Li}$, ${}^{10}_{5}\mathrm{B} \rightarrow {}^{11}_{5}\mathrm{B}$. Further strongly absorbing isotopes that can be efficiently substituted from the natural composition are ${}^{113}_{48}\mathrm{Cd}$, ${}^{149}_{62}\mathrm{Sm}$ (e.g. [134]), ${}^{151}_{63}\mathrm{Eu}$ (e.g. [135]) and ${}^{155/157}_{64}\mathrm{Gd}$, while in practice, due to significant financial effort these substitutions are only potentially efficient. Similar considerations may suggest to substitute strongly incoherently scattering isotopes, esp. ${}^{1}_{1}\mathrm{H} \rightarrow {}^{2}_{1}\mathrm{D}$.

For Li_2CuO_2 the effect of ${}^{7}Li$ concentration is discussed. As illustrated in Tab. 4.1, ${}^{6}Li$ is the by far most strongly neutron absorbing isotope in Li_2CuO_2, while the absorbtion cross section of ${}^{7}Li$ is small. Consequently substituting ${}^{6}_{3}\mathrm{Li} \rightarrow {}^{7}_{3}\mathrm{Li}$ will significantly reduce neutron absorption by the sample. Only for ${}^{6}Li$ concentrations $< 0.2\%$, the absorption is dominated by the Cu nuclei. Neutron absorption by oxygen can safely be neglected.

The neutron absorption by a sample strongly depends on the sample geometry and can analytically be calculated only for rare ideal cases. To estimate the effect of isotope substitution (${}^{6}_{3}\mathrm{Li} \rightarrow {}^{7}_{3}\mathrm{Li}$) on the count rate for inelastic scattering processes a simplified model is deployed:

Table 4.1.: Neutron cross sections (coherent, incoherent, absorption) for isotopes of Li, O and Cu (from [136]). Absorption cross sections are for $\lambda = 1.798\,\text{Å}$.

chemical symbol	natural composition	σ_{coh} [barn]	σ_{inc} [barn]	σ_{abs} [barn]
Li		0.454	0.92	70.5
$^{6}_{3}$Li	7.5 %	0.51	0.46	940
$^{7}_{3}$Li	92.5 %	0.619	0.78	0.0454
O		4.232	0.0008	0.00019
$^{16}_{8}$O	99.762 %	4.232	0	0.0001
$^{17}_{8}$O	0.038 %	4.2	0.004	0.236
$^{18}_{8}$O	0.2 %	4.29	0	0.00016
Cu		7.485	0.55	3.78
$^{63}_{29}$Cu	69.17 %	5.2	0.006	4.5
$^{65}_{29}$Cu	30.83 %	14.1	0.4	2.17

1. All scattering is assumed to be in forward direction, such that the scattering model reduces to one dimension on a sample of thickness d. The effect of this simplification is that in such model the absorption probability can be treated independently from scattering events. However, this model therefore largely overestimates the probability of coherent scattering events. In order to account for this draw-back, the coherent scattering cross sections are normalized by $1/4\pi$. The predictions of the model must thus to be taken with care, if the scattering probabilities are large.

2. Non-magnetic inelastic scattering is neglected.

3. Inelastic scattering processes do not effect the absorption coefficient of the scattered neutron.

4. The inelastic magnetic scattering cross section σ_{scatt} is assumed to be of the order of 10^{-6} of the copper coherent nuclear cross section. Note that the precise value selected does not effect the relative change of the inelastic scattering probability with ^{6}Li concentration if σ_{scatt} is small compared to the absorption cross section, which can be safely assumed. Also, the ratio of scattering probabilities for different sample compositions is then independent of the normalization of the coherent scattering probabilities.

Then, for a given sample with an atomic density n and thickness d, the probability of a neutron absorption event p_{abs} is

$$1 - p_{\text{abs}} = \frac{I(d)}{I_0} = e^{-\mu_{\text{abs}} d} \qquad \text{, where} \qquad \mu_{\text{abs}} = \sum_{\text{atoms: } i} n_i \cdot \sigma_{\text{abs},i} \tag{4.1}$$

The probability of a inelastic magnetic scattering event p_{scatt} is then given by

$$(1-p_{\text{abs}})-p_{\text{scatt}}=(1-p_{\text{abs}})e^{-\mu_{\text{scatt}}d} \qquad \text{with} \qquad \mu_{\text{scatt}}=n_{\text{Cu}^{2+}}\cdot\sigma_{\text{scatt}}. \tag{4.2}$$

Then, p_{scatt} is maximized for an optimal sample thickness d_{opt}

$$\left.\frac{\mathrm{d}p_{\text{scatt}}}{\mathrm{d}d}\right|_{d=d_{\text{opt}}}=0 \qquad \Rightarrow \qquad d_{\text{opt}}=\frac{1}{\mu_{\text{scatt}}}\ln\left(1+\frac{\mu_{\text{scatt}}}{\mu_{\text{abs}}}\right) \tag{4.3}$$

Expanding this expression for small μ_{scatt}, one obtains

$$d_{\text{opt}}=\frac{1}{\mu_{\text{abs}}}+\frac{\mu_{\text{scatt}}}{\mu_{\text{abs}}^2}+O[\mu_{\text{scatt}}]^2$$

such that d_{opt} depends only weakly on small μ_{scatt}, but is determined by the generally larger μ_{abs}. The neutron absorption cross section σ_{abs} of a nucleus

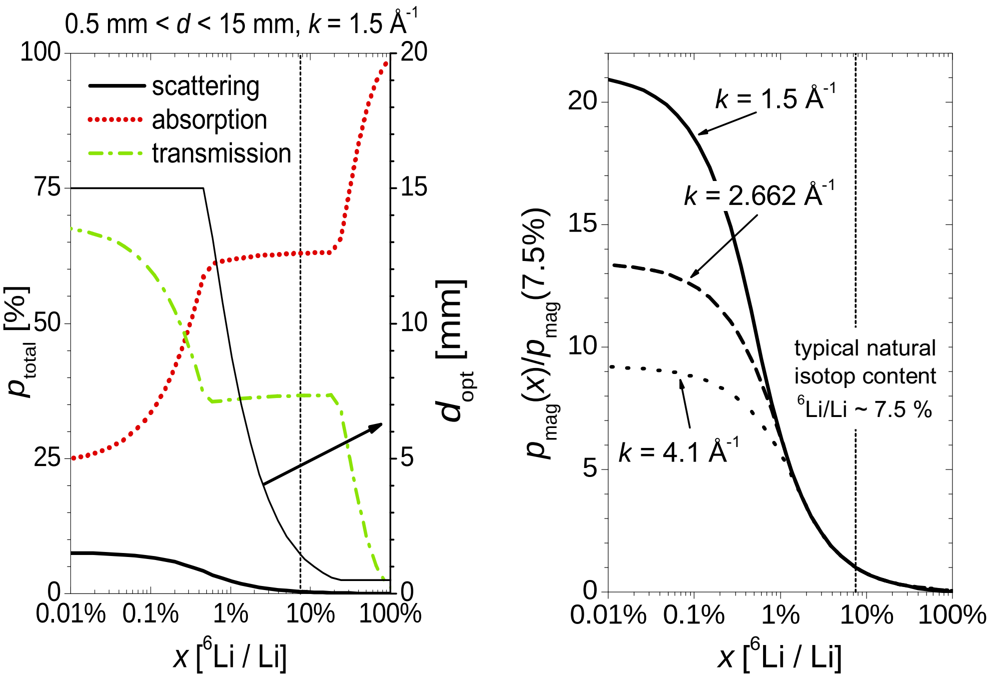

Figure 4.1.: Effect of $^{6}_{3}\text{Li} \to ^{7}_{3}\text{Li}$-substitution on the scattered intensity. Left: ^{6}Li-concentration dependence of the scattered, absorbed and transmitted incident neutron beam for $k_{\text{i}}=1.5\,\text{Å}^{-1}$ and an optimal sample thickness (thin solid line) between 0.5 and 15 mm. The finite range of sample thicknesses gives rise to the kinks in the curves. The natural ^{6}Li content is indicated by the vertical dotted line. Right: The ratio of scattered inelastic magnetic intensity from samples of optimal thickness in range 0.5 to 15 mm for typical neutron wave length vs. ^{6}Li content of the sample reveals an intensity gain of an order of magnitude for ^{6}Li depleted samples compared to samples with a natural ^{6}Li-content.

depends on the neutron wavelength λ. For cold and thermal neutrons $\sigma_{\text{abs}} \propto \lambda$ applies[1]. In Fig. 4.1 the effect of the ${}^{6}_{3}\text{Li} \rightarrow {}^{7}_{3}\text{Li}$ substitution on p_{scatt} is plotted relative to the natural isotope composition.

The employed model shows, that deployment of a ^{6}Li deficient sample will increase the detectable signal by about an order of magnitude for all incident neutron energies of interest. In other words, in inelastic neutron scattering experiments on a sample with a natural ^{6}Li content only a 10th of the data presented below could have been collected. Moreover, the weakest features of the spectrum would have been suppressed to the intensity of the experimental background.

4.2. Crystal growth and characterization

For neutron scattering experiments an isotope enriched (99.9%) ^{7}Li$_2$CuO$_2$ single crystal was grown from LiOH and CuO by the traveling solvent zone method under high pressure [137]. In order to avoid loss of Li and O during growth a 4:1 Ar:O$_2$ atmosphere of 50 bar was applied. Growth of other phases could be suppressed by a high growth rate of 10 mm/h [138]. A single crystal of $\approx$ 7 cm length, a diameter of $\approx$ 6.5 mm and a mass of $\approx$ 8.5 g was grown. The crystal was characterized by polarized light microscopy, X-ray powder diffraction and thermodynamic methods. Polarized light microscopy reveals the clear presence of a second phase, which is found in thin layers aligned about parallel to the cleaving planes (101) and $(10\bar{1})$, which could however not be identified [138]. In X-ray powder diffraction (Co-K_α-tube) all observed lines can be assigned to Li$_2$CuO$_2$ with few exceptions. At angles 35.00°, 37.25°, 39.18° and 43.14° additional reflections are found. Further, very broad lines are found near 19.3° and 27.5°, (maybe attributed to the strong (002)-reflex and (101)-reflex in Co-K_β, respectively [5]). The lines at 37.25° and 43.14° can be indexed by Li$_2$CO$_3$, which may be present due to a reaction of the powder with air-CO$_2$ [139]. The reflex at 39.18° may indicate the presence of Li$_2$O. A possible origin of the reflex at 35.00° has not been found. Importantly, the data do not indicate any presence of CuO, which would yield lines at 41.5° and 45.6° [140]. Moreover, the observed diffraction pattern does not indicate the presence of LiCuO$_2$ or Li$_{1.5}$CuO$_2$, as would be observable for larger Li deficiency of the sample [5, 141]. The crystal is observed to exhibit a significant intrinsic mosaicity, as shown in the neutron Laue-diffraction pattern Fig. 4.3. Elastic line scans of the reflexes on the three axis spectrometers 4F2/LLB, where only one single crystal was measured, reveal a full width at half maximum of up to 3.5° Fig. 4.4. The line width of this exemplary data set is particulary large and can thus be considered as representative for the crystals as used in the preformed neutron scattering experiments. The mosaicity of the smaller samples as used for the study of thermodynamic properties will generally be

---

[1] For some isotopes resonant absorption occurs at neutron energies of only few 100 meV [132].

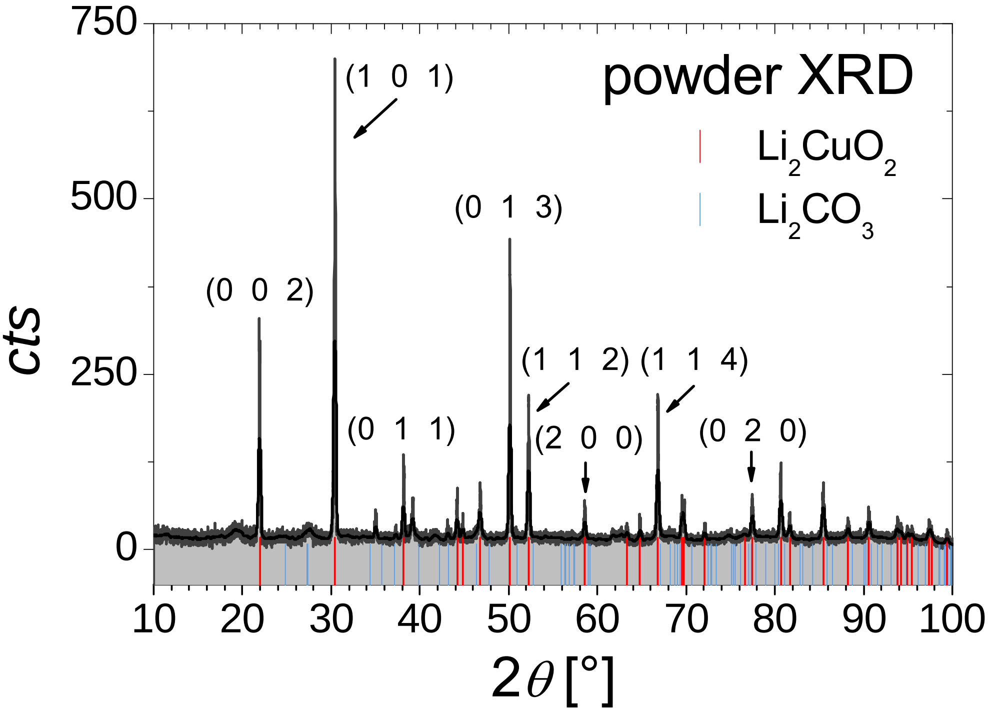

Figure 4.2.: X-ray diffraction pattern (Co-K_α) of a Li_2CuO_2 powder sample. Most reflexes can be indexed by Li_2CuO_2 (a selection of strong reflexes is indexed), some can be attributed to Li_2CO_3[139], which may result from reaction of the sample with air. The origin of some reflexes could not be identified, in particular the reflex at 35°.

less pronounced. Interestingly, a broadening of the reflex is found only for momentum transfer perpendicular to the chain, representative for a relative rotation of the crystallites about the b-axis. The origin of hereof may be related to a variation of the thickness of the inclusions of the second phase or to micro-cracks in the sample at the cleaving planes. The overall thermodynamic properties of the sample, e.g. magnetization and specific heat (cf. Part III) are in good agreement to data presented in the literature. In particular, long range order is found below $T_\mathrm{N} = 9.25(5)\,\mathrm{K}$, a weak ferromagnetic component below $\mathrm{T}_2 \approx 2.6\,\mathrm{K}$ and a meta-magnetic transition at low temperature at $H_\mathrm{c} = 10\,\mathrm{T}$, connected to an anisotropy gap of $\Delta = 1.36(2)\,\mathrm{meV}$. $\chi(T)$ data at low temperature show a slightly more pronounced Curie-like increase, which may indicate the presence of free spins. However, the size of this increase differs between samples, such that sample contamination related to the surface moisture sensitivity may be considered. However, this interpretation seems to not apply as studies on single crystals purposely exposed to air have not shown any alike change in $\chi(T)$ [112].

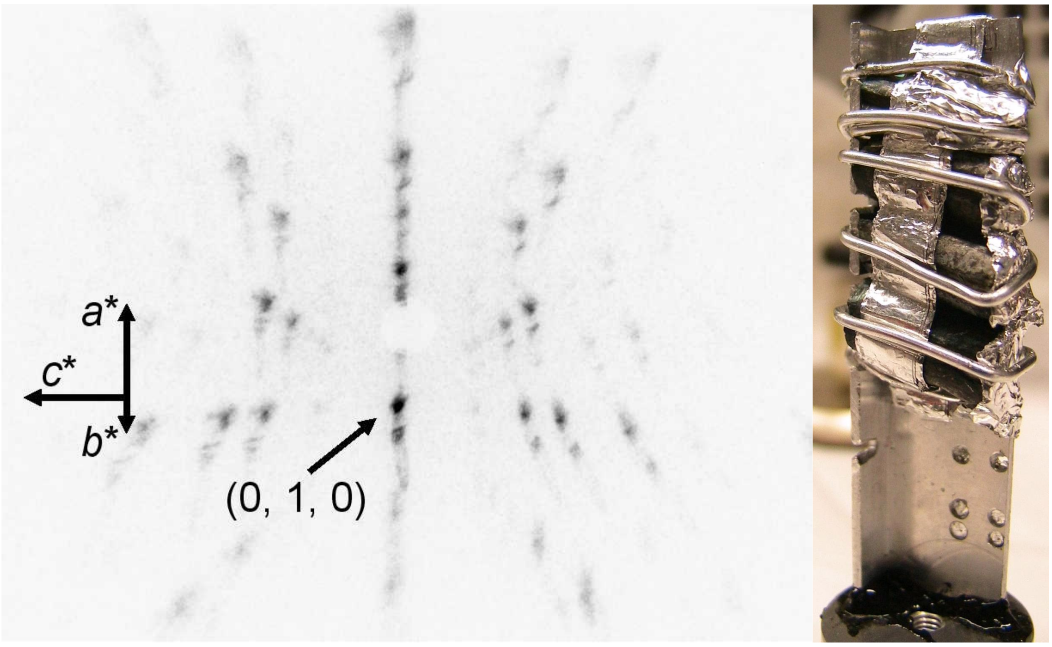

Figure 4.3.: left: Neutron Laue diffraction pattern of a Li_2CuO_2 single crystal with incident beam ⊥ to the *c*-axis. This pattern, measured at OrientExpress/ILL, reflects the intrinsic mosaicity of the sample. At least two larger crystallites can be identified. right: The 3.8 g sample as used at IN8/ILL and IN12/ILL (cf. Chapter 5) in process of co-alinement of the 4 crystallites.

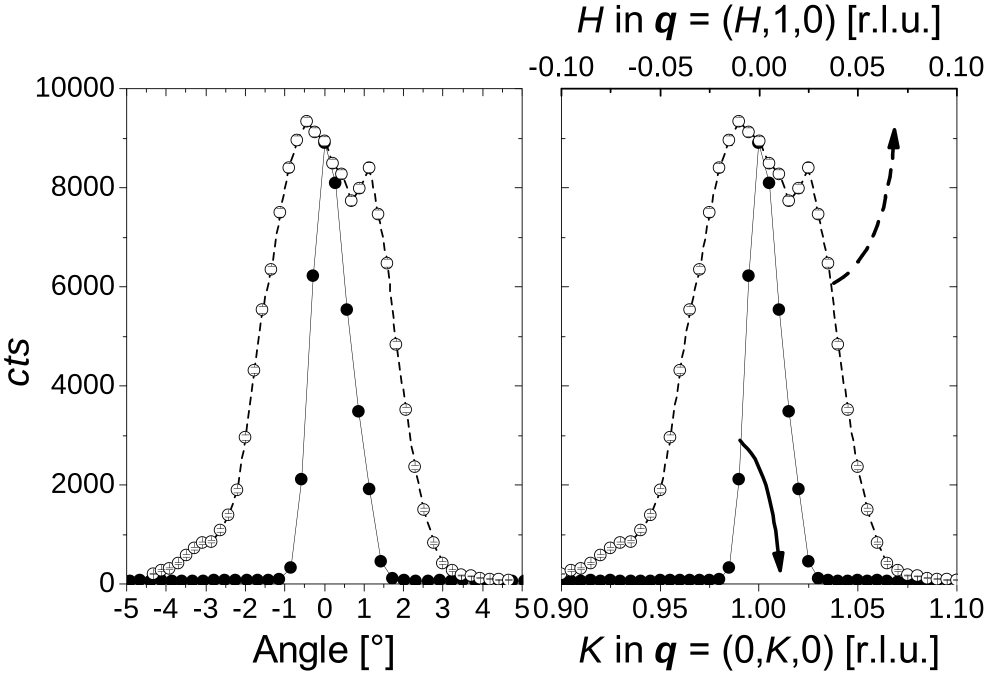

Figure 4.4.: Elastic line scans as performed during orientation of one single crystal for the experiment at 4F2/LLB show the mosaicity of the crystal. Lines are guides to the eye. For momentum transfer perpendicular to the chain several crystallites can be identified, which however appear to share a common chain axis. As a consequence of the low q-resolution deployed and given a not too steep dispersion of the excitations, the different crystallites are not to be expected to cause well distinct contributions but only a line broadening in inelastic neutron scattering data.

Part II.

Inelastic neutron scattering studies

Deadlines rule!

Jorge Hamann-Borrero

5. Magnon excitations & spin-wave analysis

The main motivation for the study of Li_2CuO_2 in the course this thesis arose from the controversy in the community on the strength of the magnetic interactions in edge-shared cuprates. The individual chains in these compounds exhibit well comparable Cu-Cu distances of $\approx 2.9\,\text{Å}$ and Cu-O-Cu bond angles of $\approx 94°$, but the reported exchange couplings vary widely, in particular for the nearest neighbor exchange [68, 71, 117, 142]. Most detailed information about the coupling constants is revealed in measurements of the magnetic excitation spectrum, e.g. by means of inelastic neutron scattering (INS). The observed dispersion can then be analyzed by a spin-wave model, based on the structure of the ground state as well as the considered exchange interactions. However, analysis of the data within spin-wave theory is not necessarily validated if the excitations are renormalized by quantum fluctuations. For Li_2CuO_2, the large value of the ordered magnetic moment at low temperatures suggests, that quantum effects are strongly suppressed as a consequence of the ferromagnetic moment arrangement in the chains in the ordered state [39]. Therefore, Li_2CuO_2, represents a valuable case in the family of edge-shared cuprates, where the exchange interactions may be identified unbiased by renormalizations of the exchange interactions.

The magnetic excitation spectrum of Li_2CuO_2 has first been studied by inelastic neutron scattering by Boehm *et al.* in 1998 [117]. The experiment revealed a conventional dispersion of excitations for momentum transfer perpendicular to the spin-chains, but unexpectedly a completely different behavior for momentum transfer along the chains. Here, strongly broadened and hardly dispersive excitations have been found, whose spin-wave analysis resulted in very small intra-chain exchange integrals. Moreover, the nearest neighbor interaction J_{010} was found to be antiferromagnetic while the next-nearest neighbor interaction J_{020} was determined as ferromagnetic, i.e both signs contrast to the expectations from the KANAMORI-GOODENOUGH-ANDERSON-rules. In the same year, Mizuno *et al.* published magnetic susceptibility and optical conductivity data analyzed by exact diagonalization of single chains of 14 sites [20]. Within their analysis $J_{010} \approx -100\,\text{K}$ (ferromagnetic) and $J_{020} \approx 80\,\text{K}$ (antiferromagnetic) are obtained, in distinct contradiction to the experimental results by Boehm *et al.* In order to account for this discrepancy, Mizuno *et al.* extended their study of the susceptibility to clusters of two coupled chains with 12×2 as well as 6×4 sites, incorporating an effective inter-chain coupling J_c[1] [32]. Implementation of this inter-chain coupling into the model significantly changed the in-chain couplings fitted to the susceptibility data. Assuming again $J_{010} = -100\,\mathrm{K}$, $J_{020} \approx 40\,\mathrm{K}$ and $J_c \approx 8\,\mathrm{K}$ are obtained. The spin-correlation function $S(\vec{q}, \omega)$ has been calculated. The spectrum of this cluster with highly frustrated chains ($\alpha = 1/4$) is found to show two main dispersive features for momentum transfer along the chain. Firstly, spectral density at low energies $\Delta E < 5\,\mathrm{meV}$ - a remnant of the isolated chain spectrum - and secondly a magnon like feature with excitation energies up to $20\,\mathrm{meV}$ with a dispersion well described by spin-wave theory. Mizuno *et al.* point out, that the spectrum observed by Boehm *et al.* cannot be attributed to the low energy feature in the studied clusters.

In order to gain a better understanding of the apparent contradiction between the available spectral data and the theoretical predicted spectrum we proposed extensive inelastic neutron scattering experiments on $\mathrm{Li_2CuO_2}$. The over-damped mode of excitations observed by Boehm *et al.* was to be studied in more detail and the high magnon related spectral density at the zone boundary predicted by Mizuno *et al.* was to be verified.

5.1. Linear spin-wave model

The data obtained in our inelastic neutron scattering experiments on the magnon dispersion have shown to be well described within a spin-wave model. As the set of experiments performed has largely been motivated by a progressive spin-wave analysis of the data, the model is presented ahead of the data. Eventually, the cooperative process of experiential study and theoretical analysis allowed to determine presumably all the relevant exchange integrals in the model. The model is based on the HEISENBERG spin HAMILTONian with uniaxial anisotropy

$$\hat{\mathcal{H}} = \frac{1}{2} \sum_{\vec{m},\vec{r}} \left[J^z_{\vec{r}} \hat{S}^z_{\vec{m}} \hat{S}^z_{\vec{m}+\vec{r}} + J_{\vec{r}} \hat{S}^+_{\vec{m}} \hat{S}^-_{\vec{m}+\vec{r}} \right] \tag{5.1}$$

where the copper sites at position $\vec{m}$ are coupled to neighbors at $\vec{m} + \vec{r}$ by an exchange interaction $J_{\vec{r}}$. Starting from the classical two sublattice NÉEL-state (approximating the antiferromagnetically ordered ground state of $\mathrm{Li_2CuO_2}$ at low temperature and ambient field), spin-wave theory predicts a magnon dispersion [143]

$$\Delta E(\vec{q}) = \sqrt{\left(J(\vec{q}) - J(0) + I(0) - D\right)^2 - \tilde{J}(\vec{q})^2} \tag{5.2}$$

where $J(\vec{q})$ and $\tilde{J}(\vec{q})$ are the FOURIER transforms $\frac{1}{2}\sum_{\vec{r}} J_{\vec{r}} \exp(\imath \vec{q}\vec{r})$ for the intra-sublattice and inter-sublattice exchange path, respectively. The exchange anisotropy $D = J^z(0) - J(0) - (I^z(0) - I(0))$ causes a magnon excitation gap $\Delta E(0) = \sqrt{D(D - 2I(0))}$.

---

[1] In [32] it assumed, that $J_c = I_{111} = I_{131}$.

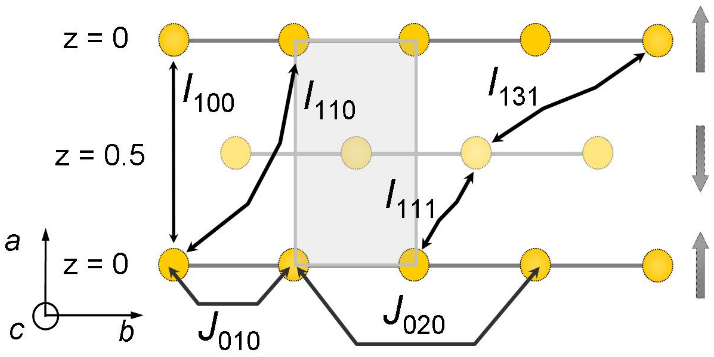

Figure 5.1.: Schematic exchange pattern for Li_2CuO_2. Spin-chains are depicted as horizontal lines formed by Cu-ions (spheres). The shaded box shows a projection of the crystallographic unit cell. Arrows at the right indicate the alternating moment orientation in the sublattices along $z[c]$. The indexed arrows indicate exchange interactions between the connected copper sites. As leading exchange constants, a ferromagnetic J_{010} is expected to compete with an antiferromagnetic J_{020}. Note the frustration between the antiferromagnetic inter-chain interactions, I_{131} and I_{100} in particular. Considering only the (dominant) inter-chain coupling I_{131}, note the induced frustration for non-collinear spin arrangement within the chains. See Section 5.6 and Section 5.7 for further details.

In order to calculate Eqn. 5.2 for Li_2CuO_2, the FOURIER transform is taken over all neighbors where non-vanishing exchange interactions are expected. The corresponding exchange paths are labeled as depicted in Fig. 5.1. Along the chain (b-direction), a nearest neighbor, next nearest neighbor and probably couplings to further neighbors must considered and are referred to as J_{010}, J_{020} and $J_{0\ldots0}$, respectively. For clarity, the inter-chain couplings are denoted as I_{xyz} instead. The strongest inter-chain coupling is expected between neighboring chains along the paths $(\frac{1}{2}, \frac{1}{2}, \frac{1}{2})$, $(\frac{1}{2}, \frac{3}{2}, \frac{1}{2})$, etc. , where the vector is in units of the crystallographic unit cell and which are denoted as I_{111}, I_{131}, $I_{1\ldots1}$, respectively. Further inter-chain exchange interactions are expected along the $(1, 0, 0)$, $(1, 1, 0)$ and $(0, 0, 1)$ directions and denoted as I_{100}, I_{110} and I_{001}.

Under neglect of further interactions, the magnon dispersion for Li_2CuO_2 can be written as

$$\Delta E = \sqrt{e^2 - g^2} \tag{5.3}$$

where the intra-sublattice exchange paths contribute to

$$\begin{aligned} e \;=\; & J_{010}\cos(k) + J_{020}\cos(2\cdot k) + \ldots \\ + \;& I_{100}\cos(h) + 2\cdot I_{110}\cos(h)\cos(k) + I_{001}\cos(l) + \ldots \\ - \;& (J_{010} + J_{020} + \ldots + I_{100} + 2\cdot I_{110} + I_{001} + \ldots) \\ + \;& 4\cdot(I_{111} + I_{131} + \ldots) \\ + \;& D_{\text{aniso}} \end{aligned} \tag{5.4}$$

with h, k, l given in $2\pi\cdot$ reciprocal lattice units ($2\pi\cdot$ r.l.u.). The inter-sublattice exchange contributes to

$$g = 4 \cdot \cos\frac{h}{2}(I_{111}\cos\frac{k}{2} + I_{131}\cos\frac{3k}{2} + \ldots)\cos\frac{l}{2} \tag{5.5}$$

and the gap $\Delta E(0)$ enters via exchange anisotropy

$$D_{\text{aniso}} = \sqrt{(4\cdot(I_{111}+I_{131}+\ldots))^2 + \Delta E(0)^2} - 4\cdot(I_{111}+I_{131}+\ldots). \tag{5.6}$$

A key property of this dispersion relation is that the term g vanishes exactly, if any of the momentum vector components h, k or l equals 0.5, such that

$$\Delta E(\vec{q} \mid \{h,k,l\} \ni 0.5) = e. \tag{5.7}$$

At corresponding wave vectors, the interactions between the sublattices (I_{111}, I_{131}, ...) cause an only constant shift of the dispersion and the sum of these interactions can consequently be determined independently from the strength of the individual inter-sublattice couplings. Also, any non-vanishing dispersion along these directions can be attributed to intra-sublattice interactions only.

5.2. Experimental setup

The inelastic neutron scattering experiments on the excitation spectrum of Li_2CuO_2 have been conduced at cold and thermal neutron three axes spectrometers installed at the research reactors of the *Institut Laue-Langevin* and the *Laboratoire Léon Brillouin*. The experiments have been performed predominantly at a sample temperature $T = 4\,\text{K}$. Boehm *et al.* have recorded the temperature dependence of the sub-lattice magnetization and the anisotropy gap, which are both found to be rather constant below $T = 5\,\text{K}$. A corresponding result is obtained also for our crystal (cf. Fig. 7.5). At $T = 4\,\text{K}$ the spectrum is thus expected to not be largely renormalized by magnon-magnon interactions that are important near the ordering temperature $T_\text{N} = 9.25(5)\,\text{K}$. At the same time, the magnetic ground state is expected to be collinear, unlike below 2.6 K, where a canted magnetic state was proposed [112]. For the spectrometers we used typical three axis operational parameters, i.e. PG(002) monochromator and analyzer with PG and LN_2-cooled Be-filter for thermal and cold neutrons, respectively.

5.3. Magnon dispersion for $\vec{q} \parallel b^*$

5.3.1. Thermal neutrons

From the dynamic magnetic scattering function as calculated by Mizuno *et al.* strong scattering of neutrons from magnons was to be expected at the

Table 5.1.: List of inelastic neutron scattering experiments on the magnon dispersion in Li_2CuO_2.

Instrument/ Institute	scattering plane	key experimental parameters
thermal neutrons		
IN8/ILL	(0,K,L)	$k_\mathrm{f} = 2.662\,\mathrm{\AA}^{-1}$, $T = 4.0\,\mathrm{K}$
cold neutrons		
IN12/ILL	(0,K,L)	$k_\mathrm{f} = 1.5\,\mathrm{\AA}^{-1}$, $T = 4.1\,\mathrm{K}$
4F1/LLB	(H,0,L)	$k_\mathrm{f} = 1.55\,\mathrm{\AA}^{-1}$, $T = 4.1\,\mathrm{K}$
4F2/LLB	(H,K,0)	$k_\mathrm{f} = 1.55\,\mathrm{\AA}^{-1}$, $T = 4.0\,\mathrm{K}$

magnetic zone boundary. In particular, the magnon excitation energy at the zone boundary was predicted to be $\approx 20\,\mathrm{meV}$ for the proposed exchange interactions. In the experiments by Boehm *et al.* only excitations with energy $< 8\,\mathrm{meV}$ were probed. In the first inelastic neutron scattering experiment on our $^7Li_2CuO_2$ crystal the predicted magnon dispersion at the zone boundary was tested. A sample composed of 4 crystals co-aligned in the $(0, K, L)$ scatting plane and a total mass of 3.8 g was prepared. The experiment was conducted at the thermal three axis spectrometer (TAS) IN8 at the *Institut Laue-Langevin*, likely the most powerful thermal TAS nowadays. With the selected PG(002) analyzer and monochromator and a fixed final neutron wave length $k_\mathrm{f} = 2.662\,\mathrm{\AA}^{-1}$, excitations with energies up to $25\,\mathrm{meV}$ are accessible. For energy transfers $> 26\,\mathrm{meV} \approx \frac{\hbar^2(4/3\,k_\mathrm{f})^2}{2m_n}$ spurious features impede the detection of reliable signals for this setup.

The magnetic zone boundary along the b^* axis with lowest momentum transfer, i.e. maximal magnetic form factor that can be reached in this experimental configuration for energy transfer up to $25\,\mathrm{meV}$ is $\vec{q} = (0, 1.5, 0)$ in reciprocal lattice units (r.l.u.). Constant q-scans (varying energy transfer) near this q vector are presented in Fig. 5.2(left). Data have been collected typically with a monitor count rate of 2500 mon., corresponding to ≈ 1 min. of measurement time per data point. The curves display two features: a peak near $12\,\mathrm{meV}$, which is spurious[2] and a second one at $\approx 19\,\mathrm{meV}$. However, intensity near $19\,\mathrm{meV}$ is found for any selected momentum transfer and hence cannot be attributed to the predicted magnon dispersion. As shown in Fig. 5.2(right), this feature does not change upon rising the temperature above T_N, and should therefore be ascribed to an about non-dispersive optical phonon.

However, at q-points close to the magnetic zone center a clearly dispersive feature is observed, which was detected e.g. between $\vec{q} = (0, 1.2, 0)$ at $\approx 4\,\mathrm{meV}$ and $\vec{q} = (0, 1.35, 0)$ at $\approx 24\,\mathrm{meV}$. As verified in Fig. 5.2(right), this feature is

---

[2] This peak is not observed in constant q-scan with slightly different q and is also absent in scans with $k_\mathrm{f} = 4.1\,\mathrm{\AA}$.

observed to be periodic with the magnetic Brillouin zone and becomes entirely smeared out upon increasing the sample temperature to 12 K > T_N. Accordingly, it appears verified to identify this feature with a coherent magnetic excitation as theoretically predicted. However, the dispersion is much steeper than expected, indicating an underestimation of the exchange constants in the calculations by Mizuno *et al.*

In order to study the dispersion in more detail, the experiment was continued by constant energy scans (varying $\vec{q}$), which are advantageous in resolving steep dispersions. Corresponding data are displayed in Fig. 5.3. The data show a number of irregular peaks with no related dispersion which are therefore attributed to spurious scattering. Near the nuclear zone center $\vec{q} = (0, 2, 0)$ acoustic phonons are observed. The dispersive magnetic excitation was observed between 5 meV and 25 meV. Unfortunately, technical problems with

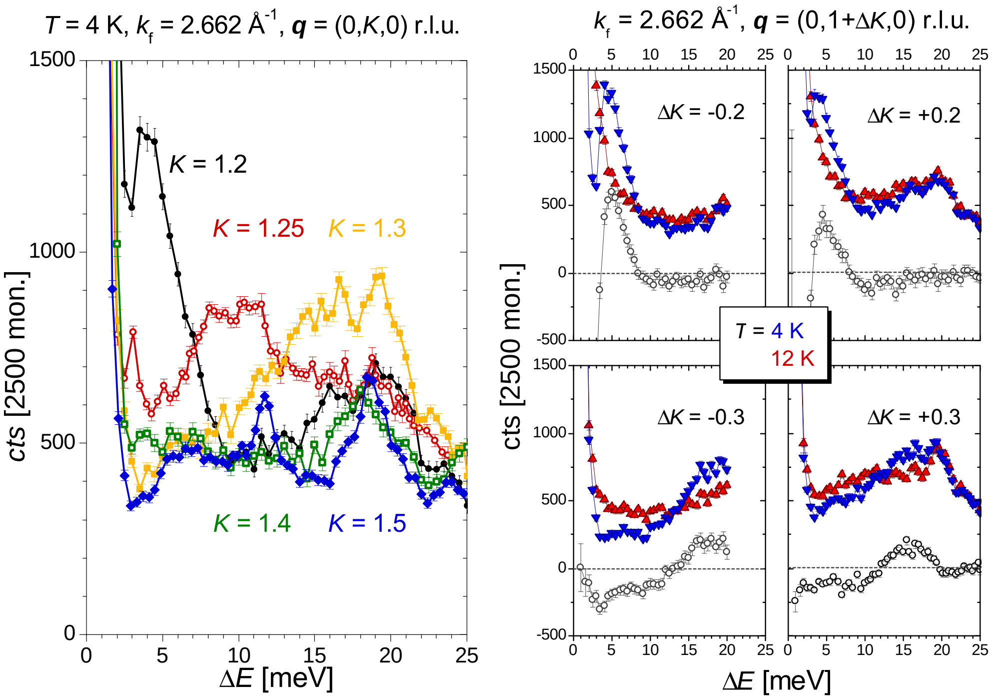

Figure 5.2.: Energy scans at constant momentum transfer measured at IN8/ILL. Left: Data taken at different momentum transfer along the chain. A non-dispersive feature near 19 meV is found in all data sets. A second, clearly dispersive feature is found near the zone center $\vec{q} = (0, 1, 0)$, whose energy is apparently > 25 meV for $\vec{q} = (0, 1.4, 0)$ and at the magnetic zone boundary $\vec{q} = (0, 1.5, 0)$. The peak at 12 meV in the latter curve is spurious. Right: The magnetic character of the dispersive feature is verified by comparison of the spectrum at equivalent $\vec{q}$-points in the magnetic Brillouin zone $\vec{q} = (0, 1 \pm \Delta K, 0)$. The curves also compare data taken at $T = 4\,\mathrm{K} < T_\mathrm{N}$ (▼) and $T = 12\,\mathrm{K} > T_\mathrm{N}$ (▲) as well as the difference of these (○).

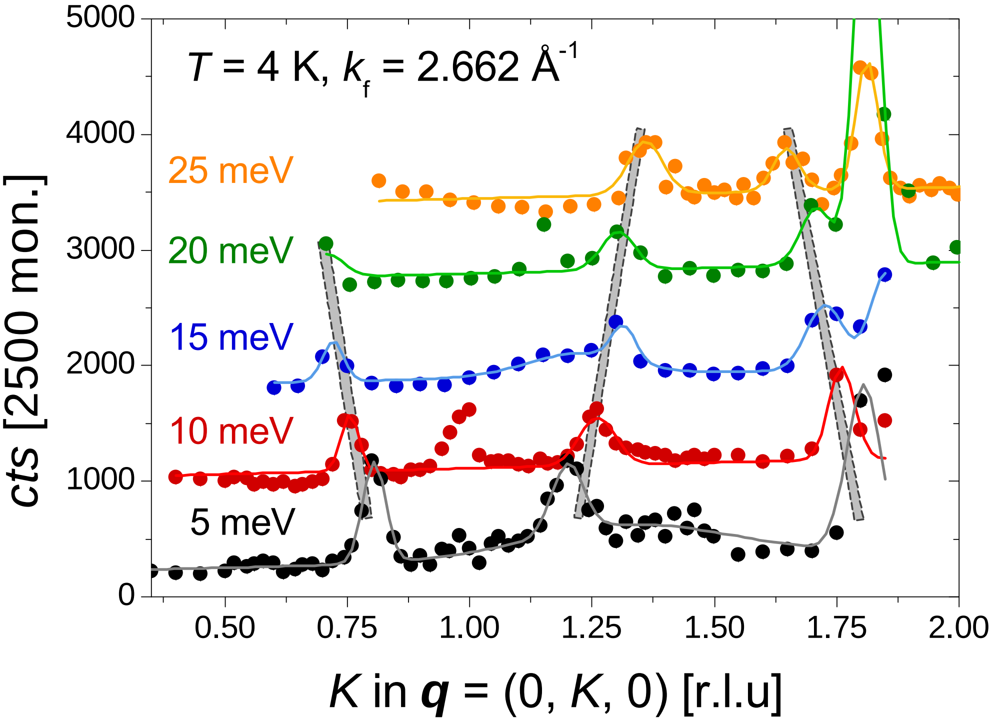

Figure 5.3.: Momentum transfer scans along $\vec{q} = (0, K, 0)$ at constant energy measured at IN8/ILL. The data display a dispersive feature which is periodic with the magnetic Brillouin zone. Bars highlight this magnetic dispersion. At high energy the data show another strong feature, which is attributed to acoustic phonons emanating from the crystallographic zone center $\vec{q} = (0, 2, 0)$. Furthermore, peaks without dispersion are found (e.g. at $(0, 1, 0)$ at 10 meV) which are considered to be spurious. The magnetic peaks are fitted by Gaussian distributions (lines).

the spectrometer did not allow to elaborate all the individual data sets in much detail and some of the peaks related to the dispersion contain only a single point. Also, the background under these peaks is not very flat, however considering all curves as an overall data set the existence of a dispersive feature is clearly evident and the position of the peaks can be determined. For fitting the data sets the background is described by a linear term and additional broad Gaussians where needed. The observed peaks related to the dispersion are fitted independently. However, for peaks with only few data points, the width of the peak was fixed manually. The peak positions as fitted confirm the periodicity of the dispersive feature with the magnetic unit cell and are used thereafter for fits of the spin-wave model in Section 5.6.

5.3.2. Cold neutrons

On the same sample, inelastic scattering experiments have been performed at the cold three-axis spectrometer IN12 at *Institut Laue-Langevin*. The selected scattering plane allowed to investigate magnetic excitations near the magnetic zone center $\vec{q} = (0, 0, 1)$ which has the lowest absolute $|\vec{q}|$ value and therefore the largest magnetic form factor. Data have been collected typically with a monitor count rate of 2.5×10^5 mon., which corresponds to ≈ 1 min. measurement time per data point. For momentum transfer along the chain axis, i.e. $\vec{q} = (0, K, 1)$, the dispersion of the magnetic excitation has been investigated with energy transfer up to 4.5 meV.

In this energy regime we expected to observe data, well comparable to those by Boehm *et al.* [117], but in much better quality. The IN12 spectrometer does provide a better energy and momentum resolution than the IN3 thermal test spectrometer used by Boehm *et al.* Moreover, deploying a ^{6}Li depleted sample is expected to increase the scattered intensity, which depends however on the incident neutron beam intensity at the two instruments. The relative gain in scattered intensity may be estimated from the height of the peak of the excitation at $\vec{q} = (0, 0, 1.1)$ which amounts to ≈ 60 *cts*/min. in the experiment of Boehm *et al.* and 610 *cts*/min. in our experiment. Nevertheless, the dispersion observed by Boehm *et al.* for momentum transfer along the chain could not be reproduced in our experiment. In Fig. 5.4, the low energy spectrum for momentum transfer $\vec{q} = (0, K, 1)$ is presented as an intensity map, individual constant energy scans are shown in Fig. 5.5. The data show a pronounced mode of col-

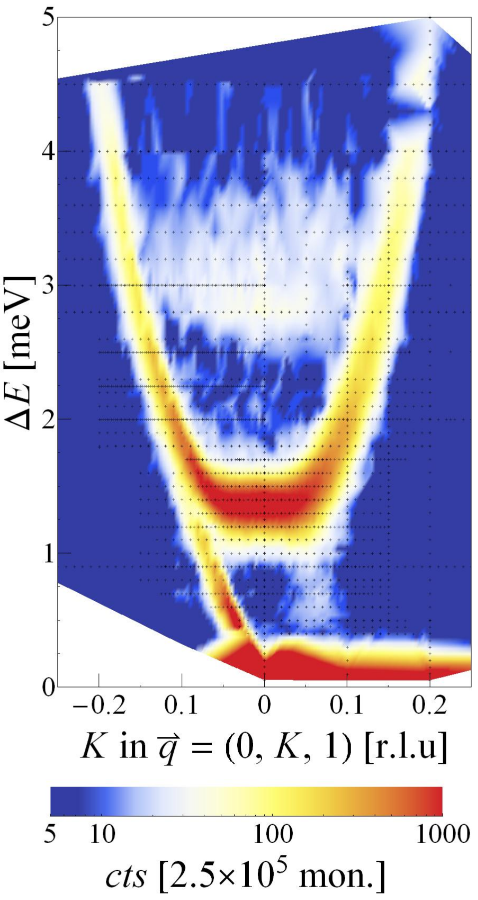

Figure 5.4: Intensity map of the low energy magnetic spectrum at $T = 4.1\,\mathrm{K}$ near the magnetic zone center $\vec{q} = (0, 0, 1)$ with the momentum transfer varied along the chain axis. The plot is interpolated from the count rate of data points taken at IN12/ILL, which are indicated by black dots. Note at the color, representing the measured count rates is scaled logarithmically. The map illustrates the magnon dispersion, a continuum of excitations above ≈ 2.7 meV and states below the magnon gap near $K \approx +0.05$. The sizeable intensity below the gap energy, at energy transfer $\lesssim$ 1 meV and $K \approx -0.05$ is due to a spurious Bragg tail from the elastic reflex at $(0, 0, 1)$.

lective excitations with a rather steep dispersion. The observed intensity is large at the zone center Γ, but falls off rapidly for larger energy transfer. At Γ, count rates of $I_\Gamma \approx 1750$/min. are to be compared with ≈ 50/min. $\lesssim 0.03 \times I_\Gamma$ at energy transfer of 4.5 meV. The individual data sets can be well described by GAUSSian distributions. The peak positions related to the magnon excitation are recorded for a spin-wave analysis as described in Section 5.6. However, just in the vicinity of the zone center a clear assignment of the observed intensity to the magnon mode is not possible. In measurements at constant momentum transfer $\vec{q} = (0, 0, 1)$ the magnon excitation does not show any unexpected broadening and the magnon gap $\Delta_\Gamma = 1.36(2)$ meV can be clearly determined (cf. Fig. 5.7). However, constant energy scans at 1.3 meV, i.e. just below the gap at Γ clearly show two separate lines. A possible interpretation hereof could be given by a slight incommensurability of the magnon. However, below the gap the two lines observed cannot be distinguished from the incommensurate excitations observed well below the magnon (cf. Chapter 6). At the same time, in constant energy scans at 1.4 meV, i.e. just above the gap, three lines are observed (cf. Fig. 5.5), where the central one is expected to be caused by the resolution broadening of the intense magnon at Γ as well as finite temperature, being strongly suppressed at $T = 1.4$ K.

A direct comparison to the data by Boehm *et al.* is difficult, as in their publication only one data set is presented: an energy scan at $\vec{q} = (0, 0.85, 2)$. These data show a broad excitation near 3 meV on a sizable background. In our experiment an energy scan at a corresponding momentum transfer $\vec{q} = (0, 0.15, 1)$ also features an excitation at 3 meV, which also is broadened as a consequence of the rather steep dispersion of the excitations. In Fig. 5.6 (left) both data sets are plotted next to another. Surprisingly, the dispersion in chain direction presented by Boehm *et al.* is well confined below 2.5 meV and one can read off an excitation energy of ≈ 2.2 meV for the corresponding momentum transfer $\vec{Q} = 0, 0.15, 0$ in the reduced unit cell (cf. Fig. 5 in [117]).

The dispersion presented by Boehm *et al.* shows a pronounced minimum near the zone boundary $\vec{Q} = (0, 0.5, 0)$ with an excitation energy of 1.65(20) meV. In our experiment, we have been able to confirm a very weak feature at $\vec{q} = (0, 0.5, 1)$ and $\Delta E = 1.71(4)$ meV. Due to the low count rate, extensive measurements on the dispersion of this feature have not been attempted. However, it has also been observed at $\vec{Q} = (0, 0.3, 1)$ at 1.80(15) meV and probably at $\vec{Q} = (0, 0.15, 1)$ at 1.75(7) meV and such is well distinct from the dispersion published by Boehm *et al.* The periodicity of the feature with the magnetic unit cell has however not been investigated in our experiment and it can hence not be excluded, that it may be related to scattering from a misaligned grain of the sample. If the feature can be shown to be an intrinsic property, they may be related to the low energy spectral weight observed in the calculations by Mizuno *et al.* [32] [3].

---

[3] Which in turn may however be due to a finite size effect.

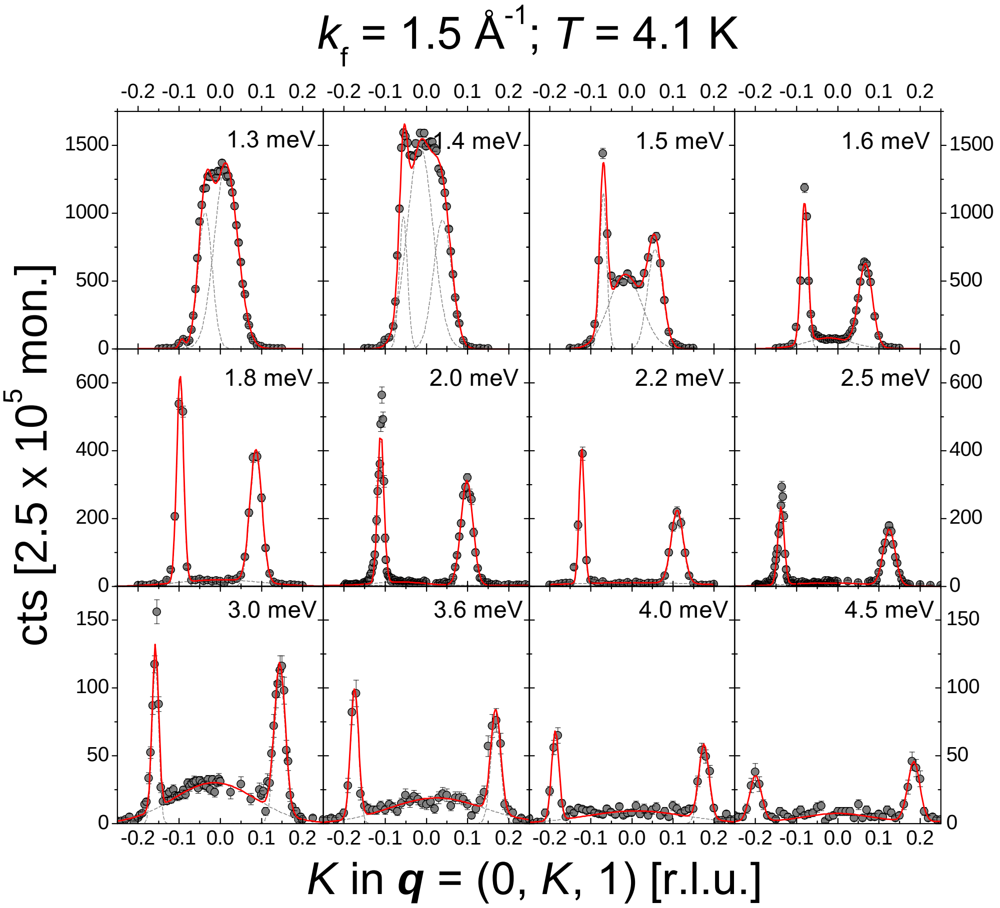

Figure 5.5.: Scans at constant energy and varied momentum transfer $\vec{q} = (0, K, 1)$ at measured at IN12/ILL. The asymmetry of the data is resolution-related. Fits are Gaussian distributions as described in the text. At energies just above the magnon gap at $\Delta E = 1.36(2)$ meV and also above $\Delta E \approx 2.7$ meV significant additional intensity is found near $K = 0$. While the first may be due to slight broadening of the magnon by instrumental resolution and temperature, the origin of the second is yet to be clarified. Note the different scales of the ordinate.

5.4. Magnon dispersion for $\vec{q} \perp b^*$

Boehm *et al.* have studied in detail the dispersion of the magnetic excitations for momentum transfer perpendicular to the chain. The drastic difference of the in-chain dispersions observed in their experiments compared to our studies motivated to revisit the dispersion perpendicular to the chains. In this section, the magnon dispersion along the $(0, 0, L)$ direction is presented in Fig. 5.7 (a), which has been obtained in the experiment at IN12/ILL described above. These data show a sharp excitation at at the zone center $(0, 0, 1)$ which can be well described by a sharp Gaussian distribution. However, increasing the momentum transfer along L, the curve broadens significantly and may even

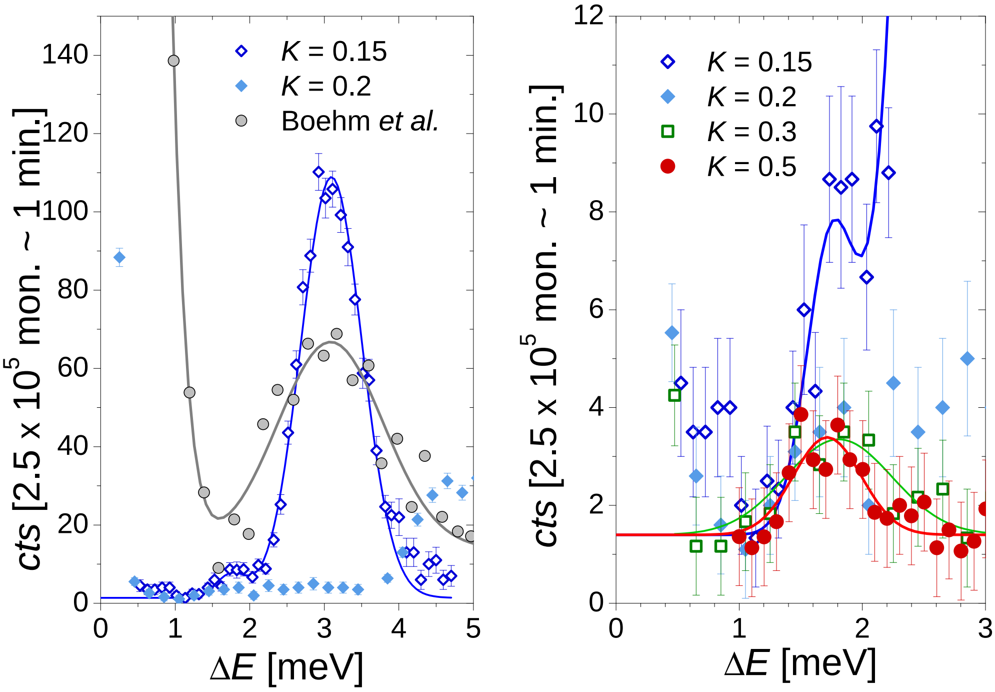

Figure 5.6.: Energy scans at constant $\vec{q}$. Left: Data from Boehm *et al.* (Fig. 4 [117]), taken at $\vec{q} = (0, 0.85, 2)$ are compared to a corresponding data set at $\vec{q} = (0, 0.15, 1)$ from our experiment. Both sets are fitted by GAUSSian distributions and show an excitation at $\approx 3\,\text{meV}$. The data by Boehm *et al.* are scaled by a factor 1.5 after subtraction of a constant background of 70 counts/5min. The steep dispersion and intensity decrease of the excitation is illustrated by a scan at $\vec{q} = (0, 0.2, 1)$. Right: At low energy $\Delta E \approx 1.8\,\text{meV}$ a weakly dispersive feature with low intensity is observed. Its periodicity with the magnetic BRILLOUIN zone is yet to be shown.

consist of two individual peaks. This effect is understood to originate from individual crystallites, i.e. slight misalignment of the 4 crystallites used and to the intrinsic mosaicity of the sample. This broadening was not observed for momentum transfer along the chain, presumably due to smaller changes of the scattering angle related to the relatively long b^* axis. Benefiting from the large scattered signal from our crystal, in further experiments dedicated to the magnon dispersion perpendicular to the chain only one single crystal has been employed.

The main experiment on interaction between the chains has been preformed at the cold 4F1 three axis spectrometer at the *Laboratoire Léon Brillouin*. A single crystal with mass $m \approx 1.2$ g has been oriented in the $(H, 0, L)$-scattering plane, i.e. for the study of excitations with $\vec{q} \perp b^*$. The magnon dispersion has been measured in constant momentum transfer scans, typically with a monitor count rate of 3000 cts corresponding to ≈ 1 min counting time per point. A summary of the experimental data is given in Fig. 5.7(b-

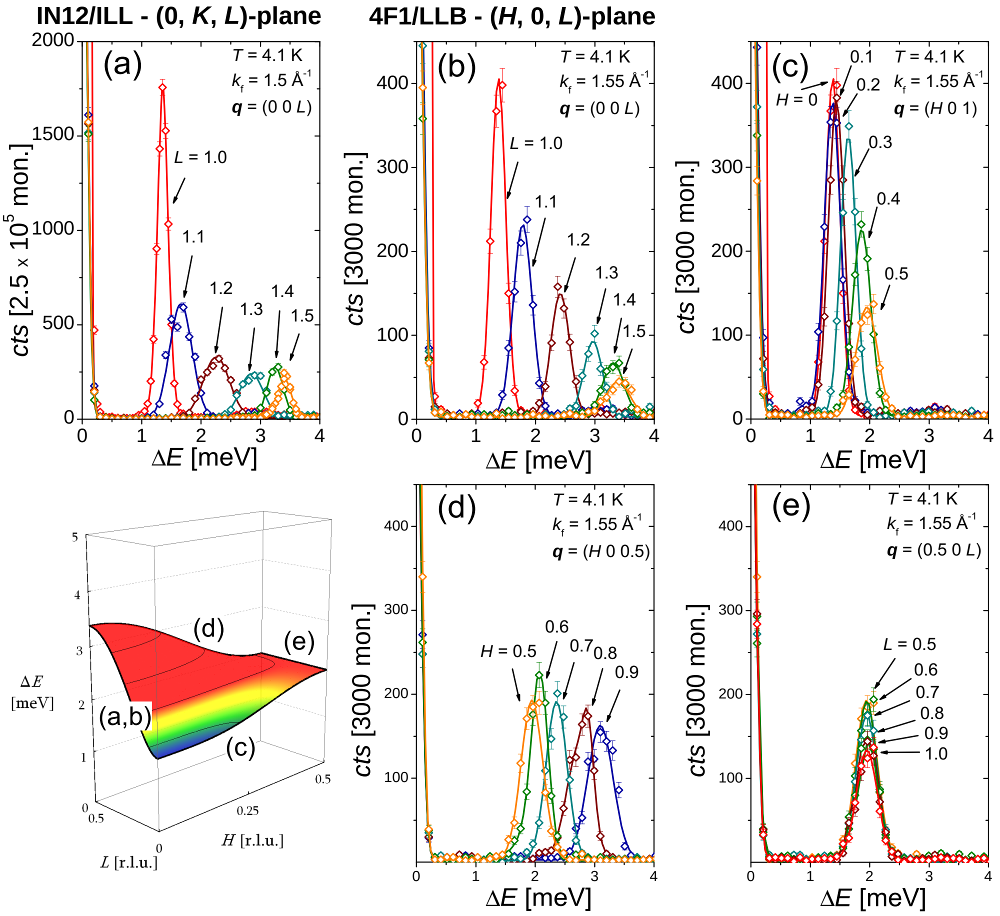

Figure 5.7.: Scans at constant momentum transfer $\vec{q} \perp b^*$. An outline of the data is given in the dispersion sheet in the reduced BRILLOUIN zone (left, bottom) (colors stress equal magnon energies), derived from the spin wave model Tab. 5.2. Fig. (a) and (b) compare the data in the $\vec{q} = (0, 0, L)$ direction as measured in the experiments at IN12/ILL and 4F1/LLB. Fig. (c), (d) and (e) display the data taken at 4F1 along the directions $\vec{q} = (H, 0, 1)$, $\vec{q} = (H, 0, 0.5)$ and $\vec{q} = (0.5, 0, L)$, respectively.

e). The dispersion along $\vec{q} = (0, 0, L)$, as obtained at IN12/ILL could be reproduced at 4F1, but there shows no broadening caused by mosaicity and the evolution of the peak height with momentum transfer is found to change continuously. The dispersion along $\vec{q} = (H, 0, 1)$ has been measured which is significantly more flat than along the $\vec{q} = (0, 0, L)$ directions, such that different exchange paths must be regarded to contribute in the respective directions. For both directions, the line shape is well described by GAUSSian distributions. Comparing the recorded peak positions with the results from Boehm *et al.* , the results from both experiments are found to be in very good agreement.

As discussed below, the interaction between the chains is mediated mainly by couplings between the magnetic sublattices. In Section 5.1 it is shown that measurement of the dispersion along the zone boundary ($\{h, k, l\} \ni 0.5$) does allow to determine further interactions unbiased by inter-sublattice interactions. In Fig. 5.7(d, e) the dispersions along $\vec{q} = (H, 0, 0.5)$ and $\vec{q} = (0.5, 0, L)$ are presented. While the former allows to observe further interactions along the a-axis, the latter is found to be vanishing, such that the interactions between the sublattices are the only once contributing to the dispersion along the c-axis.

5.5. Magnon dispersion at the zone boundary

From the above data, an interaction with an exchange path in the (a, b)-scattering plane can be predicted. However, there at at least two such possible exchange path, which should be distinguished. These exchange integrals are expected to be rather small, however the magnon dispersion is extremely sensitive to their precise ratio. More precisely, the dispersion in the $(H, K, 0)$-plane may show minima at incommensurate wave vectors with excitation energy below that at the zone center. Hence these small exchange parameters have a strong influence on the low energy excitation spectrum and such on the thermodynamic properties of Li_2CuO_2.

In the experiment at IN12/ILL (see above) the magnon dispersion has been studied in the $(0, K, L)$-plane. For momentum transfer $\vec{q} = (0, K, 0.5)$, the existence of incommensurate minima in the excitation spectrum has been shown [39]. At the cold three axis spectrometer 4F2 at the *Laboratoire Léon Brillouin* these minima in the magnon dispersion have been examined in more detail and in the (a, b)-scattering plane. In the preceding experiment at 4F1/LLB in the (a, c)-plane we have observed that the scattered magnon related intensity near $\vec{q} = (1, 0, 0)$ is approximately 2.2 times larger than at $\vec{q} = (0, 0, 1)$. As $\vec{q} = (1, 0, 0)$ is parallel to the magnetic moment direction, the dynamic structure factor is maximized and obviously outweighing the reduced magnetic form factor due to the short a-axis. As a consequence at 4F2/LLb it was possible to obtain an extensive data set on the spectrum of Li_2CuO_2 for momentum transfer between $\vec{q} = (0.5, 0, 0)$ and $\vec{q} = (1, 0, 0)$ using moreover the one single crystal deployed before at 4F1. Data have been taken mainly with monitor count of 2000 cts. corresponding to counting times of ≈ 1 min. per point. An overview of the data obtained at $T = 4.0\,\mathrm{K}$ is presented in the intensity maps in Fig. 5.8.

The spectrum observed near the zone center $\vec{q} = (1, K, 0)$ is well comparable to the IN12/ILL data taken near the zone center $\vec{q} = (0, K, 1)$ (cf. Fig. 5.4). Both the magnon dispersion as well the excitations below the magnon gap agree well in both experiments. However, the continuum observed at IN12/ILL at energies above $\approx 2.7\,\mathrm{meV}$ is absent in the data taken at 4F2/LLB. Instead, the continuum of excitations at energies just above the magnon gap, only faint in the IN12/ILL data, is a well pronounced feature in the 4F2/LLB data. The broadening does not reduce as temperature is reduced. Its intensity is

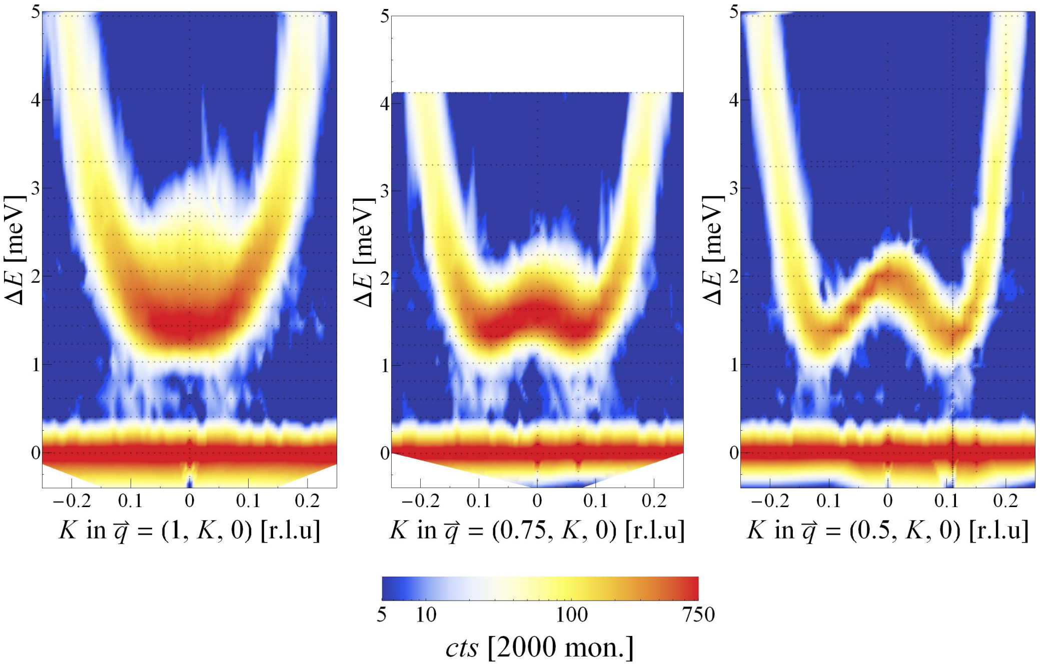

Figure 5.8.: Intensity maps of the low energy magnetic spectrum taken at $T = 4.0\,\mathrm{K}$ for momentum transfer $\vec{q} = (H, K, 0)$ with varied momentum transfer along the chain axis (K) and constant $H = 1$, $H = 0.75$ and $H = 0.5$ in the left, middle and right plot, respectively. The plots are interpolated from the count rate of data points taken at 4F2/LLB, which are indicated by black dots. Note the logarithmic intensity scale. The maps illustrate the magnon dispersion and evidence states below the magnon gap. For $H = 1$, i.e. at the zone center a broad continuum is observed above the magnon gap, which is suppressed at the zone boundary $H = 0.5$.

large at the magnetic zone center $\vec{q} = (1, 0, 0)$ but diminishes at the zone boundary $\vec{q} = (0.5, 0, 0)$ (cf. Fig. 6.4). Note that also in the study of Boehm *et al.* (cf. Fig. 7 in [117]) an asymmetric broadening of the magnon at $\vec{q} = (1, 0, 0)$ appears to be present. For data sets taken at constant momentum transfer near $\vec{q} = (1, 0, 0)$ the unknown line shape of this continuum prevents fitting of the observed peaks. However, data sets taken at constant energy transfer can well be described by GAUSSian distributions for both the magnon and the continuum in the same manner as for the data taken at IN12/ILL (cf. Fig. 5.5).

While the magnon dispersion along $\vec{q} = (1, K, 0)$ has its minimum at $K = 0$[4] the dispersion evidently has well pronounced minima at incommensurate K-values for $\vec{q} = (H, K, 0)$ and $H \notin \mathbb{Z}$. Individual data sets for $H = 0.5$ are presented in Fig. 5.9. While incommensurate minima have been expected already from the experiments discussed above, it has been a central aim of the

---

[4] In $\vec{q} = (1, K, 0)$ the same restrictions apply to the determination of the minimum as discussed for the data along $\vec{q} = (0, K, 1)$ (cf. page 51).

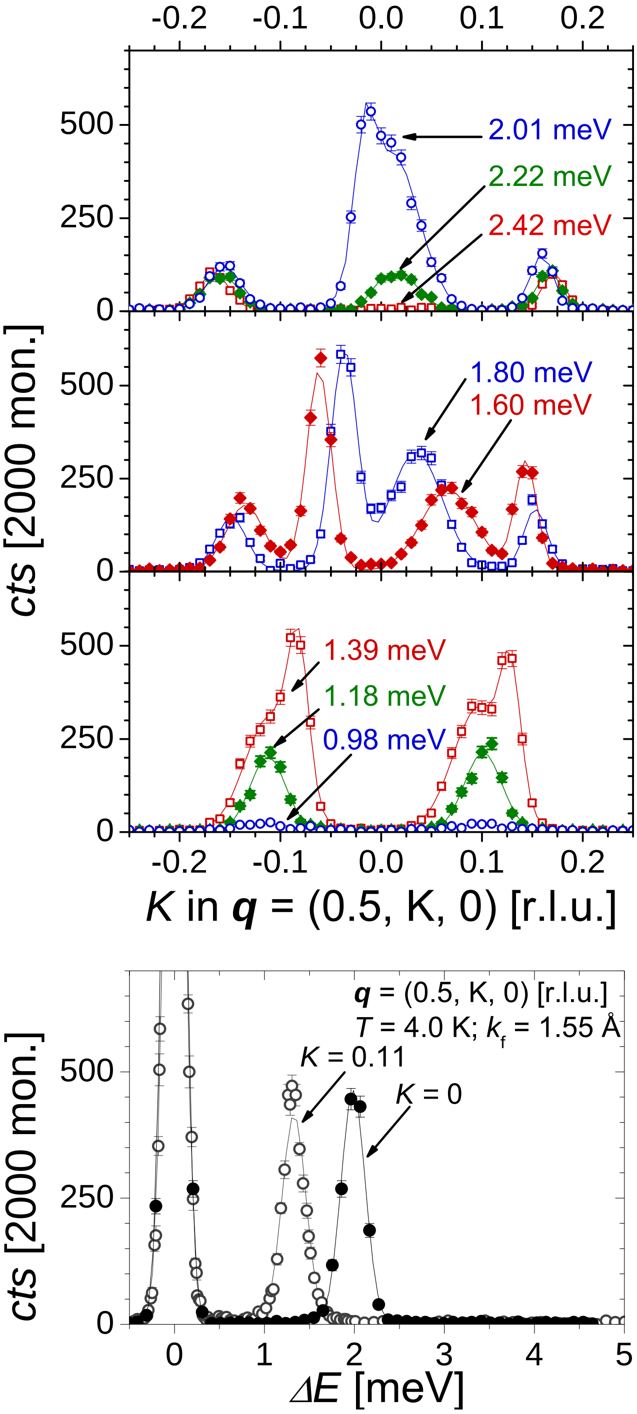

Figure 5.9: Scans at constant energy transfer (Top) and constant momentum transfer (Bottom) at the magnetic Brillouin zone boundary $\vec{q} = (0.5, K, 0)$. Data are taken at 4F2/LLB with $k_\mathrm{f} = 1.55\,\text{Å}$ at $T = 4.0\,\mathrm{K}$ (cf. Fig. 5.8(right)). Lines represent fits by Gaussian distributions. Top: Constant energy scans between energies 0.98 meV and 2.42 meV, show incommensurate minima in the dispersion near $\vec{q} = (0.5, 0.11, 0)$. At intermediate energies of about 1.7 meV four intensity maxima are observed, with a resolution induced asymmetric line width.
Bottom: Energy scans at constant momentum transfer $\vec{q} = (0.5, K, 0)$ with $K = 0$ and $K = 0.11$ show the distinctly lower excitation energy at the incommensurate position with $K = 0.11$.

experiment at 4F2/LLB to determine their energy. An exciting result of this experiment is the observation that the magnon dispersion does neither have a distinct global minimum at the zone center nor at incommensurate values. Within experimental resolution, the magnon excitations at lowest energy are not restricted to carry any particular value of momentum, as illustrated e.g. in the high resolution and low temperature data presented in Fig. 6.4.

5.6. Spin-wave analysis

From all the data sets of the inelastic neutron scattering experiments described above, fitted peak positions $\Delta E(\vec{q})$ which could be related to the magnon dispersion have been collected. Assuming strict periodicity of this dispersion with the magnetic unit cell, uniaxial anisotropy as in accord to the observed spectrum as well as a negligible deviation of the dispersion as measured partly at 4.0 and partly at 4.1 K, all data $\Delta E(\vec{q})$ are projected into the first magnetic Brillouin-zone as $\Delta E(\vec{Q})$. The geometry as well as the labelling of high symmetry points of the Brillouin-zone are depicted in Fig. 5.10.

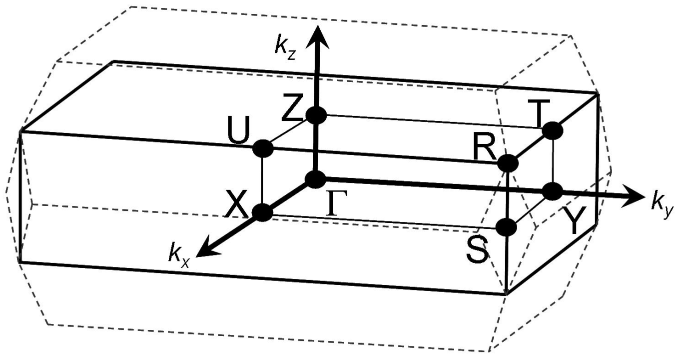

Figure 5.10: Magnetic Brillouin-zone of Li_2CuO_2 (solid lines) within the crystallographic Brillouin-zone (dashed line). Figure adapted from [30].

The complete set of almost 300 data points $\Delta E(\vec{Q})$ is fitted as a whole by the dispersion relation Eqn. 5.3 as derived within linear spin-wave theory. A short discussion on the applicability of a spin-wave model to the spectrum of Li_2CuO_2 is given at the end of this section. First results of the spin-wave analysis, concerning data in the $(0, K, L)$-plane only, have been presented in [39]. Extending this analysis here, we follow the same fitting procedure: due to the lack of available data on the dispersion at the zone boundary $K = 0.5$, the large intra-chain exchange parameters contributing along K only, can be determined only with larger error bars. However, the ratio $\alpha = -J_{020}/J_{010}$ which determines the curvature of the dispersion along K is well accessible from our data. In the fitting procedure, the parameters $\{J_{010}, J_{020}\}$, are thus replaced by $\{J_{010}, -\alpha \cdot J_{010}\}$. Moreover, the anisotropy gap $\Delta E(0)$ is not used as a free fit parameter, as it can be determined much more reliably from the spectral data taken at the zone center. In this, however, some inconsistency enters the fitting procedure. Experimentally, the gap is determined as 1.36(2) meV such that within error bars $\Delta E(0)$ could be chosen as a free parameter. The next restriction to the accuracy of the fit is the neglect of errors in the independent parameter (components of $\vec{q}$). The fit therefore overestimates the weight of points $\Delta E(\vec{Q})$ with large error in $\vec{q}$. These errors are particularly large for the high energy data taken with thermal neutrons. It turns out however, that the fitted parameters, including the intra-chain exchange constants are only weakly altered, if all high energy data are completely neglected.

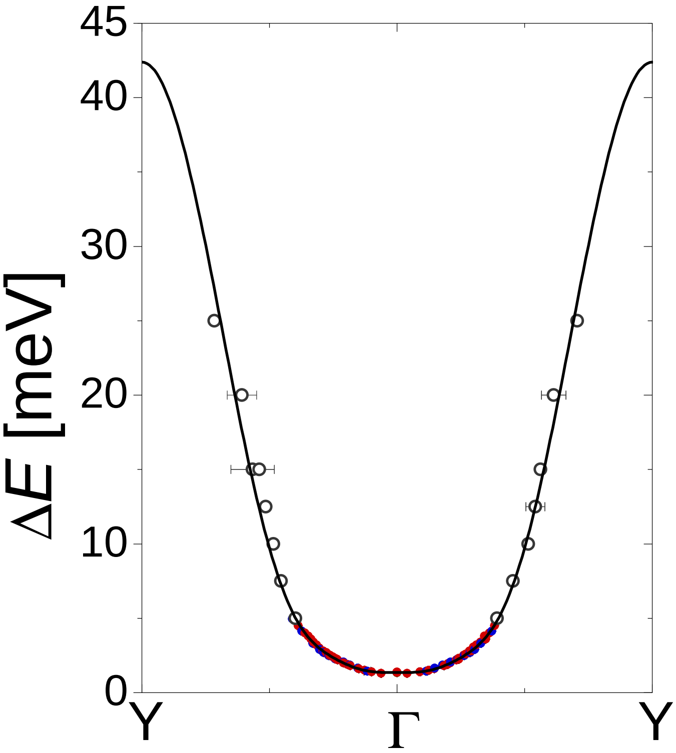

Figure 5.11: Observed features related to the magnon dispersion for momentum transfer $\vec{q} \parallel (0, K, 0)$ projected here into the first Brillouin-zone. Data points have been obtained at IN12/ILL (red ●), 4F2/LLB (blue ●) and IN8/ILL (○). The fitted spin-wave dispersion is plotted as a line. The dispersion evolves as q^4 near the zone center.

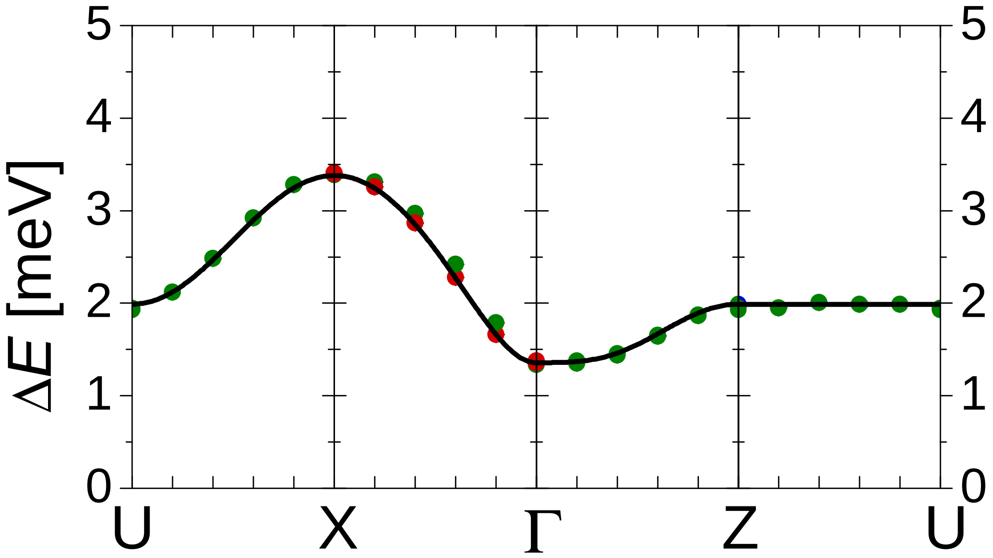

Figure 5.12.: Observed peaks related to the magnon dispersion for momentum transfer $\vec{q} \perp (0, K, 0)$ projected here into the first Brillouin-zone. Data points have been obtained at IN12/ILL (red ●) and 4F1/LLB (green ●). The fitted spin-wave dispersion is plotted as a line.

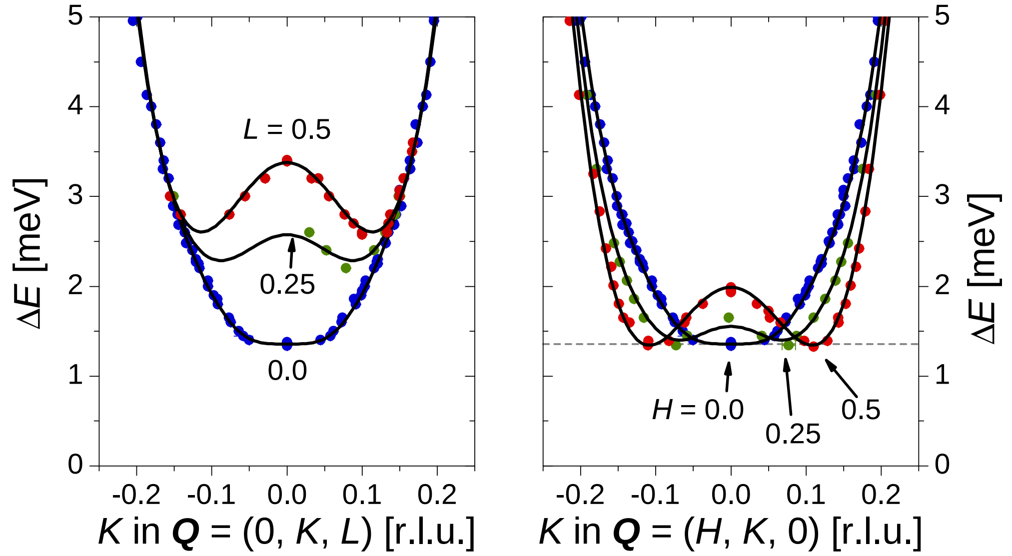

Figure 5.13.: Observed peaks related to the magnon dispersion for momentum transfer $\vec{q} \perp (H, K, L)$, for fixed values H and L, projected here into the first Brillouin-zone. Data points have been obtained at IN12/ILL (left) and 4F2/LLB (right). The data set for $\vec{Q} = (0, K, 0)$ contains data from both instruments. The fitted spin-wave dispersion is plotted as a line. Left: For $H = 0$, at the zone boundary $L = 0.5$ incommensurate minima evolve well above the gap at Γ. Right: For $L = 0$, the gap energies at Γ as well as at the incommensurate minimum for $H = 0.5$ are about identical, as indicated by the horizonal dashed line.

The exchange parameters as fitted are summarized in Tab. 5.2. Data, compared with the fitted dispersion are presented for varied momentum transfer along the chain up to high energies in Fig. 5.11, for momentum transfer perpendicular to the chain in Fig. 5.12 as well as for fixed momentum transfer perpendicular to the chain, but varied along the chain in Fig. 5.13. The plotted dispersion is the result of a fit with a minimal set of parameters, labeled as "best fit" in Tab. 5.2. All exchange interactions well distinct from zero are found to be anti-ferromagnetic, except for the large ferromagnetic interaction between nearest neighbor sites along the chain.

The minimal parameter set that is found to provide a satisfactory description of the data needs two exchange interactions along the chain, J_{010} and J_{020} between nearest and next-nearest neighbors respectively. More long ranged interactions J_{030} or even J_{040} are found to vanish within error bars and are hence neglected. Within local spin density approximation (L(S)DA+U) [38] and a $3d$O$2p$ 5-band Hubbard-model on a chain-like cluster [39] the intrachain exchange constants can be modeled theoretically. Interestingly, the large nearest neighbor coupling J_{010} obtained form our analysis of the experimental spectrum sets specific constraints to model parameters, which are usually less well known. In L(S)DA+U, the on-site Coulomb repulsion U must be

	J_{010}	α	$[J_{020}]$	J_{030}	I_{111}	I_{131}	I_{100}	I_{110}	I_{001}	$[D_{\text{aniso}}]$
present work										
best fit	−230(2)	0.326(1)	75(1)	∅	∅	9.0(1)	4.8(4)	1.6(3)	∅	3.3(1)
including J_{030}	−229(4)	0.326(4)	76(2)	0.1(6)	∅	9.0(1)	4.8(4)	1.6(3)	∅	3.3(1)
including I_{111}	−233(3)	0.327(1)	76(1)	∅	−0.5(2)	9.4(2)	4.8(4)	1.6(3)	∅	3.3(2)
including I_{001}	−230(2)	0.327(1)	76(1)	∅	∅	9.0(2)	4.8(4)	1.7(3)	0.1(2)	3.3(2)
$(0, K, L)$-plane [39]	−228(2)	0.332(1)	76(1)	∅	∅	9.04(5)	∅	∅	∅	3.3(1)
Boehm *et al.* [117]	5.6(3)	"0.67(5)"	−3.7(9)	∅	9.1(3)	∅	4.2(3)	1.9(5)	0.0(5)	3.6(3)

Table 5.2.: Exchange integrals of Li_2CuO_2 (given in units of K) as fitted by the spin-wale model Eqn. 5.3 to the peak positions $\Delta E(\vec{q})$ from our inelastic neutron scattering experiments. The exchange paths are labeled as depicted in Fig. 5.1. Parameters in brackets are not fitted, but calculated from others. Parameters neglected (set to 0) in the fit are represented as "∅". For the fits on our data the gap $\Delta E(\vec{Q} = 0) = 1.36\,\text{meV}$ is explicitly fixed. Errors are denoted as obtained from the covariance of the fit parameters and thus presumably underestimated. The fit with the minimal set of exchange parameters used ("best fit"), is compared to fits with an extended parameter set. The fit is furthermore compared to our earlier results on data taken in the $(0, K, L)$-plane only, as well as to the results of Boehm *et al.*

adjusted to a rather low value $\approx 6\,\mathrm{eV}$ (for intra-atomic $J \approx 1\,\mathrm{eV}$). In the HUBBARD-model only a large exchange interaction between Cu-d and O-p orbitals $K_{pd} \approx 80\,\mathrm{meV}$ provides results in good agreement to our data [5].

The dominant inter-chain exchange interaction is determined to be mediated between neighboring chains along the exchange path I_{131} (coupling sites along $(\frac{a}{2}, \frac{3b}{2}, \frac{c}{2})$), i.e. between next-nearest neighbors in the respective chains. This exchange path, where the Cu-sites are separated by 6.63 Å has not been considered in the study by Boehm *et al.* However, as suggested by Mizuno *et al.* [32] this interaction may well be comparable to the nearest neighbor interaction along the body diagonal I_{111} (where Cu sites are separated by 5.24 Å only). As shown in the quantum chemical study by de Graaf *et al.* [34] as well as in the generalized gradient approximation (GGA+U) studies by Xiang *et al.* [122] $I_{131} > I_{111}$ can be expected. Fitting the exchange parameters I_{111} and I_{131} to our data, it is found that I_{111} alone does not yield a reasonable description of the data and about vanishes if both parameters are considered. The interaction between neighboring chains is therefor described well by I_{131} only. Neglecting I_{111} and within the accuracy of this study I_{131} is found to be the only exchange interaction with a component along the c-axis. In particular, an exchange interaction I_{001} along the c-axis (Cu sites are separated by 9.40 Å) is absent. This is most clearly shown in the data taken for momentum transfer parallel to $\vec{Q} = (0.5, 0, L)$ (cf. Fig. 5.12(right)). As discussed in Section 5.1, I_{131} does not cause a dispersion along this direction, such that I_{001} can be observed directly. As the data along $\vec{Q} = (0.5, 0, L)$ do not show a dispersion, I_{001} must be very small.

As the exchange path I_{131} does not distinguish between moments shifted along the a- or c-axis, the dispersions along H and L, normalized to reciprocal lattice units, are expected to be identical if further inter-chain interactions were absent. However, our data show a distinct difference, such that further interactions with a component along the a-axis must be taken account for. Two exchange path are to be considered here, originally proposed by Sapiña *et al.* already in 1990 [111]: I_{100}, between nearest neighbors along a and I_{110}, where interacting moments are shifted also along the chain. A relation $I_{100}/I_{110} \approx 2$ is argued to follow from the respective orbital overlaps. In order to distinguish both exchange integrals from the experimental dispersion demands its measurement at a momentum transfer $\vec{Q} = (H, K, L)$, where both H and K must be non-zero. From measurements, where $K = 0$ only the sum $I_{100} + 2 \cdot I_{110}$ can be obtained (the factor "2" follows from the relative coordination number of the interactions). Without data with both $H \neq 0$ and $K \neq 0$, Boehm *et al.* could distinguish both interactions from the influence of the ratio I_{110}/J_{010} onto the mean field NÉEL temperature[6] [120]. From our data, taken e.g. at $\vec{Q} = (0.5, K, 0)$, where I_{131} again does not contribute to the dispersion, both

---

[5] In this study [39, 144], direct exchange between adjacent Cu-sites has not been considered.

[6] $T_\mathrm{N} = S(S+1)/3(\sum_i z_i J_i - \sum_j z_j J_j)$, with i, j labeling intra- and inter-sublattice exchange interactions J with coordination number z, respectively.

exchange integrals could be fitted directly. Their respective ratio is found as large as $I_{100}/I_{110} = 3.0(2)$. With $I_{110} = 1.6 \pm 0.3\,\mathrm{K}$, a particularly weak interaction is deduced from our data. Note however, that the sum $I_{100} + A \cdot I_{110}$ with $A = 2$ is fixed by the dispersion along $\vec{Q} = (H, 0, 0)$, while for the dispersion along e.g. $\vec{Q} = (0.5, K, 0)$ the sum $I_{100} + A \cdot I_{110}$ can be obtained, where $A \neq 2$ for $K \neq 0$. Though weak, I_{110} reflects also in a slightly reduced I_{131} and enhanced fitted value of J_{010} as compared to our earlier study [39], where I_{110} has been neglected.

The last parameter of the spin-wave model is the anisotropic exchange parameter D_{aniso}, calculated from the fitted exchange parameters and the measured gap at Γ. The magneto-crystalline anisotropy energy $\Delta E_{\mathrm{aniso}} = E(\vec{m} \perp a) - E(\vec{m} \parallel a)$ is related to $D_{\mathrm{aniso}} = 3.3 \pm 0.1\,\mathrm{K}$ as $\Delta E_{\mathrm{aniso}} = -S^2 D_{\mathrm{aniso}}$. Within density functional theory, the anisotropy of the nearest neighbor coupling in the chain has been calculated as 15.8 K [36], i.e. more than 4 times larger than the experimental result (see also [113, 125]). The large calculated anisotropy of J_{010} may be compensated by the anisotropy of other exchange interactions.

Note, that the obtained inter-chain couplings do not contribute to the dispersion along the chain for directions equivalent to $\vec{Q} = (0.25, K, 0.5)$. Just as for I_{131} at $H = 0.5$ or $L = 0.5$, I_{110} causes an only constant shift of the spectrum for $H = 0.25$. The dispersion has not been measured in this direction, but can be obtained from our spin-wave model. Its minima correspond to the classical pitch angle $\phi = \cos^{-1}(\frac{1}{4\alpha}) \approx 39.9^\circ \approx \pm 0.111\,\mathrm{r.l.u.}$ of the moment orientation in the chain. Due to the small value of I_{110} the minimum along $\vec{Q} = (0.5, K, 0)$ and $\vec{Q} = (0, K, 0.5)$ is only weakly shifted. Therefore, the dispersion shown in the intensity map Fig. 5.8 (right), with minima at $K = \pm 0.11(1)\,\mathrm{r.l.u.}$ largely resembles the dispersion as due to the intra-chain couplings only.

In summary, a very good agreement between the measured magnon dispersion and a spin-wave model with rather few parameters has been obtained. In the last part of this section, we comment on the physical meaning of these parameters. In fact, a spin-wave description of magnetic excitations is in general not applicable in low-dimensional as well as $S = 1/2$ systems. In such systems strong quantum fluctuations are to be expected, such that the excitations if described within a magnon picture gain an effective self-energy and their dispersion is renormalized. These severe complications however, do not seem to be of great relevance to $\mathrm{Li_2CuO_2}$. In the ordered state at low temperature, a large ordered moment is observed in neutron diffraction studies, such that fluctuations cannot be strong [111, 112]. Spin-wave theory itself predicts for the isotropic case a reduction of the ordered moment by 3.6% only at $T = 0$ (see [39], calculations do not regard I_{100} and I_{110}). The spin anisotropy can be expected to reduce fluctuations even more. From the point of view of the observed spectrum, the spin-wave model is verified by the observed line shape of the excitations. In general, the spectral data can be well described by GAUSSian distributions and the line width is limited by the instrumental resolution. However, some deviations are clearly observed. On one hand, weak yet distinct spectral weight is observed below the magnon gap. These features have been studied in further in detail and are discussed in Chapter 6. Moreover, for momentum transfer near Γ, the spectrum shows clearly continua, which cannot be taken account of within a linear spin-wave model. Two apparently distinct features are observed: one at energies just above the magnon gap and particularly pronounced near $\vec{q} = (1,0,0)$ and a second one above $\approx 2.7\,\mathrm{meV}$ for $\vec{q} = (0,0,1)$, but absent for $\vec{q} = (1,0,0)$. An interpretation of these features is still missing. A probable relation thereof to fluctuations of the ground state can hence not be evaluated and calls for further investigation. Nevertheless, further strong support for only weak spin-fluctuations in the compound is provided by high field magnetization measurements (cf. Section 8.2, [145]). These data show an only weak suppression of the induced magnetic moment and the measured saturation field is in great accord with the spin-wave prediction based on the exchange parameters as obtained here.

5.7. Frustration of inter-chain couplings

The frustrated interactions within the chain induce the formation of incommensurate minima in the dispersion, e.g. along $\vec{Q} = (0, K, 0.5)$ [39]. For momentum transfer along $\vec{Q} = (0, K, 0)$ the minimum of the dispersion appears loacted at the Γ-point as a consequence of the deformation of the spectrum by the dominant inter-chain coupling I_{131}. Our data on the dispersion along $\vec{Q} = (0.5, K, 0)$ (see above) however give evidence, that incommensurate minima in the dispersion exist where magnons have about the same energy as at the Γ-point. In this section it is shown, that a delicate interplay of the different exchange interactions causes a high degree of degeneracy of the low-energy magnon spectrum. This degeneracy is argued to be of essential importance to the behavior of the compound at magnetic phase transitions. The discussion is guided by the analytic description of the magnetic spectrum given by the fitted spin-wave dispersion.

A prominent feature of the magnon dispersion in $\mathrm{Li_2CuO_2}$ is the extraordinarily flat dispersion near the magnetic zone center Γ for momentum transfer along the chain. Any dispersion along some direction A (normalized to reciprocal lattice units) near a zone center can be written as a polynomial expansion with even exponents $\sum_n a_{2n} A^{2n}$. For the above dispersion however, the quadratic term a_2 is found to be almost perfectly quenched. For $\vec{Q} = (0, K, 0)$ one obtains from the fitted spin-wave model for the first terms $(a_2, a_4, ...) \approx (2.4, 10^4, ...)$. The weakly positive a_2 corresponds to a minimum of the dispersion for $K = 0$. In contrast, for momentum transfer $\vec{Q} = (0, K, 0.5)$, where I_{131} does not contribute to the dispersion, the dispersion shows well pronounced minima near $K = 0.11$, the series expansion around $K = 0$ reads $\approx (-125, 5400, ...)$. This example illustrates that the obtained commensurate minimum of the dispersion along $\vec{Q} = (0, K, 0)$ is extremely subtle. In fact, a reduction of I_{131} by less than 1% compared to the fitted value, i.e. just within error bars corresponds to the formation of incommensurate minima along $\vec{Q} = (0, K, 0)$. Also, an increase of J_{010} to $-232\,\mathrm{K}$ with α unchanged or of I_{110} to $\approx 2\,\mathrm{K}$ yield such result. A combined shift of these parameters would demand even smaller deviations from the fitted parameter set. As shown in Fig. 6.5(bottom), where the minimum of the dispersion is plotted in the $(H, K, 0)$-plane, our fit parameters cause an irregular behavior of the minimum: while located at $K = 0$ at lowest H, it shows a rather strange bifurcation to incommensurate values at small H. As the commensurate minimum for $K = 0$ is not for certain from our fit parameters, incommensurate minima even in $\vec{Q} = (0, K, 0)$ at some tiny values $\pm K_{\mathrm{min}}$ may have to be considered.

A much more obvious feature of the dispersion is the apparent absence of a distinct global minimum. Experimentally, the minima in the $(H, K, 0)$-plane for any selected H all have about the same energy (cf. Fig. 6.4). Analyzing these minima within our spin-wave model, it is found that the corresponding excitation energies vary within less than 1% around the gap determined at Γ. At the zone boundary $H = 0.5$ the minimum is located near $\vec{Q} = (0.5, 0.11, 0)$ and due to the absent dispersion along L for $H = 0.5$ also all magnons along $\vec{Q} = (0.5, 0.11, L)$ are amongst the excitations of lowest energy. This situation is illustrated in Fig. 5.14. It is important to note here, that this peculiar low energy spectrum is due only to a delicate balance of the involved competing interactions. Manually shifting any exchange integral within our spin-wave model by 1 or 2 K only is sufficient to either generate a global minimum at Γ or alternatively at an incommensurate wave-vector. The absence of a well

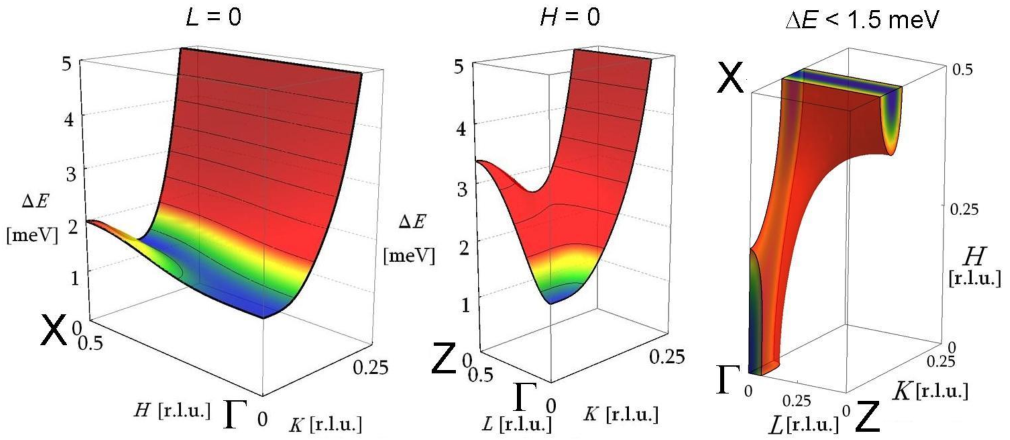

Figure 5.14.: The fitted magnon dispersion is displayed in the planes $\vec{Q} = (H, K, 0)$ (left) and $\vec{Q} = (0, K, L)$ (middle). Colors stress equal magnon energies (different scale in the right figure). Note the about vanishing dispersion along the minima in K for $\vec{Q} = (H, K, 0)$. On the right, a constant energy surface at 1.5 meV, only slightly above the gap at 1.36 meV is displayed in a section of the Brillouin-zone. Low energy excitations are present near Γ, but the spectrum is largely concentrated near incommensurate wave-vectors, in particular $\vec{Q} = (0.5, 0.11, L)$.

defined minimum in the dispersion stresses the importance of the exchange anisotropy for the stability of the commensurate ground state.

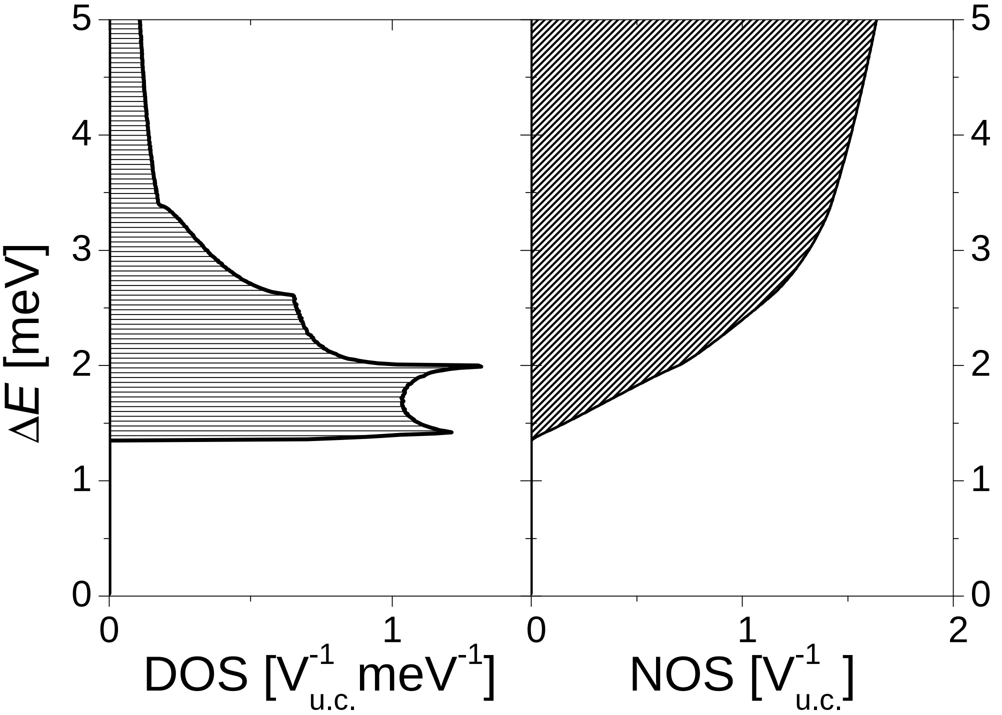

Figure 5.15.: (left) Magnon density of states (DOS), normalized to the reciprocal volume of the unit magnetic cell $V_{\text{u.c.}}^{-1}$(= volume of the magnetic Brillouin-zone as in Fig. 5.10). Note the Van Hove-singularity just above the magnon gap. (right) Integrated DOS, i.e. number of magnon states below some energy (NOS). The total NOS is normalized to $4/V_{\text{u.c.}}^{-1}$. The NOS grows about linearly at low energies above the gap.

From the fitted spin-wave dispersion (cf. Tab. 5.2), the magnon density of states (DOS) can be derived, which is presented in Fig. 5.15. The DOS is shown normalized to 4 magnons per Brillouin-zone[7]. While in non-frustrated three-dimensional antiferromagnets the DOS at low energy increases smoothly, Li_2CuO_2 at $T = 4\,\text{K}$ and in ambient field exhibits a pronounced Van Hove-singularity just above the gap (at 1.42 meV above a gap of 1.36 meV in our model). Between this singularity and excitation energies of 2 meV the DOS is rather constant with an average deviation from the mean below 7%. The low energy DOS of magnetic excitations is to be expected to determine the thermodynamic properties of a magnetic system at low temperatures. As a consequence of the about constant DOS at low energy, the energy-integrated DOS, denoted here as number of states (NOS) (cf. Fig. 5.15(right)) increases about linearly with energy. Correspondingly, the magnon related specific heat

---

[7] In an antiferromagnet, magnons with opposing momentum and associated spin per magnetic site in the primitive unit cell are to be distinguished.

at low temperatures as discussed in Chapter 9 is expected to grow linearly with temperature (if the gap was absent)[8]. The existence of low energy magnon excitations at incommensurate wave vectors must be expected to induce an unconventional behavior of the system near the phase boundaries of the collinearly ordered antiferromagnetic phase. At T_N the anisotropy gap closes and equivalently at the meta-magnetic transition at H_c one magnon branch will become degenerate with the ground state. However, just at the phase boundary the low energy excitation spectrum exhibits respective GOLDSTONE bosons which are degenerate with the emerging collinear ground state at commensurate wavevectors only. Upon leaving the collinear state in high temperatures or high magnetic fields the magnon excitation spectrum must hence soften primarily at the Γ-point. Correspondingly, the system must lift the degeneracy of the commensurate and incommensurate excitations. A respective mechanism could be given by the renormalization of exchange constants due to fluctuations near the phase transition. As discussed in Chapter 10, magnetic phase transitions in Li_2CuO_2 go along with a significant anisotropic lattice deformation, which can be expected to be accompanied by slight changes in the exchange constants. In Section 10.3.3, a model of the lattice deformation is discussed, which is based on the sensitivity of the spectrum to small changes of the exchange constants.

Incommensurate minima in the dispersion above an ambient field commensurate ground state are generally rarely reported in literature; maybe observed for the first time in $LiNiPO_4$ in 2007 [146, 147]. In this material, low temperature commensurate and high temperature/intermediate field incommensurate ground states are observed. In the commensurate phase, the dispersion along one axis is extremely flat near the zone center, however large for perpendicular momentum transfer, such that the VAN HOVE-singularity is presumably less pronounced. Generalizing our proposal on Li_2CuO_2, a complex lattice expansion scheme may be expected in particular at phase transitions between gapped commensurate and incommensurate phases, as GOLDSTONE-modes and such the corresponding low energy excitations in the ordered state have different symmetry in the respective phases. In $LiNiPO_4$ however, the situation may be more complex, as well defined excitations in the incommensurate phase seem to be absent [146].

For Li_2CuO_2, the apparent contradiction of the existence of a low energy VAN HOVE-singularity in the magnon density of states and the rapid increase of the sublattice magnetization below T_N (cf. Section 7.2) remains a puzzle to be solved.

---

[8] The analysis in Chapter 9 also considers the gap.

6. Low energy excitations

While the low energy excitation spectrum of our Li_2CuO_2 sample, examined at $T = 4\,K$ and ambient magnetic field is clearly dominated by gapped excitations with a spin-wave-like dispersion (cf. Chapter 5), it also provides evidence for features beyond the simple spin-wave picture. In this chapter, excitations that are observed at energies below the magnon gap are discussed. A first impression about these features may be provided by the intensity maps Fig. 5.4 and Fig. 5.8 which display weak spectral weight below the magnon gap at incommensurate wave vectors. More comprehensive studies of these features by means of inelastic neutron scattering experiments had a threefold motivation: Firstly, the observation of such features in Li_2CuO_2 was a mere surprise inviting of clarification, secondly their alikeness to spectral features in doped layered antiferromagnets is nearby obvious, promising interesting physics and eventually, thermodynamic studies of Li_2CuO_2 at low temperatures showed a number of features demanding explanation (cf. Section 7.4). The undertaken neutron scattering studies on these spectral features are listed in Tab. 6.1.

Table 6.1.: List of inelastic neutron scattering experiments on low energy features below the magnon gap Li_2CuO_2.

Instrument/ Institute	scattering plane	key experimental parameters
IN12/ILL	(0,K,L)	$k_\mathrm{f} = 1.5\,\text{Å}^{-1}$, $T = 4.1\,K$
IN12/ILL	(0,K,L)	$k_\mathrm{f} = 1.2\,\text{Å}^{-1}$, $T = 0.4\,K$, $\mu_0 H \leq 4\,T$
4F2/LLB	(H,K,0)	$k_\mathrm{f} = 1.3\,\text{Å}^{-1}$, $T = 1.6\,K$

First experimental evidence for states below the magnon gap was found already in the first cold neutron study of the magnon dispersion. As discussed in Section 5.7, the magnon dispersion near the magnetic zone center is extraordinarily flat and may even possess minima at incommensurate wavevectors close to the Γ-point. While energy scans at the zone center evidence a gap of 1.36(2) meV, constant energy scans at 1.3 meV with momentum transfer $\vec{q} = (0, K, 1)$ along the chain display a two-peak structure, indicative for incommensurate minima of the in-chain dispersion (cf. Fig. 5.5). However, excitations at incommensurate wave vectors could be traced to much lower energies such that they are clearly distinguished from the main magnon branch. Below, these low energy features will be referred to as "sub-gap excitations".

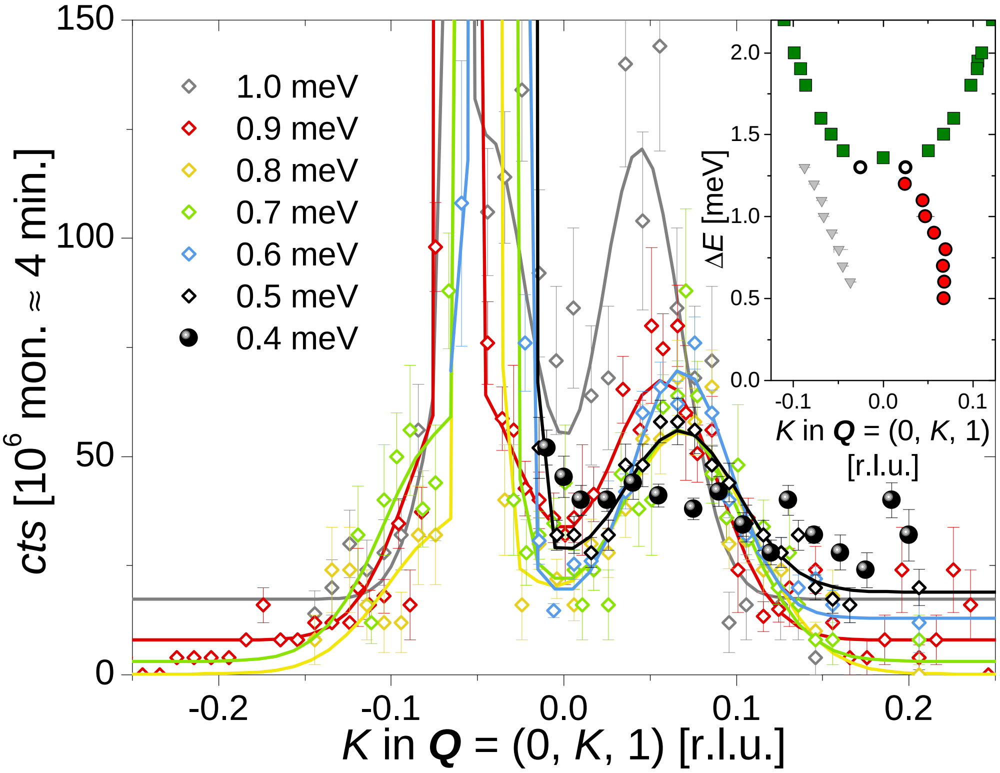

Figure 6.1.: Scans at constant energy transfer 0.4 − 1.0 meV (below the magnon gap) with momentum transfer $\vec{q} = (0, K, 1)$ taken at IN12/ILL at $T = 4K$ and fixed final neutron momenta $k_\mathrm{f} = 1.5$ Å. The data show weak, broad peaks at incommensurate wave-vectors. Note that this feature is absent at 0.4 meV. The huge intensity at $K < 0$ is due to a spurious Bragg-tail, the respective peak width indicates the experimental resolution. Lines are Gaussian fits to the data, which however demanded fixing parameters for the broad peak at $K < 0$. Inset: Data on the dispersion of the magnon (green ■), the Bragg-tail (grey ▼) and the right branch of the sub-gap states (red ●). Maxima in the spectrum at 1.3 meV (○) could not be assigned.

However, for the two-peak structure observed at 1.3 meV an assignment to either incommensurate minima of the magnon branch or sub-gap states could not be achieved.

In Fig. 6.1, scans at constant energy below the gap are shown taken at IN12/ILL at $T = 4$ K. The largest feature in these data is the Bragg tail related to the strong magnetic reflex at $(0, 0, 1)$. However, for $\vec{q} = (0, K > 0, 1)$ - unaffected by this spurious feature - weak, broadened excitations are observed near an incommensurate wave-vector. The intensity of the sub-gap features may appear marginal if compared to the intensity of the low energy magnon excitations, yet corresponds to already ≈ 25% of the intensity of magnon excitations at 5 meV. For energies between 0.5 meV and 0.9 meV these excitations are found at comparable wave-vectors $K = 0.068(1)$ and possess a similar width and intensity. At higher energy their width reduces and they are found shifted closer to $K = 0$. Their apparent increase in intensity may be explained by the experimental resolution (partial scattering from the magnon branch). At 0.4 meV the background is slightly increased due to scattering from the incoherent elastic line, however the absence of the incommensurate excitation evident. The data are fitted by GAUSSian distributions, but the quality for these fits is limited. The large width of the incommensurate features at $\pm K$ leads to an overlap at $K = 0$, but the peak at $K < 0$ cannot be fitted properly[1] due to the strong BRAGG-tail. Nevertheless, an approximate "dispersion" of the incommensurate feature at $K > 0$ could be obtained. At 0.9 meV the two peak structure the sub-gap feature was verified also at equivalent positions of the magnetic unit cell near $\vec{q} = (0, -1, 0)$ and $\vec{q} = (0, 0, 3)$.

In order to gain further insight into the nature of the sub-gap states a dedicated experiment has been performed at IN12/ILL. For more meaningful spectral data on low energy excitations, data have been collected with cold neutrons of fixed final momentum $k_\mathrm{f} = 1.2\,\mathrm{\AA}^{-1}$ only. Such, the energy resolution could be enhanced by a factor 2 to 0.07 meV at FWHM compared to 0.14 meV with $k_\mathrm{f} = 1.5\,\mathrm{\AA}^{-1}$ (monochromator and analyzed focussed in both setups). Also, the experiment was performed at low temperatures $T = 0.4\,\mathrm{K} \sim 0.035\,\mathrm{meV}$ in order to avoid thermal smearing of the spectrum, e.g. by scattering at thermally excited states. Eventually, the magnetic origin of the sub-gap states was to be probed by their response to externally applied magnetic fields. In low fields $\mu_0 H < 10\,\mathrm{T}$ applied along the easy a-axis, unconventional behavior of the magnetization has been observed before ([148], Section 7.4). The scattering plane $(0, K, L)$ was chosen to allow for application of magnetic fields along the a-axis. The experiment concerns excitations near the magnetic zone center $(0, 0, 1)$ only. A sample of three co-aligned crystallites with total mass $\approx$ 3 g was investigated (3 out of 4 of the crystals used in the earlier IN12 experiment).

At low temperature $T = 0.4\,\mathrm{K}$, the observed spectrum corresponding to sub-gap states is found to be altered significantly as compared to the data taken at $T = 4\,\mathrm{K}$. At 4 K an apparent branch of excitations width rather constant intensity was detected (cf. Fig. 6.1). At low temperature however, corresponding intensity is found to be concentrated at distinct values of energy transfer. An energy scan at constant momentum transfer $\vec{q} = (0, 0.05, 1)$ gives evidence for states at 1.13(1) meV and slightly weaker at 0.59(2) meV (cf. Fig. 6.2(left)). Also, the line shape of the elastic line is not described well by a GAUSSian distribution, indicating further inelastic intensity at low energy $\approx$ 0.2 meV. Constant energy scans with varied momentum transfer along the chain show that the feature at 0.59(2) meV is also well localized in momentum with an incommensurate wave-vector $\vec{q} = (0, 0.066(3), 1)$ and an intrinsic width along K of 0.06 r.l.u. at FWHM (cf. Fig. 6.2(right)). At constant energy 0.6 meV and momentum transfer along $\vec{q} = (0, 0.05, L)$ intensity reduces if L is shifted

---

[1] Fixing fit parameters for the peak at $K < 0$ was necessary.

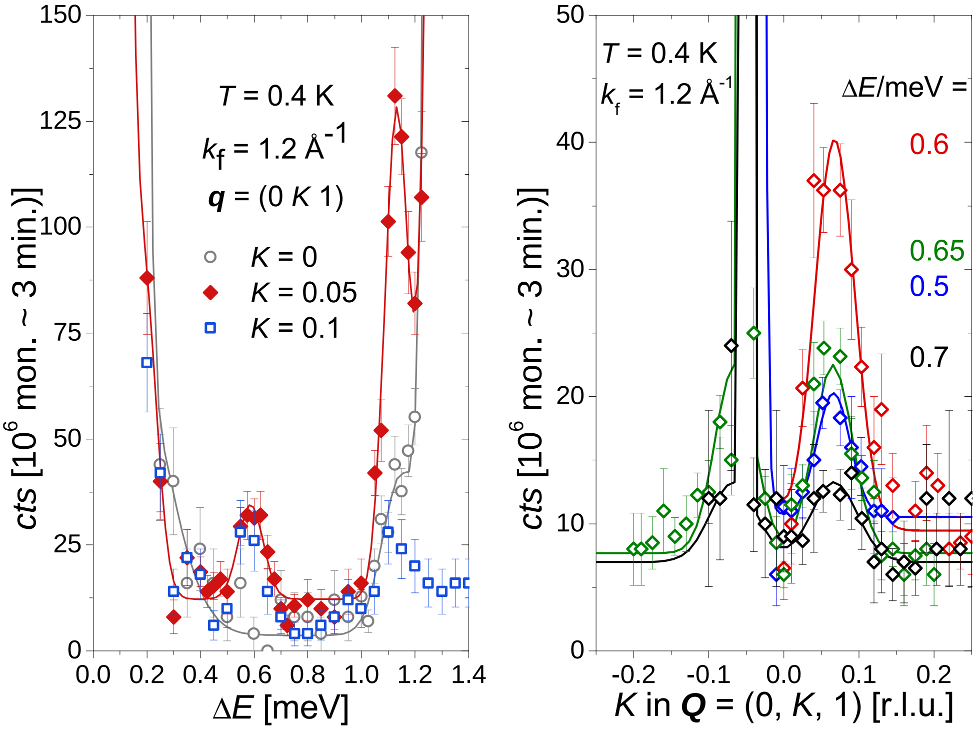

Figure 6.2.: The states below the magnon gap, as probed at low temperature $T = 0.4\,\mathrm{K}$ do not exhibit a dispersion along the chain. (left) Energy scans at constant momentum transfer $\vec{q} = (0, K, 1)$ reveal excitations at energy transfer $0.59(2)\,\mathrm{meV}$ and $1.13(1)\,\mathrm{meV}$. Lines represent fits by Gaussian distributions. Between 0.2 and $0.5\,\mathrm{meV}$ no reliable fit was obtained. (right) By constant energy scans the excitation near $0.6\,\mathrm{meV}$ is shown to be well confined in energy and momentum along the chain. The sharp feature at $K < 0$ is due to a spurious Bragg-tail, illustrating the instrumental momentum resolution and the broad line shape of the sub-gap excitation.

away from 1. If the feature exists for $L \notin \mathbb{Z}$ has not been investigated.

The response of the magnetic spectrum to magnetic fields applied along the easy a-axis has been studied at a temperature $T = 0.4\,\mathrm{K}$. Note, that for proper alinement of the sample in the $(0, K, L)$-plane a slight tilt of the cryomagnet was necessary. As a consequence, magnetic field is applied at an angle of 2° away from the easy axis. At ambient magnetic fields, the magnetic spectrum of Li_2CuO_2 exhibits two nearly degenerate branches of magnon excitations [113]. At the magnetic zone center $(0, 0, 1)$ the shift of both branches has been measured at $\mu_0 H_{\parallel a} = 4\,\mathrm{T}$. One magnon branch is shifted to lower energy by $-0.12\,\mathrm{meV}/T$ on average, while the energy of the second branch increases by $0.14\,\mathrm{meV}/\,\mathrm{T}$ (cf. Fig. A.1). This well resolvable asymmetry is accompanied by a notable broadening of the upper magnon branch. The origin thereof is yet to be clarified.

At momentum transfer $\vec{q} = (0, 0.05, 1)$ the magnetic field response of the

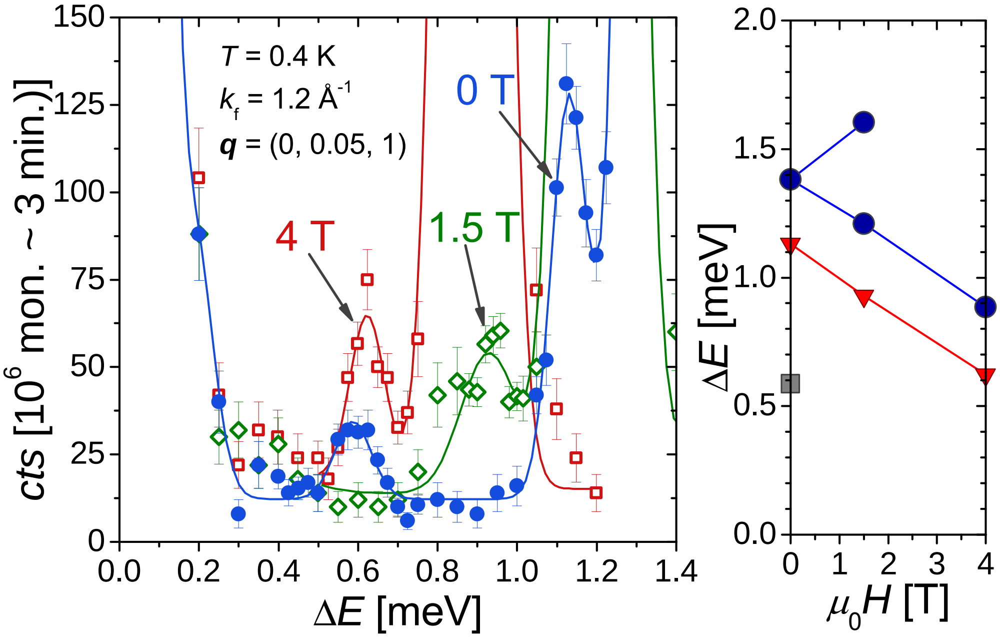

Figure 6.3.: Study on the response of the sub-gap states to externally applied magnetic field $H \parallel a$. (left) Energy scans at constant momentum transfer $\vec{q} = (0, 0.05, 1)$ in magnetic fields of 0, 1.5 and 4 T. The intense feature at high energy corresponds to magnon excitations. At energy transfer slightly below the magnon gap additional intensity is observed, indicated by arrows. For $H = 0$ a second excitations is observed at 0.59(2) meV. In magnetic fields one magnon branch and the sub-gap feature shift to lower energies. Lines at fits to be data by Gaussian distributions. Between 0.2 and 0.5 meV no reliable fit to the data was obtained, the line serves as a guide to the eye. (right) Fitted peak positions in energy vs. applied magnetic field of the magnon (blue ●), the feature just below the gap (red ▼) and the low energy feature at $H = 0$ (gray ■). Lines are guides to the eye.

sub-gap feature observed at 1.13(1) meV in ambient field was investigated (cf. Fig. 6.3). In magnetic field $\mu_0 H_{\parallel a} = 1.5\,\mathrm{T}$ and 4 T a comparable feature below the softening magnon branch is observed. Both the sub-gap feature as well as the magnon branch are shifted to lower energy by $-0.125(4)\,\mathrm{meV/T}$. At the same time, the second magnon branch shifts upwards by 0.147 meV/T [2]. The line shape of the sub-gap feature observed at 1.5 T is found broadened. A probable relation hereof to the $M(H_{\parallel a})$ anomaly in the same field may have to be considered (cf. Fig. 7.15). The sub-gap state observed at 0.59(2) meV in ambient field cannot be observed in applied field. Assuming the same magnetic field dependence for all sub-gap states it would be expected near 0.4 meV in $\mu_0 H_{\parallel a} = 1.5\,\mathrm{T}$. The data taken at 1.5 T show increased intensity near this

---

[2] The observed magnetic field shift of the two magnon branches is hence slightly different at $\vec{q} = (0, 0, 1)$ and $\vec{q} = (0, 0.05, 1)$, i.e. the shift shows a notable $\vec{q}$-dependence.

energy, but no pronounced peak. However, at 0.59 meV no intensity is found, such that this feature is also shown to be sensitive to magnetic field.

The coherent shift of the magnon and one of the sub-gap states may be attributed to a strong coupling between the sub-gap states and magnons or to the magnetic nature for the sub-gap states. In the latter case, the identical Zeeman-shift and the likely identical magnetic moments associated with both types of excitations indicate a largely similar spin-orbit coupling to apply to the respective moments.

Up to this point, the sub-gap state have only been investigated in detail for momentum transfer along the chain. In our experiment at 4F2/LLB (cf. Section 5.5) in the $(H, K, 0)$-plane states below the gap have been observed also for momentum transfer with finite component along H (cf. intensity maps Fig. 5.8 taken at $T = 4\,\mathrm{K}$ with $k_\mathrm{f} = 1.5\,\mathrm{\AA}^{-1}$). In the same experiment, these features have been studied in more detail at low temperature $T = 1.6\,\mathrm{K} \sim 0.14\,\mathrm{meV}$ and with enhanced resolution ($k_\mathrm{f} = 1.3\,\mathrm{\AA}^{-1}$). The low intensity of the sub-gap features as well as the reduced intensity of the neutron source for the selected k_f enforced longer counting times of ≈ 7 min. per point. The intensity maps indicated at significant shift of the sub-gap states along K for different H, in particular these states appeared at momentum transfer similar to the incommensurate minima in the dispersion for different H. In Fig. 6.4 energy scans at momenta $\vec{q} = (H, K, 0)$ corresponding to the minima in the magnon dispersion are presented.

A measurement at $\vec{q} = (1, 0.05, 0)$ reproduces the two anomalies at $\vec{q} = (0, 0.05, 1)$ observed at IN12/ILL. The anomaly at $\approx 1.15\,\mathrm{meV}$ is however less clearly separated from the magnon due to the not as high energy resolution and maybe due to thermal fluctuations. Selecting $(H, K, 0)$-momentum transfer close to the minima in the dispersion proved a reasonable approximation and sub-gap states could be observed for any such chosen $H \neq 0$. The most profound observation is the detection of a sub-gap state at $\approx 0.6\,\mathrm{meV}$ for any H, i.e. this feature does not shift in energy and has a finite structure factor for any H, however decreasing towards the zone boundary $H = 0.5$. A corresponding behavior is found of the feature near $\approx 1.15\,\mathrm{meV}$, yet a more detailed description is complicated by the nearby intense magnon excitations. At $H = 0.5$ a new sub-gap state is observed near $0.9\,\mathrm{meV}$, whose intensity drops towards $H = 0$. The low energy spectrum does not only display spectral weight at incommensurate wave-vectors, but also at the zone center. Due to the absence of a magnetic reflex at $(1, 0, 0)$ (cf. Section 7.4.1) low energy transfer data can be obtained at Γ. The data show a weak and broad feature below $\approx 0.3\,\mathrm{meV}$ as has already been indicated in the data taken at the $(0, 0, 1)$-reflex (cf. Fig. 6.2).

Having shown, that the sub-gap excitations at $0.6\,\mathrm{meV}$ possess a largely constant energy for momentum transfer in the $(H, K, 0)$-plane, their precise position in momentum space was to be examined. In Fig. 6.5 constant energy scans at $0.58\,\mathrm{meV}$ are shown for fixed H and varied K and the respectively

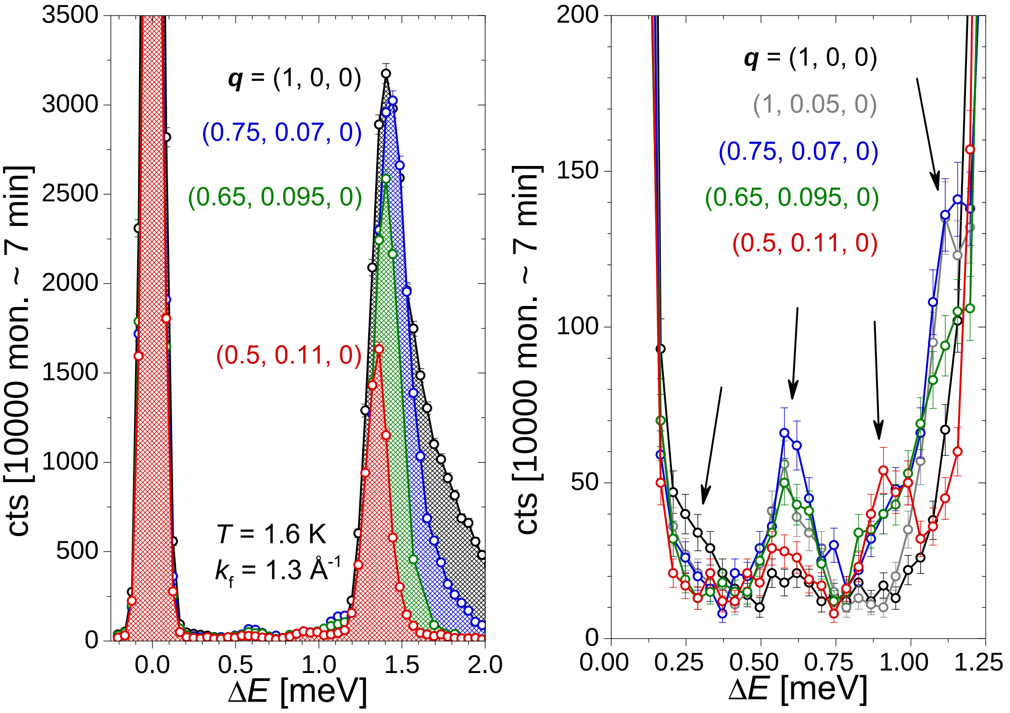

Figure 6.4.: Energy scans at constant momentum transfer $\vec{q} = (H, K, 0)$ where K is selected close to the minimum of the magnon dispersion for any value of H. Data are taken at low temperature $T = 1.6\,\mathrm{K}$ and fixed final momentum $k_f = 1.3\,\text{Å}^{-1}$. Lines are guides to the eye. (left) The magnon excitation gap for the selected values of momentum is observed to be largely constant. (right) Numerous sub-gap excitations are observed, one at lowest energy at Γ and several at higher energy and incommensurate wave-vectors. Arrows stress the observed anomalies. Note that the anomalies do not seem to shift in energy for different selected $\vec{q}$.

determined intensity maxima are shown. It is found, that the position $\vec{q} = (H, K, 0)$ of the maximal intensity of sub-gap states does not correspond well to the minima in the magnon dispersion. Instead, maxima are found at wave-vectors $\vec{q} = (H, K, 0)$, where $K(H)$ is a rather linear function between the zone center along H ($H = 0$) and the zone boundary $H = 0.5$. More data $K(H)$ would be desirable. From the present data set rather sharp kinks in $K(H)$ at $H = 0$ and $H = 0.5$ are indicated.

The dependence of the sub-gap states on momentum transfer along L has not been studied. However, the existence of states $K(H, L)$ for any H and L appears a reasonable assumption. Then, the sub-gap states correspond in momentum space to planes (H, L) with a narrow width and some modulation along the chain axis (K). In the $(H, K, 0)$-plane these excitations are found to not shift in energy. A corresponding behavior for finite momentum transfer along L cannot be deduced. In the $(H, K, 0)$-plane also all low energy magnons have about the same energy (cf. Section 5.7). Hence in this scattering plane one

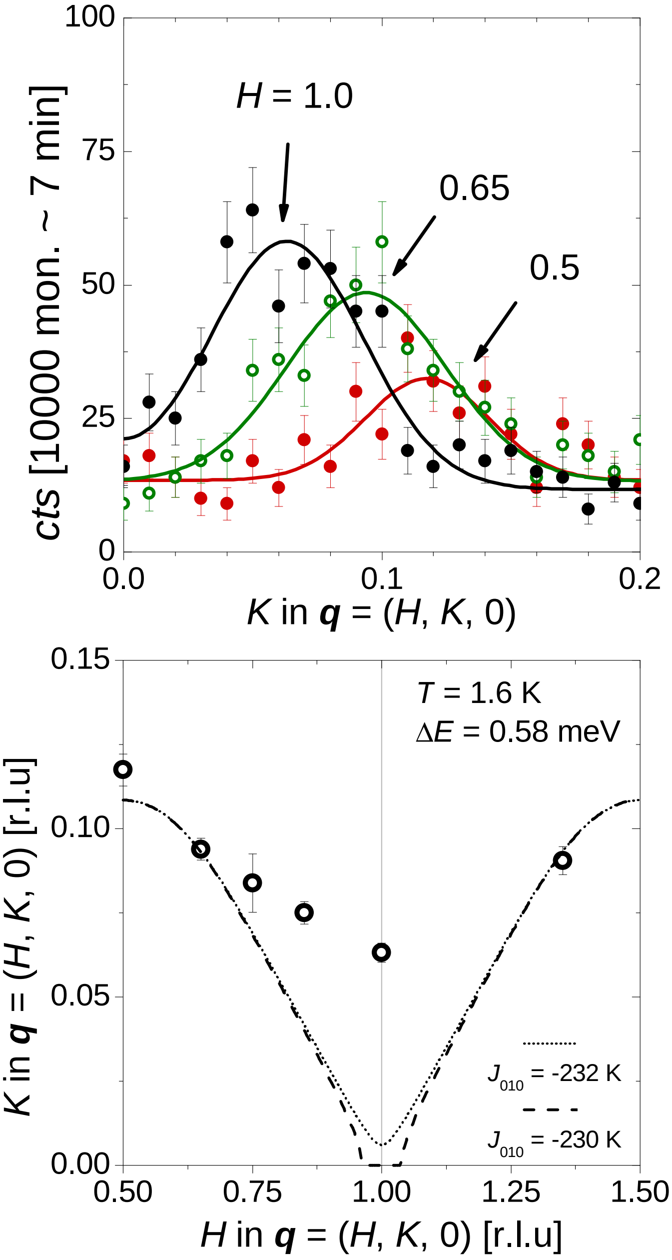

Figure 6.5: (Top) Constant energy scans probing the sub-gap excitation at $\Delta E = 0.58\,\text{meV}$. For selected values H the structure factor is probed in $\vec{q} = (H, K, 0)$. Lines represent fits by Gaussian distributions. A sizeable shift of the maximal intensity along K is observed.
(Bottom) The such determined positions of sub-gap states at $0.58\,\text{meV}$ in the $(H, K, 0)$-plane (circles $\circ$) are compared to the minima in the spin-wave dispersion (dashed line). The existence of a commensurate minimum in the dispersion at Γ is not certain and suppressed already e.g. by a shift of J_{010} with $\alpha = \text{const.}$ within error bars of the spin-wave fit. For a discussion hereof, see page 64.

cannot distinguish, if the excitation energy of the sub-gap states scales with the low energy magnon excitation or is an independent excitation above the ground state. However, the latter ignores any influence of the non-equivalence of the exchange interactions in the a and c directions. Hence an energy shift for momentum transfer along L cannot be excluded.

The most prominent property of the sub-gap states is their incommensurate wave-vector in K and the absence of a dispersion along the chain axis (K). Magnetic interactions along the chain seem to be the dominant energy scale, but there is also a weak dependence on perpendicular momentum transfer. The origin of the sub-gap excitations has however not yet been clarified. On one hand, the framework of non-linear dynamics may allow to construct exotic collective excitations that can exist only for specific momenta, on the other hand the observed features may represent local excitations associated with an incommensurate modulation of the nearby magnetic structure. Below, the latter option will shortly be discussed in order to provide a reasonable starting point for more detailed analysis.

Indeed, local excitations are not only supported by the absence of a distinct dispersion. Moreover, the large line width of the sub-gap states in momentum transfer along K gives evidence that the excitations cannot be related to delocalized states. In literature, the study which to my knowledge compares best to the spectrum of sub-gap states in Li_2CuO_2 has been presented by Xu *et al.* [48] on the quasi-one-dimensional system $Y_{2-x}Ca_xBaNiO_5$. The ground state of the undoped ($x = 0$) compound is described as a $S = 1$ spin-liquid, much different from the antiferromagnetically ordered state in Li_2CuO_2. Upon doping ($x = 5 - 15\%$), however the HALDANE-gap is found to be populated by states of comparable phenotype as the states observed in Li_2CuO_2 within the anisotropy gap. A detailed spectrum for momentum transfer along the chain has been presented for $x = 9.5\%$ which shows strong features at incommensurate momenta below the persistent HALDANE-gap. While not discussed, the data presented also indicate an energy dependence of the structure factor. The incommensurate maximum is found to shift with the impurity concentration in a manner excluding constant density charge ordering of holes. Instead, the incommensuration is suggested to refer to the modulation of antiferromagnetic spin-spin correlations in the vicinity of the impurity. The analysis of the data is done in a model dedicated to $S = 1$ chains. Doping $Y_{2-x}Ca_xBaNiO_5$ induces holes into the chain such that chain segments are expected to couple ferromagnetically. Correspondingly the ground state wave function is symmetric around a single hole [48]. In Li_2CuO_2 chain segments can be expected to interact via the antiferromagnetic next-nearest neighbor coupling J_{020}. The situation is however complicated by the strong inter-chain coupling J_{131}, which competes with antiferromagnetic correlations along the chain. For further discussion see Section 7.4.

Part III.

Studies on thermodynamic properties

0. In the battle of the righteous
1. you can't hope for prey but repute,
2. mastering that arcane craft
3. immortals shy away from.

original attributed to
Charles Percy Snow

7. The magnetic phase diagram

In the course of this thesis the magnetic phase diagram of Li_2CuO_2 is examined experimentally. In this, it is build on and extending earlier studies. All magnetic ordering phenomena of the compound have initially been detected by magnetization measurements, namely the antiferromagnetic ordering temperature in 1989 [110], the meta-magnetic transition identified as spin-flop field in 1993 [113] and the emergence of weak-ferromagnetism at low temperatures in 1998 [124]. The first systematic study of the phase diagram, also based on magnetization measurements, has been presented in 2002 [125]. In this chapter, data of magnetization, specific heat, thermal expansion and magnetostriction measurements are combined to a detailed magnetic phase diagram for magnetic fields applied along the easy *a*-axis. It is presented in Fig. 7.1. Moreover, the phase diagram for fields applied along the hard *b*-axis is studied (cf. Fig. 7.4). This chapter provides an overview of the character of the observed phases and phase transitions. It furthermore serves to outline the more detailed description of studies of the individual thermodynamic properties presented in Chapters 8 to 10.

Li_2CuO_2 represents a prototypical example of quasi-one-dimensional magnetic systems. The extraordinary competition between its one- and three-dimensional magnetic interactions makes it outstanding amongst related compounds and gives raise to one of the most fascinating issues about the material. Its one-dimensional subsystem - chains of strongly coupled magnetic moments - strives for the formation of incommensurate correlations. However, the respective frustration of the inter-chain couplings brings about an instability to ferromagnetic correlations. It is the remarkable property of Li_2CuO_2, that the weak inter-chain couplings are indeed able to outweigh the in-chain couplings and enforce collinear magnetic order at low temperatures.

At first glance, the magnetic phase diagram of Li_2CuO_2 closely resembles that of an ordinary two-sublattice antiferromagnet with weak easy-axis anisotropy (cf. Fig. 7.2). At low temperature and weak external magnetic field, the material undergoes a 2^{nd} order phase transition (T_{N}) into an antiferromagnetic state (AFM). Its evolution and the magnetic field dependence of T_{N} is discussed in Section 7.2.

Just as expected for simple antiferromagnets, applied magnetic field along the hard axes (*b*, *c*) does not establish further magnetic phases (neglecting here the emergent weak-ferromagnetism at low temperature). For field applied $H = H_{\text{c}}$ along the easy *a*-axis at low temperatures a 1^{st} order meta-magnetic phase transition is both expected and observed.

However, there is also a number of features beyond the picture of a simple antiferromagnet. First of all, in Li_2CuO_2 spin-spin correlations are non-negligible even well above the antiferromagnetically ordered phase. Thus, its high temperature phase cannot be regarded as a mean-field paramagnetic state but should be considered as a short range ordered phase (SRO). Its properties are introduced in Section 7.1.

Secondly, the meta-magnetic transition at the critical field H_c is observed to be of 1st order only at low temperatures, but apparently turns into a 2nd order transition at higher temperatures. In the low temperature region one finds the

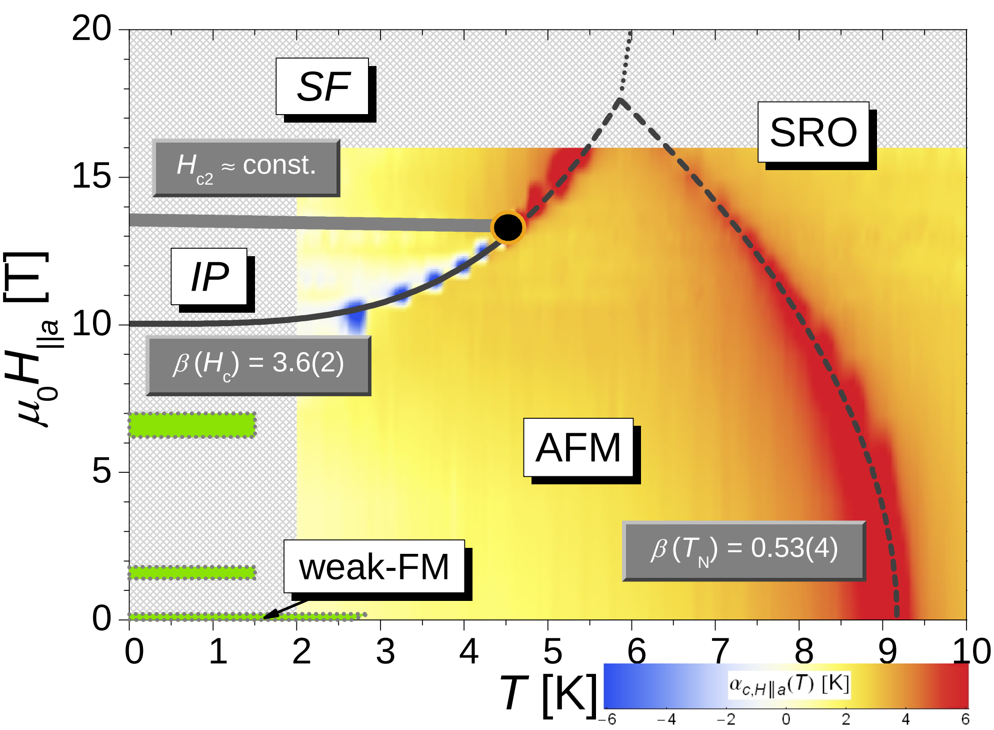

Figure 7.1.: Magnetic phase diagram of Li_2CuO_2 for magnetic field applied parallel to the easy a-axis. The saturation field $\mu_0 H_{\mathrm{sat}}(T \approx 1.45\,\mathrm{K}) = 46.4(4)\,\mathrm{T}$ is omitted. Distinguished phases are the one-dimensionally short range ordered (SRO) phase at high temperatures, the NÉEL-like antiferromagnetic (AFM) phase, an intermediate phase (IP) as well as a presumably spin-flop-like phase (SF) at high field and low temperatures. Further features detected by low temperature magnetization measurements are shown in green, including the emerging weak-ferromagnetism (weak-FM) below $\lesssim 2.6\,\mathrm{K}$. The phase transitions are drawn by a full line if showing a hysteresis and dashed if of 2nd order. The dotted line separating the SF and SRO phases has not yet been detected experimentally. The (H, T) dependence of the transitions is given with respect to Eqn. 7.1 and Eqn. 7.3. All information is superimposed on a color map interpolated from $\alpha_{c,H\|a}$-data (cf. Fig. 7.7). Here, blue/white/red coloration denotes a negative/small/positive thermal expansion coefficient, respectively.

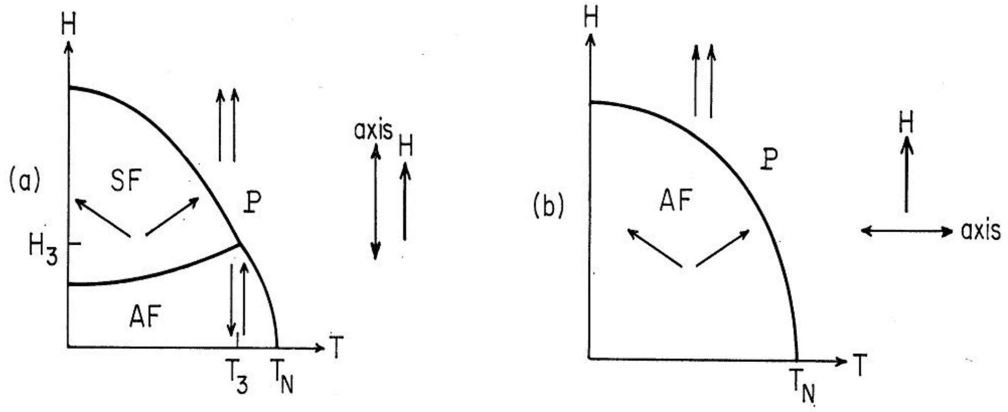

Figure 7.2.: Schematic magnetic phase diagram of a classical two-sublattice antiferromagnet with weak easy-axis anisotropy for magnetic fields applied along (a) and perpendicular (b) to the easy axis. Phase transitions are marked by thick lines, arrows indicate the prominent orientation of moments in the two magnetic sublattices. The paramagnetic (P), antiferromagnetic (AF) and spin-flopped (SF) phases are distinguished. While AF⇔SF is a 1st order phase transition, the transitions P⇔AF and P⇔SF are of 2nd order. For field applied along the easy axis, a the critical end point (T_3, H_3) of the 1st order transition is expected. Figure taken from [149].

compound to enter an intermediate phase. With increasing magnetic field, a crossover to a high field phase is observed. The crossover and the change of order of H_c are found closely related and are discussed in Section 7.3.

Furthermore, the studied material exhibits a number of features at low temperatures, which are accompanied with plateaus of the magnetization $M(H)$ in magnetic fields $H < H_\mathrm{c}$. Experimental evidence is discussed in Section 7.4.1.

7.1. High temperature short range order

As shown by our INS studies in Chapter 5, the inter-chain exchange couplings in $\mathrm{Li_2CuO_2}$ are significantly weaker than those along the spin-chains. While the former drive long range order at low temperatures the latter must be expected to establish short range correlations at much higher temperatures already. The high temperature phase of antiferromagnets is often denoted as paramagnetic. However, this description is well-founded only if the thermal energy significantly exceeds the exchange energies. Throughout this thesis, data on $\mathrm{Li_2CuO_2}$ have been obtained below temperatures $T \leq 380\,\mathrm{K}$ only, where the influence of the in-chain exchange couplings are non-negligible. In this section, data are discussed and presented which provide evidence that the high temperature phase is better referred to by the term "Short Range Ordered" (SRO).

As the exchange couplings have been examined by INS at $T = 4\,\mathrm{K}$ only, their temperature dependence has not been investigated. However, experimental evidence of short range order even at high temperatures is provided by thermodynamic studies. Most notably, susceptibility data are found at odds with simple Curie-Weiss behavior even above $T = 300\,\mathrm{K}$ (cf. Section 8.1). Likewise, specific heat measurements indicate significant, presumable magnetic contributions up to well above 40 K. Their magnetic nature is supported by the relatively low entropy change accompanied with magnetic ordering at T_N. Even the total entropy - i.e. including lattice contributions - reaches only $\lesssim 70\%$ of $R \ln 2$ at $T = 15\,\mathrm{K} > T_\mathrm{N} = 9.25(5)\,\mathrm{K}$ (cf. e.g. Fig. 9.2).

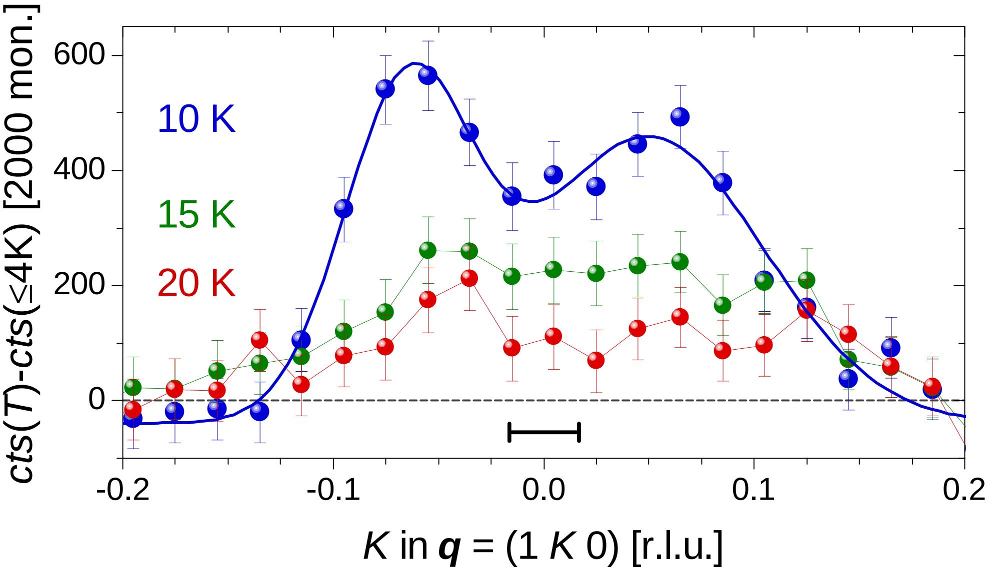

Figure 7.3.: Elastic neutron scattering intensity near $\mathbf{q} = (1, 0, 0)$ [r.l.u.], measured at 4F2/LLB. The reflex is forbidden for both the nuclear and the ordered magnetic structure. From the data taken at $T = 10$, 15 and 20 K, respectively, the intensity measured at $T \leq 4\,\mathrm{K}$ is subtracted. Short range correlations are evident up to 20 K, incommensurate along b^* at 10 K. In the bottom, a bar indicates the experimental resolution (FWHM).

In order to investigate the nature of the correlations, neutron diffraction data have been taken at the three-axis-spectrometer 4F2/LLB. The study is restricted to correlations along the spin-chains. For this purpose momentum transfer near $K = 0$ for $\mathbf{q} = (1, K, 0)$ [r.l.u.] was selected. This reciprocal lattice vector is expected especially suited for detection of weakly scattering short range correlations. First of all, the reflex is forbidden structurally, due to the body-centered crystallographic symmetry of Li_2CuO_2. Secondly, in the magnetically ordered state all moments are arranged parallel to the a-axis (besides a possible slight canting at lowest T, cf. Section 7.4.1) and therefore $\mathbf{q} = (1, 0, 0)$ is not a magnetic reflex. However, the magnetic intensity will cancel out only in case of magnetic long range order. As will be shown in Section 7.4.1, no change of scattered intensity is observed in the data taken at

$T = 1.6\,\mathrm{K}$ and $T = 4\,\mathrm{K}$. The average of both data sets provides a background signal - including incoherent, probable spurious as well as second order scattering from the nuclear $(2, 0, 0)$ reflex - which is then subtracted from data taken at temperatures $T_\mathrm{N} < T = 10, 15$ and $20\,\mathrm{K}$, respectively. As shown in Fig. 7.3 residual magnetic intensity can clearly be observed even up to $20\,\mathrm{K}$. Towards lower temperatures its intensity increases. Also, its width narrows, indicating an increasing correlation length. However, at $T = 10\,\mathrm{K}$ - just above T_N - the data clearly show not one correlation peak but two. Their observed peak intensity is located at the incommensurate wave vector $\mathbf{q} = (1, \pm 0.06(1), 0)$. Note, that any possible offset of the intensity maximum along the H or L direction has not been investigated. The cause of this incommensurate short range ordering may be twofold. Firstly, the frustration of the in-chain couplings as studied at $4\,\mathrm{K}$ should indeed favor incommensurate in-chain correlations above T_N. And secondly, at $T = 10\,\mathrm{K}$ correlations should indicate the onset of long range ordering at $T_\mathrm{N} = 9.25(5)\,\mathrm{K}$. While the dominant inter-chain coupling J_{131} alone is at odds with incommensurate in-chain correlations, they may not be completely suppressed above T_N. Indeed, our thermal expansion data give strong support for a significant influence of J_{100} and J_{110} - both competing with J_{131} - at temperatures just above T_N (cf. Section 10.3.2).

7.2. The antiferromagnetic phase

At low temperature and sufficiently low external magnetic field $\mathrm{Li_2CuO_2}$ attains antiferromagnetic long range order. The phase boundary $T_\mathrm{N}(H)$ has been studied experimentally for magnetic field applied along the easy a-axis as well as the hard b-axis. The transition temperature is identified by the maxima in $\frac{\mathrm{d}(M(T)T)}{\mathrm{d}T}$, $c_p(T)$ and $\alpha(T)$ from magnetization, specific heat and thermal expansion data, respectively. Furthermore, transitions are attributed to maxima in magnetization and magnetostriction data, i.e. in $\frac{\mathrm{d}M(H)}{\mathrm{d}H}$ and $\beta(H)$. The full set of observed anomalies attributed antiferromagnetic ordering at some temperature T_N at a a respective magnetic field denoted as H_N is depicted in Fig. 7.4.

The observed transitions in low field applied $\mu_0 H_i \leq 16\,\mathrm{T}$ can be well described by

$$H_\mathrm{N}(T_\mathrm{N}) = H_0 \left[1 - \frac{T_\mathrm{N}}{T_\mathrm{N}(0)}\right]^\beta \tag{7.1}$$

where $T_\mathrm{N}(0)$ is the antiferromagnetic ordering temperature at $H = 0$ and H_0 is the critical field at $T = 0$. The fitted exponents are $\beta = 0.53(4)$ and $\beta = 0.49(4)$ for the data for $H \parallel a$ (easy axis) and $H \parallel b$ (hard axis), respectively. This exponent agrees well to the mean-field theory prediction of a reduction of T_N proportional to H^2 [150]. An empirical expression obtained by Bienenstock [151] may be used to describe the phase boundary AFM⇔SRO up to higher

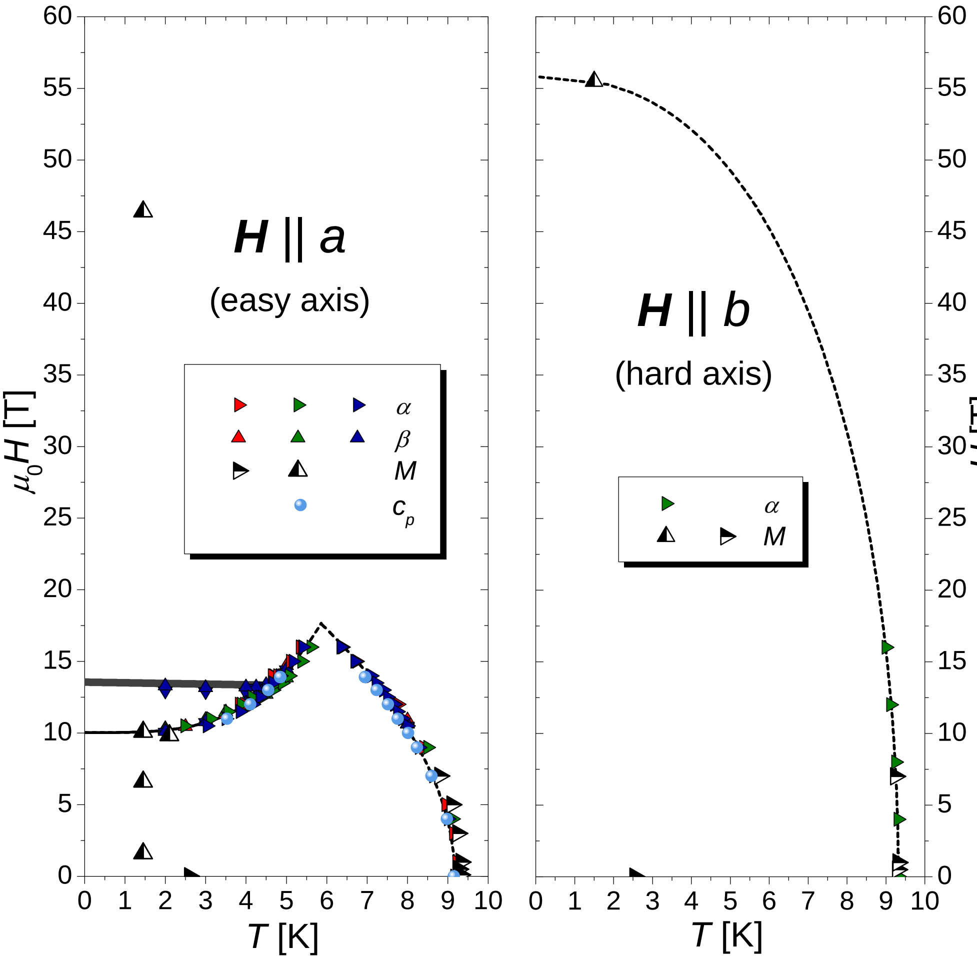

Figure 7.4.: Summary of observed phase transitions for magnetic field applied along the easy a-axis (left) and the hard b-axis (right). Transitions derived from thermal expansion (α) and magnetostriction (β) data of the a-, b and c-axis expansion are displayed as red, green and blue filled triangles, respectively. Results from magnetization measurements $M(H)$, $M(T)$ are given by half-filled triangles. Specific heat data are presented by spheres. The phase transitions H_{c} and T_{N} are shown as thin lines. The crossover at $H_{\mathrm{c2}} \approx 13\,\mathrm{T}$ is indicated by a broad line. Transitions of 2nd order are represented by dashed lines. For $H \parallel a$ the depicted phase boundaries T_{N} and H_{c} are determined from Eqn. 7.1 and Eqn. 7.3, respectively. For $H \parallel b$ the phase boundary depicted is fitted using Eqn. 7.2.

fields:

$$H_{\mathrm{N}}(T_{\mathrm{N}}) = H_0 \left[1 - \left(\frac{T_{\mathrm{N}}}{T_{\mathrm{N}}(0)} \right)^{1/\xi} \right]^{\beta} \qquad \text{with} \qquad \beta = 0.5. \tag{7.2}$$

This function was observed to describe well $T_{\mathrm{N}}(H)$ obtained from the high temperature series expansion analysis on Ising antiferromagnets. While in agreement to the mean-field prediction at $H_N/H_0 \ll 1$, Eqn. 7.2 cannot reproduce the low temperature result $H_N \propto T^{3/2}$ from spin-wave theory [152]. This restriction in mind, it serves here as an approximate expression for T_N in magnetic fields along the hard axis in Fig. 7.4.

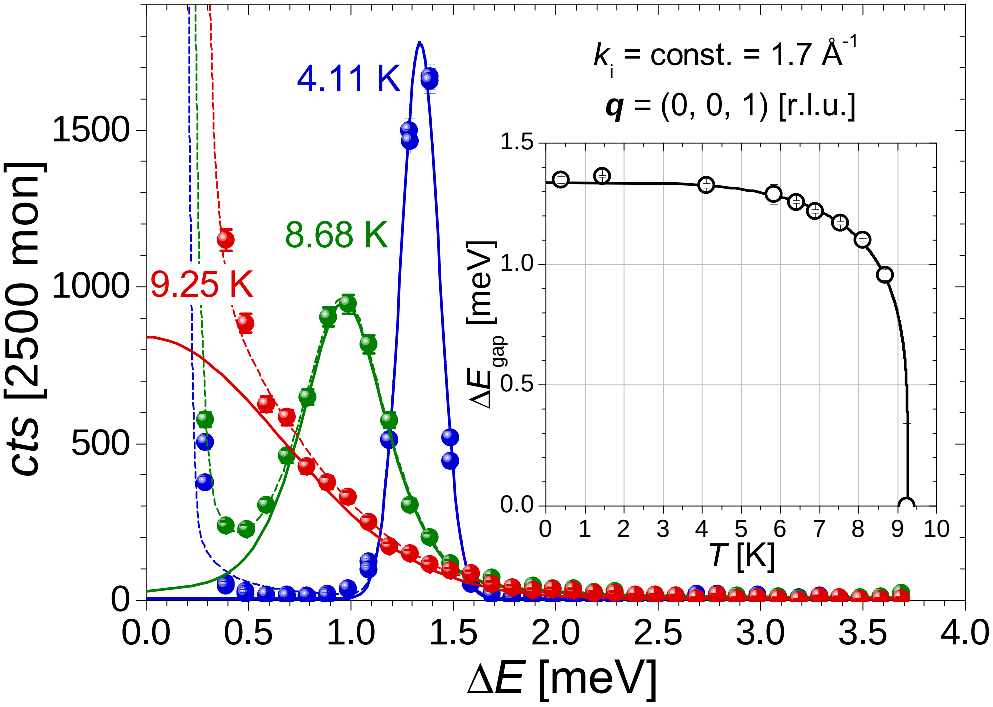

Figure 7.5.: INS intensity of the magnon anisotropy gap measured at the Γ-point $q = (0, 0, 1)$ at IN12/ILL. Note that the experiment is performed using const. k_i. The data are approximated by Pseudo-Voigt distributions. Fits of the magnetic excitations are shown as bold line. Inset: The anisotropy gap size is plotted as a function of temperature. The line is a guide to the eye.

It has been shown by Boehm *et al.* that along with the onset of long range order below T_N both the sublattice magnetization and the anisotropy gap increase rapidly and congruently [117][1]. This finding agrees with predictions of the random phase approximation method [153]. The anisotropy gap can thus be regarded as a measure of the order parameter of the antiferromagnetic transition. We have monitored the temperature dependence of the anisotropy gap at the magnetic zone center $\mathbf{q} = (0, 0, 1)$ in order to verify their magnetic origin. The data are presented in Fig. 7.5. At temperatures $T < 6\,\mathrm{K}$ the line shape of the magnon excitation is well described by a Gaussian function, i.e. the magnon energy distribution is more narrow, than the experimental resolution (FWHM $\approx 0.25\,\mathrm{meV} \approx 3\,\mathrm{K}k_B$). At higher temperatures, a pseudo-Voigt distribution is used instead to describe the increasingly broadened magnon energy distribution. Our observations confirm the strong temperature dependence of

---

[1] Data by Chung *et al.* [112] show a significantly slower increase of the sublattice magnetization with decreasing temperature than observed by Boehm *et al.* [117].

the anisotropy gap just below T_N found by Boehm *et al.* As discussed in Section 9.2, specific heat data also suggest an only narrow regime of $< 0.6\,\mathrm{K}$ below T_N to be governed by critical fluctuations.

7.3. The meta-magnetic transition and intermediate phase

For easy-axis antiferromagnets with weak anisotropy a meta-magnetic transition at critical magnetic field applied parallel to the easy axis - labeled H_c throughout this thesis - into a spin-flopped state is expected. The transition does not break the symmetry of the system and is of 1st order. In general, the temperature dependence $H_c(T)$ is a consequence of the interactions between thermally excited spin-waves. The interaction renormalizes the excitation spectrum and thus alters the stability of both the antiferromagnetic and spin-flopped states [153]. For antiferromagnets with only nearest neighbor coupling, spin-wave theory predicts $H_c \propto T^{5/2}$ [152]. In contrast, calculations by GREEN's function method find $H_c \propto T^2$ in a low temperature and weak anisotropy perturbation [154]. Furthermore, in antiferromagnets with single ion anisotropy, spin-wave based free energy calculations yield $H_c \propto T^{7/2}$ [155]. In this section, it is shown that Li_2CuO_2 undergoes a corresponding meta-magnetic transition at low temperatures. The change of the thermodynamic properties of Li_2CuO_2 at this transition are discussed in the corresponding chapters. The focuss of this section is on the temperature dependence of the phase boundary. The transition is found more complex than that from a low field collinear into a high field spin-flopped phase.

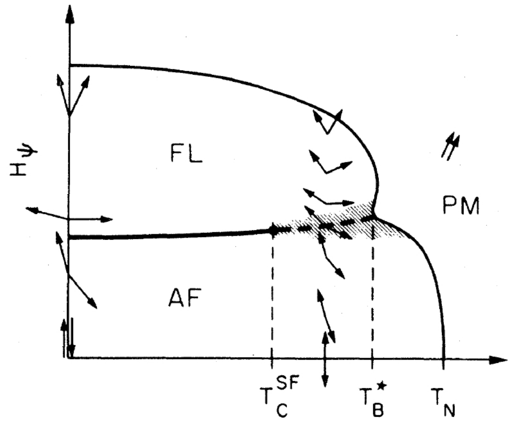

Figure 7.6: In magnetic fields H_ψ applied at an angle $\psi \neq 0$ with the easy axis the 1st order spin-flop transition is transformed into a crossover at temperatures larger then a critical temperature $T_C^{SF}(\psi)$ [156].

Conventionally, the phase boundary of the 1st order transition at H_c intersects with the transition at T_N in a critical point at some elevated temperature. From our studies on Li_2CuO_2, a critical point is indeed observed, however at well lower temperatures as is discussed below. A central issue of this section is the discrimination of the observed critical point from a conventional shift of the critical point in magnetic fields not well aligned along the easy axis. Studies on the stability of the critical end point of H_c in antiferromagnets have shown, that if additional transversal magnetic field is applied - breaking the easy axis symmetry - the first order transition is continuously suppressed. The critical end point of the meta-magnetic transition is then shifted towards lower temperatures and the transition turns into a continuous cross-over at higher temperatures (cf. Fig. 7.6).

For Li_2CuO_2, a theoretical investigation of the temperature dependence of H_c is to be expected demanding for mainly two reasons. Firstly, the origin of the magnetic anisotropy in the compound is not yet understood. Strongly anisotropic exchange is predicted for the nearest neighbor coupling along the spin-chains. However, the anisotropy of the other in-chain and inter-chain couplings is yet unknown but appears non-negligible (cf. Section 10.3.1). The overall magnetic phase diagram for simple two-sublattice antiferromagnets has been shown to depend significantly on the presence and relative strength of the anisotropy of intra- and inter-sublattice exchange [157]. Secondly, the exchange coupling scheme in Li_2CuO_2 is somewhat complex. The multiple frustration of the magnetic interactions suggests a high sensitivity to temperature renormalization of the individual exchange interactions. This is underlined by the pronouncedly close excitation energies for both commensurate as well as incommensurate low lying magnon excitations observed at $H = 0$. As a consequence, even subtle field induced changes of the individual exchange coupling strengths may strongly influence the stability of the antiferromagnetic ground state close to H_c.

In the course of this thesis, the meta-magnetic transition is observed between $T \approx 1.45\,\mathrm{K}$ at $\mu_0 H \approx 10.0\,\mathrm{T}$ and $T \approx 5.4\,\mathrm{K}$ at $\mu_0 H = 16\,\mathrm{T}$. The transition is classified as meta-magnetic by the sudden increase of the magnetization at the critical field H_c [125]. The temperature dependence of H_c (cf. Fig. 7.4 (left)) is described well by an exponential increase

$$H_c(T) = H_{c0} + AT^{\beta} \tag{7.3}$$

where the critical field $H_{c0} = H_c(T = 0)$ is evaluated as $10.0(1)\,\mathrm{T}$ along with an unexpectedly large exponent $\beta = 3.6(2)$ [2]. Extrapolating both the fitted phase boundaries T_N and H_c to high magnetic field, they intersect at $T^* \approx 5.8\,\mathrm{K}$ and $\mu_0 H^* \approx 17.7\,\mathrm{T}$. As pointed out above, H_c is expected to be a 1st order transition at temperatures below T^*. However, our data give strong evidence for a qualitative change of the transition near $T' \approx 4.5\,\mathrm{K}$ and $\mu_0 H' \approx 13\,\mathrm{T}$, which goes along with the inhibition of the observed hysteresis for $T > T'$. This change is most clearly resolved in its strong effect on the thermal expansion and magnetostriction of the c-axis.

In Fig. 7.7, data of the thermal expansion coefficient $\alpha^c_{H\parallel a}$ of the c-axis in magnetic field along the easy a-axis are presented. These data show as signif-

---

[2] From the phase diagram developed in [125] the exponent $\beta = 3.9(2)$ can be obtained .

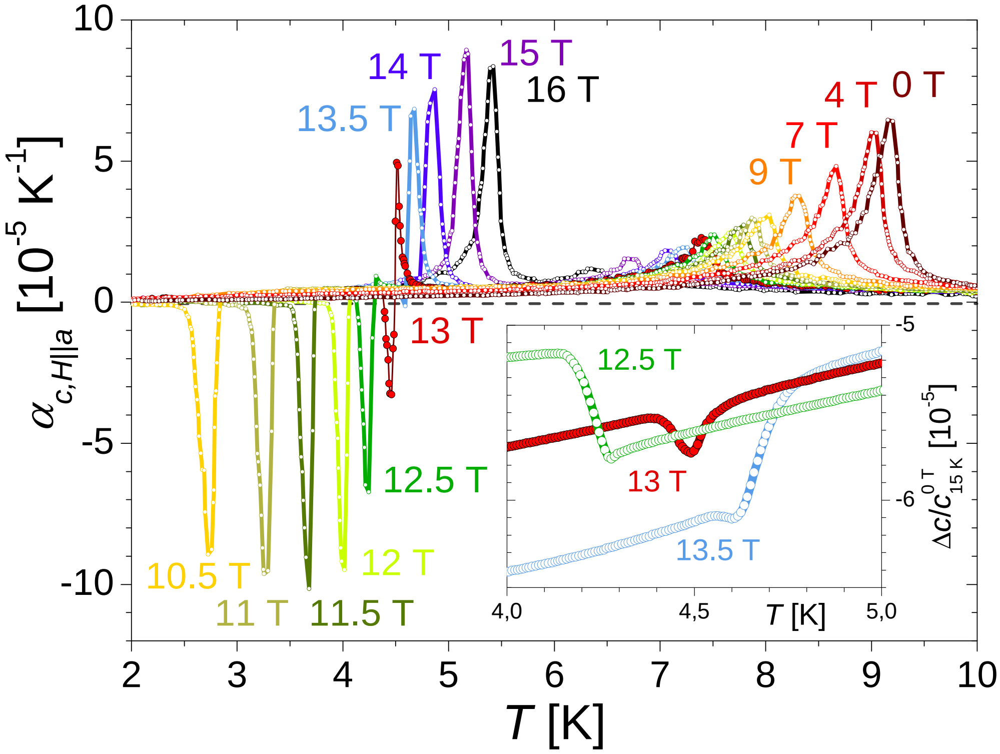

Figure 7.7.: c-axis thermal expansion coefficient $\alpha^c_{H\|a}$ in magnetic fields $\leq 16\,$T applied along the easy a-axis. At temperatures $T \gtrsim 6\,$K the anomaly associated with long range antiferromagnetic ordering is observed. At low T and $\mu_0 H_{\|a} \geq 10\,$T a significant anomaly in $\alpha^c_{H\|a}$ is observed, which is changing its sign at $\mu_0 H' \approx 13\,$T. This anomaly is related to the meta-magnetic transition. In the inset the length change $\Delta c/c$ is depicted for data sets with $H_{\|a}$ close to 13 T. Two distinguished transitions, i.e. both positive and negative slopes are observed, a negative anomaly dominant at low T and a separate positive anomaly dominating at higher T. Both are of comparable size at $\mu_0 H \approx 13\,$T.

icant signal related to the meta-magnetic transition in the thermal expansion of the c-axis at high temperatures $T < T^*$ and magnetic fields $\mu_0 H > 10\,$T. In magnetic fields $10\,\mathrm{T} < \mu_0 H \lesssim 13\,$T the meta-magnetic transition is clearly observed as a large negative anomaly in $\alpha^c_{H\|a}$. However, this anomaly changes sign and turns into a positive one for $\mu_0 H \gtrsim 13\,$T. No intermediate field is observed at which $\alpha^c_{H\|a}$ is vanishing at the transition. Instead, close to $\mu_0 H' \approx 13\,$T two separate transitions can be observed, successively replacing one another. In the vicinity of (T', H') the transition dominating at low temperatures is induced in slightly higher field, and vice versa. Ignoring this only weak shift, the exponential temperature dependence of the critical field $H_c(T)$ remains unchanged across T'.

In order to verify the expected 1$^{\text{st}}$ order nature of the meta-magnetic transition, its hysteresis has been examined both above and below (H', T') (cf. Fig. 7.8). Both for the magnetostriction and thermal expansion measurements an in-

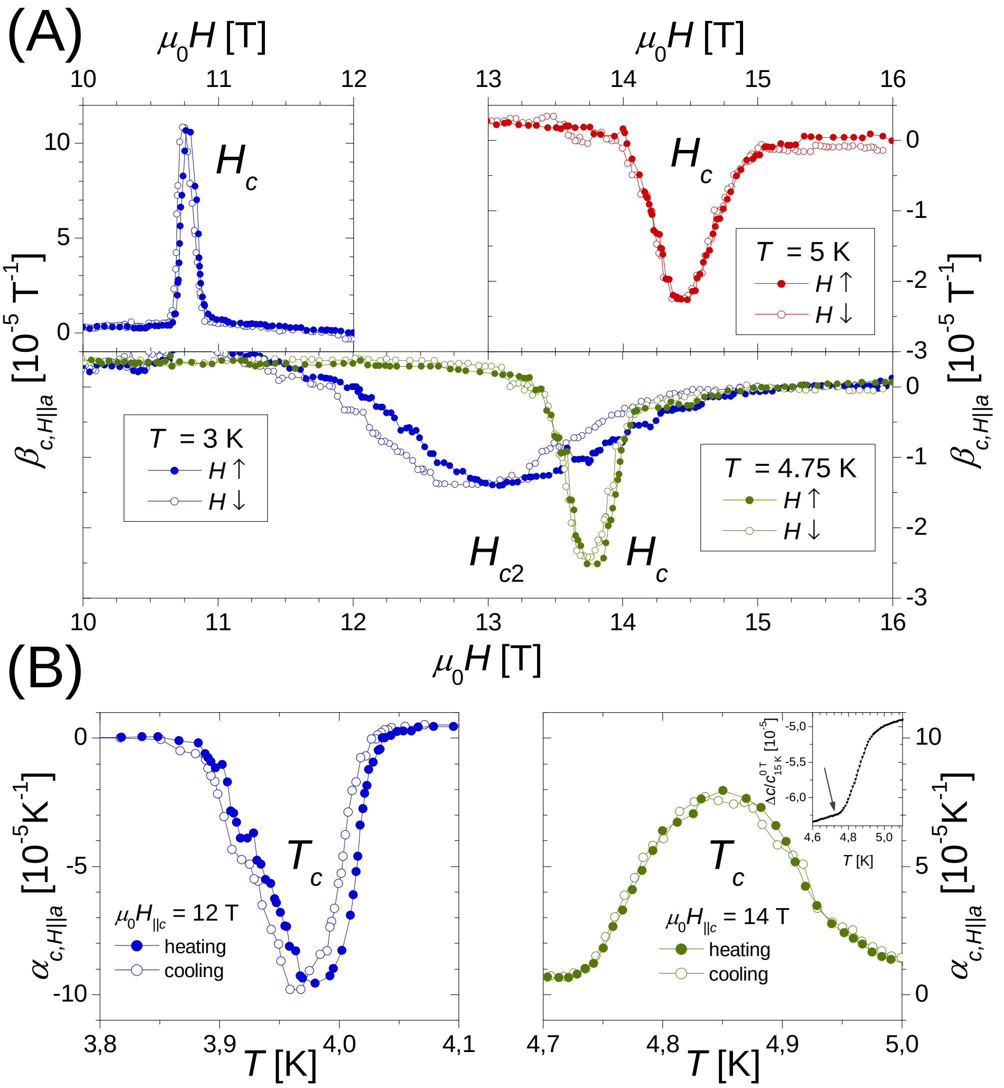

Figure 7.8.: Hysteresis of phase transitions in magnetic field observed by thermal expansion and magnetostriction of the c-axis in magnetic field $H \parallel a$. For a detailed description see text. (A) Magnetostriction data below and above $T' \approx 4.5$ K. Note the differently scaled ordinate in the upper left figure. (B) Thermal expansion at 12 and 14 T, below and above $\mu_0 H' \approx 13$ T. In the inset of the data at 14 T the remnant negative anomaly at $T \approx 4.7$ K is indicated.

strumental contribution is to be expected. In magnetostriction data, a weak hysteresis is identified by the relative offset of the transitions ΔH_c in measurements in increasing and decreasing field. In the temperature range $2 - 4.75$ K a rather constant $\Delta H_c = 0.045(5)$ T is observed, i.e. for both the positive and negative anomalies at H_c. However, at $T = 5$ K the relative offset of the transitions at $H_c \approx 14.4$ T is as narrow as $0.01(1)$ T. The hysteresis of the cryostat's magnet cannot be expected to cause this change. Nevertheless, thermal expansion measurements on the hysteresis have been taken at 12 and 14 T, where apparatus induced hysteresis effects may be caused instead by possibly different temperature gradients. The negative anomaly at 12 T and $T_\mathrm{c} \approx 3.97\,\mathrm{K}$ shows a well resolved hysteresis $\Delta T_\mathrm{c} = 0.012(2)\,\mathrm{K}$. In the data for the positive anomaly at 14 T (here a slight remnant negative anomaly is still observed) and $T_\mathrm{c} \approx 4.85\,\mathrm{K}$ the hysteresis is found reduced to $\Delta T_\mathrm{c} = 0.005(6)\,\mathrm{K}$, i.e. vanishing within error bars. Together, the data indicate the width of the hysteresis at H_c to fall off with increasing temperature $T > T'$. One origin of a ceasing 1^{st} order transition could be, that the measurements where done with insufficient alinement of $H \parallel a$ (as discussed on Fig. 7.6). However, the sharp λ-like anomalies observed in thermal expansion at high field (cf. Fig. 7.7) [3] make such interpretation unlikely, but indeed suggest a gradual transformation of H_c to a 2nd order transition for temperatures $T > T'$. The origin of this only gradual change is different from the gradual conversion between positive and negative anomalies, which are well separated in the phase diagram. Another feature, namely the cross-over at $H_{\mathrm{c}2}$ appears to be of relevance here.

Magnetization as well as thermal expansion/magnetostriction measurements provide evidence for the existence of an intermediate phase at low temperatures and magnetic fields $H \parallel a > H_\mathrm{c}$. This phase has not been described in literature before. Compared to a spin-flopped state, the intermediate phase is characterized by a reduced magnetization but higher susceptibility than expected for a spin-flopped state (cf. Fig. 8.6) as well as a significant lattice expansion (cf. Section 10.3.2). While its lower phase boundary in $H \parallel a$ is given by H_c, the high field boundary is much less distinct. Instead, a cross-over regime is observed, distinguished by a large hysteresis and about vanishing temperature dependence (i.e. entropy change). From the available data, a nominal value of the corresponding critical field $H_{\mathrm{c}2}$ cannot be deduced. The magnetization data show a steady decrease of the susceptibility χ between $\approx 12.3\,\mathrm{T}$ and $\approx 13.6\,\mathrm{T}$ such that at higher fields $M \approx \chi H$. The magnetostriction coefficient $\beta^{c}_{H\parallel a}$ (cf. Fig. 7.9) shows an anomaly between $\approx 11.5\,\mathrm{T}$ and $\approx 14.5\,\mathrm{T}$. This highly hysteretic anomaly is largest at 13.3(2) T in increasing magnetic field and 12.8(2) T in decreasing field (cf. Fig. 7.8 (A)). Accordingly, the about temperature independent $H_{\mathrm{c}2} \approx 13\,\mathrm{T}$ is used to sketch the cross-over in the magnetic phase diagrams presented here. Constrained below $H_{\mathrm{c}2}$, the intermediate phase is suppressed at higher temperatures along with the increasing magnetic field stability of the zero field phase. Taking $H_{\mathrm{c}2} = 13\,\mathrm{T}$ the intermediate phase is to be expected at $T \leq 4.5\,\mathrm{K}$ only. However, even at 4.75 K the cross-over regime is still observed. The observation of remnant hysteretic effects at H_c at temperatures $T > 4.5\,\mathrm{K}$ may hence be attributed to the not fully suppressed cross-over.

---

[3] Specific heat data, taken up to 13.9 T (cf. Fig. 9.1) indicate λ-shaped anomalies at H_c.

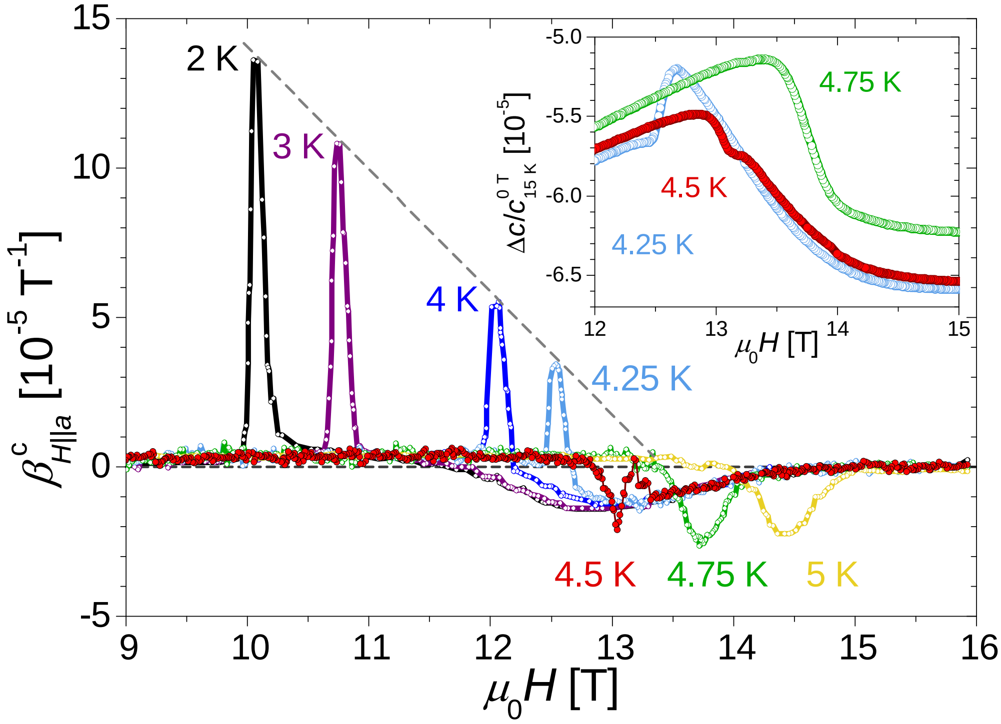

Figure 7.9.: Magnetostriction coefficient $\beta^c_{H\|a}$ of the c-axis in magnetic fields $\leq 16\,\mathrm{T}$ applied along the easy a-axis. At low temperatures $T = 2\,\mathrm{K}$, a positive anomaly is found at $H_\mathrm{c} \approx 10\,\mathrm{T}$ and a negative anomaly corresponding to a broad cross-over in the range $11.5\,\mathrm{T} \lesssim H_\mathrm{c2} \lesssim 14.5\,\mathrm{T}$. H_c increases with temperature and the corresponding anomaly in $\beta^c_{H\|a}$ is found to change sign near $T = 4.5\,\mathrm{K}$. The dashed line stresses the systematic reduction of the size of the anomaly at H_c at temperatures $< 4.5\,\mathrm{K}$. The size and shape of the anomaly at H_c2 shows an only weak temperature dependence. It is however steadily suppressed towards higher temperature as H_c increases. In the inset the length change $\Delta c/c$ is depicted for data sets with T close to $4.5\,\mathrm{K}$. Besides the cross-over, two distinguished transitions are observed, a positive anomaly dominant at low $H_{\|a}$ and a separate negative anomaly dominating at higher $H_{\|a}$, accordingly to the thermal expansion data presented in Fig. 7.7.

7.4. Low temperature anomalies

At low temperature, two further unexpected and rather fascinating features are revealed experimentally in the study of the magnetic phase diagram. Firstly, weak ferromagnetism is observed in small magnetic fields at temperatures below 2.6 K, i.e. well below the NÉEL temperature. Secondly, magnetization data $M(H)$ show a number of anomalous features, unexpected for an easy axis antiferromagnet.

7.4.1. Weak ferromagnetism

The evolution of weak ferromagnetism in Li_2CuO_2 has first been reported in 1998 by Ortega *et al.* [124]. Investigating a powder sample, they observed a weak ferromagnetic component in magnetization data below 2.8 K. An associated hysteresis at 2.2 K with a remanent magnetization of $3 \cdot 10^{-5}\,\mu_B/\,\mathrm{f.u.}$ and a coercivity field of 12 Oe have be determined. Below 2.4 K, μSR measurements by Staub *et al.* [118] observed a splitting of one of the muons precession frequencies. These muons have been interpreted to sensitively probe the magnetization at the oxygen site. The frequency splitting has been attributed to a small spin canting of 0.7° out of the easy a-axis. In specific heat data, presented by Chung *et al.* [112], no corresponding anomaly was found.

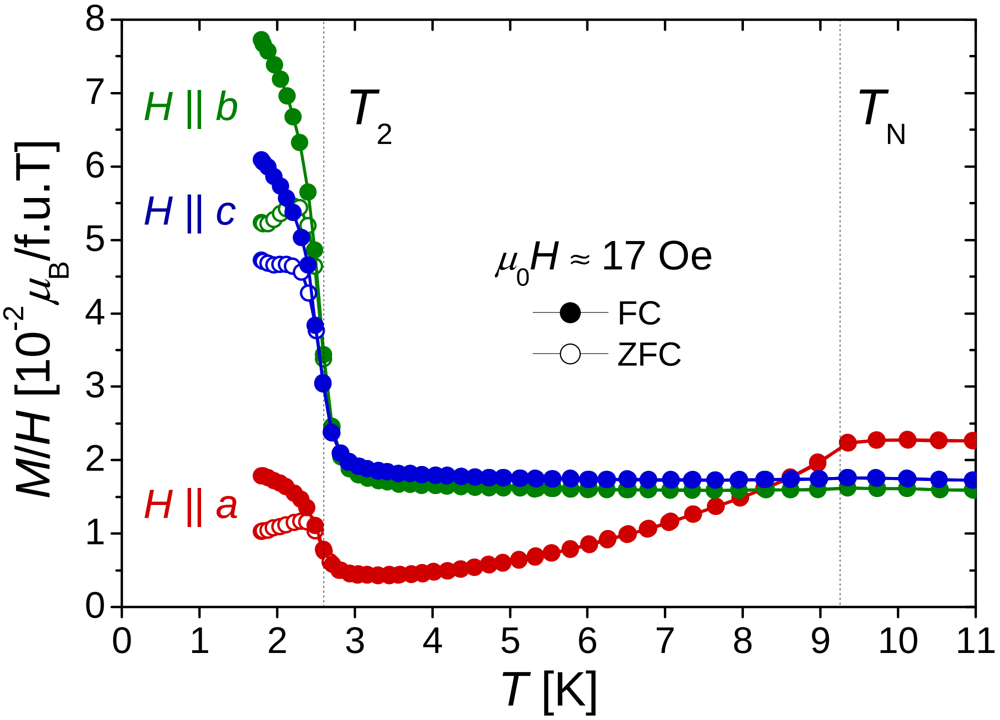

Figure 7.10.: In magnetization data in low applied magnetic field an anisotropic ferromagnetic component is observed at low temperature. In order to determine the precise magnitude of the applied field it is made use of the finding that the low field data M/H can be scaled well to data taken at $\mu_0 H = 1\,\mathrm{T}$ for all temperatures between 10 and 30 K. Data taken after cooling the sample in zero field (ZFC) and in applied field (FC) deviate below 2.6 K, used here as a lower boundary for the transition temperature T_2.

Below, magnetization measurements for our sample are presented. In $M(T)$ data in low magnetic field a ferromagnetic component is observed at low temperatures (cf. Fig. 7.10). The derivative of the magnetization $\partial M/\partial T$ assumes a pronounced minimum at 2.5 K. Comparing magnetization data for samples cooled in zero field and applied external field, history dependent ferromagnetic contributions are identified already at higher temperatures 2.6 K. A clear separation of the ferromagnetic component has not been achieved. The transition temperature $T_2 = 2.6\,\mathrm{K}$ is thus given here as a lower bound for the transition to a weakly ferromagnetic phase in low fields. In agreement to corresponding data by Chung *et al.* [112], we observe a clear anisotropy of the susceptibility with respect to the magnetic field direction. This anisotropy is well illustrated by the comparison of respective hysteresis loops. In order to separate the ferromagnetic contribution from the underlying antiferromagnetic response, we plot in figure Fig. 7.11 the difference of the magnetization $\Delta M(H) = (M_{H\downarrow} - M_{H\uparrow})/2$ as measured in decreasing and increasing magnetic field at $T = 1.8\,\mathrm{K}$. At $H = 0$ one can read off a remanent magnetization of $(2.2, 5.5, 3.9) \cdot 10^{-5}\,\mu_\mathrm{B}/\,\mathrm{f.u.}$ for magnetic field applied along the (a, b, c)-axis, respectively. The coercivity is determined from the maximal slope $\mathrm{d}M/\mathrm{d}H$ and evaluates to 12(2) Oe for any applied field direction (cf. Fig. 7.12). However, ΔM is found to not vanish up to 500 Oe (the extremal field value applied for the hysteresis loops). While for field along the hard b- and c-axes ΔM is falling off equally for $H \gtrsim 100\,\mathrm{Oe}$, ΔM is less strongly suppressed for magnetic field along the easy a-axis.

The Dzyaloshinski-Moriya-interaction provides a common mechanism for a canted magnetic moment orientation and the consequent evolution of weak ferromagnetism [158, 159]. However, this interaction is relevant only in crystal structures with low enough symmetry. Especially, it is vanishing if the center of an exchange path between magnetic ions represents an inversion center of the crystal structure. Consequently, Dzyaloshinski-Moriya-interaction is forbidden by symmetry for any exchange path between Cu-ions in $\mathrm{Li_2CuO_2}$. However, inversion centers are absent at the center of the exchange path between Cu- and O-ions, as well as between neighboring O-ions in the same chain. Here, we remind that a significant portion of the overall magnetic moment is considered to be located at the oxygen-site. While the highly symmetric Cu-site suggests that any anti-symmetric interaction should cancel out, the O-site is less distinguished. A canted spin configuration of the O-moments is thus worth investigation, especially as having already been indicated by the above mentioned μSR measurements [118].

Single crystal neutron diffraction studies have been performed on $\mathrm{Li_2CuO_2}$ by Chung *et al.* [112]. From the magnetic structure refinement magnetic moments of $0.96(1)\,\mu_\mathrm{B}/\mathrm{Cu}$ and $0.1(1)\,\mu_\mathrm{B}/\mathrm{O}$ are obtained. Further refinement has been performed assuming a possible canting of moments into the c-axis direction, which is then found as large as 14° for the moments at the Cu-site and 26° for moments at the O-site. Note that this proposed canting into the c-axis alone does not correspond to a finite Dzyaloshinski-Moriya-interaction for any exchange path. After inspection of our own diffraction data, such large canting of moments appears not justified. Chung *et al.* do not report on the observation of intensity at the $(1, 0, 0)$-reflex. This purely magnetic reflex[4]

---

[4] For the crystallographic structure ($Immm$) reflexes at (H, K, L) with $H+K+L = 2n+1$

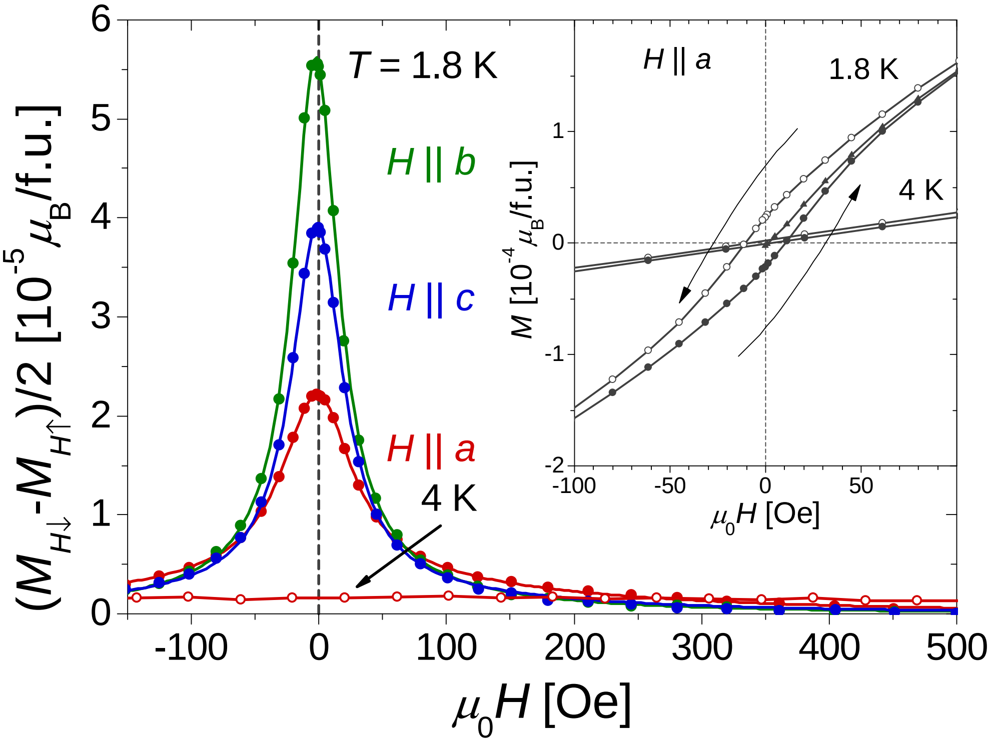

Figure 7.11.: Comparison of induced remanent magnetization for field along the crystal axes at $T = 1.8\,\mathrm{K}$. The magnetic field is cycled between $\pm 500\,\mathrm{Oe}$. For field along the a-axis, data are shown at $4\,\mathrm{K} > T_2$ (cycled between $\pm 1\mathrm{kOe}$), too. The still observed hysteresis is may be attributed to the magnet coil, has however not been studied in more detail. Inset: Hysteresis loop for magnetic field applied along the a-axis.

vanishes exactly for orientation of the magnetic moments μ along the a-axis (in diffraction, neutrons probe the time-averaged moment projection $\mu \perp q$). The $(1,0,0)$-reflex therefore represents a sensitive measure of canting of moments out of the a-axis. The observed intensity at the $(0,1,0)$-reflex $I_{(010)}$ provides a lower boundary[5] for the intensity $I_{(100)}$ to be expected at $(1,0,0)$ if the moment orientation was perpendicular to the a-axis. An upper limit for the canting angle ϕ out of the a-axis can hence be given by comparison of the observed intensities at $(1,0,0)$ and $(0,1,0)$.

$$I_{(100)} > I_{(010)} \sin^2 \phi \tag{7.4}$$

Investigating the temperature dependence of the $(1,0,0)$-reflex (cf. Fig. 7.13) no intensity related to a canted moment orientation is observed within error bars. In particular, the scattered intensity does not change below T_2. The weak

---

($n \in \mathbb{Z}$) are absent.

[5] As the a-axis is longer than the b-axis, the magnetic form factor at $(0,1,0)$ is reduced compared to $(1,0,0)$.

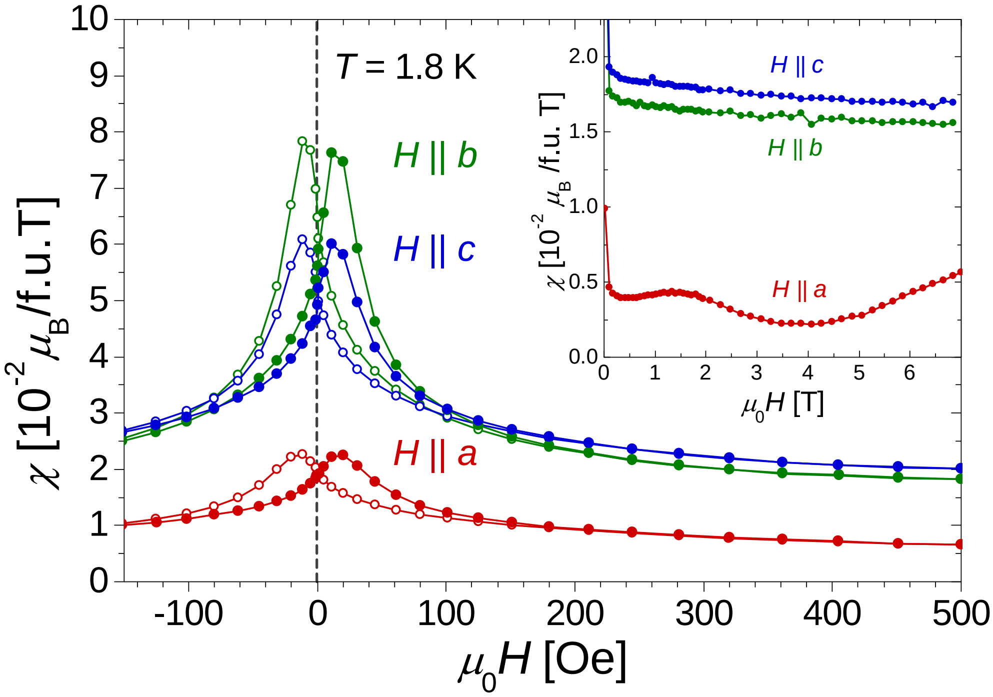

Figure 7.12.: Susceptibility $\chi = \partial M/\partial H$ at $T = 1.8\,\mathrm{K}$ for increasing (●) and decreasing (○) field applied along the crystal axes. A coercivity of 12(2) Oe is observed for each data set. Inset: Susceptibility for larger fields up to 7 T. Note the decreasing χ up to the largest field applied along the hard b- and c-axes. For $\mu_0 H_{\|a} \approx 1.6\,\mathrm{T}$ the susceptibility shows a pronounced anomaly and a minimum near $\mu_0 H_{\|a} \approx 4\,\mathrm{T}$

peak present at $(1, 0, 0)$ is found both above and below T_N. It thus should be attributed to scattering at the nuclear $(2, 0, 0)$-reflex due to remnant higher order contamination passing the employed PG-filter. Taking the error bars for the observed peak height at $(1, 0, 0)$ as an upper limit for $I_{(100)}$ the total moment is found to be canted by $\phi < 0.7°$. Considering a canting of the O-moments only for the moment distribution given by Chung *et al.* [112] a respective canting angle $\phi_\mathrm{O} > 8°$ is at odds with our data.

Returning to a DZYALOSHINSKI-MORIYA-interaction between canted O-moments one may ask for the corresponding exchange path. For the moments on oxygen ions involved in the exchange path J_{010} and I_{131} DZYALOSHINSKI--MORIYA-interaction is not allowed by symmetry. However, the next-nearest-neighbor coupling along the chain J_{020} as well as the inter-chain coupling along the a-axis I_{100} are to be considered [6]. The O-O exchange path within a chain is located in a mirror plane of the crystallographic structure perpendicular to the a-axis such that the DZYALOSHINSKI-MORIYA vector D should be parallel to the a-axis [159]. Then, to obtain a non-vanishing interaction $D \cdot (S_1 \times S_2)$ both the interacting moments S_1 and S_2 must be canted away from the easy a-

---

[6] Anisotropic exchange along I_{110} is neglected for the sake of simplicity.

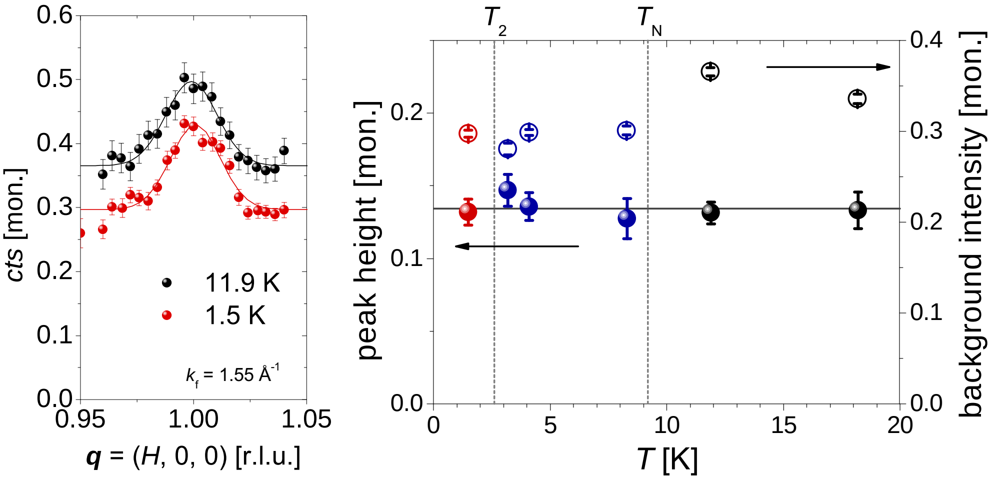

Figure 7.13.: Temperature dependence of elastic scattering at the $(1,0,0)$-reflex, measured at 4F1/LLB. (Left) Elastic intensity in a narrow region around the $(1,0,0)$-reflex above T_N and below T_2. The data are fitted by a GAUSSian peak on top of a constant background. For comparison, the intensity of the magnetic $(0,1,0)$-reflex is as large as 95 cts/mon. (Right) Temperature evolution of peak height and background intensity. The only observed effect is the increased background intensity just above T_N which is expected to arise from largely incoherent magnetic scattering (for further detail cf. Fig. 7.3). The peak at $(1,0,0)$ is attributed to scattering at the nuclear reflex $(2,0,0)$ by second order contamination of the neutron beam.

axis[7]. Also, the moments must be canted both into the b- and c-direction. For exchange along I_{100} the crystal symmetry enforces that D must to be parallel to the b-axis. Then, the canted moment orientation must have a contribution into the c-direction.

Next, we will show that rather simple magnetic structures with a non-vanishing DZYALOSHINSKI-MORIYA-interaction due to O-O-exchange can easily be constructed. In order to describe a modulation of the O-moments, such that $S_1 \times S_2 \neq 0$, a second magnetic propagation vector must be introduced. Consequently, a weak magnetic super-structure should be observable. For the exchange path I_{100} (J_{020}) the moment orientation is to be modulated along the a- (b-)axis, i.e. in the simplest case by implementation of a propagation vector $\tau_\mathrm{O} = (1/2, 0, 0)$ ($\tau_\mathrm{O} = (0, 1/2, 0)$), respectively. However, it turns out that any simple super-structure along the b-axis will be frustrated by the dominant inter-chain interaction I_{131}. In this context, we remind that this interaction is responsible for the suppression of incommensurate correlations favored by the isolated chains. However, no frustration occurs in magnetic structures with two non-equivalent O-sites. A few simple examples of super-structures with

---

[7] The same applies to the Cu-O exchange, such that the DZYALOSHINSKI-MORIYA-interaction vanishes if the Cu-moment are not canted.

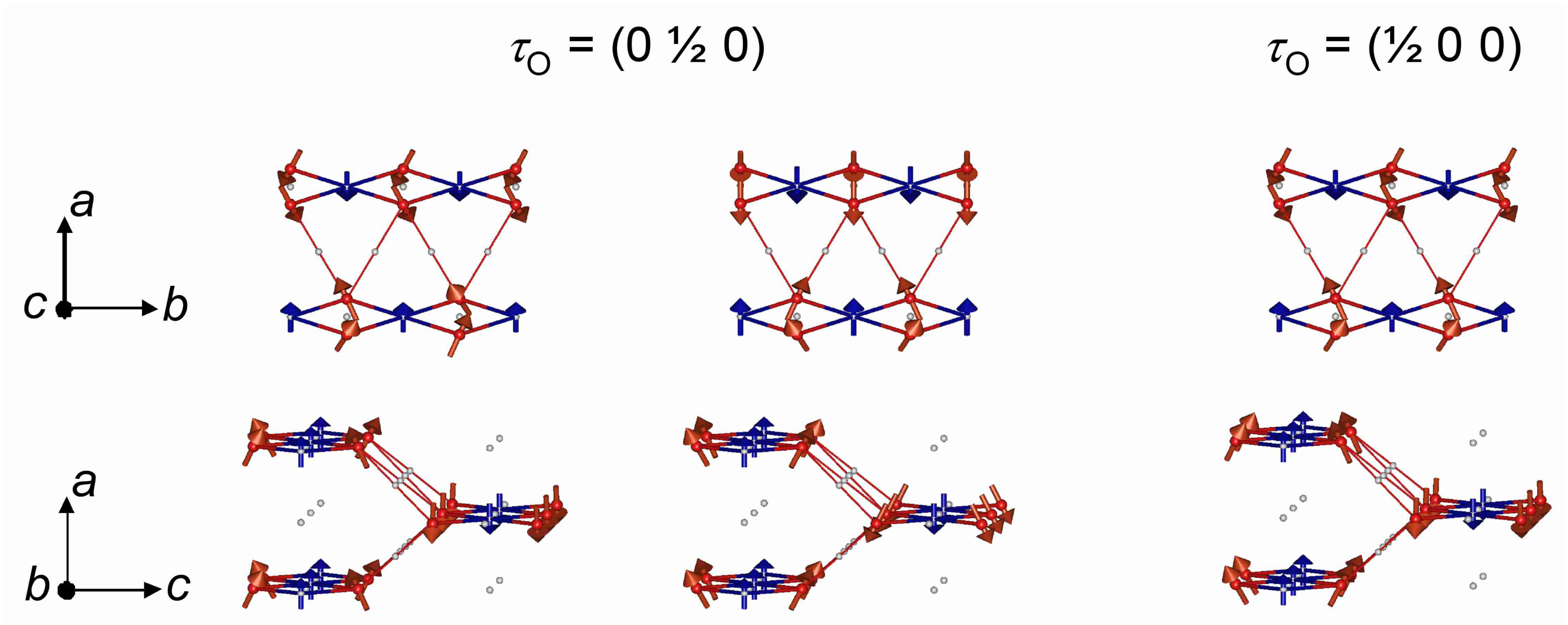

Figure 7.14.: Magnetic structures with finite Dzyaloshinski-Moriya-interaction (DMI) between neighboring oxygen sites. The non-canted Cu-moments are shown in blue, oxygen sites and (exaggerated) moments in red, centers of inversion symmetry of the nuclear structure (including the Cu-site) are represented by grey spheres. (Top) two neighboring chain segments viewed along the c-axis. (Bottom) three chain segments viewed along the chain. (Left,Middle) Two possible moment arrangements with finite DMI of oxygen-moments along b. (Left) staggered canted moment along c-axis. (Middle) staggered canted moment along b-axis. (Right) Possible magnetic structure with finite DMI along a. For any presented structure, canted moments are non-frustrated for the dominant inter-chain coupling (red line) only, if neighboring oxygen ions along $(a/2, b/2, z)$ occupy non-equivalent sites of the magnetic structure.

non-vanishing Dzyaloshinski-Moriya-interaction are presented in Fig. 7.14. We conclude, that the observed weak ferromagnetism and the μSR-observation of non-equivalent oxygen sites may be interpreted by finite Dzyaloshinski--Moriya-interactions between moments at oxygen sites. However, to verify that any and which O-moment arrangement is able to produce the observed anisotropic weak ferromagnetism demands further investigation.

Without referring to Dzyaloshinski-Moriya-interactions, an alternative mechanism to induce weak ferromagnetism is proposed in the early investigations by Ortega *et al.* [124]. It is shown, how a competition of exchange interactions and the magneto-crystalline anisotropy can cause a canting of moments. The low ferromagnetic ordering temperature is explained in terms of a temperature dependence of the anisotropy. However, within our specific heat and thermal expansion studies no anomalies at T_2 are resolved, excluding any larger change of spin-spin-correlations at this temperature. As shown e.g. for CrF_3 [160], weak ferromagnetism can be expected along with the onset of long range order. For Li_2CuO_2 however, it was shown by μSR that the ordered moment at the oxygen site develops significantly slower than at the Cu-site [118]. The low value of T_2 may therefore be related to the formation of a magnetic super-structure of the oxygen moments. In Section 9.3 we show how the specific heat anomaly at T_2 should be detected in weak external field. It is furthermore worthwhile to note, that we have observed a significant pressure dependence of T_2 in weak external magnetic field (cf. Fig. A.5).

Eventually, it is commented on the possible relation of Dzyaloshinski--Moriya-interactions to the absent inversion symmetry at the crystal surface [161]. The overall agreement of the remanent magnetization in the powder data by Ortega *et al.* [124] and in our single crystal data provides evidence, that such surface effects must be weak in Li_2CuO_2.

7.4.2. Anomalous magnetization at low T

For easy axis antiferromagnets with low anisotropy and in magnetic field applied along the hard axis the susceptibility $(\partial M/\partial H)_\perp(H)$ is expected to be largely constant. If field is applied along the easy axis, the susceptibility $(\partial M/\partial H)_\parallel(H)$ is vanishing in low field and slowly increasing due to thermal fluctuations if the field approaches a critical value H_c, associated with the meta-magnetic transition. However, the magnetization of our Li_2CuO_2 sample is found to show features beyond this simple picture both for $(\partial M/\partial H)_\perp$ and $(\partial M/\partial H)_\parallel$. Data measured in static field at $T = 2.1\,\mathrm{K}$ and $T = 1.8\,\mathrm{K}$ are presented in Fig. 8.5 and Fig. 7.12, respectively. Above the narrow low field range with large susceptibility indicating the weak ferromagnetism, $(\partial M/\partial H)_\perp$ is observed to decrease only slowly. In particular, the high resolution of our SQUID data (Fig. 7.12) evidences $(\partial M/\partial H)_\perp$ to not reach a minimal value below $\mu_0 H = 7\,\mathrm{T}$ at $1.8\,\mathrm{K}$. This behavior may point towards the presence of impurity spins which are further suggested by a weak upturn in $M(T)$-data at low temperatures (cf. Fig. 8.2) [162]. Much more strikingly, $(\partial M/\partial H)_\parallel$ is found

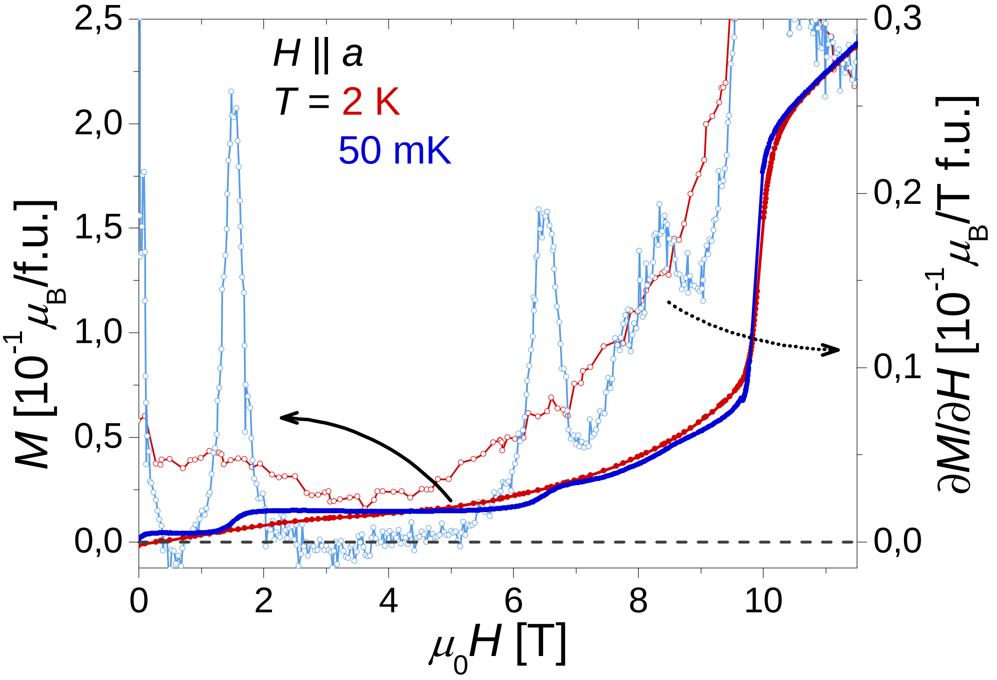

Figure 7.15.: Low temperature magnetization data in magnetic fields applied along the easy a-axis, taken by Y. Tokiwa on an independently grown single crystal [148]. Data near $H_c \approx 10\,\mathrm{T}$ are not shown. At 2 K a broad anomaly above 1 T and a minimum near 4 T in $\partial M/\partial H$ is observed. Data taken at 50 mK disclose two plateaus in the magnetization near 0.7 and 4 T. In $\partial M/\partial H$ two pronounced maxima at $\approx 1.5\,\mathrm{T}$ and 6.5 T are observed. A further anomaly may exist near 8.5 T.

to express a second maximum at $\mu_0 H \approx 1.6\,\mathrm{T}$. Comparing $(\partial M/\partial H)_{\|}$-data at different temperatures, this maximum is strongly broadened with increasing temperature, however does not appear to be shifted in H. At low temperatures $T = 50\,\mathrm{mK}$, the magnetization has been shown to increase in step-like manner at $\mu_0 H \approx 1.6\,\mathrm{T}$. An alike feature is observed at $\mu_0 H \approx 6.6\,\mathrm{T}$ (cf. Fig. 7.15) [148]. In our pulsed field magnetization data at $T \approx 1.45\,\mathrm{K}$, comparable anomalies are observed (cf. Fig. 7.16). Any of the low temperature magnetization curves shows a significant reduction of $(\partial M/\partial H)_{\|}$ at $\mu_0 H_{\|a} \approx 4\,\mathrm{T}$.

The origin of these anomalies is yet to be clarified. However, one very promising approach should still be provided, namely the assumption of presence of impurities in the investigated Li_2CuO_2 crystals. The difficult controllability of the Li-content during growth may give rise to a primarily non-magnetic contamination of the structure. Furthermore, the comparable ionic radii of Li^+- and Cu^{2+}-ions may lead to chemical disorder. Non-magnetic sites give rise to effective impurity spins by deficient compensation of the moments at neighboring magnetic sites. It has been shown on other gapped antiferromagnets that impurities can cause a number of effects yet unexplained about our

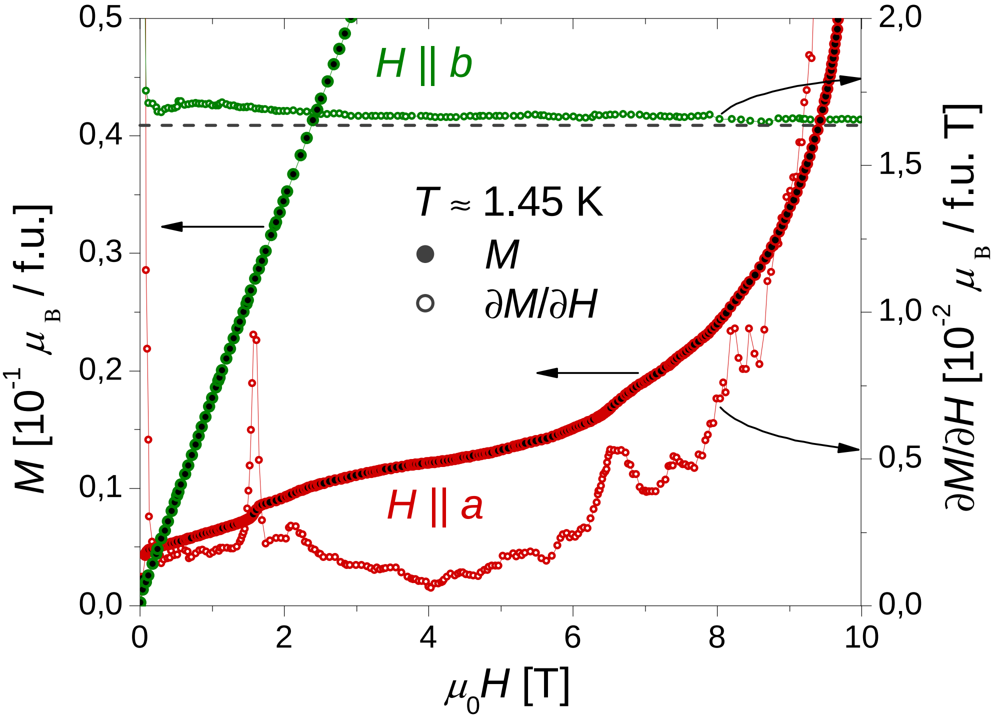

Figure 7.16.: Magnetization M and susceptibility $\partial M/\partial H$ for the easy a- and hard b-axis in intermediate fields. A subset of pulsed field magnetization measurements up to $\mu_0 H = 60\,\mathrm{T}$ Fig. 8.6 is shown. For the hard axis, $\partial M/\partial H$ is found decreasing below $\approx 9\,\mathrm{T}$. The easy axis susceptibility shows a maximum at $\approx 1.6\,\mathrm{T}$ and a weak anomaly near 6.6 T, well below the meta-magnetic transition at 10 T.

data on Li_2CuO_2. On one hand, they can cause a suppression of the 1st-order discontinuity at the meta-magnetic transition in frustrated magnets [165–167]. On the other hand, they can create magnetic excitations with excitation energies below the magnon gap which are located at incommensurate **q**-vectors [48, 168]. Furthermore, it was shown for gapped, dimerised, site-diluted antiferromagnets, that intermediate magnetic fields can induce gapless states with pseudo-plateaus in the magnetization, resulting from the interaction of disordered local moments [163, 169]. Indeed, our c_p data for Li_2CuO_2 at magnetic fields of 4 T due not indicate the presence of a gap. Clearly, the long range ordered state in Li_2CuO_2 is not closely related to the above literature examples. It neither corresponds to a spin liquid, nor are impurities expected to be present in a larger extend (cf. Chapter 4). Many aspects of impurities in three-dimensional HEISENBERG antiferromagnets have been studied continuously since the 1960s (see e.g. [170, 171]). At present, I am not aware of a study that can account for the low temperature magnetization and low energy spectrum as observed in Li_2CuO_2. In ferromagnetic-antiferromagnetic frustrated systems, the antiferromagnetic next-nearest-neighbor coupling across

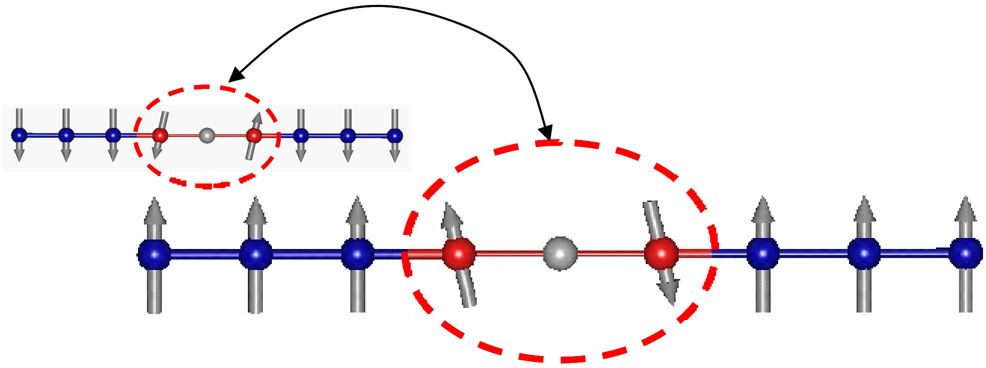

Figure 7.17.: A non-magnetic impurity within a spin-chain may lead to the formation of antiferromagnetically coupled spins at the end of the chain segments. Their dominant interaction can be expected to be comparable to the antiferromagnetic next-nearest neighbor interaction. The absent ferromagnetic nearest neighbor interactions with the impurity site may favor the formation of localized singlets. Near impurities, a modulation of the moment arrangement is to be expected which can mediate an interaction between distant impurity sites [163, 164].

a spin-vacancy may be a largely relevant constituent for the response of the local magnetic structure to impurities. The formation of non-magnetic states around vacancies within the long range ordered state, as schematically depicted in Fig. 7.17 has been proposed for the closely related system $\mathrm{LiCu}_{2-x}\mathrm{Zn}_x\mathrm{O}_2$ [172]. In $\mathrm{Li_2CuO_2}$, the observed spectral weight below the magnon gap may point to a modulation of the local magnetic structure in the vicinity of impurities (cf. Chapter 6). Such modulation can be expected to couple even distant impurities [173]. If the impurities induce magnetic moments that oppose that of the respective sublattice - on-site due to J_{020}, or due to coupling between impurities - external magnetic field may indeed show step-like features. To study the possible role of impurity states for the observed low temperature anomalies in $\mathrm{Li_2CuO_2}$ appears a promising subject. Specifically, the reduced number of interactions of spins next to an impurity may also allow to examine the yet unknown anisotropic contributions to the exchange interactions. At this stage, a probable relation between the presence of impurities and the emergence of low temperature weak-ferromagnetism cannot be excluded.

Besides theoretical analysis, AC-susceptibility measurements at low temperature are proposed in order to investigate the possible relationship of the observed anomalies in $(\partial M/\partial H)_{\|}$ and in the neutron scattering spectra. Further information is expected from a study of the magnetic field dependence of the entropy at low temperatures (cf. Section 9.3) and, most importantly, the influence of systematic impurity doping. The substitution effect of Cu → Ni has already been studied by Ebisu *et al.* Their data indicate Ni to adopt a low spin $S = 0$ state, i.e. causing a magnetic site dilution and a significant reduction of T_N already for low Ni-concentrations [123].

8. Magnetization studies

For investigation of the magnetic properties of a material, externally applied magnetic fields are the natural probe. While the response to magnetic fields is manifold, magnetization measurements provide information which solemnly reflects the magnetic constituents of the system. For any thermodynamic system which can posses a finite magnetization, an externally applied magnetic field H directly effects its thermodynamic potential. In particular, the magnetization $M = -1/V \partial F / \partial H$ is a direct measure of the change of the free energy F in external fields. Given a system to posses a number of states with energy E_n, the magnetization

$$M = \frac{N}{V} \sum_n -\frac{\partial E_n}{\partial H} e^{-E_n/k_\mathrm{B}T} \Big/ \sum_n e^{-E_n/k_\mathrm{B}T} \tag{8.1}$$

relates to the thermal occupation of all the states which are shifted in energy by the applied field [174].

In this chapter magnetization data for $\mathrm{Li_2CuO_2}$ are presented and discussed. Firstly, the temperature dependence of the magnetization at high temperatures and the onset of long range order around $T = T_\mathrm{N}$ are illustrated in Section 8.1. The long range ordered regime has been probed by magnetic field dependent magnetization measurements and results are documented in Section 8.2.

8.1. Magnetization $M(T)$

In the literature on $\mathrm{Li_2CuO_2}$, magnetization data are discussed and presented regularly. First measurements on polycrystals date back to 1988 [65]. Magnetization data on single crystals have been published by Boehm *et al.* [117], Mizuno *et al.* [20] and Chung *et al.* [112] (cf. Fig. 8.2). Furthermore, data have been presented by Klingeler [125][1].

In this section, our data on the temperature dependence of the magnetization of one single crystalline sample are discussed. The data are taken in magnetic fields applied along the 3 crystallographic axes and at temperatures up to 380 K using a *Quantum Design MPMS SQUID-VSM*. The complete data set, taken at $\mu_0 H = 0.5\,\mathrm{T}$ and $1\,\mathrm{T}$ for the easy and hard axes, respectively, is shown in Fig. 8.1. In Fig. 8.2, our data are compared with the results of Chung *et al.* ($\mu_0 H = 0.1\,\mathrm{T}$) and Mizuno *et al.* (no value of applied field given). Overall, our single crystal data and those presented in literature are found to

---

[1] In [125] data $\chi_{\parallel a}$ and $\chi_{\perp a}$ are examined.

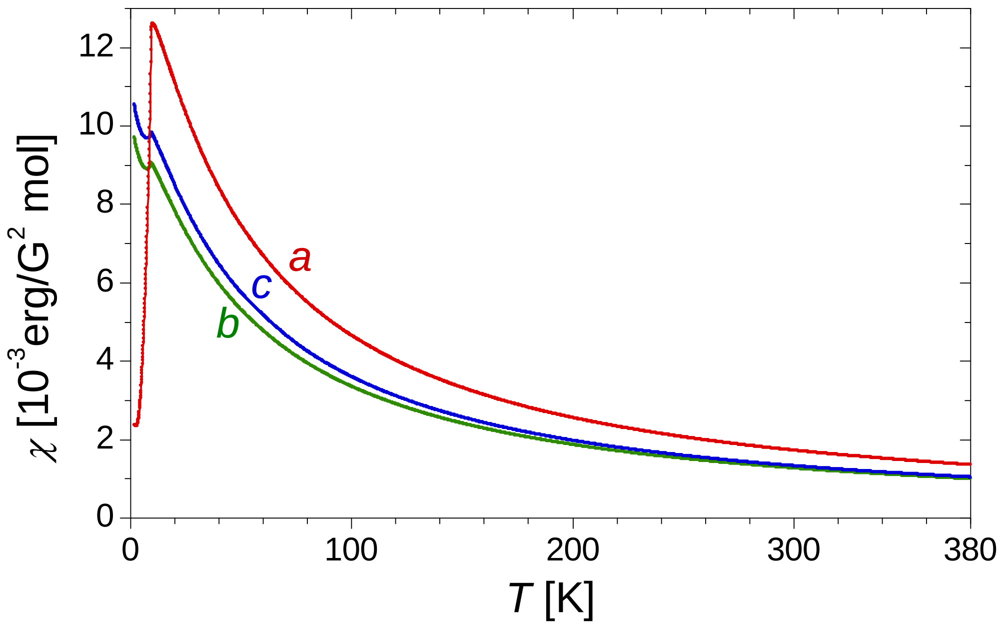

Figure 8.1.: (left) Susceptibility $\chi(T)$ of one single crystal up to $T = 380\,\mathrm{K}$ for the three crystallographic axes. The largest g-factor and a magnetic easy axis are indicated in data $H \parallel a$. Note, that the data clearly cannot be scaled by different g-factors alone.

agree in the main features, but to differ in detail. All data sets reflect the easy axis anisotropy along the a-axis, indicated by the large reduction of the magnetization $M_{H\|a}$ below T_{N}. The presence of corresponding short range correlations is indicated by a slight reduction of $M_{H\|a}$ at higher temperatures above T_{N} compared to the maximum of the susceptibility for magnetic fields applied along the hard axes. All data sets further indicate a slight reduction of the susceptibility for $H \perp a$ below T_{N}. Moreover, a reduced susceptibility along the b-axis compared to the c-axis susceptibility is observed[2]. This finding interestingly contrasts the reported ESR g-factors [115], where $g_c < g_b$. Below T_{N} our data indicate a weak increase of the susceptibility - presumably CURIE-like, slightly larger than elsewhere reported. Above T_{N}, excellent agreement of our data is found with those of Mizuno *et al.* Good quantitative agreement is also found to the data by R. Klingeler. In contrast, Boehm *et al.* and Chung *et al.* report a significantly larger susceptibility of the a-axis, i.e. a larger magnetic anisotropy.

The reciprocal susceptibility of Li_2CuO_2 does show a CURIE-WEISS-type behavior. However, analysis of the data yields a pronounced antiferromagnetic CURIE-WEISS-temperature ($-43.5\,\mathrm{K}$ [110], $-44\,\mathrm{K}$ [116]), which was understood to question the expected quasi-one-dimensional magnetic character of the compound. The large exchange parameters we have determined from the measured magnon dispersion suggest significant magnetic correla-

---

[2] In contrast the data Boehm *et al.* give indication for $\chi_{H\|b} < \chi_{H\|c}$.

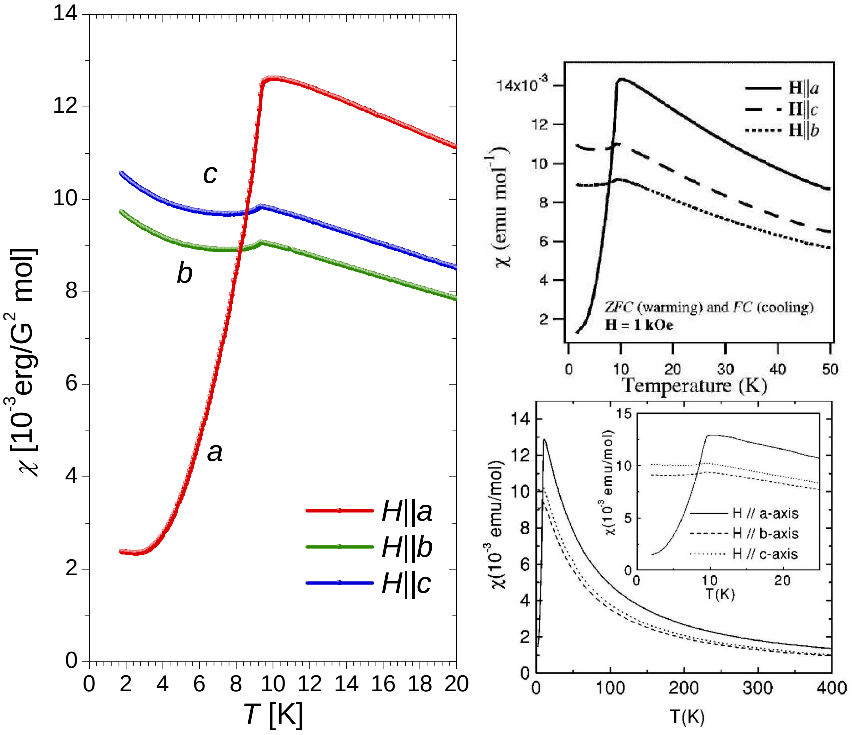

Figure 8.2.: Susceptibility $\chi(T)$ near T_N, for our sample (left) compared to literature data by Chung *et al.* [112] (upper right) and Mizuno [20] (lower right). Note the larger CURIE-like tail in our data and the more pronounced anisotropy in the data of Chung *et al.* .

tions to be present even at room temperature. One can test the applicability of the CURIE-WEISS-law by performing corresponding fits of the data in different temperature ranges $\chi(T_\mathrm{min}) \to \chi(T_\mathrm{max})$. A fit of the CURIE-WEISS-law $\chi(T) = C/(T - \theta_\mathrm{CW}) + \chi_0$ demands the determination of 3 parameters: the CURIE-constant C, the CURIE-WEISS-temperature θ_CW and a background susceptibility χ_0, which is assumed to be constant. For the available data sets, the strong correlation of the fit parameters C and θ_CW with χ_0 necessitates a reduction of the parameter set. One can disregard a constant χ_0, performing the fit on data $\partial\chi(T)/\partial T$ instead. Due to measurement noises, the derivative is scattering distinctly, but with the large density of measured data points the fit parameters evolve smoothly with the selected fit range. However, the large resulting error-bars of the fit parameters does not allow fit both C and θ_CW simultaneously[3]. With g-values fixed to ESR-results [115] or θ_CW to 55.4 K as deduced from our neutron studies, $\partial\chi(T)/\partial T$ can be fitted with only one free parameter. Subsequently χ_0 can be directly obtained for $\chi(T)$-data. The results of a corresponding analysis of our data – presented in Fig. 8.3 – show clearly, that even at the highest measured temperatures the fit parameters are not independent of the selected temperature range. It is thence to

---

[3] The resulting error bars amount to $\Delta g \approx 0.2$ and $\Delta\theta_\mathrm{CW} \approx 30$ K.

be concluded, that $\chi(T)$ cannot to be described by the Curie-Weiss-law at temperatures below 350 K.

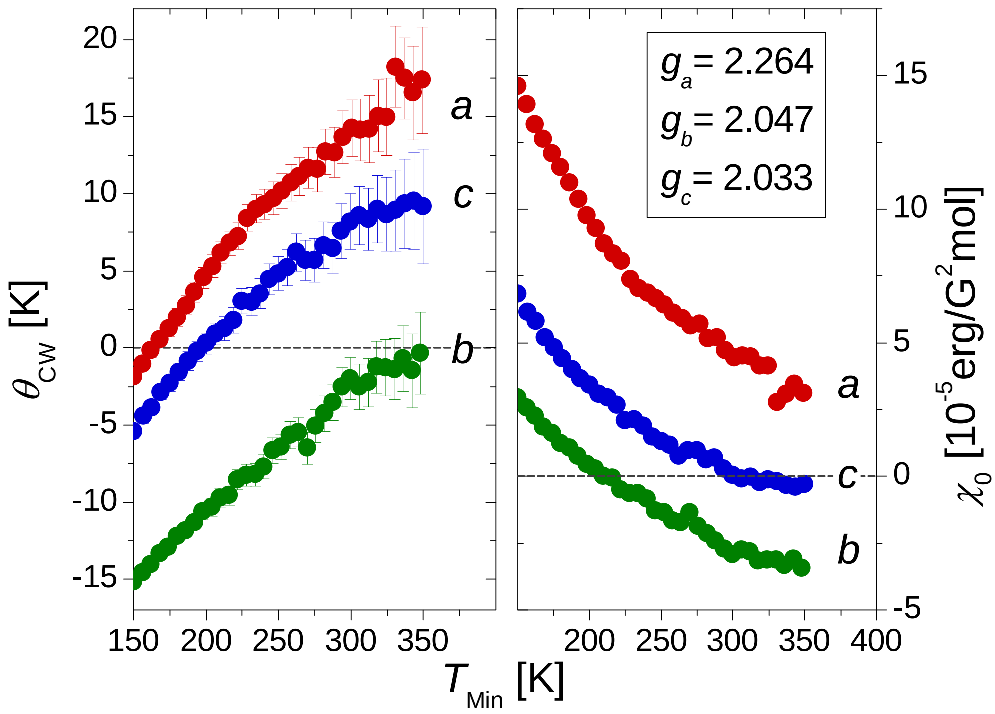

Figure 8.3.: Curie-Weiss-fits on single crystal $\chi(T)$ data for g-factors fixed to the ESR-values given in [115]. The abscissa labels the lower boundary of the fitted data range. The upper boundary is kept fixed at 380 K. The Curie-Weiss-temperature θ_{CW} is analyzed in dependently from χ_0 as described in the text.

Beyond Curie-Weiss

Analysis of magnetization data by the Curie-Weiss law can be expected to be meaningful only at temperatures well larger than the exchange energies involved. In the high-temperature expansion of the partition function for exchange coupled spin systems the Curie-Weiss law is just the leading term and, taking into account the full expansion, the susceptibility is expected to behave as [175–177]

$$\frac{\chi T}{C} = 1 + \frac{\theta_{CW}}{T} + \sum_n a_n \left(\frac{\theta_{CW}}{a_1 T}\right)^n \tag{8.2}$$

with the Curie constant C, the Curie-Weiss temperature θ_{CW} and parameters a_n which can in principle be calculated exactly on finite clusters. Nevertheless, with increasing n the calculations are computationally demanding and need approximation [176] in order to reach convergence (see e.g. [178]). Instead of calculating the high-temperature expansion in detail, one may adopt the finding that a simple power law – a so-called Generalized CURIE-WEISS-model – approximates the expansion well over a wide temperature range from about the ordering temperature up to the CURIE-WEISS regime [177, 179]. This approximation is found to describe the susceptibility well for particular spin systems, including e.g. body-centered cubic lattices with $S = 1/2$. Here the susceptibility is described as

$$\chi = \frac{C}{T}\left(\frac{T}{T - T^*}\right)^{\gamma^*} \tag{8.3}$$

with the CURIE-constant C, a generalized CURIE-WEISS temperature T^* and the correlated critical exponent γ^* (for more details see [179]). Eqn. 8.3 reduces to the CURIE-WEISS law for $\gamma^* = 1$.

Fitting $\chi(T)$ data of Li_2CuO_2 within the Generalized CURIE-WEISS-model does not enhance the quality of the fit. The exponent γ^* is found a stable fit parameter only if the fitted data set includes data at $T \lesssim 20\,\mathrm{K}$. The magnetic susceptibility for field applied along the easy axis is then fitted to scale as $\gamma_a^* = 1.25(2)$, while for the susceptibility of moments to field applied along the hard axes $\gamma_b^* = 1.17(2)$ and $\gamma_c^* = 1.15(2)$ are obtained. However, no value of γ^* – tested in the range $0.5 - 3$ – does allow to determine T^*, C and χ_0 independent of the temperature interval of the fitted data set even at temperatures $T > 300\,\mathrm{K}$. Explicit calculation of the high temperature expansion of Li_2CuO_2 would therefore be worthwhile.

Precise understanding of the magnetic susceptibility of the compound is still missing. Ebisu *et al.* analyzed their data on polycrystalline Li_2CuO_2 in a power series $\sum_i A_i T^{-i}$ assuming one effective antiferromagnetic exchange coupling. The description was found to be insufficient, which was attributed to a temperature dependence of the effective coupling.

Mizuno *et al.* calculated the susceptibility using the exact diagonalization method on clusters of 2×8 sites [20, 32]. It was shown, that the experimental data are well described at high temperatures by competing interactions along the chain and strongly influenced by antiferromagnetic inter-chain interactions. Only recently Plekhanov *et al.* reanalyzed the data by Mizuno *et al.* within the transfer matrix renormalization group (TMRG) method [180] [4]. Interestingly, this purely one-dimensional model is found to firstly describe the susceptibility of the compound very well for a broader temperature range. The main purpose of this study was to examine the influence of the anisotropy of the nearest-neighbor exchange path. It was found, that the data are best described by a frustration ratio $\alpha = 0.33$, well in accord to our INS results. However, the obtained anisotropy of the nearest-neighbor coupling $J_\perp/J_\parallel = 0.42$ appears not justified. Moreover, in Li_2CuO_2 the inter-chain coupling is clearly not a small, negligible perturbation of a predominantly one-dimensional system. As firstly shown by Mizuno *et al.* , inter-chain couplings significantly influence the susceptibility in Li_2CuO_2 and their neglect/regard in the analysis of the

---

[4] In [180] the data for $H \parallel b$ and $H \parallel c$ are mixed up.

susceptibility drastically changes the evaluated in-chain interactions [20, 32]. Drechsler *et al.* [181] point out, that treatment of the inter-chain interaction within the random phase approximation method on top of a TMRG treatment of *isotropic* intra-chain interactions provides an equally good description of the susceptibility. Notably, however, both TMRG studies demand g-factors somewhat lower than those obtained from the ESR-study by Kawamata *et al.* [115]. In particular, the g-factors for the hard b- and c-axis are required to be significantly lower than 2. It further remains unclear, on how to understand the slightly larger ESR g-factor for the c-axis, compared to the b-axis, along with the lower susceptibility of Li_2CuO_2 for magnetic fields applied along the b-axis. This is accounted for within TMRG by a g-factor $g_c \approx 1.85$ only, compared to $g_b \approx 1.92$.

The onset of long range order

The clear derivation of the magnetic susceptibility from the Curie-Weiss behavior, the low entropy at T_N and the large intra-chain exchange constants all point to pronounced magnetic correlations in Li_2CuO_2 at temperatures well above T_N. Ebisu *et al.* point out, that one-dimensional spin fluctuations may lead to a significant reduction of T_N compared to the size of the inter-chain couplings [123]. In contrast, Drechsler *et al.* [35] stress the fluctuations due to the vicinity of the 3-dimensional critical point separating helical and ferromagnetic ordering of the chains.

In this context, we present here further indication for an indeed broad critical regime of fluctuations above T_N. M. E. Fisher has pointed out that the anomaly at T_N in the magnetic specific heat of simple antiferromagnets is expected to behave similarly as $A \cdot \partial(\chi_\parallel T)/\partial T$, where $\chi_\parallel$ represents the susceptibility to magnetic field along the magnetic easy axis and A is a function slowly varying in temperature [182]. In Fig. 8.4 we show, that the two quantities indeed behave congruently in the vicinity of T_N, such that the maximum of $\partial(\chi_\parallel T)/\partial T$ can be used to extract T_N from χ-data.

Explicitly good agreement between the two data sets is found for a broad temperature regime above T_N under assumption of an empirical constant part of the $\partial(\chi_\parallel T)/\partial T$ not contributing to the specific heat. In contrast, below T_N the analogy of the two functions is present only within a narrow temperature range. This finding is also reproduced from the scaling behavior of the thermal expansion coefficient to the specific heat (cf. Section 10.2) and our analysis of the critical scaling behavior of c_p near T_N (cf. Section 9.2).

8.2. Magnetization $M(H)$

Klingeler [125] has presented a thorough study of the magnetic field dependence of the magnetization $M(H)$, based on which the easy axis magnetic phase diagram was developed. The results presented ibidem are extended here

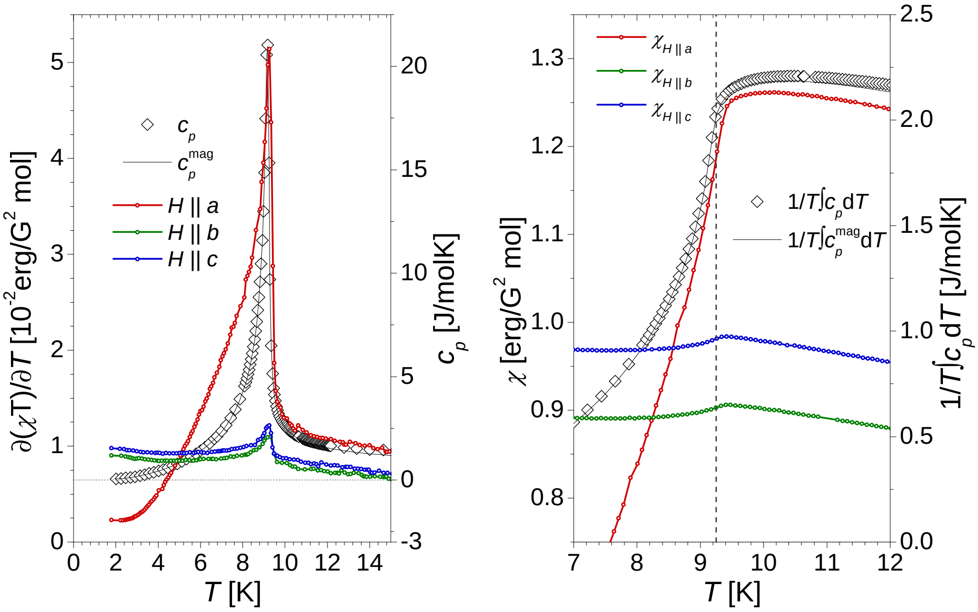

Figure 8.4.: (left) Fisher magnetic specific heat $\partial(\chi T)/\partial T$ compared to specific heat data c_p near T_N. The ordinates are scaled to highlight the great similarity of both quantities above T_N for the susceptibility $\chi_{H\|a}$. Note the sizable offset of the zero level of the ordinates. (Right) The equivalent representation of χ and $1/T \int c_p \mathrm{d}T$ with the identical offset as on the left stresses differences of both functions.

in respect to two interesting details. Firstly, Klingeler observed a significant deviation between the measured magnetization above the meta-magnetic transition and the expected behavior of a spin-flopped antiferromagnet. Specifically, the magnetization $M(H)$ in the high field phase is found to behave as $M(H) = \chi H + A$ where χ is a rather constant susceptibility and A a distinctively negative offset. Secondly, we further present here pulsed field magnetization data up to the saturation magnetization for both the easy and hard magnetic axes.

In Fig. 8.5 magnetization data $M(H_{\|a}, T = 2.1\,\mathrm{K})$ are shown, measured in an *Oxford VSM*. The data obtained indicate a different behavior of our sample compared to the one examined in [125] at the meta-magnetic transition. While the critical field $H_\mathrm{c} \approx 10\,\mathrm{T}$ at low temperatures is well comparable, both the magnetization above the critical field $M_{H_\mathrm{c}+}$ as well as the susceptibility $\chi_{H_\mathrm{c}+}$ are different. While in [125] $M_{H_\mathrm{c}+} \approx 0.21\,\mu_\mathrm{B}/\,\mathrm{f.u.}$ and $A \approx -0.07\,\mu_\mathrm{B}/\,\mathrm{f.u.}$ at $T = 2.5\,\mathrm{K}$, here we observe $M_{H_\mathrm{c}+} \approx 0.19\,\mu_\mathrm{B}/\,\mathrm{f.u.}$ and $A \approx -0.13\,\mu_\mathrm{B}/\,\mathrm{f.u.}$ at $T = 2.1\,\mathrm{K}$. From our pulsed field data (cf. Fig. 8.6), taken at $T \approx 1.45\,\mathrm{K}$ we again obtain $M_{H_\mathrm{c}+} \approx 0.19\,\mu_\mathrm{B}/\,\mathrm{f.u.}$, but an even larger offset $A \approx -0.19\,\mu_\mathrm{B}/\,\mathrm{f.u.}$. In accord to our magnetostriction data, $\partial M/\partial H$ shows a pronounced hysteresis near the maximal applied static field of 13.5 T.

The magnetization data obtained in pulsed magnetic field clearly indicate

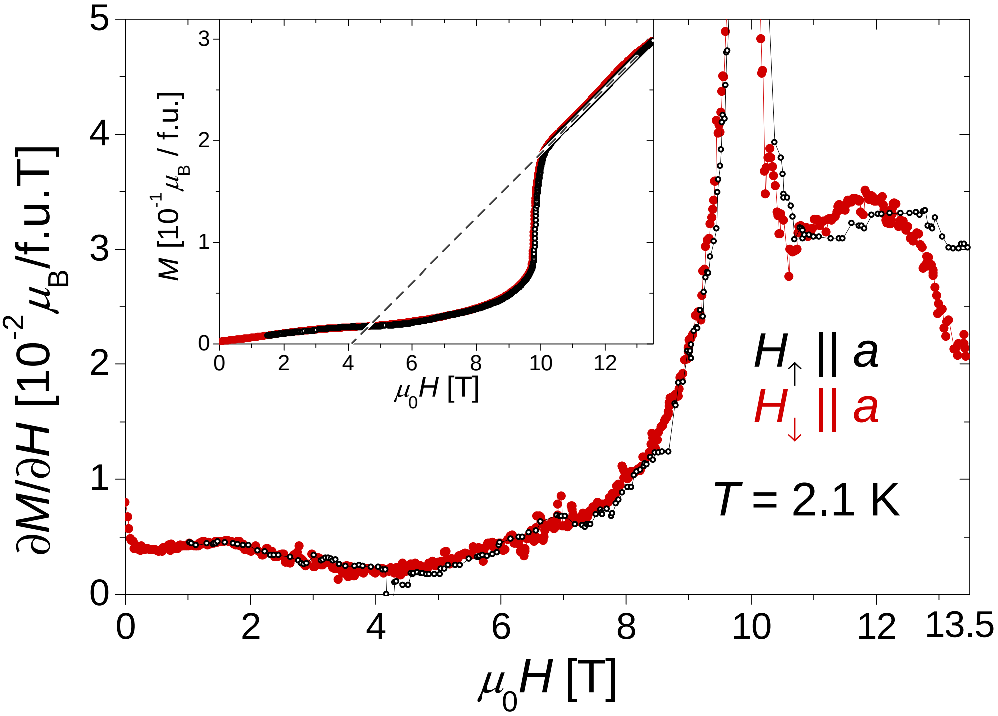

Figure 8.5.: Susceptibility $\partial M/\partial H$ for increasing and decreasing magnetic field applied along the easy a-axis at 2.1 K. Note the large hysteresis after reversal of the field sweep at 13.5 T. The inset shows the VSM magnetization data $M(H)$. The dashed line extrapolates the linear behavior of $M(H_\uparrow)$ between 11 and 13 T.

the presence of an intermediate magnetic phase in the range of $H_c \approx 10$ T to $H_{c2} \approx 13.5$ T at low temperature. At higher magnetic fields $H \parallel a$ Li_2CuO_2 enters a high field phase with clear characteristics of the classical spin flop phase where $M \propto H$ and $\chi \approx$ const.. The largely three-dimensional character of the compound in the ordered phase is particularly evident in the small value of the normalized magnetization $(M - M_{S\to\infty})/M_{sat}$ which is confined below 3% in the high-field/spin flop phase as well as for all fields applied along the hard b-axis (cf. Fig. 8.6 - here for clarity $-(M - M_{S\to\infty})/M_{sat}$ is shown below $H_{\parallel a} \leq H_c$). The absence of a transition at $H_{c2} < 16$ T in the data of Klingeler [125] along with the observation of a magnetization behavior different from a spin-flopped phase suggests a significantly enhanced H_{c2} in the respective sample.

The behavior of ferromagnetic-antiferromagnetic frustrated spin-chains in magnetic fields close to saturation field represents a topic of much current interest. The nearest-neighbor ferromagnetic coupling, which provides an attractive interaction for magnon excitations gives rise to a complex magnetic phase diagram. The excitations in the respective multipolar phases are well distinct bound states of magnons, while single magnon excitations are energet-

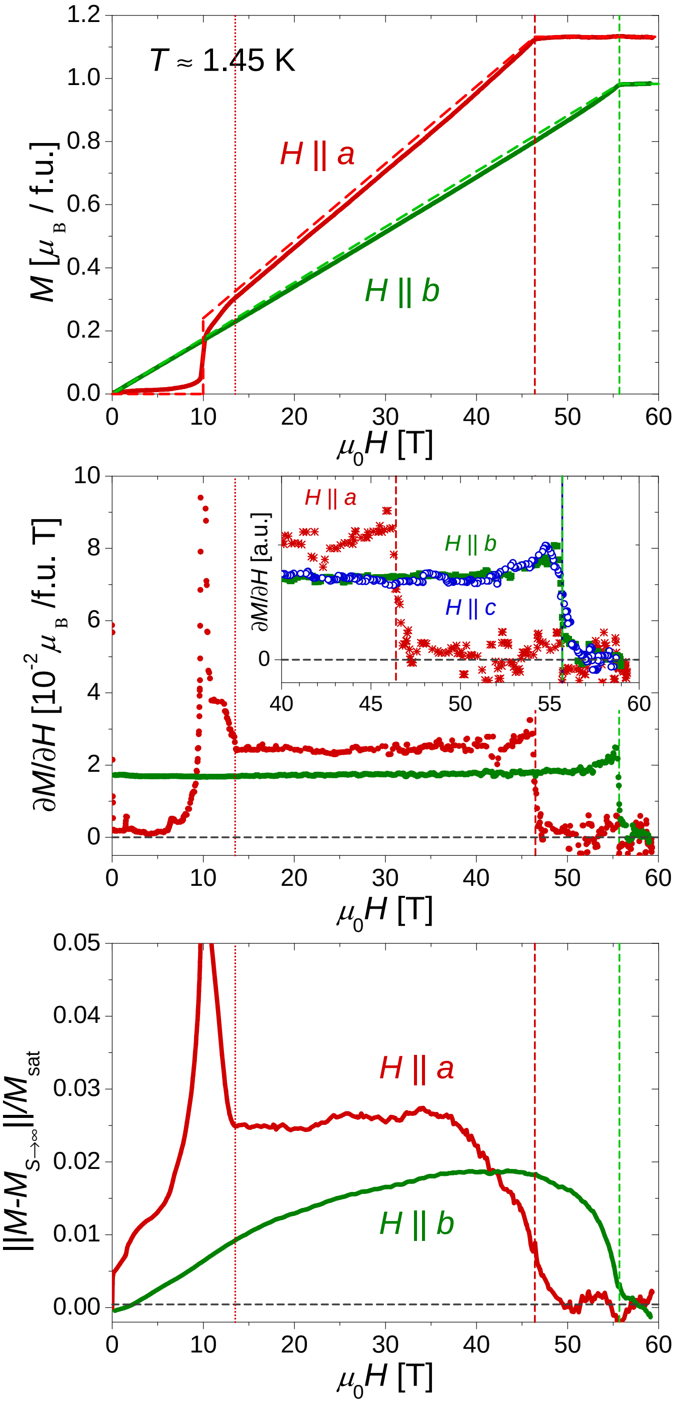

Figure 8.6: Data from pulsed field magnetization measurements for increasing field $H \parallel a$ (red), b (green) and c (blue) for $T = 1.45\,\mathrm{K}$ at $H = 0$.

(Top) Magnetization data $M(H)$, normalized as described on text. Thick dashed lines indicate the expected behavior of a classical easy axis antiferromagnet at $T = 0$.

(Middle) The susceptibility $\partial M/\partial H$ is largely constant for $H \parallel b$ and for $H \parallel a$ in the spin flop phase. The intermediate phase for $H \parallel a \lesssim 13.5\,\mathrm{T}$ is characterized an enhanced susceptibility. Inset: highlight of saturation field indicated by the sharp drop of $\partial M/\partial H$.

(Bottom) Difference of measured magnetization and classical behavior, as described in text. Fluctuations suppress the induced magnetization by less than 3%. At H_{sat}, the sample is not outright fully polarized.

ically disfavored. Much recent input to the properties of these phases has been provided from theoretical analysis on purely one-dimensional spin-chains by [88, 97, 183] and the notable study of the phase diagram by Sudan *et al.* [94]. In particular, it has been shown that for a frustration ratio as in $\mathrm{Li_2CuO_2}$ 3-magnon bound states are to be expected as the fundamental excitations in near saturation magnetic fields.

However, $\mathrm{Li_2CuO_2}$ is not a well one-dimensional magnetic system, but governed by significant inter-chain couplings. Nishimoto *et al.* have investigated in detail the influence of inter-chain couplings on the formation of multipolar phases [184]. In their study they apply spin-wave theory as well as the density matrix renormalization group method on coupled spin-chains. It is shown, that even small antiferromagnetic inter-chain couplings are sufficient to favor single magnon excitations and such to destroy multipolar phases. The applicability of the model is supported by a detailed study on $\mathrm{Li_2CuO_2}$ [145], including part of the data presented in Fig. 8.6. Here the dominant inter-chain interaction $J_{\mathrm{ic}} \equiv J_{131}$[5] couples each moment to $N_{\mathrm{ic}} = 8$ moments on neighboring chains. Under neglect of exchange anisotropy it was shown rigorously, that for $\mathrm{Li_2CuO_2}$, where $\alpha \approx 1/3$ and $J_{131} = 9.0(1)\,\mathrm{K}$ larger than a critical value $J_{\mathrm{ic},2} = 8.21\,\mathrm{K}$, the saturation field is solemnly determined by the inter-sublattice inter-chain coupling. A multipolar phase of 3-magnon states is suppressed already for a weak inter-chain coupling $\geqq J_{\mathrm{ic},1} = 2.49\,\mathrm{K}$. In this particular situation, spin-wave theory provides as an exact result at $T = 0$

$$g\,\mu_{\mathrm{B}} H_{\mathrm{sat}} = N_{\mathrm{ic}} J_{\mathrm{ic}}. \tag{8.4}$$

Below, this prediction is compared to an experimental study of H_{sat} in $\mathrm{Li_2CuO_2}$.

The magnetization of $\mathrm{Li_2CuO_2}$ was measured in pulsed magnetic field up to the 60 T. The peak magnetic field is reached after 7 ms. In the deployed measurement setup, the magnetization of the sample is detected via the induced voltage in a pick-up coil system. In order to obtain magnetization data for magnetic field applied along the hard b-axis at $T \approx 1.45\,\mathrm{K}$, the signal is normalized to static field SQUID data at 7 T. The weak temperature dependence of $\chi_{H\|b}$ allows to approximate the magnetization $T = 1.45\,\mathrm{K}$ from the data taken at $T \geq 1.8\,\mathrm{K}$. This way, a saturation magnetization $M_{\mathrm{sat},H\|b} = 0.98\,\mu_{\mathrm{B}}/\,\mathrm{f.u.}$ is obtained. For Cu^{2+} a g-factor $g \geq 2$ is to be expected. The determined slightly lower saturation magnetization indicates experimental errors. For the pulsed field data taken along the easy a-axis, the strong temperature dependence of the susceptibility does not permit normalization to static field data. Here, the data are normalized to the g-factor $g_a = 2.264$ from ESR-data [115] above H_{sat}. For the data set taken with $H \parallel c$, normalization of the signal is omitted due to insufficient quality of the obtained background data.

In the data, magnetic saturation is indicated by the observation of a typical slight increase of the susceptibility $\partial M/\partial H$ at high field, preceding its

---

[5] Within linear spin-wave theory, only inter-sublattice couplings are to be considered, intra-sublattice couplings as e.g. J_{100} do not contribute to H_{sat}.

rapid suppression at even higher field. The drop of $\partial M/\partial H$ is as narrow as $\approx 1\,\mathrm{T}$. Here, the saturation field is assigned at the field corresponding to half the height of the drop of the susceptibility, which can also be determined for $H \parallel c$. Accordingly, $H_{\mathrm{sat},\parallel a} = 46.4(1)\,\mathrm{T}$ and $H_{\mathrm{sat},\parallel b} \simeq H_{\mathrm{sat},\parallel c} = 55.7(1)\,\mathrm{T}$ are obtained. Eqn. 8.4 predicts with the inter-chain coupling J_{131} obtained from inelastic neutron scattering and g-factors from ESR by Kawamata *et al.* [115] $H_{\mathrm{sat},\parallel a} = 47.3\,\mathrm{T}$, $H_{\mathrm{sat},\parallel b} = 52.4\,\mathrm{T}$ and $H_{\mathrm{sat},\parallel c} = 52.7\,\mathrm{T}$. The overestimation of $H_{\mathrm{sat},\parallel a}$ along with the underestimation of $H_{\mathrm{sat},\perp a}$ suggests a non-negligible influence of the easy axis anisotropy on the saturation field in $\mathrm{Li_2CuO_2}$. Two further restrictions are called to attention. Firstly, the antiferromagnetic inter-chain coupling competes with ferromagnetic spin alignment. Strong magnetic field can thus be expected to cause magnetostrictive expansion of the inter-chain distances, which goes along with reduction of the inter-chain couplings. This is indicated already in weak fields $H = 16\,\mathrm{T}$ (cf. Section 10.3.2). Secondly and more importantly, Eqn. 8.4 applies to $T = 0$ only. The experimentally determined saturation field is thus to be expected systematically too low. Moreover, in pulsed magnetic field, the experiment does not take place isothermally, but quasi-adiabatically, as a consequence of insufficient coupling of the sample to the thermal bath. The precise temperature of the sample in high fields is thus unknown and may even differ for the magnetic and crystallographic subsystem. The notable deviation of the isentropic lines from the isothermal ones for $H_{\parallel a} < 14\,\mathrm{T}$ is depicted in the magnetic phase diagram in Fig. 9.4.

Nevertheless, the overall agreement of H_{sat} in experiment and from predictions by Eqn. 8.4 is indeed good. More precisely, the inter-chain coupling I_{131} as derived from the magnetization data at the saturation field deviates by as little as 6% for the hard axes and even less for the easy axis from the value obtained from our inelastic neutron scattering data measured at ambient field. Thence, the study of H_{sat} represents a promising method to determine the inter-chain couplings in related compounds [145]. Its particular strength is to provide results unbiased by probable strong spin fluctuations in the zero field state.

9. Analysis of the magnetic specific heat

Motivated by the observations of large thermal expansion anomalies observed for Li_2CuO_2 throughout the magnetic phase diagram (cf. Chapter 10) a complementary study of the specific heat $c_{p,H}(T)$ in magnetic field $H \parallel a$ has been undertaken[1]. The data provide further insight into the evolution of ordering phenomena. Moreover, the detail about the relevant excitations at low temperatures can be obtained. Access to the entropy as a state variable is provided.

The data presented in this chapter on the specific heat of Li_2CuO_2 have been measured in magnetic fields up to 13.9 T applied along the easy a-axis (field cooled from above T_N) between 2 and 15 K using standard PPMS equipment. The main features in the data obtained may be in summarized as follows. The onset of long range magnetic order at T_N is accompanied by sizable λ-anomalies subsiding in larger fields. At high field $\mu_0 H > 10\,\mathrm{T}$ the transition at H_c is observed and the size of the anomaly increases with increasing external magnetic field. The anomaly at H_c shows an irregular line shape, which may be caused first order nature transition below $H_{c2} \approx 13\,\mathrm{T}$ and are thus not precisely accessible by the PPMS thermal relaxation method. However, at 13.9 T, where thermal expansion measurements indicate H_c to be of second order the specific heat data display a λ-like shape. The data taken at 10 T and low temperature express a broad hump around 3 K. This anomaly appears to be related to fluctuation in field just below H_c. As realized before by Chung *et al.* [112] no signature of $T_2 \approx 2.6\,\mathrm{K}$ is found in the $H = 0$ data.

In this chapter, a descriptive discussion of the data at $H = 0$ is given at first: an approximate phonon specific heat is modelled in Section 9.1 showing that below T_N the specific heat is strongly dominated by magnetic contributions. The evolution of long range order at T_N is discussed in Section 9.2. More qualitative analysis is given in the subsequent sections. In Section 9.3 the temperature and magnetic field dependence of the entropy is discussed. Eventually, in Section 9.4 the data are analyzed within a model of thermal magnon excitations. It is found, that magnons cannot account for the observed low temperature specific heat.

---

[1] The specific heat $c_{p,H_{\parallel a}}$ has been studied before, with however largely inconclusive results [185].

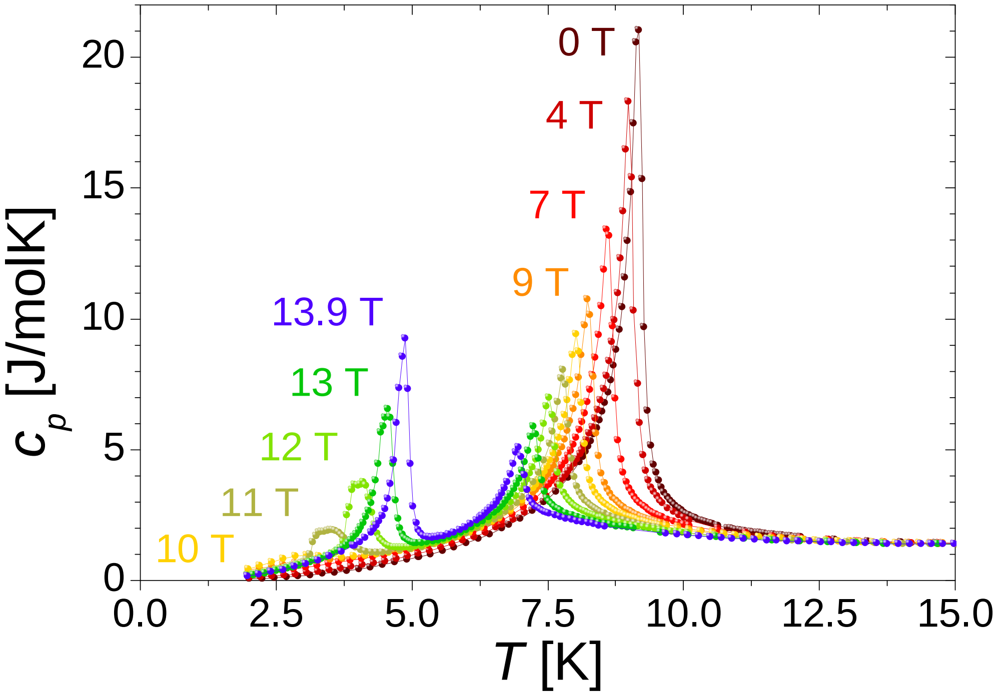

Figure 9.1.: Magnetic field dependence of the specific heat of Li_2CuO_2 for $H \parallel a$ (easy axis). At the phase boundaries T_N as as well as H_c in high field a significant change of the entropy of the system is observed.

9.1. Estimate of phononic specific heat

In order to approximate the lattice contributions to the specific heat and thus to segregate the magnetic specific heat a Debye model is adjusted to the zero field data measured up to 100 K. The Debye model can be considered a reasonable approximation at low temperatures only, such that the dispersion of the thermally excited phonons is largely linear and optical phonons are not excited. The phonon dispersion of Li_2CuO_2 has not yet been studied. Our thermal inelastic neutron scattering data (cf. Fig. 5.3)indicate acoustic phonons to be located near the crystallographic zone center even at 25 meV. Further contributions to the phonon specific heat of type of the Einstein model are not included into the model[2]. Then, the specific heat of Li_2CuO_2 at reasonably low temperatures can be written as

$$c_p(T,H) \approx c_p^{mag}(T,H) + \underbrace{c_p^{ph}(T)}_{\approx c_p^{\mathrm{D}}(T)} + \underbrace{c_p^{el}(T)}_{\approx 0} \tag{9.1}$$

$$c_p^{\mathrm{D}}(T) = 9 n_{\mathrm{eff}} k_{\mathrm{B}} \left(\frac{T}{\theta_{\mathrm{D}}}\right)^3 \int_0^{\theta_{\mathrm{D}}/T} \frac{x^4 e^x}{(e^x-1)^2} \mathrm{d}x. \tag{9.2}$$

---

[2] Including the optical phonon mode at ≈ 19 meV as indicated by thermal inelastic neutron scattering (cf. Fig. 5.2) in the model does not enhance the description of the c_p-data.

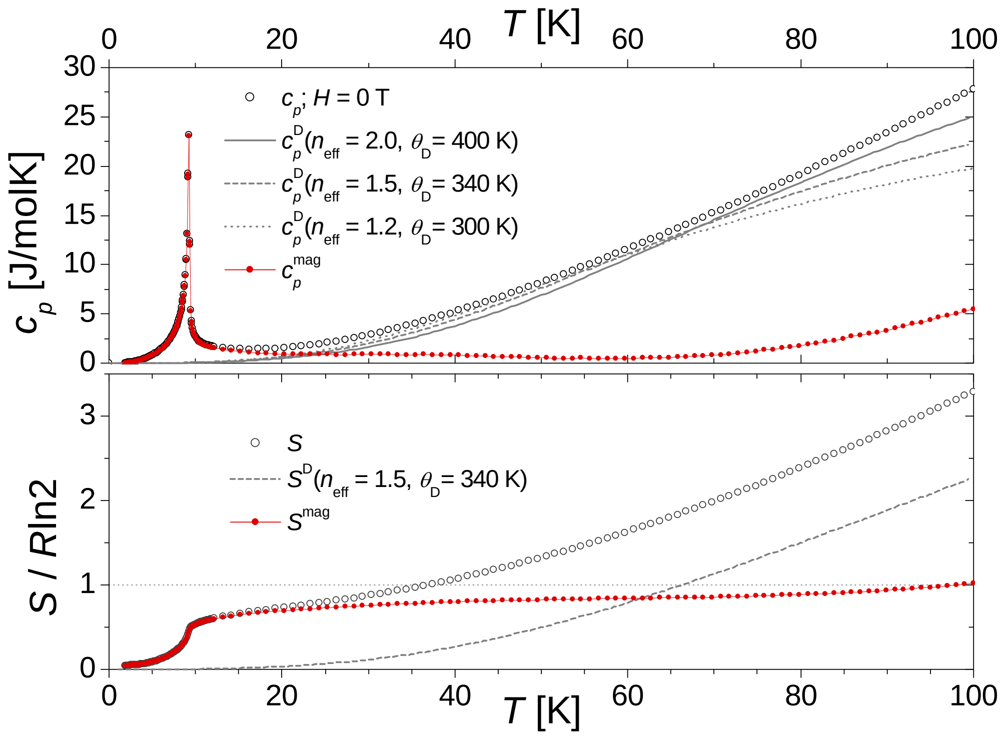

Figure 9.2.: (Top): Specific heat of Li_2CuO_2 in zero field up to 100 K (circles) compared with a set of DEBYE functions (lines). Red spheres denote the resulting magnetic specific heat after subtraction of c_p^D with $\theta_D = 340$ K and $n_{eff} = 1.5$ (dashed line). (Bottom): Magnetic entropy (red spheres) in zero field compared to the phonon (line) and total entropy (circles) as discussed in Chapter 9.3

.

With the introduction of a reduced efficient number of atoms in the basic unit cell $n_{eff} \leq n$, where $n = 5$ for Li_2CuO_2, the DEBYE phononic specific heat depends on two parameters. Indeed, the specific heat data on Li_2CuO_2 - a material not markedly hard - obtained here cannot be described with $\theta_D < 600$ K for $n_{eff} = 5$. In literature, $\theta_D = 440$ K with $n_{eff} = 2$ has been proposed [116]. A detailed discussion is given by Ebisu *et al.* on data up to 80 K [123]. There, $\theta_D = 567, 444, 350$ K for $n_{eff} = 5, 3, 2$ are derived adjusting θ_D to the specific heat at $T = 80$ K. A probably temperature dependent θ_D is suggested. The data below 30 K have been analyzed with an independent method and yield $\theta_D = 436, 368, 321$ K for $n_{eff} = 5, 3, 2$.

The analysis given here (cf. Fig. 9.2) is based on the discussion by Ebisu *et al.* , but the results differ for a variety of reasons. Firstly, while both data sets show a very similar T_N (9.3 K in [123], here 9.2 K) they deviate at high T (c_p(80 K) = 22 J/molK in [123], here 19.3 J/molK) and consequently θ_D is larger here for the same n_{eff}. Secondly, the DEBYE model is not adjusted to coincide with c_p at the highest temperatures. Instead, it is adjusted to describe a broad temperature range well, but is allowed to fail at higher temperatures, where an increase of n_{eff}, a reduction of θ_D and non-Debye behavior are to be expected. Finally, also curves with $n_{\text{eff}} < 2$ are considered here. As a matter of course, the parameters of the model are demanded to leave the corresponding magnetic entropy $S^{\text{mag}} < R \ln 2$. A number of curves is given in Fig. 9.2. Selecting a parameter set is nevertheless based on qualitative measures only.

In this sense $\theta_D = 340\,\text{K}$ and $n_{\text{eff}} = 1.5$ provides a reasonable, yet restricted description of the magnetic specific heat and entropy up to the highest temperatures accessible to the model. For the chosen parameter set the magnetic entropy is not saturated even at 60 K with uncertainty of the value at lowest T but continuously increasing, reflecting the non-vanishing magnetic correlations up to high temperatures qualitatively. A broad anomaly in the residual magnetic specific heat is observed around 40 K, already noticed by Ebisu *et al.* (cf. Fig. 9.3 (bottom)). The height of this anomaly is strongly correlated to the selected n_{eff} but cannot be suppressed in the model for $n_{\text{eff}} \geq 1$. It is not clear, whether the anomaly is of magnetic origin or an artefact of an inappropriate lattice specific heat estimate. It is noted, that this anomaly has no correspondence in susceptibility data. Above 60 K further contributions dominate the specific heat. In contrary, below 10 K Debye contributions to both c_p and S are found to be merely negligible. Nevertheless, with the known large thermal expansion anomalies at T_N the phononic specific heat is unlikely to be purely Debye-like in the vicinity of the ordering temperature. Below T_N, the magnetic specific heat is used in the next section Section 9.2 and in Section 9.4. While in Section 9.4 the data are analyzed in the low temperature range with only weak phononic specific heat, the discussion of features well above T_N in the next section is restricted by the accuracy of the estimate of the phononic specific heat.

9.2. Fluctuations, correlations near T_N

The specific heat measures the temperature dependence of the entropy of a system, i.e. the temperature induced change of the number of states the system can assume. This number of states is reduced as its compartments are correlated. The magnetic specific heat is therefore a measure of the temperature dependence of magnetic correlations. For Li_2CuO_2, two sorts of correlations are of particular interest. Firstly, the large exchange interactions along the chain will stabilize intra-chain magnetic correlations even far above the ordering temperature. The temperature dependence of the correlations and correlation lengths is complicated by the frustration of the interactions. Secondly, Li_2CuO_2 is not a highly one-dimensional system and correlations of spins on neighboring chains may be present at temperatures significantly larger than the critical fluctuation regime connected to long range order. The evolution of inter-chain correlations in Li_2CuO_2 is particularly remarkable as the ordered state suppresses the non-collinear intra-chain correlations which are to be expected from the frustration ratio. The magnetic correlations in

Li_2CuO_2 are hence an interesting topic, both at high temperatures as well as at the ordering temperature. In order to study the temperature dependence of the correlations, we adopt the approach for the analysis of critical fluctuations from the line shape of the specific heat anomaly at the ordering temperature given in [186]. Below, both the critical and non-critical behavior are attempted to be addressed by fitting exponentially decaying specific heat contributions for different temperature regimes near the second order phase transition at T_N.

In second order phase transitions the second derivative of the free energy shows a jump or divergence. In the mean-field LANDAU theory of continuous phase transitions, the specific heat - representative for the second derivative of the free energy with respect to temperature - displays a jump at the ordering temperature. Nevertheless, in experiment often not jumps but so-called λ-anomalies are observed resulting from fluctuations neglected in LANDAU's approach. These are taken into account within renormalization-group theory, predicting all temperature driven second order phase transitions to fall into a few classes with a universal critical behavior [187]. Within theory, the critical behavior is purely determined by the dimensionality of the system and the number of degrees of freedom of its constituents. In addition to the above classes with commensurate ordered states, the so-called chiral universality classes have been introduced by Kawamura [188, 189] to apply to e.g. 2-dimensional triangular magnets and 3-dimensional canted and helical magnetic systems. A rather broad set of theoretically and experimentally derived scaling parameters for the different universality classes is given in the extensive review article [190].

The validity of the categorization provided by the standard universality classes for phase transitions in real material is nevertheless questionable. On one hand, the universality classes describe idealized, pure spin systems without spin-lattice interactions or impurities. One the other hand, the temperature range in which the observed fluctuations are indeed the critical fluctuations of the phase transition should not be easy to define. As shown below, we find for Li_2CuO_2, that the possible critical regime is very narrow. In particular, the magnetic specific heat above T_N is clearly dominated by non-critical contributions. In this sense, the results provided below are not to be considered as a study of critical fluctuations, but merely a study of the temperature dependence of the specific heat near T_N. The model function used to describe the specific heat anomaly at T_N is given by

$$\begin{aligned} c_p^{\mathrm{mag}}(T)^{\pm} &= \frac{A_<^{\pm}}{\alpha_<}\left|\frac{T}{T_\mathrm{c}}-1\right|^{-\alpha_<} + N_< \\ &+ \frac{A_>^{\pm}}{\alpha_>}\left|\frac{T}{T_\mathrm{c}}-1\right|^{-\alpha_>} + N_> \qquad (9.3) \end{aligned}$$

where $c_p(T)^{\pm}$ and $A^{\pm}$ distinguish the magnetic specific heat c_p and a proportionality parameter A above and below the transition at T_c. In the small temperature range where fluctuations dominate the specific heat, any further

Table 9.1.: Fit parameters of scaling behavior of the separated magnetic specific heat near $T_\mathrm{N}(H = 0) = 9.200(5)\,\mathrm{K}$ for different fitted data subsets. For comparison, a fit of the total specific heat for one subset is given in the last line. While the quality of the fit and the derived parameters are in rather good agreement, the model does not allow for fitting a broader temperature range below T_N.

fit range [K]	data points	σ [K]	$N_<$ [J/molK]	$A^-_<$ [J/mol]	$\alpha_<$	$A^+_>$ [J/mol]	$\alpha_>$
9.0 – 9.5	9	0.0460	54.87	12.1	−0.159	0.410	0.448
8.8 – 9.6	16	0.0462	54.28	11.5	−0.156	0.385	0.477
8.7 – 10.0	25	0.0446	70.27	9.62	−0.111	0.395	0.441
8.6 – 12.0	63	0.0461	77.80	8.62	−0.094	0.394	0.450
8.7 – 10.0	25	0.0445	62.48	10.3	−0.129	0.404	0.436

contributions are approximated here by a constant background N. The scaling parameter α is shown to be identical above and below the transition within renormalization-group theory. Nevertheless, no reasonable description of the data was possible for a single α only. Therefore, the model Eqn. 9.3 implements $\alpha_<$ and $\alpha_>$ to dominate the fluctuations below and above T_N, respectively. While $A^+_<$ and $A^-_>$ were introduced to describe an overlap of the two fluctuation regimes at T_N, both are about vanishing in the fitting procedure, i.e. the parameters describing c_p^- and c_p^+ are merely independent. Furthermore, the background term $N_>$ vanishes for the positive[3] value of $\alpha_>$. In order to attribute for the absent singularity of Eqn. 9.3 at T_c in the measured data, a GAUSSian broadening of the transition due to sample inhomogeneities introduces a further fit parameter σ. Altogether, 7 parameters are used to describe the c_p-anomaly: T_c, σ, $A^-_<$, $N_<$, $\alpha_<$, $A^+_>$ and $\alpha_>$.

The large number of parameters of the applied model compared to the density of measured data points allows for fits over a rather broad temperature range only. Fit results for the transition at T_N at $H = 0$ are presented in Tab. 9.1 for different selected data set ranges, the best fit to the data is plotted in Fig. 9.3. Below T_N, the specific heat anomaly is found to be describable by the exponential behavior assumed of the model only very close by the ordering temperature ($\Delta T \leq 0.6\,\mathrm{K}$). Contrary, the magnetic specific heat above T_N indeed falls of exponentially in a very broad temperature regime. The agreement between fit functions obtained below e.g. 10 K and the magnetic specific heat is rather good even at 25 K. Note again, that above T_N the uncertainty of the lattice specific heat imposes an error on the deduced magnetic specific heat being increasingly large with increasing temperature.

The narrow temperature regime with described by the model below T_N suggests that the specific heat may be considered as dominated by critical

---

[3] For negative α, N denotes the finite height of the anomaly.

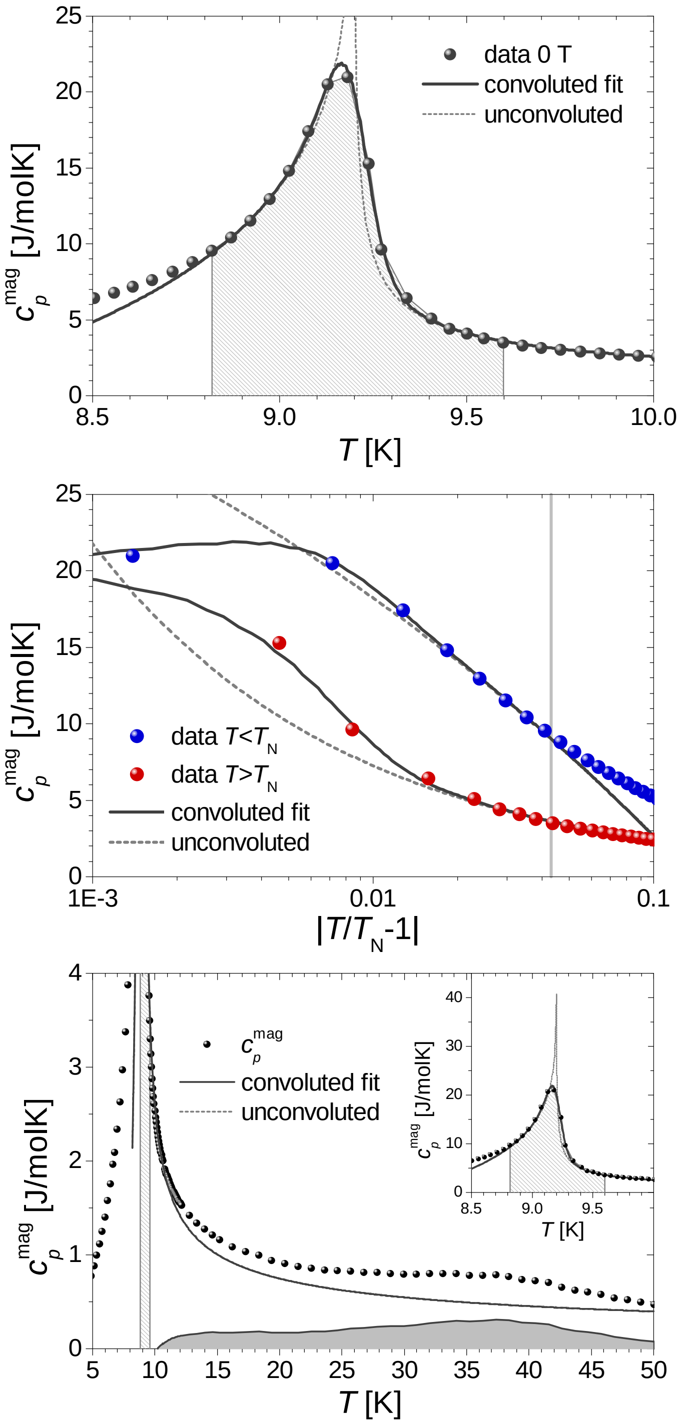

Figure 9.3: Fit of the magnetic specific heat near the NÉEL temperature in zero external field, for details see text: (Top) Data are represented by spheres, the fitted data region is shaded and the fitted curve is given as a straight line, compared with the non-convoluted model of Eqn. 9.3.
(Middle) Same fit as above on a semi-logarithmic scale. Here, the low T boundary of the fitted data set is represented by the vertical solid line
(Bottom) Details of the fitted model: the fit describes only a narrow region of the data below T_N while comparing well with the data at temperatures far above the fitted data range. The specific heat anomaly at $\approx$ 40 K is stressed and separately plotted as difference between data and model. The inset compares the convoluted with the non-convoluted model.

fluctuations. Presuming universal scaling behavior, the obtained exponent $\alpha_< = -0.15(5)$ suggests to characterize the transition as the ordering of a system with $n = 3$ internal degrees of freedom[4]. Note that for easy-axis antiferromagnets $n = 1$ (Ising symmetry class) with $\alpha_<(\mathrm{1D}) \approx +0.110(5)$ [190] is expected as fluctuations perpendicular to the the easy axis are not critical [191]. However, a fit with $\alpha_<(\mathrm{1D})$ - although somewhat able to reproduce c_p^- - would demand a non-physical, large negative specific heat background $N_<$. It this point, it remains an open question, if the determined exponent indeed provides information about the nature of the transition or if the anomaly in c_p is different from universal behavior e.g. due to disorder in the sample.

Above T_N, a scaling parameter $\alpha_> = 0.45(4)$ is determined, which is distinctly larger than the values of the collinear universality classes, however comparable to that of the chiral universality classes. Yet, the specific heat anomaly above T_N is clearly less directly related to the transition. The fits are in agreement with a divergence of c_p at T_N, but the wide overlap of the model and the magnetic specific heat suggests to consider a considerable interdependence of the short range intra-chains correlations and long order at T_N. Nevertheless, a detailed analysis of the short range order above T_N must be relinquished, especially because the separation of magnetic and lattice specific heat is quantitatively not reliable[5].

9.3. Entropy

By definition, the specific heat c_p is a direct measure of entropy changes of the system. However, the total entropy S of the system is not accessible from c_p, as within

$$S(T) = \int_0^T \frac{c_p(\tau)}{\tau} \mathrm{d}\tau + S_0 \tag{9.4}$$

one is in experiment unable to detect two relevant information. Firstly, the ground state entropy S_0 can be obtained only theoretically. Secondly, any analysis is restricted to estimates of the specific heat behavior below T^min, the lowest accessible temperatures. Here, we use

$$S(T) = \sum_{i=1}^{N(T)-1} \frac{c_p\left(T(i+1)\right) + c_p\left(T(i)\right)}{2} \left(T(i+1) - T(i)\right) + S^\mathrm{min} \tag{9.5}$$

where the sum over $N(T)$ data points i with $T(i) \leqq T$ approximates the integral. S^min is selected such, that the extrapolated entropy at $T = 0$ remains positive. While for the zero field measurement the extrapolation of the c_p data towards $T = 0$ will cause a systematic error in $S(T, H = 0) - S_0$, the

---

[4] For Heisenberg-like systems in 3 dimensions $\alpha \approx -0.12$ [190].

[5] This uncertainty is reflected in comparison with the analysis by Okuda *et al.* [116] suggesting a T^{-2} behavior below 30 K.

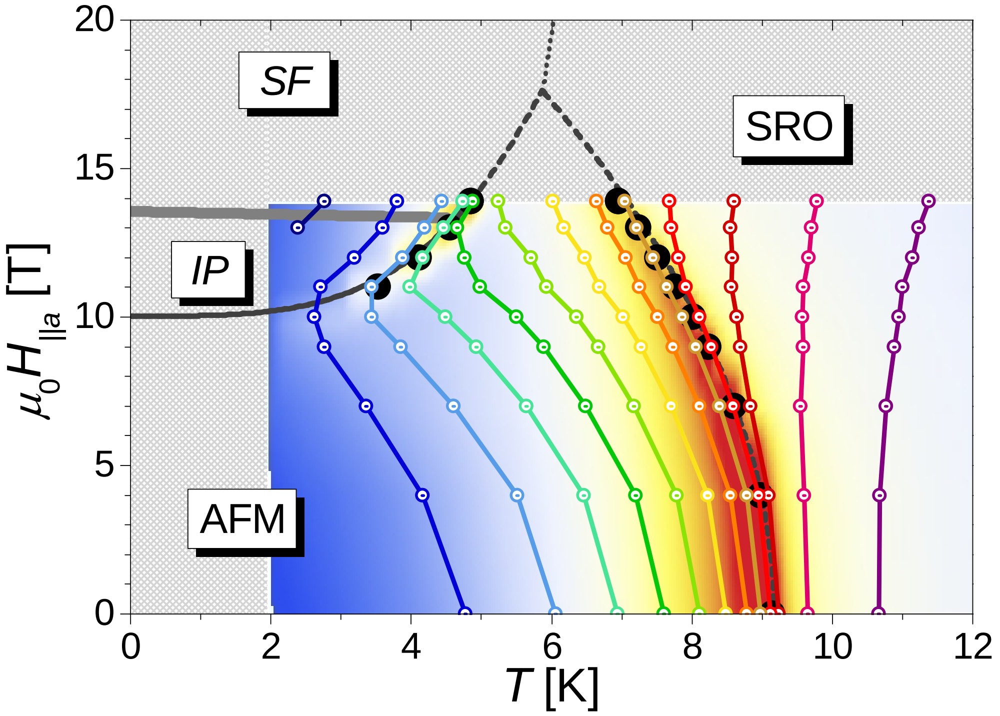

Figure 9.4.: The main features of the specific heat measurements in external field $H \parallel a$ are projected on the magnetic phase diagram (described in Chapter 7). The background color map is interpolated from the $c_{p,H}$ data presented in Fig. 9.1. Phase transitions monitored by c_p anomalies are shown by black spheres. Overlayed lines ($\odot$) denote the isentropes $S(T, H) =$ const. of the system in steps of 0.25 J/molK. Note that the lowest entropy is observed only in the largest fields for the examined temperatures and is notably higher in zero field. In the intermediate phase (IP) at $11 - 13$ T the entropy may be overestimated.

relative shift $\Delta S_T(H)$ of the entropy with applied magnetic field H can be worked out. With the set of thermodynamic data available, we can make use of a Maxwell-relation to determine the isothermal change of entropy in magnetic field without need to measure it. For any thermodynamic system under conditions of Gibbs Free Energy (cf. Section 3.1) the entropy S and the magnetic moment m are related as

$$\left(\frac{\partial S}{\mu_0 \partial H}\right)_{T,p} = \left(\frac{\partial m}{\partial T}\right)_{H,p} . \tag{9.6}$$

From our data of $\partial m/\partial T$ (see Fig. 9.5) it is found that at a temperature $T = 15$ K one can read off a constant shift $1/(\mu_0 H)\partial m/\partial T = -1.65(1)$ mJ/molKT^2 up to fields of 7 T. In comparison, the data of Klingeler on a different sample are also shown [125][6], displaying $1/(\mu_0 H)\partial m/\partial T =$ const. - slightly reduced

---

[6] The slightly lower $1/(\mu_0 H)\partial m/\partial T = -1.51(1)$ mJ/molKT^2 at $T = 15$ K is considered a

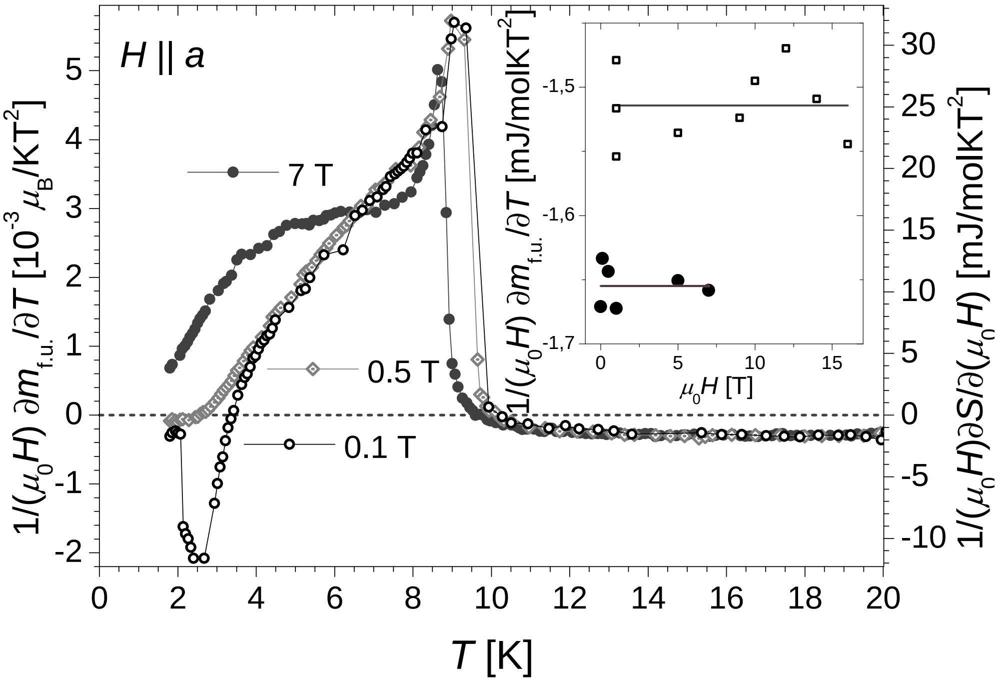

Figure 9.5.: The relative change of the entropy at constant temperature and applied magnetic field $H \parallel a$ can be accessed well at 15 K, where $1/(\mu_0 H)\left(\frac{\partial m}{\partial T}\right)_{H,p} \approx$ const. in the field range of interest. The data at 0.1 T clearly show, that although c_p in zero field shows no anomaly at $T_2 = 2.6\,$K, a significant change should be observed in weak external fields. In the inset, our $1/(\mu_0 H)\left(\frac{\partial m}{\partial T}\right)_{H,p,T=15\,\mathrm{K}}$ data (●) are compared to results from [125] (□).

compared to our result, but rather constant up to 16 T . For further discussion the value obtained from our sample is used and considered constant up to 13.9 T at 15 K [7]. Then, with

$$(S(H) - S(H=0))_{p,T} = \int_0^H \mathrm{d}H' \left(\frac{\partial S}{\partial H'}\right)_{p,T=15K,\forall H'} = -\frac{1.65\mathrm{mJ}}{\mathrm{molKT}^2}\frac{(\mu_0 H)^2}{2} \tag{9.7}$$

the calculated entropies of all measured $c_p(H)$ can be normalized to the data at $H = 0$. For paramagnets $S(H) \propto -(H/T)^2$ for low H/T and the next term in the expansion around $H = 0$ is proportional to $+(H/T)^4$. All $S(T,H)$ curves together, shown in Fig. 9.6, display several interesting properties of the entropy. Note, that here the total entropy without any subtracted phonon contribution is discussed. Above the NÉEL temperature the entropy is steadily reduced by external fields, but upon entering the long range ordered state the curves cut at temperatures where $\partial m/\partial T = 0$.

---

consequence of the lower $T_N = 8.5\,$K in [125].

[7] $M(H)$ data at 15 K (not shown here) indicate a reduction of $\partial M/\partial H$ by less then 10% below 14 T.

Just below T_N, external magnetic fields increase the entropy as the antiferromagnetic ground state is destabilized. In contrast, at low temperature and high fields the entropy is reduced upon crossing the meta-magnetic phase transition H_c. As a consequence of the measurement method, the specific heat changes related to the 1st order transition at H_c (in the data sets taken at 11, 12, 13 T) may be underestimated. However, the entropy changes at H_c appear reasonable. An estimate is provided using the Clausius-Clapeyron relation

$$\frac{\mathrm{d}T_\mathrm{c}}{\mathrm{d}B} = \frac{\Delta M}{\Delta S}. \tag{9.8}$$

From the magnetic phase diagram by R. Klingeler [125] obtained from magnetization data one reads off $\frac{\mathrm{d}T_\mathrm{c}}{\mathrm{d}B} = 0.464\,\mathrm{K/T}$ at $(H_\mathrm{c}, T_\mathrm{c}) = (12\,\mathrm{T}, 4\,\mathrm{K})$ and $\Delta M = 0.038(5)\,\mu_\mathrm{B}/\mathrm{f.u.}$, i.e. $\Delta S = 0.46(6)$ J/molK. From our specific heat data the corresponding anomaly evaluates to $\Delta S = 0.45(3)$ J/molK [8].

At the lowest temperatures $T = 2\,\mathrm{K}$, the entropy depends sizeably on magnetic field. On one hand, it decreases for $H > H_\mathrm{c}$. On the other hand however, the data taken at zero field show no tendency to approach similarly low values. As is discussed in Section 9.4, the specific heat data indicate the presence of low lying excitations gapped by only $1.6 \pm 0.3\,\mathrm{K}$ in zero field. Corresponding states should still be well populated at 2 K. Considering the rather large magnetic entropy $S(T = 2\,\mathrm{K}, H = 0)$, a sizable anomaly in c_p/T must exist below 2 K and $H < H_\mathrm{c}$ according to Nernst's law.

Already at 2 K a qualitative change of $S(H)$ is indicated. As mentioned above, $S(H)$ generally increases with field in the antiferromagnetic state. Although the available data are limited to temperatures $T \geq 2\,\mathrm{K}$, extrapolation towards lower T suggests a decrease of the entropy in external magnetic field. Note that the negative $\partial\mu/\partial T$ at lowest T and low fields (cf. Fig. 9.5) points for such effect already at higher temperatures.

Finally, the knowledge of the relative change of entropy from specific heat data also allows to construct the isentropes $S(T, H) = \mathrm{const.}$, depicted in Fig. 9.4. In this representation of the magnetic phase diagram it is well recognizable, that the phase transitions at higher temperatures, i.e. are accompanied by a large change of entropy across the transitions. For the first order transition H_c at low temperatures, this change is less pronounced, which may in part be due to the underestimation of c_p across the first order transition, however also to be expected from Eqn. 9.8. Accordingly it is evident that the crossover at $H_{\mathrm{c}2} \approx 13\,\mathrm{T}$ hardly effects the entropy. In the measured temperature regime, no extraordinarily large magnetocaloric effect $(\partial T/\partial H)_{S,p}$ is to be expected. However, isentropes and isothermals still differ significantly. This finding is particularly relevant for our magnetization data measured in pulsed magnetic field, where measurements are done under quasi-adiabatic conditions (cf. Section 8.2).

---

[8] In our phase diagram, $\frac{\mathrm{d}T_\mathrm{c}}{\mathrm{d}B}\big|_{\mu_0 H = 12\,\mathrm{T}} = 0.537\,\mathrm{K/T}$.

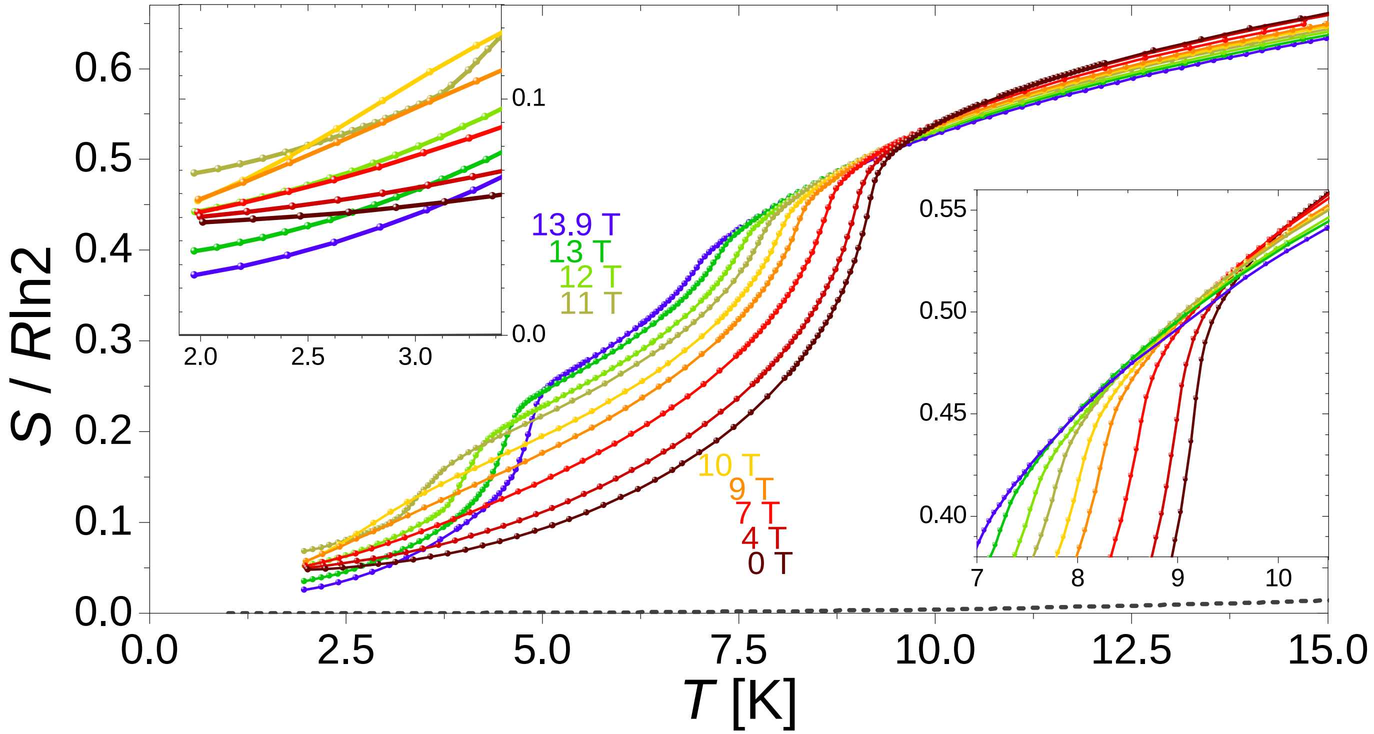

Figure 9.6.: Evolution of entropy $S(T)$ for external fields $H \parallel a$ normalized at 15 K as described in the text. The absolute value of $S = 0$ is selected to have $S > 0, \quad \forall (T, H)$. The line in the bottom off the figure is the estimated DEBYE contribution to S at $H = 0$, not subtracted from the data. The right side inset highlights the intersections of $S(H)$ curves at where $\partial m / \partial T = 0$. The left side inset shows the details of the entropy changes at low temperatures. The data indicate a sizable reduction of the field dependence of the entropy $S(H)$ below 2 K in weak external magnetic fields. For the curves at $11 - 13$ T, crossing a 1st order phase transition, the entropy is presumably overestimated at low T.

9.4. Specific heat at low temperature

At reasonably low temperatures the complexity of properties of a thermodynamic system commonly reduces with the number of thermally excitable states. Taking the system to primarily occupy its ground state and any excited states to be gapped from the ground state, specific heat measurements are in principle qualified to measure the size of this gap. This situation is to be expected to apply to ordered ferro- and antiferromagnets possessing an anisotropy gap separating the ground state from the low-lying magnon excitations. Here the specific heat is expected to behave as [192, 193]

$$c_p(T) = AT^{\epsilon} e^{-\Delta/T} \tag{9.9}$$

such that the specific heat strictly grows with temperature by some proportionality constant A and an exponent $\epsilon(T) = \text{const.}$, which depends on the low energy dispersion relation of the magnetic excitations, i.e. $\epsilon = 3$ for antiferromagnets and $\epsilon = 3/2$ for ferromagnets and Δ measures the anisotropy gap in units of K. Clearly, this model cannot attribute for low temperature anomalies in $c_p(T < 2\,\mathrm{K})$, as are predicted from the entropy analysis. It is thus assumed by the model, that this anomaly is to be neglected at the temperatures investigated. Adding a further 2-level SCHOTTKY contribution evaluates to a vanishing corresponding level splitting ($< 0.02\,\mathrm{meV}$) for all data sets. Eqn. 9.9 can be linearized, in order to provide a test of applicability of the model for a low temperature subset of $c_p(T)$ data as

$$\frac{\mathrm{d}c_p}{\mathrm{d}T}\left(\frac{c_p}{T}\right)^{-1} = \Delta T^{-1} + \epsilon. \tag{9.10}$$

The left hand side of the above equation can be obtained from the data and is demanded to behave linearly if plotted versus a reciprocal T abscissa. Vice versa such linearity can be used to imply Eqn. 9.9 to hold. This representation also allows to directly read off the exponent ϵ at $T \to \infty$. Plotting otherwise

$$\frac{\mathrm{d}c_p}{\mathrm{d}T}\left(\frac{c_p}{T^2}\right)^{-1} = \Delta + \epsilon T \tag{9.11}$$

versus T allows to read off the gap Δ at $T = 0$. However, as both representations demand to take the derivative of the data, information about the behavior at the lowest measured temperature is removed. Thence, both ϵ and Δ are eventually fitted to the raw data subset which is found to behave linearly in the above representations. The procedure to determine the fit parameters is exemplified on the data obtained in the zero field measurement. The above representations are plotted in Fig. 9.7 and are compared to the behavior expected for magnon induced specific heat in $\mathrm{Li_2CuO_2}$. The compound is known to possess a magnon gap of $\Delta_{\mathrm{aniso}} = 1.36(2)\,\mathrm{meV}$. Analyzing the magnon dispersion, a linear increase $\epsilon \approx 1$ of the number of excitable magnon states with the energy is obtained (cf. Fig. 5.15). From Fig. 9.7 it is immediately

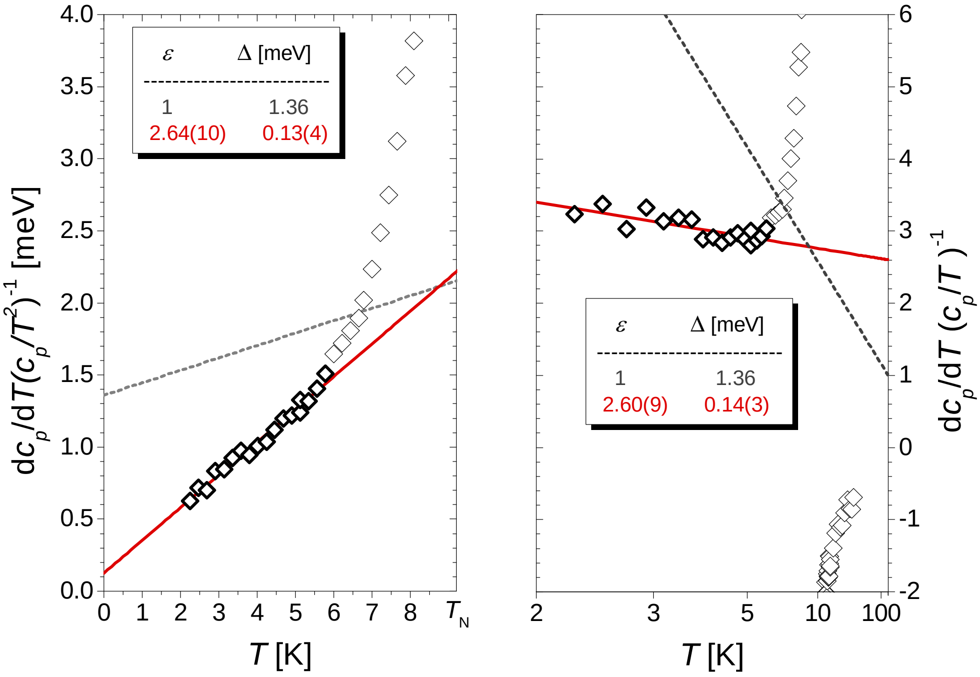

Figure 9.7.: For $c_p(H = 0)$ the applicability of Eqn. 9.9 is tested using representations of the data in form of (left) Eqn. 9.11 and (right) Eqn. 9.10. The low temperature subset of data for which linearity is considered is exaggerated. The full lines represent fits to the data. With these the left plot at $T = 0$ allows to read off a gap $\Delta \approx 0.13\,\mathrm{meV}$, while the right plot allows to read off $\epsilon \approx 2.6$ at $T \to \infty$ (the abscissa reaches up to $10^{10}\,\mathrm{K}$). The dashed line represents the expected behavior of c_p, where excitations are gapped by the magnon anisotropy gap.

clear, that the measured specific heat does not probe magnon excitations. In particular, $\Delta_{c_p} \ll \Delta_{\mathrm{aniso}}$ shows, that the specific heat must be attributed to excitations of states with a much lower gap than the magnon gap. This difference is also evident in plots of c_p. Having determined a reliable region of data for which Eqn. 9.9 holds, a fit to c_p is given in Fig. 9.8.

The same method of analysis is applied successfully to most $c_p(H)$ curves (cf. Fig. A.3). Nevertheless, it fails for the data sets at 9 T and 10 T, i.e. close to the meta-magnetic transition at H_c. At $\mu_0 H = 10\,\mathrm{T}$, no low temperature subset is found to behave as Eqn. 9.9, while at 9 T the data must be fitted by a negative exponent ϵ. This finding may indicate fluctuations near H_c to dominate c_p. A sizeable reduction of ϵ is also found for the data at $\mu_0 H = 7\,\mathrm{T}$. This data set is the only one, where both fit parameters ϵ and Δ agree well to the values excepted for magnon excitations. However, the fit parameters determined at 4 T (no magnon excitations), 7 T and 9 T (presumably fluctuation dominated) show a continuous evolution, such that the results at 7 T may coincidentally indicate magnon excitations. Further data sets in fields near

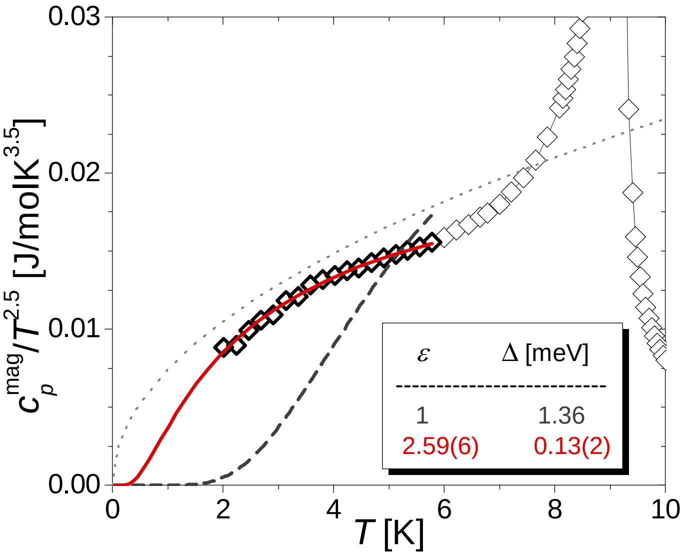

Figure 9.8: A fit (full line) of $c_p(H = 0)$ by Eqn. 9.9 reveals parameters in strong contrast to a specific heat driven by magnon excitations (dashed line). The fits are performed on c_p-data and are projected here to $c_p/T^{2.5}$ for clarity. The dotted line displays the subtracted phonon specific heat multiplied by a factor 100.

$\mu_0 = 7\,\mathrm{T}$ are required to make a distinction. For all other data sets, the exponent is determined close to $\epsilon = 2.5$, even above the meta-magnetic transition. With the excitations probed being unambiguously different from the magnon excitations, the physical meaning of ϵ is unclear.

The values determined for the size of the probed gap Δ appear much less regular. At 0 T the gap is found as $\Delta = 0.13(2)\,\mathrm{meV}$ which is (using $g_a = 2.264$ [115]) $\Delta/\,\mu_{\mathrm{B}} g_a = 1.0(2)\,\mathrm{T}$ of comparable size as the susceptibility anomaly $\chi_a(H)$ at lowest temperatures (cf. Section 8.2). Due to its low energy, corresponding excitations could not be resolved in our INS measurements. At 4 T the excitations dominating the specific heat are found to be gapless. As mentioned above, the data set at 7 T is the only one with a gap is consistent with the anisotropy gap, yet this result must be looked at critically. The absence of a magnetic field dependence of $\Delta(H > H_c)$ represents a further interesting feature.

The proportionality constant A in Eqn. 9.9 is found to be small at low fields and significantly larger but rather constant for $H > H_c$. The large value at $\mu_0 H = 7\,\mathrm{T}$ is interesting. *If* $c_p(H = 7\,\mathrm{T})$ is indeed related to magnon excitations, a rather low density of states relevant for c_p in other fields may be indicated. However, this presumption remains to be verified.

Overall, the irregularities in $c_p(H)$ allude to a complex excitation spectrum and should motivate much more detailed investigation of the evolution of $\Delta(H_a)$ for a large set of H_a and at low T. Complementing INS measurements, the analysis of specific heat data provides an efficient tool to study especially the magnetic field dependence of the sub-anisotropy-gap states which appear to be dominating c_p. A significantly enlarged data set at hand, models extending Eqn. 9.9 are to be studied. As shown in Section 9.3, data at lower temperature are therefor of particular relevance.

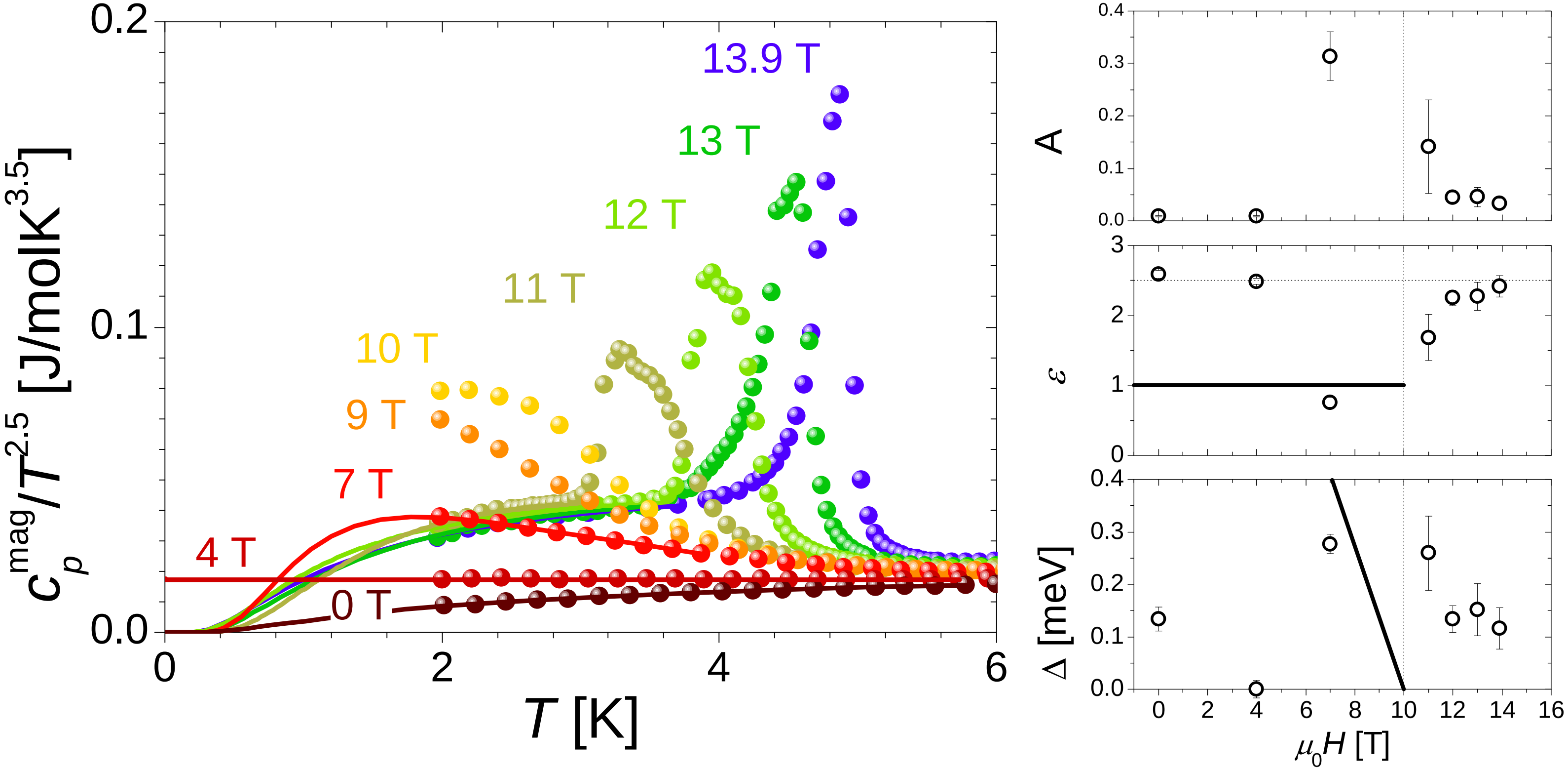

Figure 9.9.: (left) Specific heat of Li_2CuO_2 in external magnetic field over $T^{2.5}$, the most common exponent to govern c_p at low temperatures. The data are extrapolated to $T = 0$ using Eqn. 9.9. (right) From fits to the data at low T, the proportionality constant A (top), the exponent ϵ (middle), and the gap Δ to the predominantly excited state (bottom) are determined. The thick solid lines indicate the expected exponent ϵ and the magnetic field dependence of the gap Δ for magnon excitations. Dashed lines are guides to the eye, marking esp. the critical field $\mu_0 H_c = 10\,T$.

10. Magneto-elastic coupling

The thermal expansion and magnetostriction data presented in this chapter provide further detailed information on the thermodynamic properties of Li_2CuO_2. Namely, these experimental methods give access to the volumetric changes of the compound at constant pressure. Therefore, they are a direct measure of the pressure dependence of the free energy. Compared to the other thermodynamic properties studied in this thesis - i.e. magnetization and specific heat - the data obtained here more clearly reflect the complexity of a material. This deeper detail owes to the strength of the facilitated capacitive dilatometry method on a single crystalline sample to not only determine the scalar change of volume. Instead, the diagonal components of the stress tensor are measured independently and the length change of each individual unit cell lattice parameter can be investigated. In comparison, diffraction experiments allow to study even the full structural model and furthermore are able to measure these parameters as a function of actually applied external pressure. Capacitive dilatometry, admittedly, allows to measure the pressure dependence of the lattice parameters at $p \approx 0$ only. Nevertheless, the strengths of the method compared to diffraction make it a highly valuable probe, namely in being a relatively rapid lab experiment that can be performed at even lowest temperatures and largest magnetic fields with a resolution being orders of magnitude better than accessible to diffraction. As exemplified in the subsequent sections, information on the pressure dependence is of specifically high interest at pressures other experiments are usually performed at, i.e. at $p \approx 0$.

Within this chapter, the experimental method is shortly discussed in Section 10.1. In Section 10.2 thermal expansion data in zero field are used to provide a quantitative measure of the pressure dependence of T_{N} in Li_2CuO_2. The strength of the experimental method to sensitively detect pressure dependent phase transitions is explicated in Section 10.3 and Section 10.4 in the study of the magnetic phase diagram of the compound. In disclosing the large pressure dependence of the phase transitions of Li_2CuO_2 the method illustrates an interesting interplay of the exchange couplings at the phase transitions.

10.1. Remarks on the measurement setup

The experiments discussed here have been performed in a setup based on a tilted plate capacitance dilatometer of the type introduced Rotter *et al.* [194] built from silver. The peripherals of the dilatometer have been elaborated in the course of the thesis of L. Wang [195]. The dilatometer is operated in a cryomagnet with a variable temperature insert. Under standard operation the setup allows measurements at temperatures down to 2 K and magnetic fields up to 16 T. Running the dilatometer in an evacuated container (with contact gas of 40 mbar He at 300 K) and stabilizing the dilatometer temperature above the VTI temperature by a separate heater a high stability of the temperature sensor (noise, drift $< 0.0005\,\mathrm{K}$) is achieved. Note that the temperature sensor reading is not corrected for its magnetoresistivity. The analysis of the measured capacitance data implements the procedure given in [194]. The typical noise level of the data has a standard deviation of $\sigma < 3 \cdot 10^{-11}$ m, mainly attributed here to electronic noise. For a sample of 1 mm length l this corresponds to resolvable expansion anomalies with $\Delta l/l > 10^{-7}$. As already mentioned, the measurements can be performed relatively rapidly. Both, temperature and magnetic field are changed continuously and rates of 0.3 K/min and 0.3 T/min, respectively, are found to be well applicable to the sample examined. Faster sweep rates to not immediately cause experimental artifacts, yet go along with a reduced relative sampling rate limited by the data acquisition frequency of the utilized *Andeen Hagerling 2500 A 1 kHz Ultraprecision Capacitance Bridge* of $\leq 2\ \mathrm{s}^{-1}$. A high density data set is worthwhile for the calculation of the expansion coefficients α, β, respectively, from the measured length changes.

Nevertheless, some criticism of the method must be given, before presenting obtained data to the reader. Indeed, the apparatus does have its drawbacks, which are mainly due to the deficient reproducibility of systematic errors. Even though the self-compensating design of the dilatometer, compared to others, has the principle strength to produce a reduced background signal in thermal expansion measurements, this strength is outranged to our opinion by the mechanical stresses introduced by the needle-bearings fixing the capacitor plates with respect to each other. The soft Ag bearings are unavoidably squeezed and gradually worn off. Especially at low temperatures it meanwhile takes hours after initial cooldown till stress induced capacitance drifts reduce. As an effective method to relax the dilatometer prior to measurement at low temperatures short high power heat pulses ($\Delta T \approx 15\,\mathrm{K}$ within ≈ 3 s) and subsequent cooldown as well as a magnetostriction measurement at 0.8 T/min, $0 \to 16 \to 0\,\mathrm{T}$ were employed. The last step also serves as primary characterization e.g. of proper alignment of the sample while stabilizing temperature gradients in the VTI. Another unpleasant consequence we relate to the worn off bearings are differences in the measured signal after remounting the sample. A related issue is a possible slight canting of the sample whilst mounting, which cannot be controlled due to the closed design of the dilatometer. While corresponding large artifacts are easily recognized, it is not obvious for a number of qualitatively similar data sets which set is the quantitatively most reliable. Updated measurements of the background signal of the dilatometer have been performed for the dilatometer in configuration to measure parallel as well as perpendicular to external field for both magnetostriction (at 3 K and 0.3 T/min) and thermal expansion (at 0 T and 0.3 K/min). Another feature of the measurements is the significantly different thermal expansion signal at some constant temperature of the dilatometer, if cooling the VTI with liquid or gaseous He. This is still puzzling as there is no direct contact between the VTI and the dilatometer. For Li_2CuO_2, lowest temperatures are important to reach and the VTI is therefor to be cooled with liquid He. For thermal expansion consistent background signals could thus be obtained only below $T \lesssim 25\,\mathrm{K}$.

10.2. Uniaxial pressure dependence of T_N

In this section the thermal expansion data of Li_2CuO_2 measured in zero applied magnetic field and at $H_{\parallel a} = 12\,\mathrm{T}$ are discussed. The length changes of the lattice parameters are determined individually. At the NÉEL temperature the coupling between magnetic and structural degrees of freedom is found unexpectedly large and highly anisotropic. Data taken at $H = 0$ are shown in Fig. 10.1. They display a rather small influence of the magnetic order onto the chemically rigid CuO_2-chains along the b-axis. In contrast, the distance between the chains is altered strongly. The thermal expansion coefficient of the a-axis is found to be negative at T_N, somewhat compensating the positive expansion of the b-axis, yet the overall volume expansion is completely dominated by the sizable positive thermal expansion coefficient of the c-axis. For second order phase transitions, the EHRENFEST-relation

$$\left.\frac{\partial T_\mathrm{N}}{\partial p^i}\right|_{p^i \to 0} = V_m T_\mathrm{N} \frac{\Delta\alpha_p^i}{\Delta c_p} \tag{10.1}$$

with the molar volume of a formula unit V_m provides access to the uniaxial pressure dependence of the ordering temperature for pressure applied along the direction i. Nevertheless, the mean-field jumps $\Delta\alpha_p$, Δc_p at the phase transition are usually covered by fluctuations. Close to T_N an approximation is provided by the differential form [196]

$$\alpha^i(t)|_{t\to 0} = \frac{c_p(t)|_{t\to 0}}{T_\mathrm{N} V_\mathrm{m}} \left.\frac{\partial T_\mathrm{N}}{\partial p^i}\right|_{p^i \to 0} + \text{const.} \tag{10.2}$$

with the reduced temperature $t = T/T_\mathrm{N} - 1$. The derived uniaxial pressure dependencies at $p = 0$ are given in Tab. 10.1. Note the performed analysis assumes T_N as the only relevant energy scale and neglects background contributions to α and c_p, which will in general have to be described by a different GRÜNEISEN-parameter but are small compared to the anomaly at T_N. Scaling c_p and α_i works well close to T_N and $T > T_\mathrm{N}$, yet both thermodynamic properties behave less alike below T_N, especially for the chain-axis. In total, the hydrostatic pressure dependence of the ordering temperature is found as large as 0.72(9) K/GPa. In comparison, the pressure dependence of the spin-PEIERLS-transition of $GeCuO_3$ with 4.5(4) K/GPa [197], 5.1 K/GPa [196] is

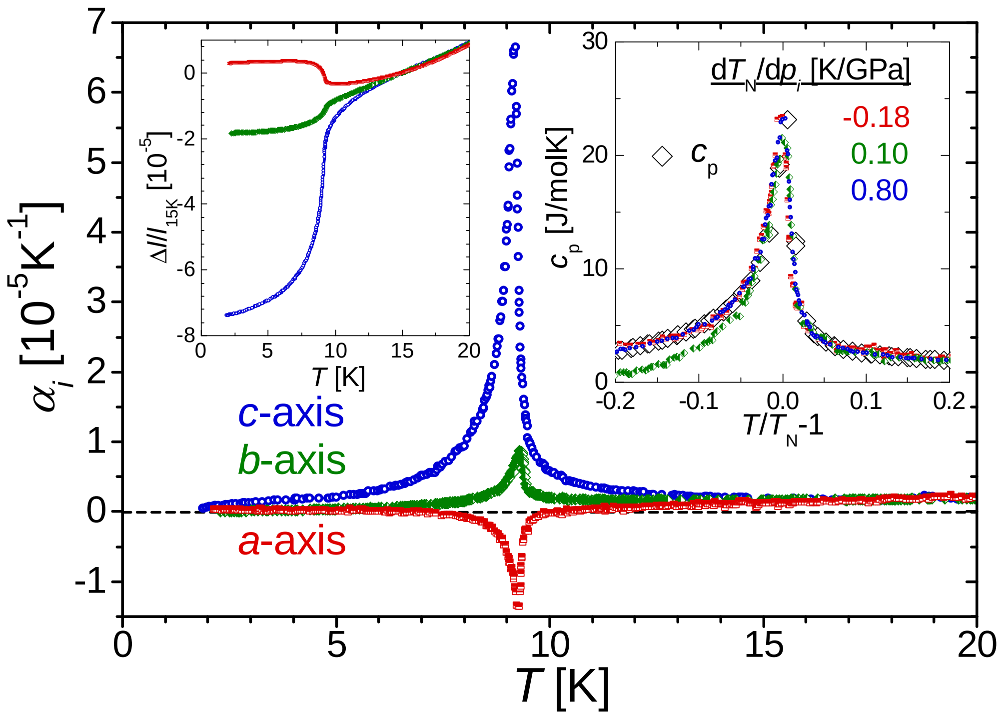

Figure 10.1.: Thermal expansion coefficients α_i of Li_2CuO_2 for $H = 0$. (Left inset) relative length change of unit cell axes normalized to the length at $T = 15\,K$. (Right inset) Scaling behavior of α_i projected onto c_p.

significantly larger. However, for Li_2CuO_2 T_N is accompanied by a much larger specific heat anomaly and no actual structural instability at T_N is observed in diffraction experiments [3, 108–112].

In order to understand the origin of this large effect it is helpful to have a look at the exchange couplings driving the magnetic ordering. Of special importance is here the inter-chain exchange path labeled J_{131} (cf. Section 5.1). It is the only known spin exchange coupling with a component along the c-axis. From the analysis of our INS data it is shown that this coupling is the dominant inter-chain coupling. Also, it inhibits incommensurate correlations along the spin-chains. Upon leaving the collinearly ordered state at temperatures $T > T_N$ the compound appears to develop incommensurate short range order (cf. Section 7.2). The elongation of c at T_N towards higher temperatures is thus indeed to be expected.

For the expansion of the other crystallographic directions the situation is more complex, as further exchange paths must be considered. For the a-axis J_{131} is competing with both J_{100} and J_{110}. If J_{100} and J_{110} were absent one would expect a similar length change of the a-axis as observed for the c-axis due to J_{131}. This length change will be reduced by a counteracting length change related to strength of J_{100} and J_{110}. The dilatometric measurements show, that the sign of the expansion of the a-axis even opposes that of the c-axis. Consequently, the expansion of the a-axis below T_N therefore goes along with

Table 10.1.: Uniaxial pressure dependence of magnetic transitions in Li_2CuO_2. The hydrostatic pressure dependence is given by the sum of the uniaxial quantities.

p_i	$T_N(H = 0)$ [K/GPa]	$T_N(\mu_0 H = 12\,\mathrm{T})$ [K/GPa]	$H_c(T = 2\,\mathrm{K})$ [T/GPa]
a	-0.18(3)	-0.15(5)	-0.65(16)
b	0.10(3)	0.035(10)	-0.11(2)
c	0.80(3)	0.90(5)	0.89(12)
hydrostatic	0.72(9)	0.79(11)	0.1(3)

a reduction of J_{131}. However, this reduction is apparently over-compensated by a concomitant attenuation of J_{100} and J_{110}, such that the collinear state is effectively stabilized.

At T_N towards lower T the b-axis, i.e. the chain is shrinking. Again, the shrinking is supportive for J_{131}. However, the behavior of the chains is likely dominated by the much larger in-chain couplings J_{010} and J_{020}. Their respective change with the Cu-Cu distance is not obvious, yet *if* the length change of the chains is indeed dominated by the in-chain exchange, the positive thermal expansion coefficient at T_N may provide a hint here. At T_N the system can reduce its energy by suppressing the incommensurability favored by the in-chain interactions. In return, the evolution of the commensurate state should favor a reduction of the frustration ratio at $T \leq T_N$. This line of reasoning concludes a reduction of the frustration ratio $|J_{020}/J_{010}|$ to go along with a reduction of the in-chain Cu-Cu distance.

At $\mu_0 H = 12\,\mathrm{T}$ (cf. Fig. A.4) the transitions are less pronounced both in c_p and α_i, therefore reducing the quality of the data. However, the pressure dependence of T_N can still be analyzed well and is found to change towards an even higher anisotropy, i.e. increasingly important dependence of T_N on pressure along the c-axis (cf. Tab. 10.1).

It was shown that at room temperature and $p_{\mathrm{crit}} = 5.4$ GPa Li_2CuO_2 undergoes a structural transition from orthorhombic *Immm* to monoclinic (potentially *C2/m*) [126], with an arrangement of the chains similar to the orthorhombic *Cmc2*$_1$ structure reported for $Cu(OH)_2$ [75]. The analysis of the pressure dependencies from thermal expansion is therefore restricted to low pressures $p \ll p_{\mathrm{crit}}$. In order to verify the hydrostatic pressure dependence of T_N, hydrostatic pressure experiments have been undertaken. SQUID-magnetization measurements have been performed on a polycrystalline sample in a CuBe pressure cell. The pressure in the cell is obtained from the onset of the superconducting transition of a Pb sample [198] inside the pressure cell at applied fields of 20 Oe - assumed to have a negligible effect on the transition with a critical field $H_{\mathrm{SC}} > 800$ Oe at ambient pressure [199] (cf. Fig. A.5 (left)). The pressures applied are constraint to $\leq 0.63(5)$ GPa. The magnetization

Figure 10.2: $T_\mathrm{N}(p)$ as determined from anomaly in $\frac{\partial(\chi T)}{\partial T}$ in magnetization measurements at $\mu_0 H = 1\,\mathrm{T}$ under externally applied hydrostatic pressure (■). $T_\mathrm{N}(p = 0)$ was determined as 9.30(4) K (cf. Section A.4). The data show a larger hydrostatic pressure dependence (- -) than $\mathrm{d}T_\mathrm{N}/\mathrm{d}p$ obtained from specific heat and thermal expansion (—) with errors (···) (cf. Tab. 10.1).

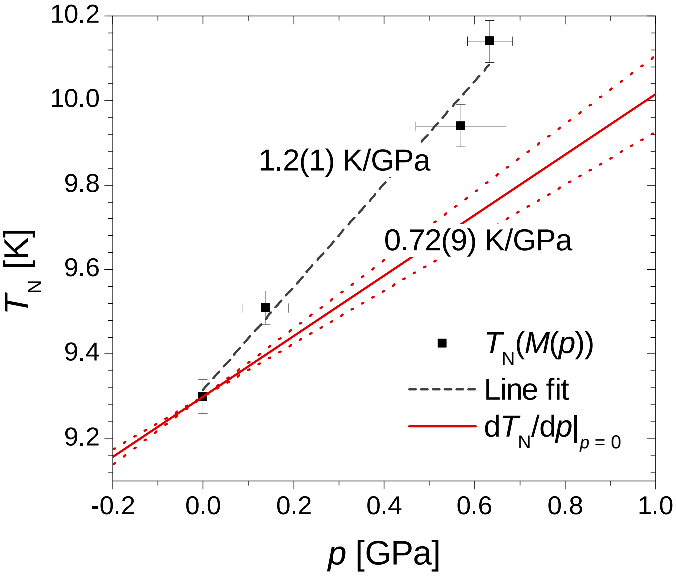

of the sample was measured at 1 T and T_N was obtained from the maximum in $\mathrm{d}(\chi T)/\mathrm{d}T$. Due to missing background data of the pressure cell, further quantitative detail cannot be obtained from the data, shown in Fig. A.6. Nevertheless, the data on the transition temperature $T_\mathrm{N}(p)$ - behaving rather linearly - clearly show a larger pressure dependence compared to the results from thermal expansion at $p = 0$ (cf. Fig. 10.2). The origin of the disagreement is yet to be clarified. The considerably smeared out superconducting transition of the Pb sample indicates too coarse graining of the crystal and a too large ratio of sample to pressure medium, which can yield stresses on the sample and an underestimation of the exerted pressure. Then again, the neglect of the background contributions to c_p and α may be considered to yield some inaccuracy in the determination of the pressure dependence from Eqn. 10.2.

Interestingly, while thermal expansion data do not indicate (detect) a pressure dependence of $T_2 = 2.6\,\mathrm{K}$ - the onset of low temperature weak ferromagnetism - its increase with pressure is evident in the magnetization experiments under pressure. From the corresponding anomaly in $\mathrm{d}M/\mathrm{d}T$ it is found as large as $\mathrm{d}T_2/\mathrm{d}p \approx 1\,\mathrm{K}/$ GPa (cf. Fig. A.5 (right)).

As shown above, hydrostatic pressure allows to distinctly shift the NÉEL temperature towards higher temperatures. It would however be more interesting, to investigate Li_2CuO_2 for a significantly reduced ordering temperature. To effectively reduce T_N in experiment applying uniaxial pressure along the a-axis is not very promising, first of all due to the fragility of the crystal. Alternatively, negative chemical pressure could be expedient. However, hitherto attempts to grow stoichiometric Na_2CuO_2 have not yet been successful. For $Na_{2-x}CuO_2$, with $x > 0$, a number to chain compounds have been synthesized [200, 201].

10.3. Exploration of the easy axis magnetic phase diagram

Using thermal expansion and magnetostriction measurements, the magnetic phase diagram of Li_2CuO_2 has been examined in the range $2\,\mathrm{K} \leq T \leq 15\,\mathrm{K}$ and $0 \leq \mu_0 H \leq 16\,\mathrm{T}$. A broad set of data for magnetic field applied along the easy a-axis has been recorded. It provides a fascinating number of information on the details of the magnetic phases and transitions.

In Section 10.3.1 magnetostriction data at low temperature $T = 2\,\mathrm{K}$ are presented. Here, the uniaxial pressure dependence of the meta-magnetic transition at $\approx 10.2\,\mathrm{T}$ is investigated correspondingly to the analysis of T_N in Section 10.2. Thereafter, a comprehensive presentation of thermal expansion and magnetostriction data is given in Section 10.3.2 and discussed on the basis of a phenomenological model in Section 10.3.3.

10.3.1. Low temperature magnetostriction

In Section 10.2 the pressure dependence of the antiferromagnetic ordering temperature T_N has been analyzed in zero magnetic field, neglecting the interplay between the pressure dependence and the sample magnetization. Just as T_N merely depends on weak magnetic fields, the meta-magnetic transition at H_c can be expected only weakly temperature dependent at low temperatures. $T = 2\,\mathrm{K}$ is the lowest temperature that was stabilized in the experiment. From the magnetic phase diagram (cf. Fig. 7.1) a low temperature dependence of H_c, $\frac{\partial H_\mathrm{c}}{\partial T}\big|_{T=2\,\mathrm{K}} < 0.29\frac{\mathrm{T}}{\mathrm{K}}$ is obtained. Magnetostriction experiments have been performed at $T = 2\,\mathrm{K}$ for each unit cell axis in magnetic fields $H \parallel a$ up to $16\,\mathrm{T}$. The data, presented in Fig. 10.3, reproduce the finding from thermal expansion, in that the deformation of the crystal is dominated by the c-axis and is weak along the b-, i.e. chain-direction.

Several features of magneto-elastic coupling Li_2CuO_2 are found in the data. Firstly, just below the meta-magnetic transition observed at $H_\mathrm{c} \approx 10.2\,\mathrm{T}$, a positive expansion of all crystallographic axes is observed. Correspondingly, a negative hydrostatic pressure dependence of the magnetization follows from the MAXWELL relations. Clearly, this is to be expected for simple antiferromagnets close to a meta-magnetic transition if the strength of the antiferromagnetic exchange coupling decreases monotonously with an increase of interatomic spacings. However, Li_2CuO_2 is not described by antiferromagnetic couplings only. Just like at T_N, for the expansion of b-axis (chain) the question remains to be clarified, if it is triggered by the b-component of the antiferromagnet inter-chain coupling J_{131} or reflects an interrelation of in-chain correlations and the frustration ratio. Just at H_c the situation is clearly in favor for the second mechanism. At this 1^{st} order phase transition (cf. Chapter 7), the c-axis expands considerably, while both the a- and b-axes shrink. The expansion of the a-axis directly at H_c is found significantly amplified by fluctuations.

At low temperatures the compound enters an intermediate phase, which is presumably steadily diminished for $H_{c2} \gtrsim 13\,\mathrm{T}$. Hereupon, the c-axis shrinks again notably, accompanied by the b-axis. The opposing behavior of the a-axis reconfirms the argument of competition of the inter-chain couplings along the a- and c-axes.

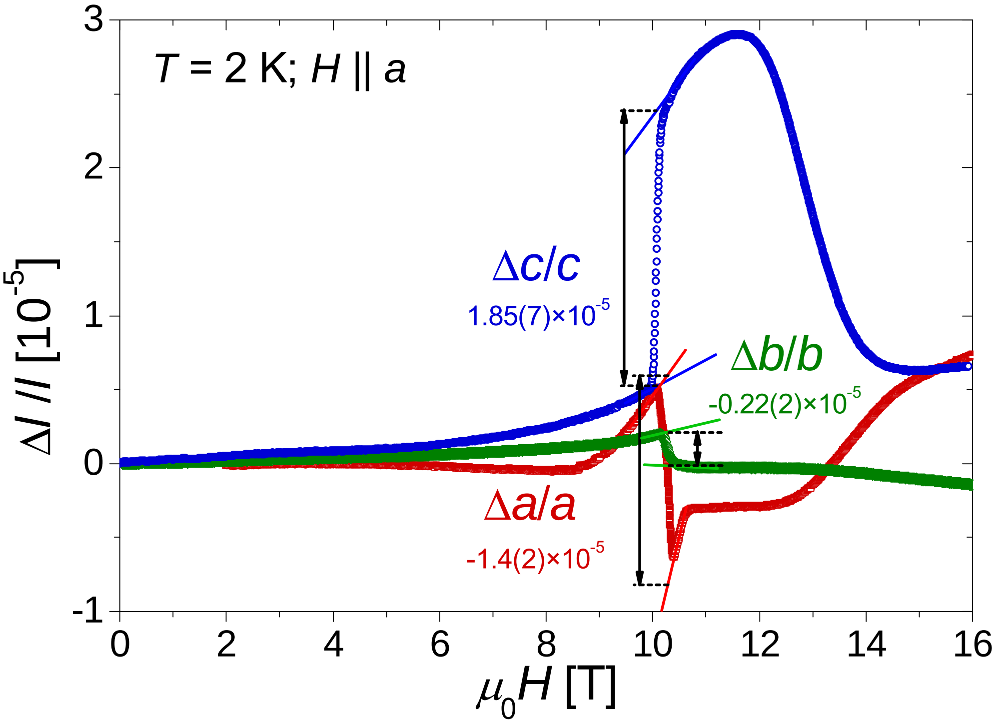

Figure 10.3.: Magnetostriction data $\Delta l/l$ for each unit cell axis in $\mathrm{Li_2CuO_2}$ at $T = 2\,\mathrm{K}$ and magnetic fields $\mu_0 H_{\|a} \leq 16\,\mathrm{T}$. At the meta-magnetic transition $\mu_0 H_\mathrm{c} \approx 10.2\,\mathrm{T}$, the lattice shows a sizeable deformation accompanied by fluctuations. Linear extrapolation of the fluctuation regime towards H_c is used to determine the amplitude of the anomaly.

The existence of a crossover at $H_{c2} \approx 13\,\mathrm{T}$ is clearly evidenced for the first time by magnetostriction. As shown in Section 8.2 it also is observable in our magnetization measurements, however as a broad and only weak feature in the susceptibility.

For H_c being a transition of first order the expansion at H_c may be analyzed by means of the Clausius-Clapeyron relation

$$\left.\frac{\partial H_\mathrm{c}}{\partial p^i}\right|_{p\to 0} = V_m \frac{\Delta l^i/l^i}{\Delta M}. \tag{10.3}$$

Unfortunately, magnetization data at $T = 2.0\,\mathrm{K}$ are not available. Along with the thermal fluctuations near H_c the size of ΔM is intensely temperature dependent. Klingeler obtained at $T = 2.5\,\mathrm{K}$ $\Delta M = 0.081(5)\,\mu_\mathrm{B}/\mathrm{f.u.}$ [125]. Data taken at 2.1 K show $\Delta M = 0.103(3)\,\mu_\mathrm{B}/\mathrm{f.u.}$. Pulsed field data at $T \approx 1.45\,\mathrm{K}$ (Section 8.2) give $\Delta M = 0.172(5)\,\mu_\mathrm{B}/\,\mathrm{f.u.}$. Interpolating, $\Delta M(T = 2\,\mathrm{K}) = 0.11(1)\,\mu_\mathrm{B}/\,\mathrm{f.u.}$ is approximated. For the amplitude of the magnetostriction anomalies, error bars are estimated from the variation found in a series of experiments. The resulting values of the uniaxial pressure dependencies of H_c are given in Tab. 10.1. For hydrostatic pressure $\frac{\partial H_\mathrm{c}}{\partial p} = 0.1(3)\,\mathrm{T}/\,\mathrm{GPa}$ is found, vanishing within error bars. However, it is evident that the volume is changing across the transition. In fact, the "structural fluctuations" experienced by the a-axis close to H_c compensate the hydrostatic pressure dependence of H_c.

Nevertheless, the critical field H_c, determined by the magnon anisotropy gap Δ_aniso, shows a significant uniaxial pressure dependence. This raises the question if the anisotropy itself is pressure dependent. The anisotropy originating from the nearest-neighbor coupling along the chains through 90° Cu-O-Cu binding is believed to be extraordinarily strong [114, 202], yet the calculated anisotropy for $\mathrm{Li_2CuO_2}$ substantially overestimates the experimental values [36]. The magnetostriction data given above may indicate a significant compensation of the anisotropy of the in-chain exchange by anisotropic inter-chain couplings.

However, a more direct picture to the uniaxial pressure dependence may be provided by inspection of the low energy magnon excitations. In $\mathrm{Li_2CuO_2}$, their dispersion is very flat near the zone center and can attain minima at incommensurate position which are lowered by weak alternations of the interchain couplings irrespective of the exchange anisotropy (cf. Section 5.7). As will be illustrated below, the lattice expansion in intermediate phase points to the formation of a state with non-collinear order of collinear chains (cf. Section 10.3.3).

10.3.2. Comprehensive survey of thermal expansion and magnetostriction data

Having introduced the thermal expansion data at $H = 0$ in Section 10.2 and the magnetostrictive behavior at lowest temperature in Section 10.3.1 in a quantitative manner, this section focusses on a qualitative comparison of the behavior of the unit cell axes throughout the whole examined magnetic phase diagram. The both informative, but complex behavior of the length change of the three crystallographic directions is presented. The data on the expansion of each axis are discussed separately. The observations made for the data sets are interpreted in a simple scheme of the competing magnetic exchange interactions in the compound. Thereafter, a largely coherent qualitative model for the expansion of the unit cell is explicated in Section 10.3.3. In this section, familiarity of the reader with the magnetic phase diagram (cf. Fig. 7.4 on page 86) and the exchange coupling scheme (cf. Fig. 5.1 on page 45) is presumed.

Before going into details, some generic properties for the lattice expansion in $\mathrm{Li_2CuO_2}$ are outlined: While the expansion of any axis is widely different from the others, common behavior - i.e. rather isotropic volume expansion - is rare: in general all axes show a positive thermal expansion, esp. above T_N but also at lowest temperatures. Furthermore, the expansion with magnetic field in a narrow region below the transition at H_c is positive. For any other point in the phase diagram one of the axis shows an expansion with opposite sign than that of the other axes. Mostly, it is the a- and c-axes expansion to express such anti-correlation.

Expansion of the c-axis, mediating the dominant inter-chain coupling

To start with, the thermal expansion and magnetostriction data of the c-axis in magnetic field $H \parallel a$ are presented in Fig. 10.4. For the experiment, a sample with thickness $l_c = 1.72$ mm was prepared. Among the three crystal axis, the relative length change of the c-axis largely dominates in most regions of the magnetic phase diagram and involves a corresponding volume expansion.

As shown by our INS data analysis, the inter-chain coupling J_{131} is the dominant coupling to trigger long range magnetic order. Furthermore, it is responsible for the suppression of incommensurate order along the spin-chain. The significant reduction of c just at the ordering temperature (cf. Section 10.2) suggests an intimate correlation between the strength of the inter-chain coupling and the c-axis expansion. Above the ordering temperature T_N as well as in the ordered phase, if $H < H_\mathrm{c}$, the c-axis is shirking with temperature while expanding in magnetic field. Looking at the c-axis alone, its expansion mimics the stability of the collinear ground state.

The behavior of the c-axis changes drastically in large fields $H \geqq H_\mathrm{c}$. Its extension shows a pronounced saddle-point near $T \approx 4.5\,\mathrm{K}$ and $H_\mathrm{c}(4.5\,\mathrm{K}) \approx 13\,\mathrm{T}$. Here, as shown in Fig. 7.7 and Fig. 7.9 on pages 90 and 93, respectively, the thermal expansion coefficient as well as the magnetostriction coefficient are changing sign. On one side, at temperatures $T > 4.5\,\mathrm{K}$ and $H > H_\mathrm{c}$ a high field phase is entered which is characterized by a decrease of c with field. On the other side, at temperatures $T < 4.5\,\mathrm{K}$, i.e. in the intermediate phase and for magnetic fields $\mu_0 H \lesssim 12\,\mathrm{T}$ the c-axis expands with temperature, but shrinks with increasing field $12\,\mathrm{T} \lesssim \mu_0 H \lesssim 15\,\mathrm{T}$.

For the a- and b-axis the intermediate phase is characterized by a rather constant magnetostriction coefficient β_a and β_b, respectively. In contrast, β_c is changing continuously and no distinct onset of the crossover to the high field phase can be identified. It is therefore the c-axis to most pronouncedly reflect the crossover character of $H_{\mathrm{c}2}$ and to be used to identify this transition. For corresponding analysis of β_c-data, see Section 7.3.

Another observation is made in magnetostriction data at $T = 6\,\mathrm{K}$. Here, $\mathrm{Li_2CuO_2}$ is not observed to show any phase transition below $16\,\mathrm{T}$ (H_N is to be expected at $\approx 17.2\,\mathrm{T}$). However, a presumable remnant of the transitions observed at low temperature is indicated by the sign change of β_a and β_b (see below). For β_c such sign change does not exist, but an inflection point at $\mu_0 H = 12(2)\,\mathrm{T}$.

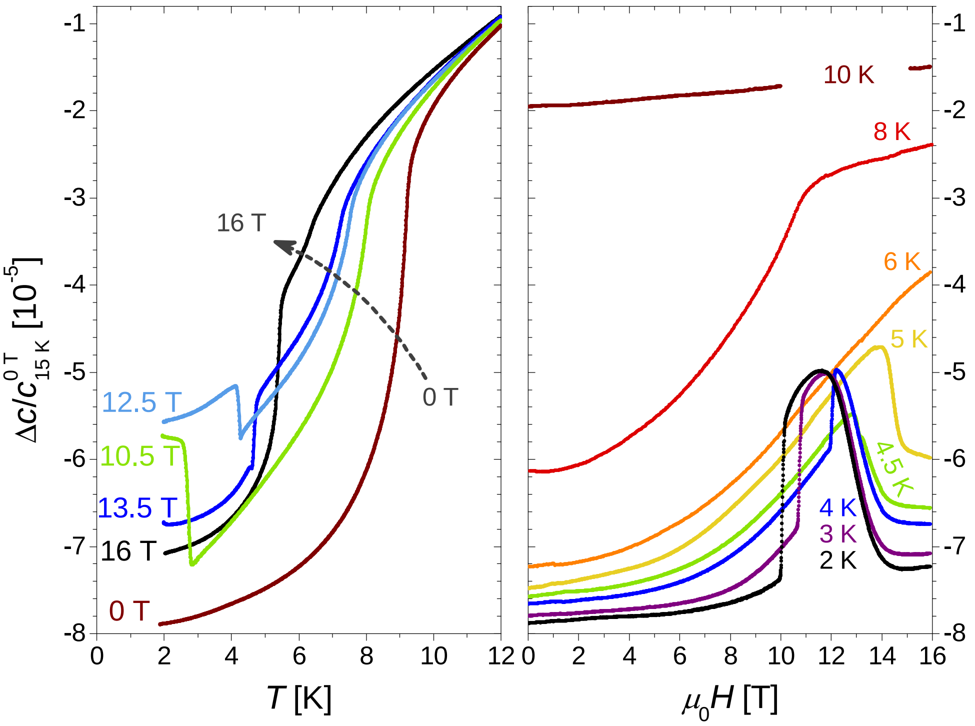

Figure 10.4.: (left) Thermal expansion of Li_2CuO_2 and (right) magnetostriction of the c-axis in magnetic fields $H \parallel a$. Its large dilatation excesses that of the other axes, mostly yielding changes of the crystal volume. The magnetostriction data disclose the presence of an intermediate phase at low temperatures between 10 T and $\approx$ 14 T. Thermal expansion data taken across the phase boundary reveal a sign change of the thermal expansion coefficient at ≈ 13 T. For further detail see Fig. 7.7.

Expansion of the a-axis, mediating frustration of inter-chain couplings

To prepare a sample of Li_2CuO_2, small enough to fit the available sample space $\varnothing = 3$ mm, but extended and polished for measurements of the a-axis expansion is a matter to challenge luck. The material easily cleaves along the $(1,0,1)$ and $(1,0,\bar{1})$ planes. Cleaving of the crystal is about unavoidable in the preparation of samples of dimensions in the mm^3 range. If cleaving occurs, the sample size is confined by the ratio $a/c \approx 0.4$ and $c < \varnothing$. A $l_a = 1.26$ mm thick sample could be prepared. However, it cleaved unusable before any self-consistent experiment yielding a larger data set. A comprehensive study of the expansion of the a-axis is therefore still due. Anyhow, a less extensive set of data was obtained, which is presented in Fig. 10.5.

Amongst the 3 crystallographic directions, the expansion of the a-axis is most complex. It incorporates all the particular features found for the expansion of the b- and c-axes. Throughout most of the magnetic phase diagram, especially at the magnetic phase transitions as well as in magnetic fields $\mu_0 H \lesssim 8$ T in the ordered phase, the expansion of the a-axis strictly opposes

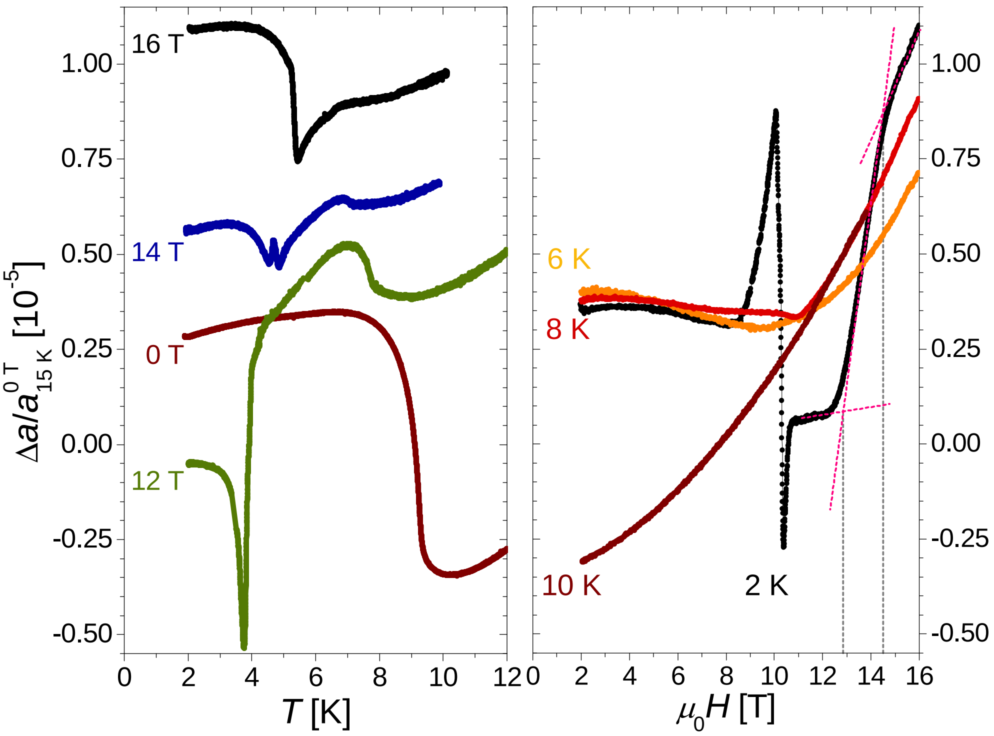

Figure 10.5.: (left) Thermal expansion of Li_2CuO_2 $\Delta a/a$ and (right) magnetostriction of the a-axis in magnetic fields $H \parallel a$. The irregular and noisy magnetostriction data for $\mu_0 H < 2\,\mathrm{T}$ are omitted. The precision of the normalization to $H = 0$, $T = 15\,\mathrm{K}$ is thus restricted. The data show the a-axis to expand remarkably above T_N in magnetic field, along with a strong suppression of the anomaly at T_N for larger field values. A reduced expansion of a is observed in the intermediate phase (12 T, low T), especially pronounced in the fluctuation regime above H_c. Data at $T = 2\,\mathrm{K}$ in increasing high fields show the crossover at H_c2 between $\approx 12.9\,\mathrm{T}$ and $\approx 14.6\,\mathrm{T}$.

that of the c-axis. Most notably, it possesses a negative thermal expansion coefficient at T_N. From the data one can extrapolate, that the a-axis does not approach its minimal expansion at $T = 0$. Instead it develops a pronounced minimum at $T = 10.3(1)\,\mathrm{K} > T_\mathrm{N}$ in zero field.

However, there are also at least two important features where a- and c-axis expansion act corroboratively, causing volume changes. Firstly, both axis expand in magnetic fields applied at temperatures $T > T_\mathrm{N}$. Secondly, in the fluctuation regime in magnetic fields just below the critical field H_c the magnetostriction coefficient is positive for both axis, even though they have different sign at the transition itself. As shown above (cf. Section 10.3.1) this causes a significant reduction of the hydrostatic pressure dependence of H_c. Furthermore, it causes the a-axis to reach a pronounced minimum in the narrow fluctuation regime - just above H_c in the intermediate phase. In the set of magnetostriction experiments done at 2 K, the amplitude of the

$\Delta a/a$-anomalies in the fluctuation regime above and below H_c varied broadly, however their respective sign clearly represents an intrinsic sample property. Note that, just at H_c there is no excitation gap to be expected between the antiferromagnetic ground state in low field and the magnetic state entered above H_c. The observation of the minimum in the a-axis expansion along with the concomitant expansion of the c-axis suggests a significant influence of the weak couplings J_{100} and J_{110} onto the magnetic order in the intermediate phase above H_c.

In even larger fields, the a-axis expands again. Two broad kinks in $\frac{\Delta a}{a}$ are observed around $\approx 12.9\,\mathrm{T}$ and $\approx 14.6\,\mathrm{T}$ in increasing field. Alternatively, a broad maximum in the magnetostriction coefficient may be identified around 13.6 T. The width of hysteresis of these features is $\approx 0.5\,\mathrm{T}$. The thermal expansion of the a-axis at the critical field H_c shows a sign change from a positive to a negative thermal expansion coefficient below 14 T.

In the ordered phase at low magnetic fields $\mu_0 H \leq 9\,\mathrm{T}$ the overall expansion of the a-axis is weaker than for the other axes. However it increases notably in magnetic fields $\gtrsim 10\,\mathrm{T}$. Similarly to the b-axis, the magnetostriction data at 6 K - not crossing any phase transition - are observed to possess an extremal value at $\mu_0 H \approx 10\,\mathrm{T}$.

Expansion of the chain, i.e. b-axis

Eventually, the expansion of the rigid b-(chain)-axis is presented in figure Fig. 10.6. Note, that the magnitude of the relative length change $\frac{\Delta b}{b}$ is much lower than of the c-axis. However, it is trivial to cut samples of Li_2CuO_2 large along the chain direction (here $l_b = 3.96$ mm) yielding well resolvable absolute signals $\frac{\Delta b}{b} l_b$.

The data on the thermal expansions show a positive thermal expansion coefficient throughout almost the whole magnetic phase diagram [1]. The b-axis is shrinking in magnetic field for temperatures $T > T_N$, supportive for the above statement of a reduction of the frustration ratio with shrinking of the chain. In the ordered state the compound at first expands in low field before shrinking in higher field. At low temperatures b reaches its maximum value in magnetic fields just below the critical field H_c. However, at temperatures $T \gtrsim 4.5\,\mathrm{K}$ it is largest at fields $\mu_0 H \approx 12.5\,\mathrm{T} < H_c$. This feature is a probable remnant of the transition at $H_{c2} \approx 13\,\mathrm{T}$ to be observed at lower temperatures. At $T = 2\,\mathrm{K}$, the transition at H_c is identified by the steepest slope observed at $H_c = 10.3\,\mathrm{T}$ and $H_c = 10.2\,\mathrm{T}$ for increasing and decreasing field, respectively. Importantly, while the expansion at T_N shows the same sign as the expansion of the c-axis, the sign is opposite at the transition at H_c. This observation supports the argument, that the expansion of the chain axis is not mediated by J_{131}. Notably, in contrast to the other crystal axes, H_{c2} is only weakly

---

[1] The only exception is found in the fluctuation regime below H_c and temperatures $\lesssim 4.5\,\mathrm{K}$, as shown e.g. in the data set taken at $\mu_0 H_{\parallel a} = 10.5\,\mathrm{T}$.

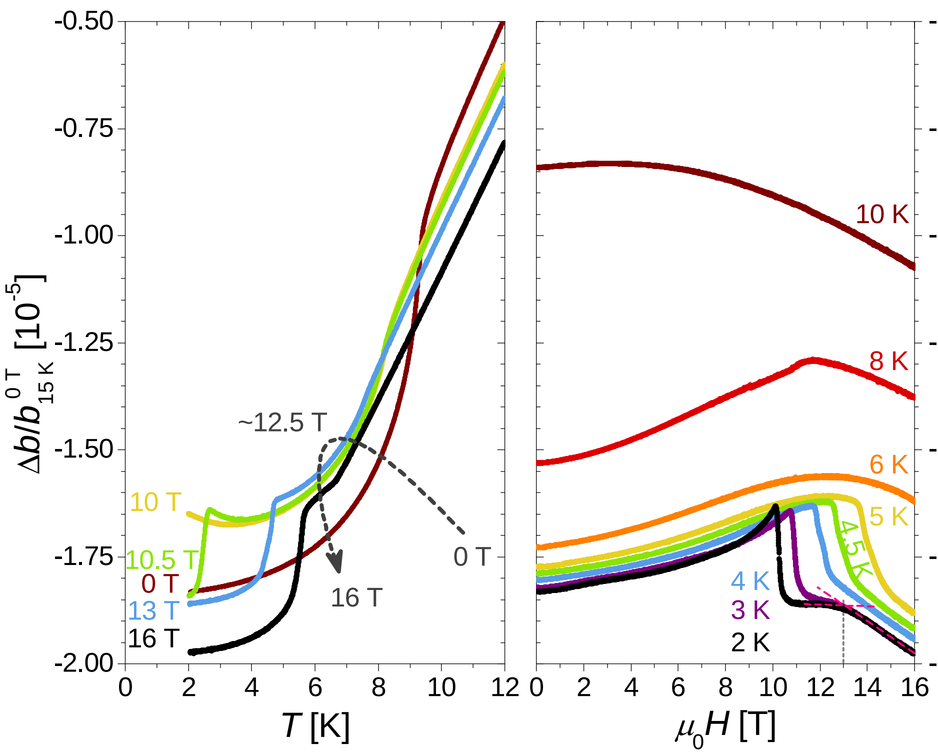

Figure 10.6.: (left) Thermal expansion of Li_2CuO_2 $\Delta b/b$ and (right) magnetostriction of the b-axis in magnetic fields $H \parallel a$. Compared to be other lattice directions, the b-axis expansion displays the least magnetic field dependence. The general tendency of $\Delta b/b$ to shrink in magnetic field is not followed in low fields in the ordered state. Above $\approx 4.5\,\mathrm{K}$ the axis expansion develops a maximum around 12.5 T, i.e. still in the low field phase. At lowest temperatures $T = 2\,\mathrm{K}$ magnetostriction data show two transitions at 10.2 and $\approx 13\,\mathrm{T}$.

pronounced along the b-axis. In particular, the magnetostriction coefficient has the same (negative) sign at both H_c and H_{c2}. As a consequence, the thermal expansion coefficient of the b-axis does not change sign at the critical point ($T \approx 4.5\,\mathrm{K}, \mu_0 H \approx 13\,\mathrm{T}$). The transition at H_{c2} can be identified by the intersection point of the extrapolated linear behavior around H_{c2}. From the data at $T = 2\,\mathrm{K}$ one finds $H_{c2} = 13.0\,\mathrm{T}$ and $H_{c2} = 12.7\,\mathrm{T}$ for increasing and decreasing field, respectively.

10.3.3. A phenomenological model

In Tab. 10.2 the relative length change of the individual axis and the volume is given for distinguished points in the magnetic phase diagram. Also, the change of the direct Cu-Cu distance is given for the spin exchange paths. Our data show clearly, that the expansion of the lattice is largely anisotropic and accompanied by volume changes, i.e. by a sizable pressure dependence of the entropy and magnetization. The Cu-Cu distances are influenced by the

Table 10.2.: Relative length change $\Delta l/l^{0\,\mathrm{T}}_{15\,\mathrm{K}}[10^{-5}]$ of the crystal axes in the disordered ($T = 10\,\mathrm{K}$) and ordered phases ($T = 2\,\mathrm{K}$). With (131) and (110) the Cu-Cu distances of two further spin exchange paths are given. The shortest axis expansions are printed **bold**. Note that the exchange path (100) and (110) are shortest above T_{N} in zero field and in the intermediate phase.

Crystal	10 K		2 K		
axis	0 T	16 T	0 T	12 T	16 T
a, (100)	**−0.3**	+1.0	+0.3	+0.1	+1.1
b, (010)	−0.8	−1.1	−1.8	−1.9	**−2.0**
c, (001)	−2.0	−1.5	**−7.9**	−5.1	−7.2
(131)	−1.4	−1.1	**−4.7**	−3.3	−4.4
(110)	−0.5	+0.2	−0.5	**−0.7**	−0.1
volume $\Delta V/V[10^{-5}]$	−3.1	−1.6	**−9.5**	−6.9	−8.1

strength of covalent bonding and thence depend on the spin-spin correlation on the Cu-sites. A change of Cu-Cu distances is furthermore representative for the change of the overlap of orbitals mediating the exchange interactions. The lattice expansion is therefore related to changes of exchange integrals and changes of the spin-spin correlations. The frustration induced extraordinary degeneracy of the low energy magnon excitations in Li_2CuO_2, as discussed in Section 5.7 must be expected to induce a strong sensitivity of the magnetic ground state to even weak changes of the relative strength of the exchange interactions. This is especially relevant in the vicinity of the phase transitions, where the uniaxial anisotropy does not stabilize the ground state. As a consequence of the sizable magnetization / entropy changes at phase transitions in Li_2CuO_2 a significant volume expansion is indeed to be expected.

In this section, a phenomenological model for the lattice expansion of Li_2CuO_2 is proposed. It is based on the assumption, that the strength of the exchange integrals falls off with an increasing distance of the coupled sites. Note however, that due to the symmetry of the unit cell, its dimensions are directly related to the Cu-Cu distances, but say nothing about shifts of the positions of the Li- and the O-ions which are mediating the spin exchange. The relation "distance $\propto$ coupling strength" is thus not mandatory.

However, this assumption proves useful, as will be illustrated below. From our INS studies, we have obtained a largely complete picture of the relevant exchange couplings at $T = 4\,\mathrm{K}$ in zero field. In the following it is furthermore assumed, that throughout the examined region of the phase diagram, the respective strength of the interactions is altered only slightly.

To gain insight into the mechanisms driving the lattice expansion, understanding of the dominant "diagonal" inter-chain coupling J_{131} is most important, as it contributes to the expansion of all axes. A therefore crucial observation is the absence of clearly cooperative effects of the different axes expansions to shorten the exchange path of J_{131} which would enhance the action of J_{131} under the above assumption. The expansion of each axis can therefore be treated as due to distinguishable mechanisms. A rather comprehensive microscopic, yet qualitative model of the lattice expansion is found to be provided with the following set of arguments:

1. commensurate antiferromagnetic inter-chain correlations are favored by the dominant inter-chain coupling J_{131} and reflected in a reduction of the c-axis,
2. the competition between the inter-chain couplings due to J_{100} and J_{110}, disfavoring collinear inter-chain correlations is reduced by an expanding a-axis,
3. shrinking of the b-axis reduces the frustration ratio of the in-chain couplings and such the tendency to incommensurate in-chain correlations.

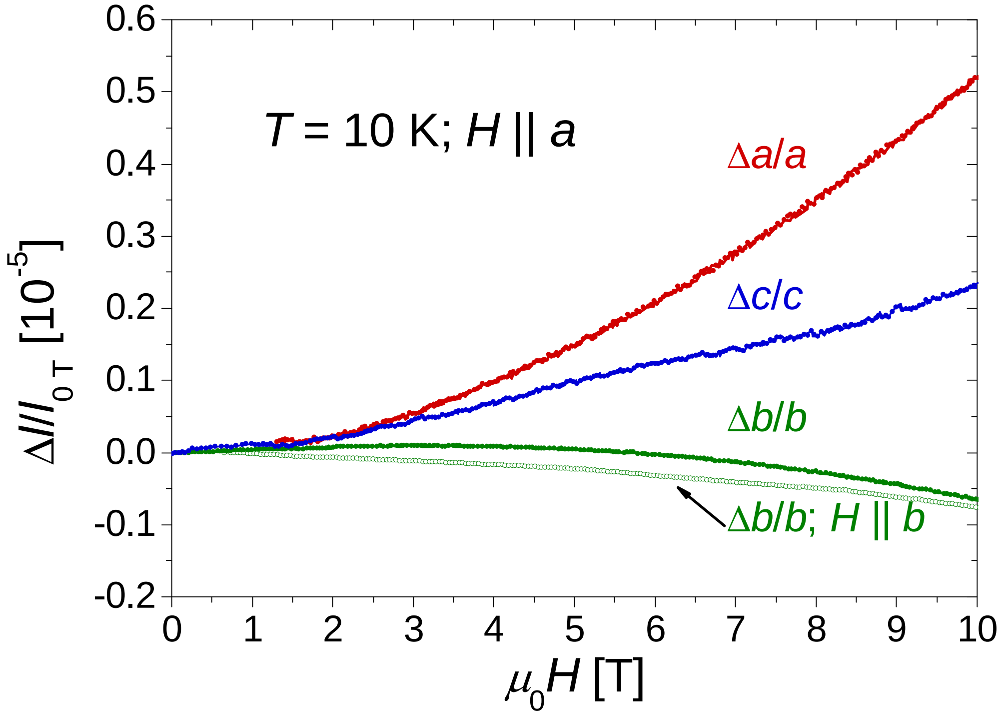

Figure 10.7.: Magnetostriction data at $T = 10\,\mathrm{K}$ display an expansion of the a- and c-axis but a shirking of the b-axis (chain) in applied magnetic field $H \parallel a$. For $H \parallel b$ the chain behaves qualitatively similar.

In the below enumeration, the observations made by thermal expansion and magnetostriction are shown to be well described by this simple model. Nonetheless, a complete picture is still elusive. In particular, for the high field phases the missing knowledge on the ground state does not allow to verify the model, but a ground state in accord to the model may be proposed. An interpretation for the anomaly in magnetostriction data at $T \approx 6\,\mathrm{K}$ and $\mu_0 H \geqq 8\,\mathrm{T}$ has not yet been attained. Note further, that this model applies to low uniaxial pressures. As shown in the room temperature diffraction experiments by You *et al.* [126], isotropic pressure > 1 GPa go along with an increase of the Cu-O-Cu binding angle in the chain, getting as large as $\approx 97.5°$ at 5.5 GPa. Recent band structure calculations suggest an increase of α under isotropic pressure [203].

- Above T_N the lattice expands in field $H \parallel a$ in both the a- and c-direction but shrinks along the b-axis. At $10\,\mathrm{K}$, the magnetization has a negative pressure dependence (cf. Fig. 10.7). This is expected to reflect field induced ferromagnetic correlations, which oppose the antiferromagnetic couplings along the a- and c- axis. For the chain (b-axis) ferromagnetic correlations are favored for a reduced frustration ratio. The shrinking of the b-axis for $H \parallel a$ may also point to the action of the easy-axis anisotropy along the a-axis. However, this shrinking is also observed for $H \parallel b$. Note, that the pressure dependence is negative only in a narrow temperature range at above T_N. Above $\approx 15\,\mathrm{K}$ $\beta^c_{H\|a}$ appears to change sign, while $\beta^a_{H\|a}$ and $\beta^b_{H\|a}$ remain largely unchanged. For the magnetic field dependence of the entropy cf. Fig. 9.4 (maximum of $\chi(T, H_{\|a} = 0.5\,\mathrm{T}) = 11.0(3)\,\mathrm{K}$). In this context it may be relevant, that J_{131} does not only represent an antiferromagnetic inter-chain coupling, but also promotes ferromagnetic intra-chain correlations, which appear to be present up to very high temperatures $T \gg T_\mathrm{N}$ [8, 9]. Magnetostriction measurements at higher temperatures are suggested.

- At the transition at T_N, discussed in more detail in Section 10.2, the c-axis significantly shrinks towards lower temperatures and I_{131} mediates long range commensurate order. The frustration induced by the interactions along the a-axis is reduced by the expansion of a at T_N. The spin chains are forced to assume a ferromagnetic spin arrangement, which is disfavored by a large frustration ratio. The observed shrinking of b thus indicates a reduction of the frustration ratio.

- In the ordered state in low fields $\mu_0 H \lesssim 8\,\mathrm{T}$ the b- and c-axes expand, while the a-axis shrinks. This is in agreement with mixing of incommensurate excitations into the collinear zero field ground state. Indeed, the INS spectra presented in this thesis are strongly supportive for such scenario (cf. Section 5.7).

- At low temperatures, in magnetic field just below H_c, all axes expand. The corresponding volume expansion indicates a sizable pressure dependence of the magnetization (non-zero for $T > 0$). Here, a sizable mixing of magnons into the antiferromagnetic state is to be expected. Just as at $T > T_\mathrm{N}$, a reduction of the antiferromagnetic inter-chain couplings along a and c with increasing ferromagnetic inter-chain correlations is imperative. The expansion of the b-axis would be in agreement with a largely incommensurate nature of the magnons, again supported by the INS magnon spectrum.

- Entering the intermediate phase at low temperatures goes along with an expansion of the c-axis, while both the a- and b-axes are shrinking. An interpretation of this behavior is complicated by missing knowledge of the ground state and the excitation spectrum in this phase. The excitation spectrum can be expected especially important as the excitation gap should be small. However, the proposed model on the relation between lattice expansion, exchange coupling scheme and spin-spin correlations suggests a ground state well distinguished from the zero field ground state and a spin-flopped state. While, the contraction of the b-axis points to a state with persistent ferromagnetic in-chain correlations, the elongation of the c-axis indicates a reduction of antiferromagnetic correlations between neighboring chains. The concomitant shrinking of the a-axis reflects a reduction of ferromagnetic correlations between chains along this direction. Within this interpretation, the lattice expansion suggests a state of the intermediate phase characterized by a non-collinear arrangement of ferromagnetic chains. This proposal should be verified experimentally.

- In magnetic fields $\geqq 13\,\mathrm{T}$ the intermediate phase is continuously suppressed by a crossover to a high field phase. The magnetization at higher fields closely resembles that of a spin-flopped antiferromagnet. For $\mu_0 H > 14.5\,\mathrm{T}$, i.e. above the crossover regime, the suppression of antiferromagnetic correlations by the magnetic field can be expected to cause an expansion of the lattice along the antiferromagnetic exchange paths. This can clearly be observed for the a-axis and c-axis. In high field J_{131} cannot stabilize collinear correlations along the chain. However, the chain is observed to contract to values even lower than in zero field, indicating continued ferromagnetic in-chain correlations.

10.4. Thermal expansion in magnetic fields along the hard axes

In order to trace the magnetic field dependence of T_N in magnetic field applied along the hard axes, the thermal expansion the b-axis for magnetic field $H \parallel b$ has been examined, data are given in Fig. 10.8. For magnetic fields applied along the c-axis, a similar phase boundary is expected. The experiment has been performed on the same $l_b = 3.96$ mm crystallite as used for measurements with $H \parallel a$ (see above). Note, that in comparison the thermal expansion coefficient $\alpha_b(H = 0, T = T_\mathrm{N})$ is observed here $\approx 15\%$ larger, maybe due to slight canting of the sample in the (b, c)-plane. The thermal expansion coefficient close to T_N is found to show about no broadening with applied field as to be expected for a sample canted in the (a, b)-plane. Thus, the data can be regarded reliable for the construction of the magnetic phase diagram for magnetic field applied along the hard b-axis (cf. Fig. 7.4) from the maxima of the thermal expansion coefficient.

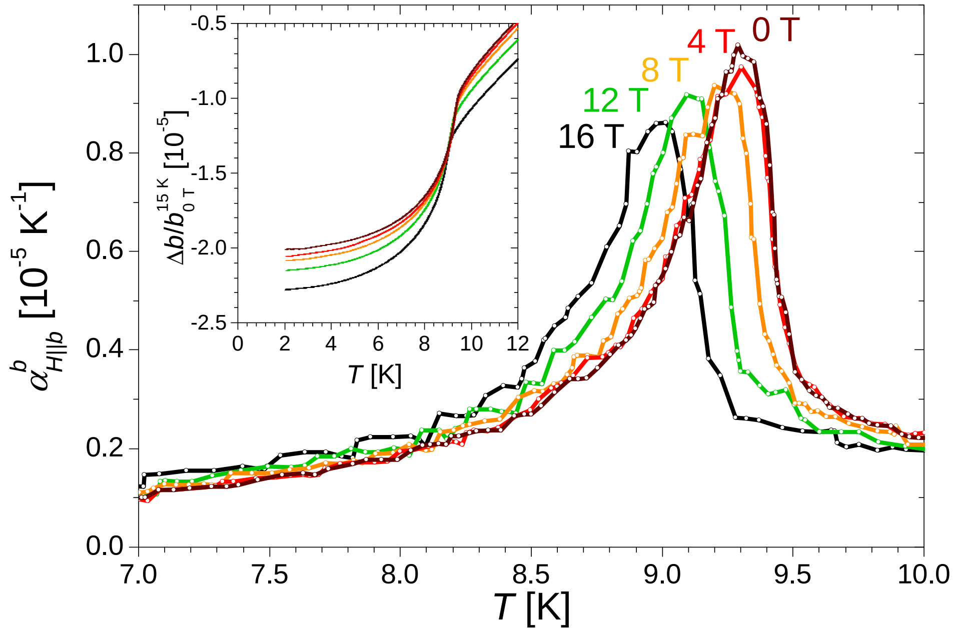

Figure 10.8.: The thermal expansion coefficient α^b of Li_2CuO_2 in magnetic fields $H_{\|b} \leq 16\,\mathrm{T}$ indicates an only weak magnetic field dependence of T_N. Also, the height of the anomaly is scarcely reduced in field. (Inset) The relative length change $\Delta b/b$ normalized at $T = 15\,\mathrm{K}$ and $H = 0$.

Part IV.

Conclusion

That's a Chaos Emerald.
It's said this gem can transform
your thoughts into power.
Collect seven, and a miracle
's supposed to happen.

Blaze the Cat

11. Summary and Outlook

In this thesis, experimental studies on the spin-dynamics of the cuprate Li_2CuO_2 are presented. All experiments have been performed on a high quality single crystal of $^7Li_2CuO_2$. The fundamental properties of this sample are in general agreement to the once previously reported in literature. Employing inelastic neutron scattering and thermodynamic methods the magnetic excitations spectrum and the magnetic phase diagram have been investigated. As a conclusion to this thesis this section provides an overview over the most well verified results and intruding open questions.

Inelastic neutron scattering experiments have been undertaken predominantly in the low temperature long range antiferromagnetically ordered phase. The magnetic excitation spectrum is observed to be dominated by two nearly degenerate branches of excitations which could not be distinguished in measurements in zero magnetic field. For momentum transfer along the CuO_2 chains, that are characteristic for the material's crystallographic structure, the excitations show a pronounced dispersion, but are comparably flat for perpendicular momentum transfer. Hereby the distinct quasi-one-dimensional nature of the magnetic interactions in the compound, as predicted theoretically, was unequivocally evidenced by experiment for the first time.

The observed dispersion of excitations has been analyzed within a spin-wave model. This approach is justified by the mostly narrow line width of the observed excitations as well as the large ordered moment reported in literature. In return, spin-wave theory predicts only weak fluctuations using the exchange parameters obtained from a spin-wave fit to our data. These exchange parameters include a strong ferromagnetic exchange between nearest neighbors in the chain. The obtained value of $-230(2)\,\mathrm{K}$ is significantly larger that expected from theory, but can be described adopting a strong Cu-O direct exchange $K_{pd} \approx 80\,\mathrm{meV}$ in a 5-band HUBBARD-model. The ferromagnetic nearest neighbor coupling is found to be strongly frustrated by an antiferromagnetic next-nearest neighbor exchange coupling in chain direction. The respective frustration ratio is larger than the critical value in pure one-dimensional chains and the ground state should thus be helical, in contrast to the observed magnetic structure. The collinear spin-order is shown to be stabilized by the dominant inter-chain coupling and exchange anisotropy. Three different inter-chain interactions could be identified which compete with another. As a consequence of this rather delicate competition, spin-waves at lowest energy are not only found at the magnetic zone center, but also at incommensurate wave-vectors and the density of states shows a pronounced VAN

Hove-singularity just above the anisotropy gap. This singularity is considered to significantly influence the low temperature thermodynamic properties and stresses the importance of the anisotropy for the stability of the ground state.

Besides the magnon excitations, the spectrum exhibits excitations at energies below the magnon gap, which have been investigated extensively. A clear interpretation hereof is however yet missing. Modulations of the spin-structure near impurity sites are suggested.

A further feature of the spectrum are excitation continua at energies larger than the magnon gap. These continua are shown to not be due to thermal fluctuations and to posses a non-trivial dynamic structure factor. Their presence may indicate non-negligible, remnant one-dimensionality of the spectrum. In this thesis the excitation continua have however not been discussed in detail.

The thermodynamic properties of Li_2CuO_2 have been probed by magnetization, specific heat, thermal expansion and magnetostriction measurements. With these techniques the magnetic phase diagram has been mapped out and the observed phases and phase transitions have been characterized. From specific heat and magnetization measurements isentropes for magnetic field along the easy axis are constructed. Connections between the observed features and the exchange interactions obtained from inelastic neutron scattering are pointed out.

The temperature dependence of the magnetization is shown to not follow a Curie-Weiss-behavior even above 300 K. Short range magnetic correlations are also observed in specific heat data up to $T > 40\,\mathrm{K}$. Long range antiferromagnetic order sets in below 9.25(5) K and the phase boundary shifts to lower temperatures in magnetic fields with a mean-field exponent. Magnetic ordering is found to be accompanied by a notable anisotropic volume reduction. A correspondingly large pressure dependence of the ordering temperature is determined from thermal expansion and specific heat data and verified by magnetization measurements under applied pressure. The large pressure dependence of T_N strongly suggests to put effort into the growth of Na_2CuO_2, although the production of the compound seems to be far from trivial.

Also, the meta-magnetic transition, which is observed at low temperatures in magnetic fields along the easy axis is found to go along with strong anisotropic deformation of the sample. The lattice expansion at the meta-magnetic transition and at T_N is interpreted in terms of the Van Hove singularity in the magnon density of states and a corresponding stark sensitivity of the low energy spectrum to weak changes of the exchange interactions. At the meta-magnetic transition and low temperatures, the compound is shown to enter an intermediate phase. At higher magnetic fields a cross-over to a spin-flop-like phase is observed. From pulsed-field magnetization measurements the saturation field has been determined. Calculations of the saturation field within DMRG and spin-wave theory confirm the inter-sub-lattice interaction obtained from spin-wave analysis of the excitation spectrum. The weak fluctuations in high magnetic field and the agreement between the DMRG results and experiment on the saturation field provide good evidence, that the spin-wave analysis of the excitation spectrum is justified and the obtained exchange parameters are indeed reliable.

The low temperature weak ferrimagnetism of the compound was investigated by magnetization measurements. As an underlying mechanism, DZYALOSHINSKI-MORIYA interaction between moments at oxygen sites is proposed and suggested to induce the formation of a magnetic superstructure at low temperature.

The low temperature magnetization and specific heat data in magnetic field along the easy axis cannot be explained in terms of a gapped antiferromagnet. While a connection to the respective anomalies to the low energy excitations observed by inelastic neutron scattering is likely, as a rigorous proof hereof AC-susceptibility $\chi(H)$ measurements are suggested. Furthermore, specific heat measurements down to lowest temperatures are expected to provide deeper insight into the sub-magnon-gap excitation spectrum. Controlled reduction of the Li-content of the sample is suggested in order to verify, if impurity sites are the origin of the sub-magnon-gap states.

The origin of the exchange anisotropy in Li_2CuO_2 is yet unclear. Although weak, the anisotropy is certainly is one of the crucial factors that determine its macroscopic and microscopic properties. The anisotropy also determines the ground state of the isolated chain in ferromagnetic-antiferromagnetic frustrated systems. Analysis of the excitation spectrum in magnetic field is suggested in order to distinguish anisotropies of the different exchange parameters. Another important open question refers to the value of T_N and in particular to the evolution of intra-chain and inter-chain correlations above T_N.

Part V.

Appendix

A. Supplementary data

A.1. Excitation spectrum in applied magnetic field

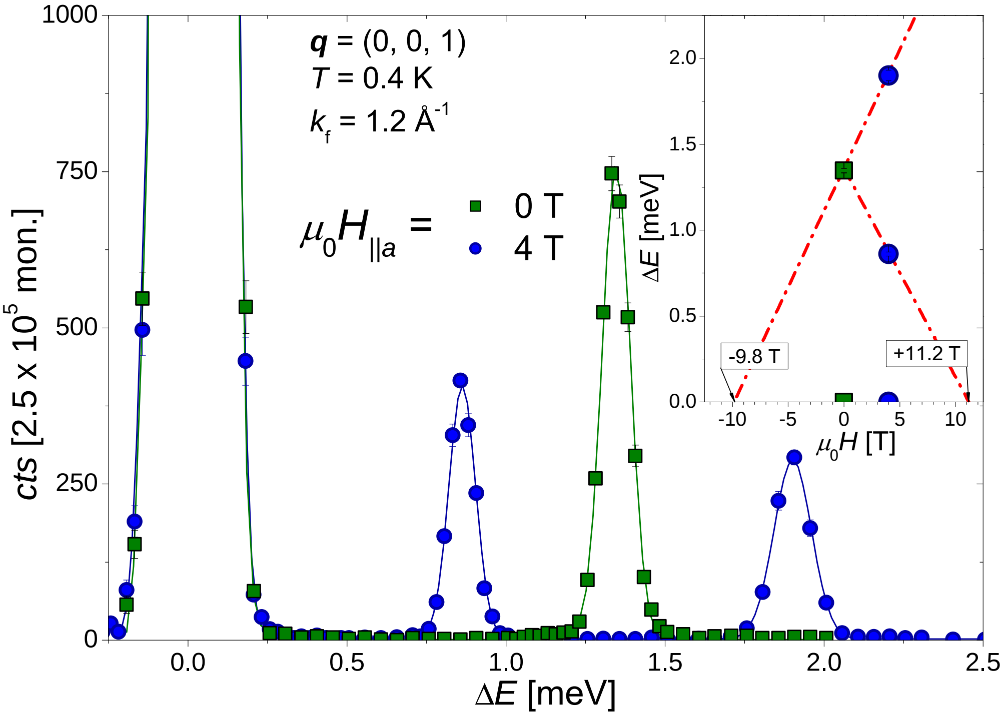

Figure A.1.: INS energy transfer scans at the magnetic zone center $\vec{q} = (0, 0, 1)$ at low temperaute $T = 0.4\,\mathrm{K}$ in externally applied magnetic fields $\mu_0 H_{\|a} = 0\,\mathrm{T}$ and $4\,\mathrm{T}$. The slight asymmetry of the Bragg-peak (peak height $1.7 \cdot 10^6 cts$) is due to some intensity near $\Delta E \approx 0.04\,\mathrm{meV}$. Note the significant increase of the line-width of the magnon branch shifted to higher energy. Lines represent fits by Gaussian distributions. The inset shows the fitted peak positions. Note the asymmetric shift of both magnon branches with magnetic field. Data taken at IN12/ILL.

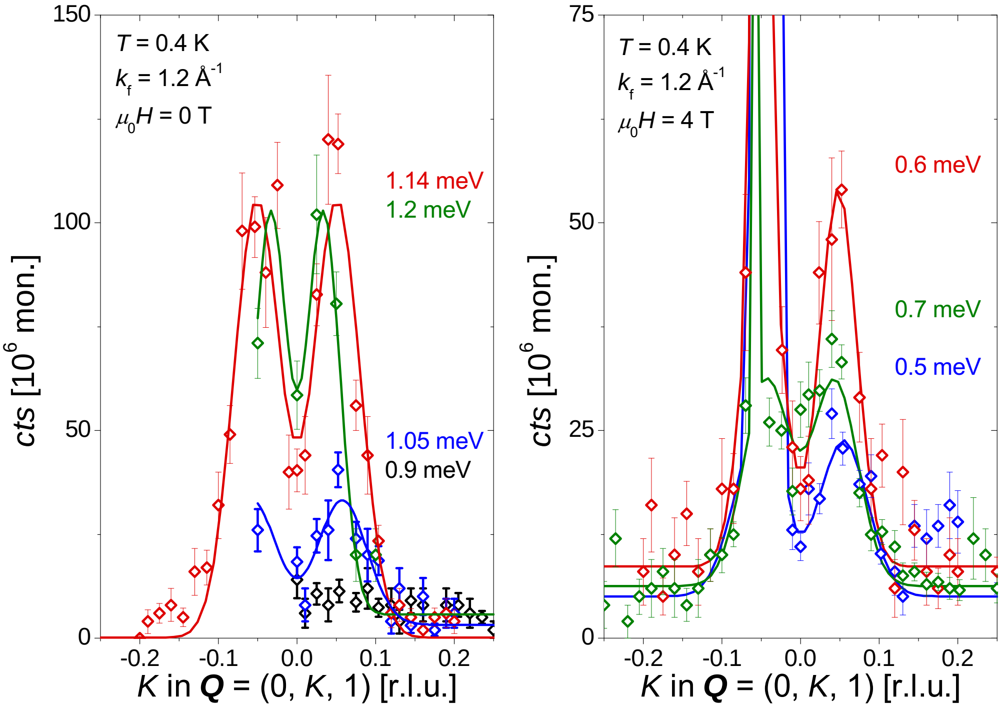

Figure A.2.: Complementing constant momentum transfer scans at $\vec{q} = (0, 0.05, 1)$ in magnetic fields $H_{\parallel a}$ in Fig. 6.3, constant energy scans with momentum transfer varied along the chain are shown for the sub-gap state just below the gap . This feature, observed at 1.13(1) meV in zero field is located near $K = 0.051(1)$ (left). Shifted in energy in $H_{\parallel a} = 4\,\mathrm{T}$ to 0.62(1) meV it remains at the same position in momentum space $K = 0.048(2)$, within experimental accuracy (right). The strong and narrow peak at low energy transfer and $K < 0$ is due to spurious scattering at the magnetic $(0, 0, 1)$-reflex. Lines represent fits by Gaussian distributions assuming symmetry of the excitations around $K = 0$. Data taken at IN12/ILL.

A.2. Low temperature specific heat

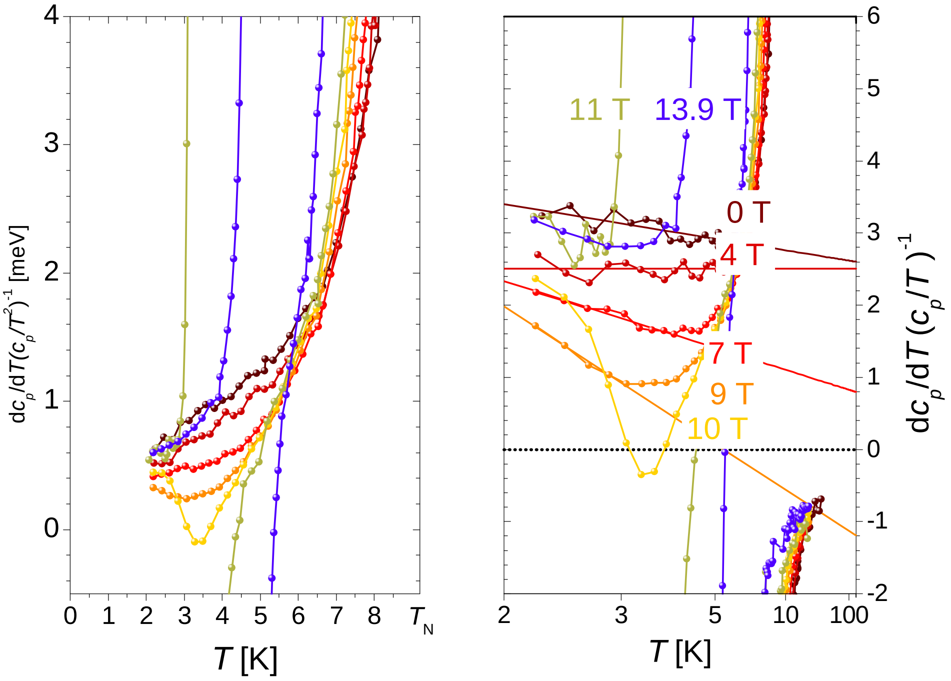

Figure A.3.: For c_p the applicability of Eqn. 9.9 is tested equivalently to the description given for the data in $H = 0$ presented in Fig. 9.7. The data at 12 and 13 T are omitted in order to increase clarity of the figures. The curves are largely positive (negative) below (above) phase transitions. Note the extraordinary behavior of the data set at 10 T, here just slightly below H_c.

A.3. Pressure dependence of T_N for $H_{\|a} = 12\,\mathrm{T}$

With the data along the different crystallographic axes measured in independent experiments with unavoidable differences in misalignment of the crystals with respect to the applied field, the analysis of volume changes in magnetic field is more error-prone than for $H = 0$. Just as for the specific heat and thermal expansion data in zero magnetic field (cf. Section 10.2) the pressure dependence of the NÉEL temperature is determined data taken at $\mu_0 H_{\|a} = 12\,\mathrm{T}$ (cf. Fig. A.4). The transition is less pronounced, also the data are relatively more noisy than for the data at $H = 0$. The well corresponding magnetic phase diagrams derived from the experiments suggest a well comparable alignment of the samples easy axis along the field direction. The EHRENFEST scaling (cf. Eqn. 10.2) indicates a further increase of the uniaxial pressure dependence of T_N for pressures along the c-axis and a reduction for pressure applied along a and b in 12 T compared to the results obtained from zero field data.

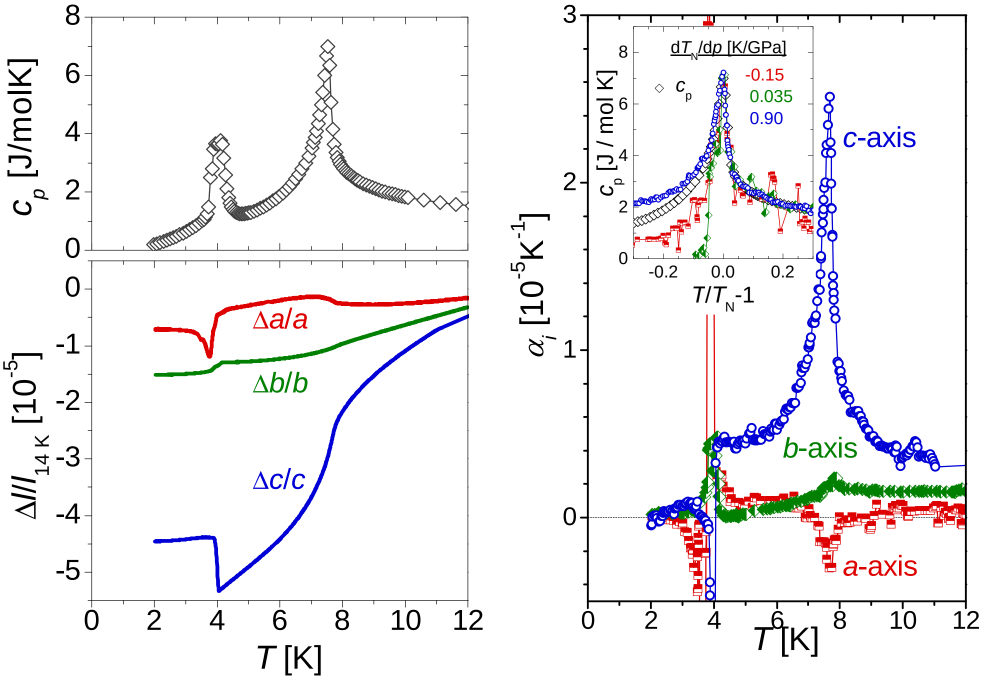

Figure A.4.: (left) specific heat and thermal expansion of Li$_2$CuO$_2$ at $\mu_0 H_{\|a} = 12\,\mathrm{T}$. (right) Thermal expansion coefficients α_i of Li$_2$CuO$_2$ at $\mu_0 H_{\|a} = 12\,\mathrm{T}$. Inset: scaling behavior of α_i projected onto c_p near T_N.

A.4. Pressure dependence of magnetization

In a SQUID magnetometer the pressure dependence of the magnetization of polycrystalline Li$_2$CuO$_2$ has been coarsely examined. No background contribution of the pressure cell is taken account for. The large pressure dependence of T_N obtained from thermal expansion could be verified. Nevertheless, the data show a set of further interesting features. Firstly, also T_2 is found to be pressure dependent (cf. Fig. A.5). To obtain high quality data on the sample at low T and H is however challenging. The superconducting (SC) Pb samples, which are used to determine the pressure in the cell (inside pressure cell 0.67 mg, outside 1.03 mg) produces a sizeable background.

This background produced by the Pb samples is expected to be small for the data measured in field far above the critical field H_{SC}(Pb) breaking SC in Pb. Here, besides the already mentioned shift of T_N, an increase of M with p at $T > T_\mathrm{N}$ is obvious in the data measured. This shift is found rather constant in the range of $11.5 \leq T \leq 50\,\mathrm{K}$, form comparison of the data taken at $p = 0$ and "$p = 650$ kg". Note that such positive pressure dependence contradicts our single crystal magnetostriction data for $H \parallel a$, verified in the range $10\,\mathrm{K} \leq T \leq 15\,\mathrm{K}$ (cf. Fig. 10.7). Careful determination of the pressure cell background is expected to clarify this discrepancy.

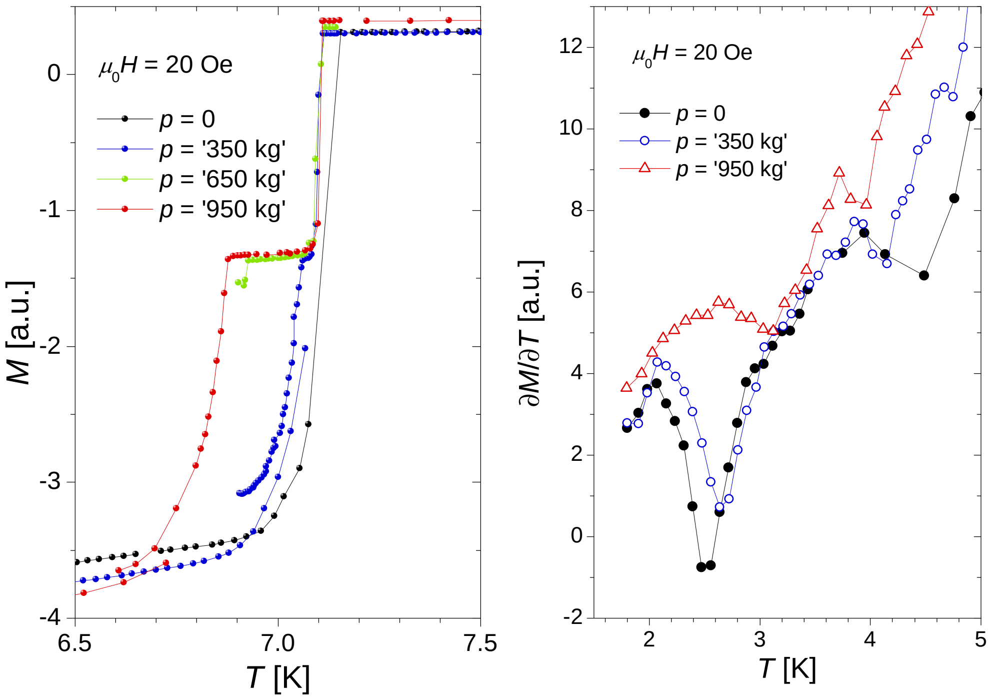

Figure A.5.: (left) Using two tiny Pb samples inside and outside the pressure cell the internal pressure is obtained from the onset of the SC transition in external fields of 20 Oe. Data with low density in T are measured sweeping T while more precise determination of T_c with higher data point density is performed in T-settle-mode. The curves are labeled by the weight applied to the pressure cell prior to the experiment. For the curve named ”$p = 650$ kg” the transition is not clearly observed in the measured T-range and thus assumed to be between the initially applied pressure and the lowest one in agreement with the data. Under pressure, the superconducting transition significantly broadens, presumably due to stresses in the Pb sample. The average pressure in the cell may therefore be larger than indicated by the onset of the transition. (right) At lowest temperature and $\mu_0 H = 20$ Oe the data are dominated by the SC Pb even in $\partial M/\partial T$. Nevertheless, the onset of weak ferromagnetism in Li_2CuO_2 at T_2 - indicated by the low T minimum in dM/dT - is clearly observed. The data provide evidence for an very large positive pressure dependence. Around 4 K another pressure dependent feature is observed, absent in the single crystal data in Chapter 8.

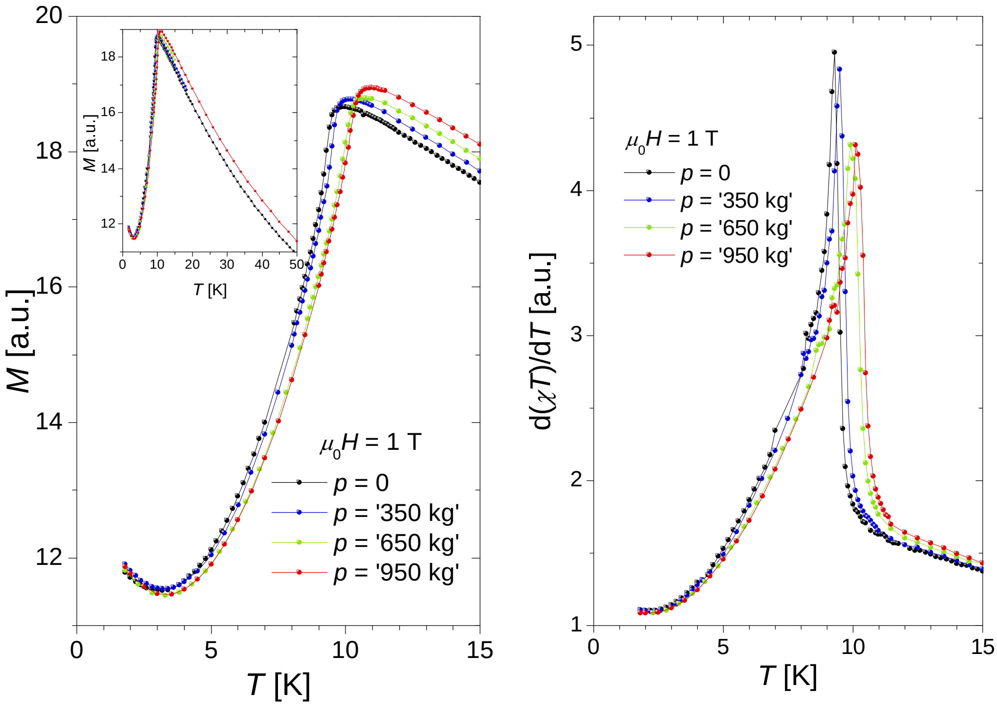

Figure A.6.: (left) magnetization data of polycrystalline Li_2CuO_2 under external pressure. The inset stresses the pressure dependence of M up to $T = 50\,\mathrm{K}$. Note, that along with thermal expansion of pressure cell and sample the pressure (assigned at $T \approx 7\,\mathrm{K}$) as well as background contributions to the data are temperature dependent. (right) The NÉEL temperature is identified from the maximum of the FISHER specific heat $\partial(\chi T)/\partial T$. The accordingly obtained $T_{\mathrm{N}}(p)$ data are compared with the pressure dependence of $T_{\mathrm{N}}(p)\big|_{p=0}$ obtained from thermal expansion in Fig. 10.2 on page 138.

Bibliography

[1] H. A. Frith, Butterfly, Big Life, 1994, Oyster.

[2] P. W. Anderson, *Science* **177**, 393 (1972).

[3] R. Hoppe and H. Rieck, *Z. anorg. allg. Chem.* **379**, 157 (1970).

[4] G. Vitins, E. A. Raekelboom, M. T. Weller, and J. R. Owen, *J. Power Sources* **119-121**, 938 (2003).

[5] A. S. Prakash, D. Larcher, M. Morcrette, M. S. Hegde, J.-B. Leriche, and C. Masquelier, *Chem. Mater.* **17**, 4406 (2005).

[6] N. Imanishi, K. Shizukaa, T. Ikenishi, T. Matsumura, A. Hirano, and Y. Takeda, *Solid State Ionics* **177**, 1341 (2006).

[7] L. M. Palacios-Romero and H. Pfeiffer, *Chem. Lett.* **37**, 862 (2008).

[8] C. Monney, V. Bisogni, K. Zhou, R. Kraus, V. Strocov, J. Geck, and T. Schmitt, unpublished.

[9] S.-L. Drechsler, private communications.

[10] E. Dagotto, *Science* **309**, 257 (1996).

[11] S. Nakatsuji, S. Ikeda, and Y. Maeno, *J. Phys. Soc. Jpn.* **66**, 1868 (1997).

[12] S. A. Grigera, R. S. Perry, A. J. Schofield, M. Chiao, S. R. Julian, G. G. Lonzarich, S. I. Ikeda, Y. Maeno, A. J. Millis, and A. P. Mackenzie, *Science* **294**, 329 (2001).

[13] S. Lee, J.-G. Park, D. T. Adroja, D. Khomskii, S. Streltsov, K. A. McEwen, H. Sakai, K. Yoshimura, V. I. Anisimov, D. Mori, R. Kanno, and R. Ibberson, *Nature materials* **5**, 471 (2006).

[14] B. J. Kim, H. Ohsumi, T. Komesu, S. Sakai, T. Morita, H. Takagi, and T. Arima, *Science* **323**, 1329 (2009).

[15] J. Zaanen, G. A. Sawatzky, and J. W. Allen, *Phys. Rev. Lett.* **55**, 418 (1985).

[16] J. B. Torrance, P. Lacorre, C. Asavaroengchai, and R. M. Metzger, *Physica C* **182**, 351 (1991).

[17] T. Böske, K. Maiti, O. Knauff, K. Ruck, M. S. Golden, G. Krabbes, J. Fink, T. Osafune, N. Motoyama, H. Eisaki, and S. Uchida, *Phys. Rev. B* **57**, 138 (1998).

[18] R. Neudert, H. Rosner, S.-L. Drechsler, M. Kielwein, M. Sing, Z. Hu, M. Knupfer, M. S. Golden, and J. Fink, *Phys. Rev. B* **60**, 13413 (1999).

[19] Z. Hu, S.-L. Drechsler, J. Málek, H. Rosner, R. Neudert, M. Knupfer, M. S. Golden, J. Fink, J. Karpinski, G. Kaindl, C. Hellwig, and C. Jung, *Europhys. Lett.* **59**, 135 (2002).

[20] Y. Mizuno, T. Tohyama, S. Maekawa, T. Osafune, N. Motoyama, H. Eisaki, and S. Uchida, *Phys. Rev. B* **57**, 5326 (1998).

[21] S. Atzkern, M. Knupfer, M. S. Golden, J. Fink, C. Waidacher, J. Richter, K. W. Becker, N. Motoyama, H. Eisaki, and S. Uchida, *Phys. Rev. B* **62**, 7845 (2000).

[22] M. Knupfer, J. Fink, S.-L. Drechsler, R. Hayn, J. Málek, and A. Moskvin, *J. El. Spec. Rel.* **137–140**, 469 (2004).

[23] K. Okada and A. Kotani, *Phys. Rev. B* **63**, 045103 (2001).

[24] Y.-J. Kim, J. P. Hill, F. C. Chou, D. Casa, T. Gog, and C. T. Venkataraman, *Phys. Rev. B* **69**, 155105 (2004).

[25] D. Qian, Y. Li, M. Hasan, D. Casa, T. Gog, Y.-D. Chuang, K. Tsutsui, T. Tohyama, S. Maekawa, H. Eisaki, and S. Uchida, *J. Phys. Chem. Sol.* **66**, 2212 (2005).

[26] T. Learmonth, C. McGuinness, P.-A. Glans, J. E. Downes, T. Schmitt, L.-C. Duda, J.-H. Guo, F. C. Chou, and K. E. Smith, *Europhys. Lett.* **79**, 47012 (2007).

[27] F. Vernay, B. Moritz, I. S. Elfimov, J. Geck, D. Hawthorn, T. P. Devereaux, and G. A. Sawatzky, *Phys. Rev. B* **77**, 104519 (2008).

[28] R. Weht and W. E. Pickett, *Phys. Rev. Lett.* **81**, 2502 (1998).

[29] N. Tanaka, M. Suzuki, and K. Motizuki, *J. Magn. & Magn. Mater.* **196–197**, 667 (1999).

[30] N. Tanaka, M. Suzuki, and K. Motizuki, *J. Phys. Soc. Jpn.* **68**, 1684 (1999).

[31] H. Rosner, R. Hayn, and S.-L. Drechsler, *Physica B* **259–261**, 1001 (1999).

[32] Y. Mizuno, T. Tohyama, and S. Maekawa, *Phys. Rev. B* **60**, 6230 (1999).

[33] N. Tanaka, M. Suzuki, and K. Motizuki, *Physica B* **284–288**, 1388 (2000).

[34] C. de Graaf, I. de P. R. Moreira, F. Illas, Ò. Iglesias, and A. Labarta, *Phys. Rev. B* **66**, 014448 (2002).

[35] S.-L. Drechsler, J. Richter, J. Málek, A. S. Moskvin, R. Klingeler, and H. Rosner, *J. Magn. & Magn. Mater.* **290–291**, 345 (2005).

[36] D. Mertz, R. Hayn, I. Opahle, and H. Rosner, *Phys. Rev. B* **72**, 085133 (2005).

[37] S.-L. Drechsler, J. Richter, R. Kuzian, J. Málek, N. Tristan, B. Büchner, A. S. Moskvin, A. A. Gippius, A. Vasiliev, O. Volkova, A. Prokofiev, H. Rakoto, J.-M. Broto, W. Schwelle, M. Schmitt, A. Ormeci, C. Loison, and H. Rosner, *J. Magn. & Magn. Mater.* **316**, 306 (2007).

[38] J. Málek, S.-L. Drechsler, U. Nitzsche, H. Rosner, and H. Eschrig, *Phys. Rev. B* **78**, 060508(R) (2008).

[39] W. E. A. Lorenz, R. O. Kuzian, S.-L. Drechsler, W.-D. Stein, N. Wizent, G. Behr, J. Málek, U. Nitzsche, H. Rosner, A. Hiess, W. Schmidt, R. Klingeler, M. Loewenhaupt, and B. Büchner, *Europhys. Lett* **88**, 37002 (2009).

[40] S.-L. Drechsler, J. Málek, S. Nishimoto, U. Nitzsche, R. Kuzian, H. Eschrig, and H. Rosner, *J. Phys.: Conf. Ser.* **145**, 012060 (2009).

[41] S.-L. Drechsler, J. Málek, R. Kuzian, S. Nishimoto, U. Nitzsche, W. Lorenz, R. Klingeler, B. Büchner, and M. Knupfer, *Physica C* **470**, S84 (2010).

[42] U. Schollwöck, J. Richter, D. J. J. Farnell, and R. F. Bishop, editors, *Quantum Magnetism*, volume 645 of *Lect. Notes Phys.*, Springer, Berlin Heidelberg, 2004.

[43] N. D. Mermin and H. Wagner, *Phys. Rev. Lett.* **17**, 1133 (1966).

[44] P. C. Hohenberg, *Phys. Rev.* **158**, 383 (1967).

[45] S. Coleman, *Commun. Math. Phys.* **31**, 259 (1973).

[46] S. Itoh, Y. Endoh, K. Kakurai, H. Tanaka, S. M. Bennington, T. G. Perring, K. Ohoyama, M. J. Harris, and C. D. Frost, *Phys. Rev. B* **59**, 14406 (1999).

[47] F. D. M. Haldane, *Phys. Rev. Lett.* **50**, 1153 (1983).

[48] G. Xu, G. Aeppli, M. E. Bisher, C. Broholm, J. F. DiTusa, C. D. Frost, T. Ito, K. Oka, R. L. Paul, H. Takagi, and M. M. J. Treacy, *Science* **289**, 419 (2000).

[49] E. Dagotto and T. M. Rice, *Science* **271**, 618 (1996).

[50] V. O. Garlea, A. Zheludev, T. Masuda, H. Manaka, L.-P. Regnault, B. Ressouche, E. Grenier, J.-H. Chung, K. Qiu, Y. Habicht, K. Kiefer, and M. Boehm, *Phys. Rev. Lett.* **98**, 167202 (2007).

[51] L. D. Faddeev and L. A. Takhtajan, *Phys. Lett. A* **85**, 375 (1981).

[52] D. A. Tennant, T. G. Perring, R. A. Cowley, and S. E. Nagler, *Phys. Rev. Lett.* **70**, 4003 (1993).

[53] M. Kenzelmann, Y. Chen, C. Broholm, D. H. Reich, and Y. Qiu, *Phys. Rev. Lett.* **93**, 017204 (2004).

[54] C. Kim, A. Y. Matsuura, Z.-X. Shen, N. Motoyama, H. Eisaki, S. Uchida, T. Tohyama, and S. Maekawa, *Phys. Rev. Lett.* **77**, 4054 (1996).

[55] A. Lascialfari, R. Ullu, M. Affronte, F. Cinti, A. Caneschi, D. Gatteschi, D. Rovai, M. G. Pini, and A. Rettori, *Phys. Rev. B* **67**, 224408 (2003).

[56] J. W. Bray, H. R. Hart, L. V. Interrante, I. S. Jacobs, J. S. Kasper, G. D. Watkins, and S. H. Wee, *Phys. Rev. Lett.* **35**, 744 (1975).

[57] M. Hase, I. Terasaki, and K. Uchinokura, *Phys. Rev. Lett.* **70**, 3651 (1993).

[58] G. Castilla and V. J. Chakravarty, S adn Emery, *Phys. Rev. Lett.* **75**, 1823 (1995).

[59] A. Zheludev, M. Kenzelmann, S. Raymond, T. Masuda, K. Uchinokura, and S.-H. Lee, *Phys. Rev. B* **65**, 014402 (2001).

[60] N. Motoyama, H. Eisaki, and S. Uchida, *Phys. Rev. Lett.* **76**, 3212 (1996).

[61] J. Kanamori, *J. Phys. Chem. Solids* **10**, 87 (1959).

[62] J. B. Goodenough, *Phys. Rev.* **100**, 564 (1955).

[63] P. W. Anderson, *Theory of Magnetic Exchange Interaction: Exchange in Insulators and Semiconductors*, Academic, New York, 1963.

[64] W. Geertsma and D. Khomskii, *Phys. Rev. B* **54**, 3011 (1996).

[65] K. Sreedhar and P. Ganguly, *Inorg. Chem.* **27**, 2261 (1988).

[66] S. A. Caster, B. Batlogg, R. J. Cava, J. J. Krajewski, W. F. Peck, and T. M. Rice, *Phys. Rev. Lett.* **77**, 1378 (1996).

[67] M. Matsuda, K. Ohoyama, and M. Ohashi, *J. Phys. Soc. Jpn.* **68**, 269 (1999).

[68] T. Masuda, A. Zheludev, A. Bush, M. Markina, and A. Vasiliev, *Phys. Rev. Lett.* **92**, 177201 (2004).

[69] L. Capogna, M. Mayr, P. Horsch, R. K. Kremer, M. Sofin, A. Maljuk, M. Jansen, and B. Keimer, *Phys. Rev. B* **71**, 140402 (2005).

[70] M. Hase, K. Ozawa, O. Suzuki, H. Kitazawa, G. Kido, H. Kuroe, and T. Sekine, *J. Appl. Phys.* **97**, 10B303 (2005).

[71] M. Enderle, C. Mukherjee, B. Fåk, R. K. Kremer, J.-M. Broto, H. Rosner, S.-L. Drechsler, J. Richter, J. Málek, A. Prokofiev, W. Assmus, S. Pujol, J.-L. Raggazzoni, H. Rakoto, M. Rheinstädter, and H. M. Rønnow, *Europhys. Lett.* **70**, 237 (2005).

[72] S.-L. Drechsler, N. Tristan, R. Klingeler, B. Büchner, J. Richter, J. Málek, O. Volkova, A. Vasiliev, M. Schmitt, A. Ormeci, C. Loison, W. Schwelle, and H. Rosner, *J. Phys. Cond. Matt.* **19**, 145230 (2007).

[73] M. Baran, A. Jedrzejczak, H. Szymczak, V. Maltsev, G. Kamieniarz, G. Szukowski, C. Loison, A. Ormeci, S.-L. Drechsler, and H. Rosner, *Phy. Stat. Sol. C* **3**, 220 (2006).

[74] M. Schmitt, O. Janson, M. Schmidt, S. Hoffman, W. Schnelle, S.-L. Drechsler, and H. Rosner, *Phys. Rev. B* **79**, 245119 (2009).

[75] H. R. Oswald, A. Reller, H. W. Schalle, and E. Dubler, *Acta Cryst.* **C46**, 2279 (1990).

[76] V. Gnezdilov, P. Lemmens, A. A. Zvyagin, V. O. Cheranovskii, K. Lamonova, Y. G. Pashkevich, R. K. Kremer, and H. Berger, *Phys. Rev. B* **78**, 184407 (2008).

[77] C. P. Landee and R. D. Willett, *Phys. Rev. Lett.* **43**, 463 (1979).

[78] K. Kopinga, A. M. C. Tinus, and W. J. M. de Jonge, *Phys. Rev. B* **25**, 4685 (1982).

[79] H.-J. Mikeska and M. Steiner, *Adv. Phys.* **40**, 191 (1991).

[80] M. Takahashi, P. Turek, Y. Nakazawa, M. Tamura, K. Nozawa, D. Shiomi, M. Ishikawa, and M. Kinoshita, *Phys. Rev. Lett.* **74**, 1673 (1995).

[81] S. J. Blundell and F. L. Pratt, *J. Phys.: Cond. Matter* **16**, R771 (2004).

[82] K. Takeda, K. Konishi, K. Nedachi, and K. Mukai, *Phys. Rev. Lett.* **74**, 1673 (1995).

[83] S. Mahdavifar, *J. Phys.: Cond. Mat.* **20**, 335230 (2008).

[84] C. Itoi and S. Qin, *Phys. Rev. B* **63**, 224423 (2001).

[85] D. V. Dmitriev, V. Y. Krivnov, and J. Richter, *Phys. Rev. B* **75**, 014424 (2007).

[86] R. D. Somma and A. A. Aligia, *Phys. Rev. B* **64**, 024410 (2001).

[87] R. Jafari and A. Langari, *Phys. Rev. B* **76**, 014412 (2007).

[88] T. Hikihara, L. Kecke, T. Momoi, and A. Furusaki, *Phys. Rev. B* **78**, 144404 (2008).

[89] D. V. Dmitriev and V. Y. Krivnov, *Phys. Rev. B* **77**, 024401 (2008).

[90] I. Harada and T. Tonegawa, *J. Magn. & Magn. Mater.* **90–91**, 234 (1990).

[91] A. V. Chubukov, *Phys. Rev. B* **44** (1991).

[92] M. Hase, H. Kuroe, K. Ozawa, O. Suzuki, H. Kitazawa, G. Kido, and T. Sekine, *Phys. Rev. B* **70**, 104426 (2004).

[93] L. Svistov, T. Fujita, H. Yamaguchi, S. Kimura, K. Omura, A. Prokofiev, A. Smirnov, Z. Honda, and M. Hagiwara, *JETP Letters* **93**, 21 (2011).

[94] J. Sudan, A. Lüscher, and M. A. Läuchli, *Phys. Rev, B* **80**, 140402(R) (2009).

[95] F. Heidrich-Meisner, I. P. McCulloch, , and A. K. Kolezhuk, *Phys. Rev. B* **80**, 144417 (2009).

[96] J. C. Bonner and M. E. Fisher, *Phys. Rev.* **135**, A640 (1964).

[97] F. Heidrich-Meisner, A. Honecker, and T. Vekua, *Phys. Rev. B* **74**, 020403(R) (2006).

[98] M. Härtel, J. Richter, D. Ihle, and S.-L. Drechsler, *Phys. Rev. B* **78**, 174412 (2008).

[99] J. Sirker, *Phys. Rev. B* **81**, 014419 (2010).

[100] R. Zinke, S.-L. Drechsler, and J. Richter, *Phys. Rev. B* **79**, 094425 (2009).

[101] S.-W. Cheong and M. Mostovoy, *Nature materials* **6**, 13 (2007).

[102] S. Park, Y. J. Choi, C. L. Zhang, and S.-W. Cheong, *Phys. Rev. Lett.* **98**, 057601 (2007).

[103] Y. Naito, K. Sato, Y. Yasui, Y. Kobayashi, Y. Kobayashi, and M. Sato, *J. Phys, Soc. Jpn.* **76**, 023708 (2007).

[104] S. Seki, T. Kurumaji, S. Ishiwata, H. Matsui, H. Murakawa, Y. Tokunaga, Y. Kaneko, T. Hasegawa, and Y. Tokura, *Phys. Rev. B* **82**, 064424 (2010).

[105] Y. Yasui, M. Sato, and I. Terasaki, *J. Phys. Soc. Jpn.* **20**, 033707 (2011).

[106] A. S. Moskvin, Y. D. Panov, and S.-L. Drechsler, *Phys. Rev. B* **79**, 104112 (2009).

[107] S.-L. Drechsler, S. Nishimoto, R. Kuzian, J. Málek, W. E. A. Lorenz, J. Richter, J. van den Brink, M. Schmitt, and H. Rosner, *Phys. Rev. Lett.* , in print (2011).

[108] W. Losert and R. Hoppe, *Z. anorg. allg. Chem.* **515**, 95 (1984).

[109] M. T. Weller and D. R. Lines, *J. Solid State Chem.* **82**, 21 (1989).

[110] R. Hoffmann, R. Hoppe, and W. Schäfer, *Z. anorg. allg. Chem.* **578**, 18 (1989).

[111] F. Sapiña, J. Rodríguez-Carvajal, M. J. Sanchis, R. Ibáñez, A. Beltrán, and D. Beltrán, *Solid State Commun.* **74**, 779 (1990).

[112] E. M. L. Chung, G. J. McIntyre, D. . Paul, G. Balakrishnan, and M. R. Lees, *Phys. Rev. B* **68**, 144410 (2003).

[113] H. Ohta, N. Yamauchi, T. Nanba, M. Motokawa, S. Kawamata, and K. Okuda, *J. Phys. Soc. Jpn.* **62**, 785 (1993).

[114] V. Y. Yushankhai and R. Hayn, *Europhys. Lett.* **47**, 116 (1999).

[115] S. Kawamata, K. Okuda, and K. Kindo, *J. Magn. & Magn. Mater.* **272–276**, 939 (2004).

[116] K. Okuda, S. Noguchi, K. Konishi, H. Deguchi, and K. Takeda, *J. Magn. & Magn. Mater.* **104–107**, 817 (1992).

[117] M. Boehm, S. Coad, B. Roessli, A. Zheludev, M. Zolliker, P. Böni, D. M. Paul, H. Eisaki, N. Motoyama, and S. Uchida, *Europhys. Lett.* **43**, 77 (1998).

[118] U. Staub, B. Roessli, and A. Amato, *Physica B* **289–290**, 299 (2000).

[119] S. Giri, H. Chudo, H. Nakamura, and M. Shiga, *J. Magn. & Magn. Mater.* **300**, 335 (2006).

[120] M. Boehm, Magnetische Anregungen in Li_2CuO_2, Master's thesis, ETH Zürich, TU Graz, 1998.

[121] V. Y. Yushankhai and R. Hayn, *Physica B* **312–313**, 726 (2002).

[122] H. J. Xiang, C. Lee, and W. M.-H., *Phys. Rev. B* **76**, 220411(R) (2007).

[123] S. Ebisu, T. Komatsu, N. Wada, T. Nashiguchi, P. Kichambare, and S. Nagata, *J. Phys. Chem. Solids* **59**, 1407 (1998).

[124] R. J. Ortega, P. J. Jensen, K. V. Rao, F. Sapiña, A. Beltrán, Z. Iqbal, J. C. Cooley, and J. L. Smith, *J. Appl. Phys.* **83**, 6542 (1998).

[125] R. Klingeler, *Spin- und Ladungsordnung in Übergangsmetalloxiden: Thermodynamische und magnetische Untersuchungen*, PhD thesis, RWTH Aachen, 2002.

[126] S. You, L. Zhi, Y. Liuxiang, D. Cheng, C. Liangcheng, J. Cangqing, H. Jingzhu, S. Guoyin, and M. Hokwang, *J. Solid State Chem.* **182**, 3085 (2009).

[127] T. H. K. Barron, J. G. Collins, and G. K. White, *Adv. Phys.* **29**, 609 (1980).

[128] M. Matsumoto and M. Sigrist, *J. Phys. Soc. Jpn.* **74**, 2310 (2005).

[129] G. Squires, editor, *Introduction to the Theory of Thermal Neutron Scattering*, Dover Publications, 1996.

[130] T. Chatterji, editor, *Neutron Scattering from Magnetic Materials*, Elsevier B. V., 2006.

[131] F. Hippert, E. Geissler, E. Lelièvre-Berna, and J.-R. Regnard, editors, *Neutron and X-ray Spectroscopy*, Springer, 2006.

[132] A.-J. Dianoux and G. Lander, editors, *Neutron Data Booklet*, *Institut Laue-Langevin*, 2003.

[133] E. Prince, editor, *International Tables for Crystallography Volume C: Mathematical, physical and chemical tables*, Springer, 2006.

[134] G. J. Tomka, C. Ritter, P. C. Riedi, C. Kapusta, and W. Kocemba, *Phys. Rev. B* **58**, 6330 (1998).

[135] H. G. Bohn, W. Zinn, B. Dorner, and A. Kollmar, *Phys. Rev. B* **22**, 5447 (1980).

[136] Neutron Scattering Lengths and cross sections, http://www.ncnr.nist.gov/resources/n-lengths/list.html.

[137] G. Behr, W. Löser, D. Souptel, G. Fuchs, I. Mazilu, C. Cao, A. Köhler, L. Schultz, and B. Büchner, *J. Cryst. Growth* **310**, 2268 (2008).

[138] N. Wizent, G. Behr, W. Löser, B. Büchner, and R. Klingeler, *J. Crystal Growth* **318**, 995 (2011).

[139] H. Effenberger and J. Zemann, *Z. Krist.* **150**, 133 (1979).

[140] S. Åsbrink and L.-J. Norrby, *Acta Cryst.* **B26**, 8 (1970).

[141] H. Maeter, Electrochemistry and magnetism in the low dimensional quantum spin system $Li_{2-x}CuO_2$, Master's thesis, TU Braunschweig, 2007.

[142] M. Matsuda, H. Yamaguchi, T. Ito, C. H. Lee, K. Oka, Y. Mizuno, T. Tohyama, S. Maekawa, and K. Kakurai, *Phys. Rev. B* **63**, 180403(R) (2001).

[143] T. Oguchi, *Phys. Rev.* **117**, 117 (1960).

[144] S.-L. Drechsler, J. Málek, W. Lorenz, R. Kuzian, R. Klingeler, S. Nishimoto, U. Nitzsche, M. Knupfer, N. Wizent, G. Behr, H. Rosner, H. Eschrig, and B. Büchner, *J. Phys.: Conf. Ser.* **200**, 012028 (2010).

[145] S. Nishimoto, S.-L. Drechsler, R. O. Kuzian, J. van den Brink, J. Richter, W. E. A. Lorenz, Y. Skourski, R. Klingeler, and B. Büchner, *arXiv:1004.3300v2* (2010).

[146] T. B. S. Jensen, *Magnetic structures, phase diagram and spin waves of magneto-electric LiNiPO$_4$*, PhD thesis, Technical University of Denmark, 2007.

[147] T. B. S. Jensen, N. B. Christensen, M. Kenzelmann, H. M. Rønnow, C. Niedermayer, N. H. Andersen, K. Lefmann, M. Jiménez-Ruiz, F. Demmel, J. Li, J. L. Zarestky, and D. Vaknin, *Phys. Rev. B* **79**, 092413 (2009).

[148] Y. Tokiwa, unpublished, 2004, faraday balance data, MPI-CPfS Dresden.

[149] Y. Shapira and S. Foner, *Phys. Rev. B* **1**, 3083 (1970).

[150] P. Heller, *Phys. Rev.* **146**, 403 (1966).

[151] A. Bienenstock, *J. Appl. Phys.* **37**, 1459 (1966).

[152] J. Feder and E. Pytte, *Phys. Rev.* **168**, 640 (1968).

[153] F. B. Anderson and H. B. Callen, *Phys. Rev.* **136**, 1068 (1964).

[154] V. G. Morozov, *Phys. Stat. Sol. B* **50**, 479 (1982).

[155] B. C. S. Grandi and W. Figueiredo, *Phys. Lett. A* **139**, 281 (1989).

[156] A. R. King and H. Rohrer, *Phys. Rev. B* **19**, 5864 (1979).

[157] Y. Tanaka, K. Osaki, and N. Uryû, *J. Phys. Soc. Jpn.* **45**, 1457 (1978).

[158] I. Dzyaloshinski, *J. Phys. Chem. Solids* **4**, 241 (1958).

[159] T. Moriya, *Phys. Rev.* **102**, 91 (1960).

[160] R. M. Bozorth and V. Kramer, *J. Phys. Radium* **20**, 393 (1959).

[161] M. Bode, M. Heide, K. von Bergmann, P. Ferriani, S. Heinze, G. Bihlmayer, A. Kubetzka, O. Pietzsch, S. Blügel, and R. Wiesendanger, *Nature* **447**, 190 (2007).

[162] D. G. Clarke, T. Giamarchi, and B. I. Shraiman, *Phys. Rev. B* **48**, 7070 (1993).

[163] T. Roscilde, *Rev. Sci. Instrum.* **69**, 2742 (1998).

[164] T. J. Apollaro, A. Cuccoli, A Fubini, F. Plastina, and P. Verrucchi, *Phys. Rev. A* **77**, 062314 (2008).

[165] Y. V. Fyodorov, I. Y. Korenblit, and E. F. Shender, *Europhys. Lett.* **4**, 827 (1987).

[166] J. Kushauer and W. Kleemann, *J. Magn. & Magn. Mater.* **140–144**, 1551 (1995).

[167] S. Galam, C. S. O. Yokoi, and S. R. Salinas, *Phys. Rev. B* **57**, 8370 (1998).

[168] C. Paduani, D. P. Belanger, J. Wnag, H. S-J, and R. M. Nicklow, *Phys. Rev. B* **50**, 193 (1994).

[169] R. Yu, T. Roscilde, and S. Haas, *New. J. Phys.* **10**, 013034 (2008).

[170] S. W. Lovesey, *J. Phys. C* **1**, 102 (1968).

[171] S. Shinkevich, O. F. Syljuåsen, and S. Sebastian Eggert, *Phys. Rev. B* **83**, 054423 (2011).

[172] H. C. Hsu, J.-Y. Lin, W. L. Lee, M.-W. Chu, T. Imai, Y. J. Kao, C. D. Hu, H. L. Liu, and F. C. Chou, *Phys. Rev. B* **82**, 094450 (2010).

[173] S. Eggert, O. F. Syljuåsen, F. Anfuso, and M. Andres, *Phys. Rev. Lett.* **99**, 097204 (2007).

[174] J. Jensen and A. R. Mackintosh, *Rare earth magnetism - structures and excitations*, Clarendon press, Oxford, 1991.

[175] P. W. Anderson and H. Hasegawa, *Phys. Rev.* **100**, 675 (1955).

[176] G. A. Baker, Jr., G. S. Rushbrooke, and H. E. Hilbert, *Phys. Rev.* **135**, A1272 (1964).

[177] A. S. Arrott, *Phys. Rev. B* **31**, 2851 (1985).

[178] N. Elstner and A. P. Young, *Phys. Rev. B* **50**, 6871 (1994).

[179] M. Fähnle and J. Souletie, *Phys. Rev. B* **32**, 3328 (1985).

[180] E. Plekhanov, A. Avella, and F. Mancini, *J. Phys.: Conf. Ser.* **200**, 022047 (2010).

[181] S.-L. Drechsler, unpublished.

[182] M. E. Fisher, *Philosophical Magazin* **7**, 1731 (1962).

[183] D. V. Dmitriev and V. Y. Krivnov, *Phys. Rev. B* **79**, 054421 (2009).

[184] S. Nishimoto, S.-L. Drechsler, R. Kuzian, J. Richter, and J. van den Brink, *arXiv:1005.5500v2* (2010).

[185] R. Schöneberger, *Spezifische Wärme von* $La_{5/8-x}Pr_xCa_{3/8}MnO_3$ *und* Li_2CuO_2, PhD thesis, Universität zu Köln, 2002.

[186] J. Wosnitza, *J. Low Temp. Phys.* **147**, 249 (2007).

[187] K. G. Wilson, *Phys. Rev. B* **4**, 3174,3184 (1971).

[188] H. Kawamura, *J. Phys. Soc. Jpn.* **54**, 3220 (1985).

[189] H. Kawamura, *J. Phys. Soc. Jpn.* **55**, 2095 (1986).

[190] A. Pelissetto and E. Vicari, *Physics Reports* **368**, 549 (2002).

[191] J. M. Kosterlitz, D. R. Nelson, and M. E. Fisher, *Phys. Rev. B* **13**, 412 (1976).

[192] K. Niira, *Phys. Rev.* **117**, 129 (1960).

[193] A. R. Mackintosh, *Phys. Lett.* **4**, 140 (1963).

[194] M. Rotter, H. Müller, E. Gratz, M. Doerr, and M. Loewenhaupt, *Rev. Sci. Instrum.* **69**, 2742 (1998).

[195] L. Wang, *Thermal Expansion and Magnetostriction Studies on Iron Pnictides*, PhD thesis, Technische Universität Dresden, 2010.

[196] T. Lorenz, *Thermodynamische Eigenschaften des Spin-Peierls-Systems* $CuGeO_3$, PhD thesis, Universität zu Köln, 1998.

[197] H. Winkelmann, E. Gamper, B. Büchner, M. Braden, A. Revcelovschi, and G. Dhalenne, *Phys. Rev. B* **51**, 12884 (1994).

[198] M. J. Clark and T. F. Smith, *J. Low Temp. Phys.* **32**, 495 (1978).

[199] S. Alterovitz and D. E. Mapother, *Phys. Rev. B* **11**, 139 (1975).

[200] P. Horsch, M. Sofin, M. Mayr, and M. Jansen, *Phys. Rev. Lett.* **94**, 076403 (2005).

[201] S. van Smaalen, R. Dinnebier, and M. Jansen, *Acta Cryst.* **B63**, 17 (2007).

[202] S. Tornow, O. Entin-Wohlman, and A. Aharony, *Phys. Rev. B* **60**, 10206 (1999).

[203] H. Rosner, U. Nitzsche, R. Kuzian, and S.-L. Drechsler, unpublished.

Acknowledgements

My thesis defended by now, it is my strong desire and great pleasure to thank all the many people[1] that have had their share in this project. Within this record I am avoiding to use terms like "I did" and "my results" but speak of "we" and "our". Presenting here my very own work, clearly none of it is purely my own, but inspired and motivated throughout continuous discussions I have had with and the collaboration of a wide number of people. People actually, whose curiosity, endeavor, creativity, professionalism and not least whose kindness made this project a fascinating one to work on with pleasure.

Hence first of all I'd like to acknowledge the IFW-Dresden and the IFF in particular as a great environment to learn and work at, providing me with the opportunities to accomplish as much as I was able to in a field I knew little about when starting. As the major responsible for this I wish to thank Prof. B. Büchner, under whose auspices this thesis came into being, his generous support and various substantial, competent suggestions. The comprehensive support I got from Prof. Rüdiger Klingeler, concerning thermodynamics in particular, yet most importantly his teachings on scientific work in general are a key stone of this thesis. I have been greatly impressed by and profiting much from the unshared attention he showed to my questions at any occasion. I'd like to distinctly express my thank and respect to S.-L. Drechsler for all the many insightful discussions I have had with him, for his patience with my questions and his interest in my results. It was this a great pleasure, a strong motivation and hard to overestimate inspiration for my work.

The experiments presented in this thesis would not have been possible without the support of the many people I have been working with. First and most of all I owe my thank to Nadja Wizent for this great xtal of $^7Li_2CuO_2$ grown and for being moreover such a pleasant person to work with. For the results obtained in the neutron scattering experiments I have performed on that sample I wish to acknowledge the instrument scientists at the respective three-axis spectrometers, that is to Arno Hiess (IN8), Wolfgang Schmidt (IN12), Daniel Lamago (1T1) and Sylvain Petit (4F1&4F2). In this context I moreover thank Astrid Schneidewind and Peter Link for teaching and support and the highly appreciated cooperation with Wolf-Dieter Stein. Eventually, I am much obliged to Prof. M. Loewenhaupt, not just for having been the first at IN12 to recognize those sub-gap excitations as indeed systematic, but for suggesting me to get into this project at all. Moreover it was him to recom-

---

[1] I am afraid so, therefore please apologize if I forgot to mention further substantial support.

mend attending the HERCULES course I have been profiting much from[2] - a suggestion, that I wish to pass on to anyone starting out in neutron and/or X-ray scattering.

The experiments on the thermodynamic properties of Li_2CuO_2 have been performed with the support of the respective instrument responsibles, too. Explicitly I wish to express my thank to Norman Leps, whose insight into PPMS and MPMS systems was highly valuable, surpassed by his candid and pleasant interest to exchange experiences and to discuss new insights into our common business. For the MPMS measurements I wish to thank Sebastian Gass, too. For initiation into MPMS measurements under applied pressure I thank Markus Hücker. For the pulsed field magnetization measurements performed I wish to acknowledge my cooperation with Yurii Skourski. The PPMS data presented in this thesis have been obtained with pleasant support by Mahmoud Abdel-Hefaz Mohamed and K. Nenkov. For instructions on the details of the dilatometric measurement setup and for being such nice office mate I kindly thank Liran Wang. For discussions on those above thermodynamic methods I furthermore acknowledge Natalia Tristan, Ulrike Stockert and Anja U. B. Wolter, the later one moreover sharing her fascination on those blue crystals. For various helpful hints and discussions I furthermore owe thank to Yulieth Arango, Nikolai Hlubek and Saicharan Aswartham. For helpful discussion on their subject I wish to also express my thank to Christian Hess and Vladislav Kataev. I would also like to thank Prof. Andrey Zheludev for the great motivation and the discussion on a some of my neutron data provided in the finalizing stage of this project. Also I have been profiting from various kind discussions and e-mail exchange with Roman O. Kuzian, whom I wish to thank for patiently sharing his insight into various theoretical models and methods. For her friendly support on one project I owe thank to Christine Täschner. I furthermore wish to thank Falk Herold for the various, partially rather complex sample supports manufactured. For their very friendly organizational contributions to this project I own a great dept of gratitude to Mrs. Höllerer and Manja Maluck.

I have moreover been profiting much from my 'associate membership' at the IFP/TUD. Besides the chance to measure at the VSM I am much grateful for various discussions in particular to Julia Arndt, Mathias Dörr, 'one in a billion' Fei Tang, Mathias Frontzek, Hemke Maeter, Johannes Spehling, Elke Wachsmuth and once over Prof. M. Loewenhaupt.

Eventually, dear Sissi: I owe you one.

---

[2] Supported by IFF/IFW.

Erklärung

Diese Dissertation, "On the Spin-Dynamics of the Quasi-One-Dimensional, Frustrated Quantum Magnet Li_2CuO_2 - Studies by means of Inelastic Neutron Scattering and Thermodynamic Methods", wurde am Institut für Festkörperforschung des Leibniz Instituts für Festkörper- und Werkstoffforschung Dresden (IFW Dresden) unter der wissenschaftlicher Betreuung von Prof. Dr. Bernd Büchner angefertigt.
Hiermit versichere ich, dass ich die vorliegende Arbeit ohne unzulässige Hilfe Dritter und ohne Benutzung anderer als der angegebenen Hilfsmittel angefertigt habe; die aus fremden Quellen direkt oder indirekt übernommenen Gedanken sind als solche kenntlich gemacht. Die Arbeit wurde bisher weder im Inland noch im Ausland in gleicher oder ähnlicher Form einer anderen Prüfungsbehörde vorgelegt.

Ich erkenne die geltende Fassung der Promotionsordnung der Fakultät Mathematik und Naturwissenschaften an der Technischen Universität Dresden an.

Wolfram E. A. Lorenz Dresden,